



UNIVERSITÀ DI PISA
DIPARTIMENTO DI FISICA

Search for $\mu \rightarrow eX$ with the MEG II experiment
QED corrections with MCMULE and expected sensitivity

TESI DI LAUREA MAGISTRALE IN FISICA

Candidato
Andrea GURGONE

Relatori
Prof.ssa Angela PAPA
Prof. Adrian SIGNER

Anno Accademico 2019/2020

Contents

Acronyms	5
Introduction	7
1 QED corrections with MCMULE	11
1.1 Overview	11
1.2 Synopsis of QED	13
1.2.1 QED beyond leading order	14
1.2.2 QED beyond fixed order	16
1.3 FDF regularisation scheme	17
1.3.1 Dimensional regularisation	17
1.3.2 FDF formulation of DREG	17
1.4 FKS ^ℓ subtraction scheme	21
1.4.1 FKS: NLO scheme	22
1.4.2 FKS ² : NNLO extension	25
1.4.3 FKS ^ℓ : N ^ℓ LO generalisation	32
1.5 Structure of MCMULE	33
1.6 Monte Carlo integration	38
1.6.1 VEGAS algorithm	38
1.6.2 Phase-space generation	42
1.7 Implementing new processes in MCMULE	44
1.7.1 A working example: $\mu \rightarrow eX$	44
1.7.2 One calculation in MATHEMATICA	50
2 Muon decay $\mu \rightarrow e\nu\bar{\nu}$ at NNLO+LL	54
2.1 Theoretical model	54
2.1.1 Fermi theory	55
2.1.2 Neutrino average	57
2.2 Numerical setup	58
2.3 LO contribution	62
2.4 NLO corrections	66
2.5 NNLO corrections	73
2.6 LL corrections	82

2.7	Final results	86
2.7.1	Theoretical error	88
3	Muon decay $\mu \rightarrow eX$ at NLO	91
3.1	Theoretical model	91
3.2	QED corrections	94
3.3	Background comparison	100
4	The MEG II experiment at PSI	103
4.1	Muons at PSI	103
4.2	The MEG II experiment	106
4.2.1	Signal and background	106
4.2.2	Beamline and target	107
4.2.3	Photon calorimeter	108
4.2.4	Positron spectrometer	110
5	Search for $\mu \rightarrow eX$ with MEG II	113
5.1	MEG II beyond $\mu \rightarrow e\gamma$	113
5.2	MC event generator	115
5.3	Positron reconstruction	121
5.4	Positron energy spectrum	130
5.5	Expected sensitivity	134
5.5.1	Statistics	134
5.5.2	Systematics	136
6	Conclusion and outlook	139
A	Conventions	141
	Acknowledgement	142
	Bibliography	143

Acronyms

AIF	A nnihilation I n F light
ALP	A xion- L ike P article
BR	B ranching R atio
BTS	B eam T ransport S olenoid
CDCH	C ylindrical D rift C Hamber
CDR	C onventional D imensional R egularisation
CL	C onfidence L evel
cLFV	charged L epton F lavour V iolation
cLL	collinear L eading L ogarithm
COBRA	C Oonstant B ending R adius
CW	C ockcroft- W alton
DAQ	D ata A quisition
DREG	D imensional R EGularisation
ECR	E lectron C yclotron R esonance
EFT	E ffective F ield T heory
EW	E lectro W eak
FF	F ermi- F ierz
FDF	F our- D imensional formulation of FDH
FDH	F our- D imensional H elicity
FKS	F rixione- K unzt- S igner
HIP	H igh I ntensity P roton A ccelerator
HPL	H armonic P oly L ogarithm
IR	I nfra R ed
KLN	K inoshita- L ee- N auenberg
LF	L epton F lavour
LL	L eading L ogarithm
LO	L eading O der
LXe	L iquid X enon

MC	Monte Carlo
McMule	Monte carlo for Muons and other leptons
MEG	Mu to E and Gamma
$\overline{\text{MS}}$	Modified Minimal Subtraction
NLL	Next-to-Leading Logarithm
NLO	Next-to-Leading Order
NNLO	Next-to-Next-to-Leading Order
NP	New Physics
OS	On-Shell
QED	Quantum Electrodynamics
QFT	Quantum Field Theory
RDC	Radiative Decay Counter
RF	Radio Frequency
RMD	Radiative Muon Decay
sLL	soft Leading Logarithm
SM	Standard Model
SiPM	Silicium PhotoMultiplier
SSB	Spontaneous Symmetry Breaking
TOF	Time Of Flight
TDAQ	Trigger and Data Acquisition
PCS	Pseudo-Collinear Singularity
PDF	Probability Density Function
PDG	Particle Data Group
PID	Particle Identification
PMT	PhotoMultiplier Tube
PNGB	Pseudo-Nambu-Goldstone Boson
PQ	Peccei-Quinn
PS	Parton Shower
PSI	Paul Scherrer Institut
pTC	pixelated Timing Counter
PV	Passarino-Veltman
UL	Upper Limit
UV	UltraViolet
VUV	Vacuum UltraViolet
YFS	Yennie-Frautschi-Suura

Introduction

The Standard Model (SM) provides a comprehensive description of the fundamental constituents of matter and their interactions, supported by an unprecedented number of experimental tests. However, it is unable to explain several known phenomena, such as the matter-antimatter asymmetry in the Universe, the origin of neutrino mass, the existence of dark matter and energy. These failures motivate the search for a more fundamental theory of particle physics, usually referred to as New Physics (NP).

In addition to the on-shell production of new particles in high-energy collisions, the search for signals beyond the SM can be pursued through precision measurements of flavour physics. In this context, a key tool is provided by the search for charged Lepton Flavour Violation (cLFV), especially in processes involving muons like $\mu \rightarrow e\gamma$, $\mu \rightarrow eee$ or $\mu N \rightarrow eN$ [1]. In fact, although the discovery of neutrino oscillation showed that lepton flavour is not a sacred symmetry of Nature [2], so far no evidence of cLFV has been reported [3]. Specifically, lepton flavour is an exact symmetry of the SM with massless neutrinos, albeit its origin is an accidental consequence of the formal request of renormalisable interactions. And even assuming non-vanishing mass for neutrinos, the SM predicts unmeasurable branching ratios of $\mathcal{O}(10^{-55})$ for cLFV processes. Consequently, the observation of such a violation would be an unambiguous signature of NP.

The MEG II experiment [4] at the Paul Scherrer Institut (PSI) searches the cLFV decay $\mu^+ \rightarrow e^+\gamma$ using a continuous beam of $7 \cdot 10^7$ antimuons per second, obtained from the most intense proton beam in the world [5]. In three years of data acquisition the experiment is expected to reach a sensitivity of one order of magnitude below the upper limit on the branching ratio set by the previous MEG experiment [6] to $\mathcal{B}(\mu^+ \rightarrow e^+\gamma) < 4.2 \cdot 10^{-13}$ at 90% of confidence level (CL) [7].

Furthermore, MEG II appears to be competitive in searching more exotic processes, in which the lepton flavour violation is mediated by a light scalar boson X^0 , which may be identified as a pseudo-Nambu-Goldstone boson (PNGB) arising from a spontaneous breaking of a global $U(1)$ symmetry [8–10]. Typical examples are the majoron [11–13], the familon [14–16] and the axion [17–20], that are respectively associated with the spontaneous breaking of the lepton number, the lepton family number and the Peccei-Quinn (PQ) symmetry. The search for such axion-like particles (ALPs) is an unique opportunity

for the MEG II experiment to complement the main search for $\mu \rightarrow e\gamma$ with additional competitive physics channels.

The aim of this thesis is to study the feasibility of searching for the two-body decay $\mu^+ \rightarrow e^+X$ with the MEG II experiment, addressing the theoretical and the experimental difficulties of hunting such an elusive signal. In fact, since the light particle X cannot be detected, the only signature of $\mu^+ \rightarrow e^+X$ is a monochromatic signal in the high-energy region of the positron spectrum, which has to be reconstructed with the highest precision possible. The MEG II spectrometer appears to be a suitable detector with its new ultra-low mass Cylindrical Drift Chamber (CDCH) providing an energy resolution of approximately 100 keV for 50 MeV positrons [21–23]. The most stringent limit on the branching ratio of the decay was set by the TWIST experiment [24] at TRIUMF. Depending on the assumed couplings and masses for X , the TWIST result varies up to $\mathcal{B}(\mu^+ \rightarrow e^+X) < 5.8 \cdot 10^{-5}$ at 90% of CL [25]. To reach such a sensitivity, an accurate theoretical evaluation of the SM background $\mu^+ \rightarrow e^+\nu_e\bar{\nu}_\mu$ as well as an exhaustive Monte Carlo (MC) simulation of the experimental setup are essential. Both are goals of this thesis.

Since the SM is not an exactly solvable theory, the development of more precise experiments has to be accompanied by the computation of more accurate theoretical predictions. The necessity to provide reliable predictions for the new generation of experiments at the intensity frontier led to the creation of MCMULE, or Monte Carlo for MUons and other LEptons. MCMULE is a unified framework for the numerical computation of higher-order QED corrections for low-energy scattering and decay processes involving leptons [26–28]. Loop divergences are regularised applying the FDH and FDF formulations of dimensional regularisation [29–32], while renormalisation is performed in OS and $\overline{\text{MS}}$ schemes. Soft singularities arising from the phase-space integration are subtracted employing the novel FKS^ℓ scheme [33–35] and cancelled with the soft poles emerging from the loop integration. Furthermore, collinear singularities are eliminated by keeping all fermion masses non-vanishing. The FKS^ℓ treatment of phase space allows its numerical integration in four dimensions, performed through the adaptive MC algorithm VEGAS [36–38], based on importance sampling. The software is written in FORTRAN95 with the addition of supplementary tools in Python and MATHEMATICA, respectively for data analysis and analytical calculations.

Besides the implementation and computation of the two muon decays $\mu \rightarrow eX$ and $\mu \rightarrow e\nu\bar{\nu}$ at the required accuracy, an important purpose of this thesis is therefore to test, debug, optimise and further develop MCMULE as a valuable tool for the forthcoming experiments with leptons. Moreover, this project constitutes an important benchmark of the entire MCMULE framework, being its first direct application to an experimental problem. Last but not least, the thesis aspires to be a guide on how to implement new

processes in the code and analyse the results, specifically tuned for other master students that desire to work on MCMULE.

The signal $\mu \rightarrow eX$ is described using a low-energy effective field theory (EFT), derived assuming the spontaneous breaking of a model-independent $U(1)$ flavour symmetry. The resulting leading order (LO) is then complemented with the QED next-to-leading order (NLO) corrections, including diagrams with an additional virtual or real photon. In particular, the potential emission of a real photon makes the signal spectrum no longer perfectly monochromatic, due to the addition of a smooth radiative tail.

The SM background $\mu \rightarrow e\nu\bar{\nu}$ is computed up to next-to-next-to-leading order (NNLO), including diagrams with two-loop, two real photons and one-loop with one real photon. However, the potential emission of soft photons makes the QED corrections arbitrarily large in proximity of the high-energy endpoint $E_e^{\max} \simeq m_\mu/2$, introducing asymptotic terms proportional to the soft logarithm $\log(1 - 2E_e/m_\mu)$. Moreover, the presence of the collinear logarithm $\log(m_\mu^2/m_e^2)$ further increases the strength of radiative corrections. The combination of these two factors makes the fixed-order calculations no longer sufficient to achieve the precision required for searching $\mu \rightarrow eX$ in the high-energy region of positron spectrum. The problem is addressed resumming the analytical soft leading logarithms (sLL) terms to all orders, exploiting the Yennie-Frautschi-Suura (YFS) exponentiation for QED soft singularities [39]. The soft resummation is complemented with the inclusion of the analytical collinear leading logarithms (cLL) terms contained in the N³LO corrections.

All calculations are fully differential, i.e. allow to compute any differential distribution $d^n\Gamma/(dx_1 \dots dx_n)$, where $x_1 \dots x_n$ is an arbitrary set of inclusive observables, each of which can be generically constrained to reproduce experimental acceptances and cuts. Furthermore, all calculations include the effect due to a generic muon polarisation as well as the full dependency from the electron mass. On this basis, the computation of $\mu \rightarrow e\nu\bar{\nu}$ presented in this thesis constitutes the most precise fully differential predictions ever made for such a decay, giving a concrete proof of MCMULE's great potential.

For both decays, the thesis specifically presents the computation of the polarised double-differential decay width $\mathcal{G}_e = d^2\Gamma/(dE_e d\cos\theta_e)$, where θ_e is the angle between the muon polarisation and the positron momentum. The knowledge of \mathcal{G} is then exploited to develop a new MC positron event generator in GEANT4, which has been included in the MEG II simulation and analysis software [40], replacing the former implementation of $\mu \rightarrow eX$ at LO and $\mu \rightarrow e\nu\bar{\nu}$ at NLO.

After the validation of the new MC generator, the MEG II simulation framework is used to study the experimental reconstruction of positrons, both for $\mu \rightarrow eX$ and $\mu \rightarrow e\nu\bar{\nu}$. More

precisely, all simulations are repeated with and without the new radiative corrections, in order to evaluate their effect on the reconstructed variables and assess the need for even more refined calculations. Furthermore, after evaluating the spectrometer performances, the expected positron energy spectrum is fitted considering the experimental acceptances and resolutions, as well as the updated theoretical predictions.

The result is employed to estimate the upper limit which MEG II could set on $\mathcal{B}(\mu \rightarrow eX)$ at 90% of CL, applying a cut-and-count approach. In addition to the statistical effects, the evaluation considers the theoretical uncertainty and the systematic errors arising in the measurement of positron energy. Furthermore, the expected sensitivity is estimated for different masses of X in the range 0 – 40 MeV, assuming isotropic, left-handed or right-handed couplings. The latter option is particularly promising, because the muon polarisation effect can be used to reject the left-handed SM background.

The thesis is organised as follows. In Chapter 1 we present the MCMULE theoretical and numerical framework, describing its general and technical aspects. In Chapter 2 we exhibit the numerical computation of the background $\mu \rightarrow e\nu\bar{\nu}$ at NNLO with MCMULE and the analytical calculation of LL contribution. Similarly, Chapter 3 is dedicated to the numerical computation of the signal $\mu \rightarrow eX$ at NLO. Chapter 4 describes the MEG II experiment and its potential in searches besides $\mu \rightarrow e\gamma$. In Chapter 5 we study the expected sensitivity of the experiment on $\mu \rightarrow eX$, after implementing a new MC event generator based on the theoretical calculations of the previous chapters. Finally, in Chapter 6 we examine the future prospect of this work, discussing the further development of MCMULE and the upcoming physics runs of MEG II. Appendix A summarises the conventions used throughout the text.

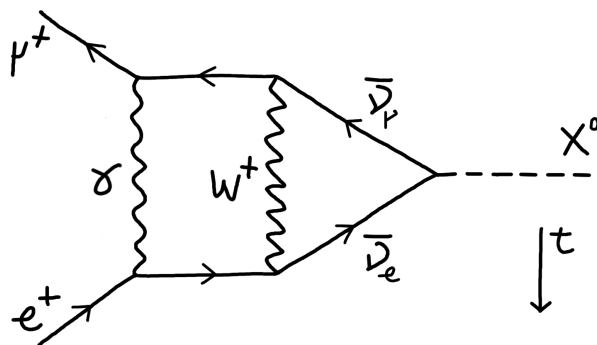


Figure Virtual correction to $\mu^+ \rightarrow e^+ X$ according to the majoron model.

Chapter 1

QED corrections with McMULE

1.1 Overview

MCMULE¹ is a novel framework for the numerical computation of fully differential higher-order QED corrections for decay and scattering processes involving leptons [26–28]. Loop divergences are regularised using the FDH or FDF formulations of dimensional regularisation [29–32], while renormalisation is performed in OS or $\overline{\text{MS}}$ scheme. Soft singularities arising from the phase-space integration are subtracted employing the novel FKS^ℓ scheme [33–35] and cancelled with the soft poles emerging from the loop integration. Furthermore, collinear singularities are eliminated by keeping all fermion masses non-vanishing. This results in a substantial complication of multi-loop amplitudes, eventually affordable through the massification procedure [41–45], which allows to obtain the leading mass terms from the massless amplitudes. The FKS^ℓ treatment of phase space allows its numerical integration in four dimensions, performed through the adaptive MC algorithm VEGAS [36, 37], based on importance sampling. The software is written in FORTRAN95 with the addition of supplementary tools in Python and MATHEMATICA, respectively for data analysis and analytical calculations.

The public version of the code² can be found at

<https://gitlab.com/mule-tools/mcmule>

The list of the implemented processes is provided in Table 1.1.

MCMULE aims to provide accurate theoretical predictions for the new generation of experiments at the intensity frontier, such as MEG II [7], Mu3e [46, 47] and MUSE [48] at PSI, Belle II [49, 50] at KEK, MUonE [51–53] at CERN, Padme [54] at LNF and P2 [55] at MESA, including potential applications to the future lepton colliders [56–62]. The

¹Monte Carlo for MUons and other LEptons.

²Authors: P. Banerjee, T. Engel, A. Gurgone, N. Schalch, A. Signer and Y. Ulrich.

Fermilab experiments $g - 2$ [63] and Mu2e [64], as well as their respective counterparts at J-PARC [65, 66], are not omitted by chance, since MCMULE is not designed for $g - 2$ or nuclear conversion calculations. The same holds for the precision experiments based on hadronic collider, such as LHCb Upgrade [67].

The ultimate precision of these experiments requires in many cases the computation of the QED corrections up to NNLO for several leptonic processes. The creation of a unified framework for the systematic and fully differential calculation of these corrections is MCMULE's main goal. Specifically, even if several of these processes were already computed up to NNLO, MCMULE represents the first comprehensive framework that includes all of them in fully differential way, thus allowing theoretical studies with arbitrary observables and cuts. In this context, MCMULE is designed also for experimental users, since running it does not require any knowledge of higher-order QFT. Specifically, MCMULE allows to get the expected distribution for any user-defined observable with the further possibility of implementing the detector acceptances as well as trigger preselections. Hence, MCMULE's results can be extensively used both in the planning and data analysis phase of an experiment. Besides the several experimental applications, MCMULE constitutes a comprehensive set of tools for the theoretical study of low-energy processes at unprecedented precision.

Process	Order	Status	Process	Order	Status
$\ell' \rightarrow \ell\nu\bar{\nu}$	NNLO	* *	$ee \rightarrow \nu\bar{\nu}$	NNLO	*
$\ell' \rightarrow \ell\nu\bar{\nu}\gamma$	NLO	*	$ee \rightarrow ee$	NNLO	†
$\ell' \rightarrow \ell\ell\ell\nu\bar{\nu}$	NLO	*	$e\mu \rightarrow e\mu$	NNLO	†
$\ell' \rightarrow \ell\nu\bar{\nu}\gamma\gamma$	LO	*	$ee \rightarrow \mu\mu$	NNLO	†
$\ell' \rightarrow \ell X$	NLO	* *	$ee \rightarrow \gamma\gamma$	NNLO	†
$\ell' \rightarrow \ell X\gamma$	NLO	†	$\ell p \rightarrow \ell p$	NNLO	*

Table 1.1 List of implemented (*) or currently in implementation (†) processes. The decays discussed in this thesis are denoted with (*). Furthermore $\ell = \{e, \mu, \tau\}$.

In the following we describe the mentioned theoretical and numerical tools. We start in Section 1.2 with a brief summary of QED to fix notations and concepts, while in Section 1.3 we introduce the FDF formulation of dimensional regularisation. We continue in Section 1.4 with a detailed discussion of FKS ^{ℓ} scheme, the true theoretical pillar of the numerical algorithm. Finally, we present the MCMULE code, describing its general structure in Section 1.5 and the MC algorithm in Section 1.6. In Section 1.7 we briefly explain how to implement a new process in MCMULE, referring to $\mu \rightarrow eX$ as a working example.

1.2 Synopsis of QED

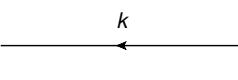
Quantum Electrodynamics (QED) is the relativistic quantum field theory describing the electromagnetic interaction between fermions and photons. The well-known $U(1)$ gauge-invariant Lagrangian of QED is

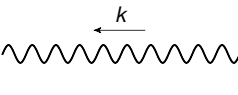
$$\begin{aligned}\mathcal{L}_{\text{QED}} &= -\frac{1}{4}F_{\mu\nu}F^{\mu\nu} + \sum_i \bar{\psi}_i(i\gamma^\mu D_\mu - m_i)\psi_i \\ &= -\frac{1}{4}F_{\mu\nu}F^{\mu\nu} + \sum_i \bar{\psi}_i(i\gamma^\mu \partial_\mu - e\gamma^\mu A_\mu - m_i)\psi_i\end{aligned}\tag{1.1}$$

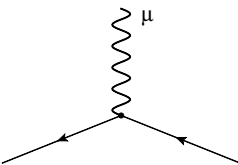
where ψ_i denotes the spinor field of the i -th fermionic flavour, $F_{\mu\nu} = \partial_\mu A_\nu - \partial_\nu A_\mu$ the electromagnetic field tensor, A_μ the photon field and $D_\mu = \partial_\mu + ieA_\mu$ the gauge covariant derivative, which defines the interactions between fermions and photons. Like any quantum field theory of phenomenological relevance, QED is not exactly solvable. Nevertheless, perturbation theory is a well-established tool to provide accurate theoretical descriptions of QED scattering and decay processes. Specifically, we can expand a cross section or a decay width according to

$$\sigma = \sigma^{(0)} + \left(\frac{\alpha}{\pi}\right)^1 \sigma^{(1)} + \left(\frac{\alpha}{\pi}\right)^2 \sigma^{(2)} + \left(\frac{\alpha}{\pi}\right)^3 \sigma^{(3)} + \dots\tag{1.2}$$

where $\alpha = e^2/4\pi \simeq 1/137$ is the electromagnetic coupling. The term $\sigma^{(0)}$ constitutes the leading order (LO) of the expansion, $\sigma^{(1)}$ the next-to-leading order (NLO), $\sigma^{(2)}$ the next-to-next-to-leading order (NNLO) and so on. A simple way to get transition amplitudes in perturbation theory is drawing all connected and amputated Feynman diagrams with a fixed number of vertices and applying the relative Feynman rules. The well-know QED rules are given by

Fermion propagator:  = $\frac{i(\not{k} + m)}{p^2 - m^2 + i\epsilon}$

Photon propagator:  = $\frac{-i}{k^2 + i\epsilon} \left(g_{\mu\nu} - (1 - \xi) \frac{k_\mu k_\nu}{k^2} \right)$

QED vertex:  = $-ie\gamma^\mu$

where ξ is the gauge-fixing parameter, arising from the unphysical term

$$\mathcal{L}_{\text{QED}} \longrightarrow \mathcal{L}_{\text{QED}} - \frac{1}{2\xi} \partial_\mu A^\mu \partial_\nu A^\nu \quad (1.3)$$

added to (1.1) in order to properly quantise the theory in the path integral formalism. In this thesis we assume the Feynman - 't Hooft gauge $\xi = 1$.

All diagrams are formally distinguished between tree-level and loop diagrams, where the latter class includes all diagrams with at least one internal momentum not fixed by the momenta of the external particles. To simplify the discussion, we assume that only tree-level diagrams contribute to $\sigma^{(0)}$. In other words, we do not consider loop-induced processes such as $\gamma\gamma \rightarrow \gamma\gamma$. Accordingly, an arbitrary term $\sigma^{(\ell)}$ gets contributions from diagrams containing up to ℓ loops. At LO the cross section for a process with n particles in the final state is obtained by integrating the squared tree-level amplitude $\mathcal{A}_n^{(0)}$ over the Born phase space $d\Phi_n$

$$\sigma^{(0)} = \int d\Phi_n |\mathcal{A}_n^{(0)}|^2 = \int d\Phi_n \mathcal{M}_n^{(0)} \quad (1.4)$$

where we have introduced the LO (squared) *matrix element* $\mathcal{M}_n^{(0)}$.

1.2.1 QED beyond leading order

The higher-order contributions to a cross section or decay width are commonly divergent, due to the integration over the unresolved loop momenta. Such integrals can be divergent for large or small momenta. In the first case, we talk about ultraviolet (UV) singularities, while in the latter of infrared (IR) singularities, distinguishing between soft and collinear divergences. The first step to address all of them is to define a *regularisation* procedure, in order to parametrise the singular contributions. In MCMULE this is achieved through dimensional regularisation (DREG), in which the four dimensional space-time is generalised to an arbitrary dimension $d \equiv 4 - 2\epsilon$. Remarkably, this approach regularises all the unphysical divergences preserving the gauge and Lorentz invariances of the theory. We will discuss DREG and its FDF formulation (used in this thesis) in Section 1.3.

UV divergences

The UV divergences can be eliminated applying the *renormalisation* procedure. The idea is to redefine the *bare* parameters and fields in (1.1) in order to absorb all UV singularities. Hence, we define the *renormalised* parameters and fields of the theory as

$$\psi_i = Z_{2,i}^{1/2} \psi_{i,r} \quad m_i = Z_{m,i} m_{i,r} \quad A^\mu = Z_3^{1/2} A_r^\mu \quad e = \frac{Z_1}{Z_{2,i} \sqrt{Z_3}} e_r \quad (1.5)$$

where we introduced the *renormalisation constants* Z_i . Substituting the renormalised quantities into the *bare Lagrangian* (1.1), we obtain

$$\mathcal{L} = -\frac{1}{4}Z_3 F_{\mu\nu}^r F_r^{\mu\nu} + \sum_i Z_{2,i} \bar{\psi}_{i,r} (i\cancel{\partial}_\mu - Z_{m,i} m_{i,r}) \psi_{i,r} - \sum_i Z_1 e_r \bar{\psi}_{i,r} \cancel{A}_r \psi_{i,r} \quad (1.6)$$

The Ward–Takahashi identity for QED imposes to all orders

$$Z_1 = Z_{2,i} \quad (1.7)$$

for all flavours i . Since we need to introduce only a finite number of renormalisation constants Z_i to absorb all UV singularities of an arbitrary diagram, QED is called a *renormalisable theory*. It is easy to show that this property holds because the electromagnetic coupling α is dimensionless. The divergent part of every Z_i is uniquely fixed by the requirement that all UV singularities are absorbed. In DREG this is equivalent to requiring all poles $1/\epsilon_{\text{UV}}$ to cancel. However, we need to choose a suitable *renormalisation scheme* to systematically treat the finite parts $\mathcal{O}(\epsilon_{\text{UV}}^0)$ of every Z_i . In MCMULE the default choice is the On-Shell (OS) scheme, which is constructed to reproduce the classical limit for the input parameters at $Q^2 = 0$ as faithfully as possible, where Q is the typical energy of the process. Since MCMULE is designed for low-energy processes, the OS scheme can be used to its full potential. Alternatively, we employ the modified Minimal Subtraction ($\overline{\text{MS}}$) scheme, especially for contributions beyond the SM. In the $\overline{\text{MS}}$ scheme only the UV poles and the common factors $\sim (\ln 4\pi - \gamma_E)$ with $\gamma_E \approx 0.577$ are subtracted from the amplitudes.

IR divergences

After the UV renormalisation, the loop integrals are still IR divergent. According to the Kinoshita-Lee-Nauenberg (KLN) theorem [68, 69], the IR singularities arising from the integration over ℓ loops are eliminated by the ones arising from the phase-space integration over the emission of ℓ additional photons. In DREG this means that the poles $1/\epsilon_{\text{IR}}$ due to ℓ loops are exactly cancelled by the poles $1/\epsilon_{\text{IR}}$ due to ℓ extra photons in the final state. To understand the classification of the IR singularities into soft and collinear, we consider the emission of a real photon with energy E_γ from a charged fermion with velocity β . The corresponding matrix element \mathcal{M}_{n+1} is proportional to

$$\mathcal{M}_{n+1}^{(\ell)} \propto \frac{1}{E_\gamma^2} \frac{1}{1 - \beta \cos \theta} \quad (1.8)$$

where θ is the angle between the photon and the fermion. The expression is divergent both in the *soft limit* $E_\gamma \rightarrow 0$ and in the *collinear limit* $\theta \rightarrow 0$ with $\beta \rightarrow 1$. According to the KLN theorem, the soft and collinear singularities due to the real emissions cancel

their respective counterparts in loops. Since there are no massless charged fermions, the collinear singularities can occur only if the fermion mass is neglected to simplify the loop calculation. In MCMULE all fermion masses are kept non-vanishing. This choice complicates the computation of integrals, but eliminates any collinear singularity in loops and phase spaces. We will discuss in depth how MCMULE systematically treat the soft singularities in Section 1.4.

1.2.2 QED beyond fixed order

If a process features widely different kinematic scales μ_i , logarithms as $L = \log(\mu_1/\mu_2)$ can become very large, enhancing the perturbative corrections. Specifically, each new loop not only introduces a new power of α but also two powers of L , one due to soft emissions and one due to collinear emissions. For sufficiently large values of L , this spoils the convergence of the QED perturbative expansion. Accounting for the logarithm pattern, we can rewrite (1.2) as

$$\begin{aligned} \sigma &= \sigma_{0,0} + \left(\frac{\alpha}{\pi}\right)^1 L^2 \sigma_{1,2} + \left(\frac{\alpha}{\pi}\right)^1 L^1 \sigma_{1,1} + \left(\frac{\alpha}{\pi}\right)^1 L^0 \sigma_{1,0} \\ &+ \left(\frac{\alpha}{\pi}\right)^2 L^4 \sigma_{2,4} + \left(\frac{\alpha}{\pi}\right)^2 L^3 \sigma_{2,3} + \left(\frac{\alpha}{\pi}\right)^2 L^2 \sigma_{2,2} + \left(\frac{\alpha}{\pi}\right)^2 L^1 \sigma_{2,1} + \left(\frac{\alpha}{\pi}\right)^2 L^0 \sigma_{2,0} \quad (1.9) \\ &+ \left(\frac{\alpha}{\pi}\right)^3 L^6 \sigma_{3,6} + \left(\frac{\alpha}{\pi}\right)^3 L^5 \sigma_{3,5} + \left(\frac{\alpha}{\pi}\right)^3 L^4 \sigma_{3,4} + \dots \end{aligned}$$

The rows of the equation correspond to the *fixed-order* terms of (1.2). Excluding the LO term $\sigma_{0,0}$, the first column (or *tower*) is known as leading logarithm (LL) contribution, the second as next-to-leading logarithm (NLL) and so on. We can improve the QED perturbation theory by including the dominant terms according to the powers of $\alpha L^2/\pi$ instead of simply α/π . Since the logarithm-driven terms usually follow a predictable pattern, it is possible to include the dominant columns of (1.9) to all orders. This procedure is known as *resummation*. A generic and powerful way to resum the entire LL tower is the implementation of a QED *parton shower* (PS), which accounts for the emission of cascades of soft and collinear photons. Any logarithmic resummation needs to be properly matched to the fixed-order calculations, in order to avoid double counting between the rows and the columns of (1.9).

1.3 FDF regularisation scheme

1.3.1 Dimensional regularisation

As already mentioned, amplitudes with at least one loop are usually divergent and require to be regularised. In MCMULE this is achieved using DREG [70, 71], i.e. shifting the space-time dimensionality from four to

$$d \equiv 4 - 2\epsilon \quad (1.10)$$

thus $\epsilon \rightarrow 0$ for $d \rightarrow 4$. The loop integration measure is accordingly changed to

$$\int \frac{d^4 k}{(2\pi)^4} \longrightarrow \mu^{4-d} \int \frac{d^d k_{[d]}}{(2\pi)^d} \equiv \int [dk] \quad (1.11)$$

where μ is an arbitrary mass scale, introduced by rescaling the coupling as

$$\alpha_{[d]} \rightarrow \mu^{4-d} \alpha_{[4]} \quad (1.12)$$

In this way, the UV and IR divergences manifest as $1/\epsilon^n$ poles, allowing us to express the loop integrals as Laurent series around $\epsilon \sim 0$.

At this point, we note that (1.11) only specifies the dimensionality of k without introducing any constraint on the dimensionality of other objects such as the γ -matrices or external momenta. This observation results in several formulations of DREG, based on different treatments of the various dimensionalities. The most common schemes are HV [72], CDR [73], FDH [29, 30] and FDF [31]. For a recent review see [32].

1.3.2 FDF formulation of DREG

In the following we introduce FDF, the formulation of DREG used in this thesis. The idea behind FDF is to deal with the loop integrals as much as possible in four dimensions, in order to simplify their computation and regularise the divergences at the same time. Conversely, in the conventional CDR all quantities are d -dimensional, including γ -matrices and external momenta. This traditional approach not only results in a substantial complications of algebraic calculations, but also complicates the application of a subtraction scheme such as FKS^ℓ. We will discuss this aspect in Section 1.4.

Following [27, 32], the formal construction of FDF can be understood introducing the four-dimensional Minkowski space $S_{[4]}$ and the two infinite-dimensional Hilbert spaces $QS_{[d]}$ and $QS_{[-2\epsilon]}$. The two $QS_{[\text{dim}]}$ spaces are equipped with a Minkowski-like metric

tensor fulfilling the formal condition

$$\text{QS}_{[\text{dim}]} \longrightarrow \left(g_{[\text{dim}]}^{\mu\nu} \right)^2 = \text{dim} \quad (1.13)$$

i.e. they have a finite quasi-dimensionality dim . The hierarchy between these spaces is

$$\text{S}_{[4]} \subset \text{QS}_{[d]} \quad \text{QS}_{[d]} = \text{S}_{[4]} \oplus \text{QS}_{[-2\epsilon]} \quad (1.14)$$

Hence, we can write

$$g_{[d]}^{\mu\nu} = g_{[4]}^{\mu\nu} + g_{[-2\epsilon]}^{\mu\nu} \quad \gamma_{[d]}^\mu = \gamma_{[4]}^\mu + \gamma_{[-2\epsilon]}^\mu \quad (1.15)$$

from which we obtain the relations

$$(g_{[d]} g_{[-2\epsilon]})^\mu{}_\nu = 0 \quad \{\gamma_{[\text{dim}]}^\mu, \gamma_{[\text{dim}]}^\nu\} = 2g_{[\text{dim}]}^{\mu\nu} \quad \{\gamma_{[d]}^\mu, \gamma_{[-2\epsilon]}^\nu\} = 0 \quad (1.16)$$

The four rules of FDF

At this point we can write the loop momentum k as

$$k_{[d]}^2 = (k_{[4]} + k_{[-2\epsilon]})^2 = k_{[4]}^2 + k_{[-2\epsilon]}^2 \equiv k_{[4]}^2 - \mu^2 \quad (1.17)$$

where we have denoted with $-\mu^2$ the square of the $(2-\epsilon)$ -dimensional component of the loop momentum³. For γ -matrices the split is realised by setting [32]

$$\not{k}_{[d]} = \not{k}_{[4]} + i\gamma^5 \mu \quad (\text{Rule I})$$

The systematic substitution of [Rule I](#) allows to perform all the algebraic calculations involving γ -matrices in $\text{S}_{[4]}$, i.e. in four dimensions. Furthermore, all external momenta are kept in four dimensions. The side effect is the appearance of μ -terms, nevertheless they can be simplified by applying [31, 32]

$$\text{Odd powers of } \mu \text{ are vanishing} \quad (\text{Rule II})$$

After completing the γ -matrices algebra, the loop integrand will feature $k_{[4]}^2$ -terms at numerator and $k_{[d]}^2$ -terms at denominator. In fact, the latter were not touched by [Rule I](#). To simplify terms of this kind, we can reverse (1.17) by applying

$$\int [dk] \frac{k_{[4]}^2}{k_{[d]}^2 \mathcal{D}_2 \cdots \mathcal{D}_n} = \int [dk] \frac{1}{\mathcal{D}_2 \cdots \mathcal{D}_n} + \int [dk] \frac{\mu^2}{k_{[d]}^2 \mathcal{D}_2 \cdots \mathcal{D}_n} \quad (\text{Rule III})$$

³It has not to be confused with the mass scale μ introduced in (1.12)

where we denoted with \mathcal{D}_i the usual factors introduced at denominator by propagators. At this stage the numerators will include only terms as $k_{[4]} \cdot p_{[4]}$, where $p_{[4]}$ denotes any external momenta. Since external momenta have no contributions in $\text{QS}_{[-2\epsilon]}$, such terms are equivalent to $k_{[d]} \cdot p_{[4]}$. Hence, we can set $k_{[4]} \rightarrow k_{[d]}$ and solve the μ -independent integrals using the standard loop calculus. To solve the remaining μ -integrals we can exploit the propriety [74]

$$\int [d^d k] \frac{(\mu^2)^r}{\mathcal{D}_1 \cdots \mathcal{D}_n} = -\epsilon (4\pi)^r \frac{\Gamma(r - \epsilon)}{\Gamma(1 - \epsilon)} \int [d^{d+2r}] \frac{1}{\mathcal{D}_1 \cdots \mathcal{D}_n} \quad (\text{Rule IV})$$

where $r \in \mathbb{N}$.

We have defined a formal procedure to regularise the UV and IR singularities arising from loop integration. In contrast to CDR, this was achieved without introducing unnecessary terms due to the extension in d dimensions of algebraic objects such as γ -matrices. Nevertheless, the results obtained though the two schemes are totally equivalent. At one-loop level and in absence of massless flavours (i.e. collinear singularities), the matrix elements computed in the two schemes are related by [32]

$$\mathcal{M}_{\text{FDF}}^{(1)} = \frac{\mathcal{M}_{\text{FDF}}^{(0)}}{\mathcal{M}_{\text{CDR}}^{(0)}} \mathcal{M}_{\text{CDR}}^{(1)} \quad (1.18)$$

The dependency on the regularisation scheme disappears at cross-section level, once integrating over the phase space.

γ^5 in FDF

So far we have not discussed the treatment of γ^5 in FDF. In $S_{[4]}$ the fifth γ -matrix γ^5 is defined through the two equivalent relations

$$\{\gamma_{[4]}^\mu, \gamma_{[4]}^5\} \equiv 0 \quad (1.19)$$

$$\gamma_{[4]}^5 \equiv \frac{i}{4!} \varepsilon_{\mu\nu\rho\sigma}^{[4]} \gamma_{[4]}^\mu \gamma_{[4]}^\nu \gamma_{[4]}^\rho \gamma_{[4]}^\sigma \equiv \frac{i}{4!} \varepsilon_{[4]} \Gamma_{[4]} \quad (1.20)$$

However, the equivalence between these two relations fails in d dimensions, because $\gamma^5 \propto \varepsilon_{[4]} \Gamma_{[d]}$ anti-commutes with each γ^μ for even values of d , but commutes for odd values of d . In DREG there are two common ways to approach the problem: choose one of the two relations as the *true* definition of γ^5 and generalise it to any dimension. Accordingly, one possible solution is to algebraically define γ_{AC}^5 so that the anti-commutator vanishes [75, 76]

$$\{\gamma_{\text{AC}}^5, \gamma_{[d]}^\mu\} \equiv 0 \quad (1.21)$$

The second possible solution, proposed by Breitenlohner and Maison [77], is to satisfy the

trace relation by setting

$$\gamma_5^{\text{BM}} \equiv \frac{i}{4!} \varepsilon_{[4]}^{\mu\nu\rho\sigma} \Gamma_{[d]} \quad (1.22)$$

In FDF we have unconsciously chosen this approach applying [Rule I](#). In fact, due to our construction of $\text{QS}_{[-2\epsilon]}$, the FDF's γ^5 is not completely anti-commuting [\[78\]](#). Specifically, assuming $\gamma^5 = \gamma_{\text{BM}}^5$, we find the (anti-)commutation relations

$$\{\gamma_{\text{BM}}^5, \gamma_{[4]}^\mu\} = 0 \quad [\gamma_{\text{BM}}^5, \gamma_{[-2\epsilon]}^\mu] = 0 \quad \{\gamma_{\text{BM}}^5, \gamma_{[d]}^\mu\} = 2\gamma_{[-2\epsilon]}^\mu \gamma_{\text{BM}}^5 \quad (1.23)$$

As a side effect, the definition [\(1.22\)](#) introduces tedious γ -matrices calculations in $\text{QS}_{[d]}$. However, this is irrelevant in FDF, because the entire γ -matrices algebra is performed in $\text{S}_{[4]}$. A more important problem is originated by the breaking of the chiral symmetry by [\(1.22\)](#). In fact, the two operators

$$P_L = (1 - \gamma^5)/2 \quad P_R = (1 + \gamma^5)/2 \quad (1.24)$$

are chiral projectors for both ψ and $\bar{\psi}$ only if $\{\gamma^0, \gamma^5\} = 0$. Hence, to restore the chiral symmetry we require the finite renormalisation [\[79\]](#)

$$\gamma_5^{\text{BM}} \rightarrow Z_5 \gamma_5^{\text{BM}} \quad P_{L,R} \rightarrow P_{L,R} = (1 \mp Z_5 \gamma^5)/2 \quad (1.25)$$

which results in a further counter-term in the renormalised Lagrangian. The solution is applicable to any formulation of DREG employing γ_{BM}^5 . The FDF value of Z_5 turns out to be remarkably simple [\[78\]](#)

$$Z_5 = 1 + \frac{\alpha}{\pi} + \mathcal{O}(\alpha^2) \quad (1.26)$$

1.4 FKS $^\ell$ subtraction scheme

As we already mentioned in Section 1.2, cross sections and decay widths beyond LO are usually IR divergent. According to the KLN theorem, the soft singularities arising from the integration over ℓ loops are eliminated by the ones arising from the phase-space integration over the emission of ℓ additional photons in the final state. Hence, an IR finite NLO contribution to an arbitrary cross section σ is⁴

$$\sigma^{(1)} = \int \left(d\sigma_v^{(1)} + d\sigma_r^{(1)} \right) = \int d\Phi_n \mathcal{M}_n^{(1)} + \int d\Phi_{n+1} \mathcal{M}_{n+1}^{(0)} \quad (1.27)$$

which includes all the (renormalised) matrix elements $\mathcal{M} \sim |\mathcal{A}|^2$ with an additional power of α respect to the LO cross section. The individual IR-divergent contributions are characterised as follows.

- The virtual (V) corrections $d\sigma_v^{(1)}$ are obtained by integrating the renormalised n -particle matrix element $\mathcal{M}_n^{(1)}$ over the Born phase space $d\Phi_n$. Specifically, $\mathcal{M}_n^{(1)}$ consists of the interference term between the renormalised one-loop amplitude and the tree-level amplitude.
- The real (R) corrections $d\sigma_r^{(2)}$ are obtained by integrating the tree-level $(n+1)$ -particle matrix element $\mathcal{M}_{n+1}^{(0)}$ with an additional final photon phase space $d\Phi_{n+1}$. Specifically, $\mathcal{M}_{n+1}^{(0)}$ corresponds to the tree-level process $\mathcal{M}_n^{(0)}$ with an additional photon in the final state.

In principle, we need to perform the phase-space integration in d dimensions when using DREG, in order to properly allow the cancellation of the $1/\epsilon_{\text{IR}}$ poles. However, the analytical integration of phase spaces is usually prohibitive for higher-order contributions, therefore it is desirable to solve them numerically. Unfortunately, this cannot be done in an arbitrary number of dimensions. A common and efficient way to address the problem is the application of a *subtraction scheme* for IR divergences. The idea is to rearrange the extra photon emission according to

$$\underbrace{\int_{n+1} d\sigma_{n+1}}_{\substack{\text{difficult \&} \\ \text{divergent}}} = \underbrace{\int_{n+1} (d\sigma_{n+1} - d\text{CT})}_{\substack{\text{difficult \& finite} \\ \rightarrow \text{numerically}}} + \underbrace{\int_n \int_1 d\text{CT}}_{\substack{\text{easy \& divergent} \\ \rightarrow \text{analytically}}} \quad (1.28)$$

where the integral subscripts refer to the number of integrated particles. The soft counter-term dCT is built so that the first integral is IR-finite, i.e. numerically integrable in four dimensions. At the same time dCT is defined to be easily integrated analytically in d

⁴In the following discussion we will refer both to cross sections and decay widths as cross sections σ .

dimensions over the one-particle phase space. In MCMULE this is achieved through the implementation of a particular extension of the FKS subtraction scheme, the FKS^ℓ scheme, formulated on purpose. The original FKS scheme was proposed for NLO calculations in perturbative QCD [34, 35]. In massive QED the scheme is greatly simplified, due to the absence of collinear singularities in the initial or final state. As we will show in the following, this facilitation permits the extension of the FKS scheme to any perturbative order ℓ . At N^ℓLO we will refer to the new scheme as FKS^ℓ [27, 33].

1.4.1 FKS: NLO scheme

In this section we discuss how the original FKS scheme can be applied to massive QED at NLO, in order to introduce all the essential concepts needed for its generalisation to N^ℓLO . To simplify the treatment, we assume that the final state of the tree-level process $\mathcal{M}_n^{(0)}$ does not include any photon. Therefore, the only particle in $\mathcal{M}_n^{(1)}$ which may become soft is the extra photon $n + 1$, simplifying the combinatorial factors without affecting the essential part of our discussion. We will explicitly derive the scheme for a decay, considering the frame of the decaying particle. However, the discussion can be easily generalised for a scattering process in the centre-of-mass frame. Furthermore, without loss of generality, we define the z axis along the momentum of one outgoing particle, eventually rotating the coordinate system afterwards. Hence, we parametrise the momenta of the decaying particle as

$$p_0 = M(1, \mathbf{0}_\perp, 0) = \sqrt{s}(1, \mathbf{0}_\perp, 0) \quad (1.29)$$

where \sqrt{s} is the invariant mass of the process. Following [34], we parametrise the momentum of the extra photon as

$$k_1 = p_{n+1} = \frac{\sqrt{s}}{2} \xi_1 \left(1, \sqrt{1 - y_1^2} \mathbf{e}_\perp, y_1 \right) \quad (1.30)$$

where \mathbf{e}_\perp is a $(d-2)$ -dimensional unit vector, $-1 \leq y_1 \leq 1$ and $0 \leq \xi_1 \leq \xi_{\max}$. The physical interpretation of ξ_1 and y_1 is straightforward: ξ_1 corresponds to the scaled energy $\xi_1 = 2E_{n+1}/\sqrt{s}$ of the extra photon, while $y_1 = \cos \theta_{n+1}$ measures the angle between the photon momentum and the z axis. The upper bound ξ_{\max} depends on the masses of the outgoing particles, specifically

$$\xi_{\max} = 1 - \frac{1}{s} \left(\sum_i m_i \right)^2 \quad (1.31)$$

We write the d -dimensional single-particle phase-space element as

$$d\phi_1 = \mu^{4-d} \frac{d^{d-1}k_1}{(2\pi)^{d-1} 2k_1^0} = \frac{\mu^{2\epsilon}}{2(2\pi)^{d-1}} \left(\frac{\sqrt{s}}{2}\right)^{d-2} \xi_1^{1-2\epsilon} (1-y_1^2)^{-\epsilon} d\xi_1 dy_1 d\Omega_1^{(d-2)} \quad (1.32a)$$

$$\equiv d\Upsilon_1 d\xi_1 \xi_1^{1-2\epsilon} \quad (1.32b)$$

where we collected in $d\Upsilon_1$ the angular integrations and the trivial factors. In this notation the real differential cross section $d\sigma_r^{(1)}$ becomes

$$d\sigma_r^{(1)} = d\Phi_{n,1} d\phi_1 \mathcal{M}_{n+1}^{(0)} = d\Upsilon_1 d\Phi_{n,1} d\xi_1 \xi_1^2 \mathcal{M}_{n+1}^{(0)} \xi_1^{-1-2\epsilon} \quad (1.33)$$

where we denoted the remaining part of the $(n+1)$ -th particle phase space with $d\Phi_{n,1}$, i.e. $d\Phi_{n+1} = d\Phi_{n,1} d\phi_1$. To isolate the soft singularities of the phase space, we define the c -distribution $(1/\xi^n)_c$ so that it acts on a test function $f(\xi)$ as

$$\int_0^1 d\xi \left(\frac{1}{\xi^n}\right)_c f(\xi) \equiv \int_0^1 d\xi \frac{f(\xi) - f(0)\theta(\xi_c - \xi)}{\xi^n} \quad (1.34)$$

where θ is the Heaviside step function and $n \in \mathbb{C}$. Hence, we can expand $\xi_1^{-1-2\epsilon}$ by applying the identity

$$\xi^{-1-2\epsilon} = -\frac{\xi_c^{-2\epsilon}}{2\epsilon} \delta(\xi) + \left(\frac{1}{\xi^{1+2\epsilon}}\right)_c \quad (1.35)$$

We have introduced an unphysical cut parameter ξ_c which can be chosen arbitrarily within the range $0 < \xi_c \leq \xi_{\max}$ [34, 35]. Since ξ_c is totally unphysical and no approximation was introduced so far, the NLO cross section $\sigma^{(1)}$ must be ξ_c -independent. We can now use (1.35) to split the differential real cross section $d\sigma_r^{(1)}$ into soft and hard contributions

$$d\sigma_r^{(1)} = d\sigma_s^{(1)}(\xi_c) + d\sigma_h^{(1)}(\xi_c) \quad (1.36a)$$

$$d\sigma_s^{(1)}(\xi_c) = -d\Upsilon_1 d\Phi_{n,1} \frac{\xi_c^{-2\epsilon}}{2\epsilon} \delta(\xi_1) d\xi_1 \left(\xi_1^2 \mathcal{M}_{n+1}^{(0)}\right) \quad (1.36b)$$

$$d\sigma_h^{(1)}(\xi_c) = d\Upsilon_1 d\Phi_{n,1} \left(\frac{1}{\xi_1^{1+2\epsilon}}\right)_c d\xi_1 \left(\xi_1^2 \mathcal{M}_{n+1}^{(0)}\right) \quad (1.36c)$$

The hard contribution $d\sigma_h^{(1)}$ is free from $1/\epsilon_{\text{IR}}$ poles, so it can be integrated numerically in four dimensions after setting $\epsilon = 0$. Conversely, the soft contribution $d\sigma_s^{(1)}$ is IR divergent, nevertheless its integration over ξ_1 is almost straightforward. To perform it systematically, we define the soft limit \mathcal{S}_i of the i -th photon as

$$\mathcal{S}_i \mathcal{M}_m^{(0)} \equiv \lim_{\xi_i \rightarrow 0} \xi_i^2 \mathcal{M}_m^{(0)} = \mathcal{E}_i \mathcal{M}_{m-1}^{(0)} \quad \text{with} \quad \xi_i = \frac{2E_i}{\sqrt{s}} \quad (1.37)$$

where $\mathcal{M}_{m-1}^{(0)}$ is the matrix element of the process without the i -th photon. In (1.37) we have introduced the *eikonal factor*

$$\mathcal{E}_i \equiv \sqrt{4\pi\alpha} \sum_{j,k} \frac{p_j \cdot p_k}{p_j \cdot n_i p_k \cdot n_i} \text{sign}_{jk} \quad \text{with} \quad n_i = p_i/\xi_i \quad (1.38)$$

where $\text{sign}_{jk} = (-1)^{n_{jk}+1}$ with n_{jk} number of incoming particles or outgoing antiparticles between the two particles j and k . Furthermore, we define the *integrated eikonal* as

$$\hat{\mathcal{E}}(\xi_c) \equiv -\frac{\xi_c^{-2\epsilon}}{2\epsilon} \int d\Upsilon_i \mathcal{E}_i = \xi_c^{-2\epsilon} \hat{\mathcal{E}}(1) \quad (1.39)$$

which has been calculated for an arbitrary process in [34, 35]. Integrating $d\sigma_s^{(1)}$ over $d\Upsilon_1$ and $d\xi_1$, we obtain

$$d\sigma_s^{(1)}(\xi_c) \xrightarrow{\int d\Upsilon_1 d\xi_1} d\Phi_n \hat{\mathcal{E}}(\xi_c) \mathcal{M}_n^{(1)} \quad (1.40)$$

The remaining $d\sigma_s^{(1)}$ is now an n -particle contribution, so we can combine it with $d\sigma_v^{(1)}$

$$d\sigma_n^{(1)}(\xi_c) = d\sigma_v^{(1)}(\xi_c) + d\sigma_s^{(1)} = \int d\Phi_n \left(\mathcal{M}_n^{(1)} + \hat{\mathcal{E}}(\xi_c) \mathcal{M}_n^{(0)} \right) \quad (1.41)$$

It is now easy to show that the $1/\epsilon_{\text{IR}}$ poles in $\mathcal{M}_n^{(1)}$ cancel the ones in $\hat{\mathcal{E}}$, making $d\sigma_n^{(1)}(\xi_c)$ IR-finite. As showed long time ago by Yennie, Frautschi and Suura [39], the IR divergences of QED exponentiate to all orders, i.e. the matrix elements accomplish the relation

$$\sum_{\ell=0}^{\infty} \mathcal{M}_n^{(\ell)} = e^{-\alpha S} \times \text{finite} \quad (1.42)$$

where the factor S contains all the IR singularities of $\mathcal{M}_n^{(\ell)}$. Using the definition (1.39), we can complete (1.42) by writing [34, 35]

$$\sum_{\ell=0}^{\infty} \mathcal{M}_n^{(\ell)} = e^{-\alpha \hat{\mathcal{E}}(\xi_c)} \sum_{\ell=0}^{\infty} \mathcal{M}_n^{(\ell)f} \quad (1.43)$$

where we denoted with $\mathcal{M}_n^{(\ell)f}$ the IR finite ℓ -loop matrix element. Expanding (1.43) up to $\mathcal{O}(\alpha)$, as required at NLO, we find

$$\mathcal{M}_n^{(1)f} = \mathcal{M}_n^{(1)} + \hat{\mathcal{E}}(\xi_c) \mathcal{M}_n^{(0)} + \mathcal{O}(\alpha^2) \quad (1.44a)$$

$$d\sigma_n^{(1)}(\xi_c) = d\Phi_n \left(\mathcal{M}_n^{(1)} + \hat{\mathcal{E}}(\xi_c) \mathcal{M}_n^{(0)} \right) = d\Phi_n \mathcal{M}_n^{(1)f} \quad (1.44b)$$

i.e. $d\sigma_n^{(1)}$ is manifestly free from $1/\epsilon_{\text{IR}}$ poles. We are finally able to write the NLO cross section $\sigma^{(1)}$ using only four-dimensional integrations

$$\sigma^{(1)} = \sigma_n^{(1)}(\xi_c) + \sigma_{n+1}^{(1)}(\xi_c) \quad (1.45a)$$

$$\sigma_n^{(1)}(\xi_c) = \int d\Phi_n^{d=4} \left(\mathcal{M}_n^{(1)} + \hat{\mathcal{E}}(\xi_c) \mathcal{M}_n^{(0)} \right) = \int d\Phi_n^{d=4} \mathcal{M}_n^{(1)f} \quad (1.45b)$$

$$\sigma_{n+1}^{(1)}(\xi_c) = \int d\Phi_{n+1}^{d=4} \left(\frac{1}{\xi_1} \right)_c \left(\xi_1 \mathcal{M}_{n+1}^{(0)f} \right) \quad (1.45c)$$

where we have replaced $\mathcal{M}_{n+1}^{(0)} \rightarrow \mathcal{M}_{n+1}^{(0)f}$ according to the notation introduced in (1.43). Since $\sigma_n^{(1)}$ and $\sigma_{n+1}^{(1)}$ are separately finite in four dimensions, they can be integrated numerically as we requested initially. Referring to (1.28), we have found

$$\int_{n+1} (d\sigma_{n+1} - d\text{CT}) = \int d\Phi_{n+1}^{d=4} \left(\frac{1}{\xi_1} \right)_c \left(\xi_1 \mathcal{M}_{n+1}^{(0)f} \right) \quad (1.46a)$$

$$d\text{CT} = \int_1 \hat{\mathcal{E}}(\xi_c) \mathcal{M}_n^{(0)} \quad (1.46b)$$

1.4.2 FKS²: NNLO extension

We have now all the tools to discuss the extension of FKS to NNLO, i.e. the FKS² scheme [33]. An arbitrary NNLO cross section can be written as

$$\begin{aligned} \sigma^{(2)} &= \int \left(d\sigma_{vv}^{(2)} + d\sigma_{rv}^{(2)} + d\sigma_{rr}^{(2)} \right) \\ &= \int d\Phi_n \mathcal{M}_n^{(2)} + \int d\Phi_{n+1} \mathcal{M}_{n+1}^{(1)} + \int d\Phi_{n+2} \mathcal{M}_{n+2}^{(0)} \end{aligned} \quad (1.47)$$

which includes all the (renormalised) matrix elements with two additional powers of α respect to the LO cross section. As before, we denote with $n+1$ and $n+2$ the presence of two additional (potentially soft) photons in the final state. For the KLN theorem, the inclusion of $d\sigma_{rv}^{(2)}$ and $d\sigma_{rr}^{(2)}$ in $\sigma^{(2)}$ remove all the virtual soft singularities of $d\sigma_{vv}^{(2)}$. The single separately IR-divergent terms are characterised as follows.

- The double-virtual (VV) corrections $d\sigma_{vv}^{(2)}$ are obtained by integrating the renormalised n -particle matrix $\mathcal{M}_n^{(2)}$ over the Born phase space $d\Phi_n$. Specifically, $\mathcal{M}_n^{(2)}$ contains the renormalised one-loop squared amplitude and interference term between the renormalised two-loop amplitude and the tree-level amplitude.
- The real-virtual (RV) corrections $d\sigma_{rv}^{(2)}$ are obtained by integrating the renormalised $(n+1)$ -particle matrix $\mathcal{M}_{n+1}^{(1)}$ over the $(n+1)$ -particle phase space $d\Phi_{n+1}$. The only

contribution to $\mathcal{M}_{n+1}^{(1)}$ is the interference term between the renormalised $(n+1)$ -particle one-loop amplitude and the corresponding tree-level amplitude.

- The double-real (RR) corrections $d\sigma_{rr}^{(2)}$ are obtained integrating the tree-level $(n+2)$ -particle matrix $\mathcal{M}_{n+2}^{(0)}$ over the $(n+2)$ -particle phase space $d\Phi_{n+2}$. Specifically, $\mathcal{M}_{n+2}^{(0)}$ corresponds to the leading-order diagram with two extra photons in the final state.

The production of one fermion-antifermion pair is usually included among NNLO corrections, however its contribution is finite in massive QED. Hence, we will not consider such a case for the construction of FKS². Only in a second step we will include the tree-level contribution due to a pair production (PP) in $\sigma^{(2)}$.

Real-virtual corrections

The real-virtual term

$$d\sigma_{rv}^{(2)} = d\Phi_{n+1} \mathcal{M}_{n+1}^{(1)} \quad (1.48)$$

can be treated similarly to $d\sigma_r^{(1)}$, being a $(n+1)$ -particle contribution. Hence, we can use (1.35) to split $d\sigma_{rv}^{(2)}$ into soft and hard contributions

$$d\sigma_{rv}^{(2)} = d\sigma_s^{(2)}(\xi_{c_A}) + d\sigma_h^{(2)}(\xi_{c_A}) \quad (1.49)$$

where we have introduced a further unphysical cut parameter ξ_{c_A} . The analogy with the NLO case is complete for $d\sigma_s^{(2)}$, since there are no one-loop contributions to the eikonal factor \mathcal{E} , as showed in [80, 81]. The soft limit of the real-virtual matrix element is therefore

$$\mathcal{S}_{n+1} \mathcal{M}_{n+1}^{(1)} = \mathcal{E}_{n+1} \mathcal{M}_n^{(1)} \quad (1.50)$$

Similarly to (1.40), by integrating $d\Upsilon_1$ and $d\xi_1$, we obtain

$$d\sigma_s^{(2)}(\xi_{c_A}) \xrightarrow{\int d\Upsilon_1 d\xi_1} d\Phi_n \hat{\mathcal{E}}(\xi_{c_A}) \mathcal{M}_n^{(1)} \quad (1.51)$$

Nevertheless, while the NLO soft term $d\sigma_s^{(1)}$ includes only the pole $1/\epsilon_{\text{IR}}$ contained in the integrated eikonal $\hat{\mathcal{E}}$, the NNLO soft term $d\sigma_s^{(2)}$ features a double pole $1/\epsilon_{\text{IR}}^2$, arising from the overlap between the IR poles of $\hat{\mathcal{E}}$ and $\mathcal{M}_n^{(1)}$. Furthermore, unlike the NLO case, the hard term $d\sigma_h^{(2)}$ is still singular, due to the pole $1/\epsilon_{\text{IR}}$ contained in $\mathcal{M}_n^{(1)}$. To further isolate this divergence, we use (1.43) to rewrite the real-virtual matrix element as

$$\mathcal{M}_{n+1}^{(1)} = \mathcal{M}_{n+1}^{(1)f}(\xi_{c_B}) - \hat{\mathcal{E}}(\xi_{c_B}) \mathcal{M}_{n+1}^{(0)} \quad (1.52)$$

where we have introduced a further unphysical cut parameter ξ_{c_B} . According to the YFS split, the soft pole of $\mathcal{M}_{n+1}^{(1)}$ is now included in $\hat{\mathcal{E}}(\xi_{c_B}) \mathcal{M}_{n+1}^{(0)}$, so that the *eikonal-subtracted*

matrix element $\mathcal{M}_{n+1}^{(1)f}$ is finite. We can now write

$$\begin{aligned} d\sigma_h^{(2)}(\xi_{c_A}) &= d\Upsilon_1 d\Phi_{n,1} d\xi_1 \left(\frac{1}{\xi_1^{1+2\epsilon}} \right)_{c_A} (\xi_1^2 \mathcal{M}_{n+1}^{(1)}) \\ &= d\sigma_f^{(2)}(\xi_{c_A}, \xi_{c_B}) + d\sigma_d^{(2)}(\xi_{c_A}, \xi_{c_B}) \end{aligned} \quad (1.53)$$

where

$$d\sigma_f^{(2)}(\xi_{c_A}, \xi_{c_B}) = d\Upsilon_1 d\Phi_{n,1} d\xi_1 \left(\frac{1}{\xi_1^{1+2\epsilon}} \right)_{c_A} (\xi_1^2 \mathcal{M}_{n+1}^{(1)f}(\xi_{c_B})) \quad (1.54a)$$

$$d\sigma_d^{(2)}(\xi_{c_A}, \xi_{c_B}) = -d\Upsilon_1 d\Phi_{n,1} d\xi_1 \left(\frac{1}{\xi_1^{1+2\epsilon}} \right)_{c_A} (\hat{\mathcal{E}}(\xi_{c_B}) \xi_1^2 \mathcal{M}_{n+1}^{(0)}) \quad (1.54b)$$

The contribution $d\sigma_f^{(2)}$ is manifestly finite, so that it can be integrated numerically in four dimensions by setting $\epsilon = 0$. On the other hand, integrating $d\sigma_d^{(2)}$ over the complete d -dimensional phase space, we obtain

$$\int d\sigma_d^{(2)}(\xi_{c_A}, \xi_{c_B}) \equiv -\mathcal{I}(\xi_{c_A}, \xi_{c_B}) \quad (1.55)$$

where $\mathcal{I}(\xi_{c_A}, \xi_{c_B})$ is a process-dependent function, generally singular in four dimensions. Furthermore, the analytical expression of \mathcal{I} is usually difficult to compute and handle. In fact, it is known for only a few simple processes, such as the scattering $e^+e^- \rightarrow \nu_e \bar{\nu}_e$ [82]. Luckily, as we will see shortly, its contribution is exactly cancelled by the double-real term $d\sigma_{rr}^{(2)}$. In conclusion, the real-virtual corrections are given by

$$d\sigma_{rv}^{(2)} = d\sigma_s^{(2)}(\xi_{c_A}) + d\sigma_f^{(2)}(\xi_{c_A}, \xi_{c_B}) + d\sigma_d^{(2)}(\xi_{c_A}, \xi_{c_B}) \quad (1.56)$$

Double-real corrections

For the double-real term

$$d\sigma_{rr}^{(2)} = d\Phi_{n+2} \mathcal{M}_{n+2}^{(0)} \quad (1.57)$$

we extend the parametrisation (1.30) accordingly to

$$k_1 = p_{n+1} = \frac{\sqrt{s}}{2} \xi_1 (1, \sqrt{1 - y_1^2} \vec{e}_\perp, y_1) \quad (1.58a)$$

$$k_2 = p_{n+2} = \frac{\sqrt{s}}{2} \xi_2 R_\phi (1, \sqrt{1 - y_2^2} \vec{e}_\perp, y_2) \quad (1.58b)$$

where R_ϕ indicates a $(d - 2)$ -dimensional rotation matrix, while $-1 \leq y_i \leq 1$ and $0 \leq \xi_i \leq \xi_{\max}$ with the same ξ_{\max} of (1.31). In analogy with (1.30) and (1.33), we write

the phase space as

$$d\Phi_{n+2} = d\Phi_{n,2}d\phi_1d\phi_2 \quad (1.59)$$

in order to obtain

$$\begin{aligned} d\sigma_{rr}^{(2)} &= d\Phi_{n,2}d\phi_1d\phi_2 \frac{1}{2!} \mathcal{M}_{n+2}^{(0)} \\ &= d\Upsilon_1d\Upsilon_2d\Phi_{n,2} d\xi_1 d\xi_2 \frac{1}{2!} (\xi_1^2\xi_2^2\mathcal{M}_{n+2}^{(0)}) \xi_1^{-1-2\epsilon} \xi_2^{-1-2\epsilon} \end{aligned} \quad (1.60)$$

where the factor $1/2!$ arises from the symmetry of the two identical extra photons. Once again, we apply (1.35) to split $d\sigma_{rr}^{(2)}$ into

$$d\sigma_{rr}^{(2)} = d\sigma_{ss}^{(2)}(\xi_{c_1}, \xi_{c_2}) + d\sigma_{sh}^{(2)}(\xi_{c_1}, \xi_{c_2}) + d\sigma_{hs}^{(2)}(\xi_{c_1}, \xi_{c_2}) + d\sigma_{hh}^{(2)}(\xi_{c_1}, \xi_{c_2}) \quad (1.61)$$

where we have introduced two further cut parameters ξ_{c_1} and ξ_{c_2} . Explicitly, we have

$$d\sigma_{ss}^{(2)}(\xi_{c_1}, \xi_{c_2}) = d\Sigma_{n,2} \frac{\xi_{c_1}^{-2\epsilon}}{2\epsilon} \delta(\xi_1) \frac{\xi_{c_2}^{-2\epsilon}}{2\epsilon} \delta(\xi_2) d\xi_1d\xi_2 \left(\xi_1^2\xi_2^2\mathcal{M}_{n+2}^{(0)} \right) \quad (1.62a)$$

$$d\sigma_{hs}^{(2)}(\xi_{c_1}, \xi_{c_2}) = -d\Sigma_{n,2} \frac{\xi_{c_2}^{-2\epsilon}}{2\epsilon} \delta(\xi_2) \left(\frac{1}{\xi_1^{1+2\epsilon}} \right)_{c_1} d\xi_1 d\xi_2 \left(\xi_1^2\xi_2^2\mathcal{M}_{n+2}^{(0)} \right) \quad (1.62b)$$

$$d\sigma_{sh}^{(2)}(\xi_{c_1}, \xi_{c_2}) = -d\Sigma_{n,2} \frac{\xi_{c_1}^{-2\epsilon}}{2\epsilon} \delta(\xi_1) \left(\frac{1}{\xi_2^{1+2\epsilon}} \right)_{c_2} d\xi_1d\xi_2 \left(\xi_1^2\xi_2^2\mathcal{M}_{n+2}^{(0)} \right) \quad (1.62c)$$

$$d\sigma_{hh}^{(2)}(\xi_{c_1}, \xi_{c_2}) = d\Sigma_{n,2} \left(\frac{1}{\xi_1^{1+2\epsilon}} \right)_{c_1} \left(\frac{1}{\xi_2^{1+2\epsilon}} \right)_{c_2} d\xi_1d\xi_2 \left(\xi_1^2\xi_2^2\mathcal{M}_{n+2}^{(0)} \right) \quad (1.62d)$$

where we have defined for simplicity

$$d\Sigma_{n,2} \equiv \frac{1}{2!} d\Upsilon_1d\Upsilon_2d\Phi_{n,2} \quad (1.63)$$

Note that for $\xi_{c_1} = \xi_{c_2} \equiv \xi_c$ we have

$$\int d\sigma_{sh}^{(2)}(\xi_c, \xi_c) = \int d\sigma_{hs}^{(2)}(\xi_c, \xi_c) \quad (1.64)$$

The term $d\sigma_{hh}^{(2)}$ is finite, so that it can be integrated numerically in four dimensions by setting $\epsilon = 0$. For the mixed terms $d\sigma_{hs}^{(2)}$ and $d\sigma_{sh}^{(2)}$ we apply the soft limit

$$\mathcal{S}_i\mathcal{M}_{n+2}^{(0)} = \mathcal{E}_i\mathcal{M}_{n+1}^{(0)} \quad i \in \{n+1, n+2\} \quad (1.65)$$

Integrating $d\sigma_{hs}^{(2)}$ over ξ_2 and $d\Upsilon_2$, as well as $d\sigma_{sh}^{(2)}$ over ξ_1 and $d\Upsilon_1$, we get

$$\int d\sigma_{hs}^{(2)}(\xi_{c_1}, \xi_{c_2}) = \int d\Upsilon_1 d\Phi_{n,1} \frac{1}{2!} \int d\xi_1 \left(\frac{1}{\xi_1^{1+2\epsilon}} \right)_{c_1} (\xi_1^2 \mathcal{M}_{n+1}^{(0)}) \hat{\mathcal{E}}(\xi_{c_2}) \quad (1.66a)$$

$$\int d\sigma_{sh}^{(2)}(\xi_{c_1}, \xi_{c_2}) = \int d\Upsilon_2 d\Phi_{n,1} \frac{1}{2!} \int d\xi_2 \left(\frac{1}{\xi_2^{1+2\epsilon}} \right)_{c_2} (\xi_2^2 \mathcal{M}_{n+1}^{(0)}) \hat{\mathcal{E}}(\xi_{c_1}) \quad (1.66b)$$

Comparing the obtained expressions with (1.54) and (1.55), we obtain

$$\int d\sigma_{hs}^{(2)}(\xi_{c_1}, \xi_{c_2}) = \frac{1}{2!} \mathcal{I}(\xi_{c_1}, \xi_{c_2}) \quad (1.67a)$$

$$\int d\sigma_{sh}^{(2)}(\xi_{c_1}, \xi_{c_2}) = \frac{1}{2!} \mathcal{I}(\xi_{c_2}, \xi_{c_1}) \quad (1.67b)$$

On the other hand, for the double-soft term $d\sigma_{ss}^{(2)}$ we note that

$$\left(\mathcal{S}_i \circ \mathcal{S}_j \right) \mathcal{M}_{n+2}^{(0)} = \left(\mathcal{S}_j \circ \mathcal{S}_i \right) \mathcal{M}_{n+2}^{(0)} = \mathcal{E}_i \mathcal{E}_j \mathcal{M}_n^{(0)} \quad i \neq j \in \{n+1, n+2\} \quad (1.68)$$

i.e. the integrals over ξ_1 and ξ_2 in (1.62a) factorise. Hence, we can independently perform the integrations over $d\xi_1 d\Upsilon_1$ and $d\xi_2 d\Upsilon_2$, obtaining

$$d\sigma_{ss}^{(2)}(\xi_{c_1}, \xi_{c_2}) \xrightarrow{\int d\Upsilon_{1,2} d\xi_{1,2}} d\Phi_n \frac{1}{2!} \hat{\mathcal{E}}(\xi_{c_1}) \hat{\mathcal{E}}(\xi_{c_2}) \mathcal{M}_n^{(0)} \quad (1.69)$$

Combination

We are now ready to collect all contributions together. We start noticing that so far we have introduced four different cutting parameters: ξ_{c_A} , ξ_{c_B} , ξ_{c_1} and ξ_{c_2} . Since all of them are unphysical, the total NNLO cross section $\sigma^{(2)}$ must be independent from each of them. So far we have divided $\sigma^{(2)}$ into eight different contributions:

- the two finite terms $d\sigma_f^{(2)}$ and $d\sigma_{hh}^{(2)}$
- the two divergent soft terms $d\sigma_s^{(2)}$ and $d\sigma_{ss}^{(2)}$
- the three divergent auxiliary terms $d\sigma_d^{(2)}$, $d\sigma_{sh}^{(2)}$ and $d\sigma_{hs}^{(2)}$
- the divergent double-virtual term $d\sigma_{vv}^{(2)}$.

The three auxiliary terms can be written together as

$$\begin{aligned} \int d\sigma_{aux}^{(2)}(\xi_{c_i}) &\equiv \int \left(d\sigma_d^{(2)}(\xi_{c_A}, \xi_{c_B}) + d\sigma_{hs}^{(2)}(\xi_{c_1}, \xi_{c_2}) + d\sigma_{sh}^{(2)}(\xi_{c_1}, \xi_{c_2}) \right) \\ &= -\mathcal{I}(\xi_{c_A}, \xi_{c_B}) + \frac{1}{2!} \mathcal{I}(\xi_{c_1}, \xi_{c_2}) + \frac{1}{2!} \mathcal{I}(\xi_{c_2}, \xi_{c_1}) \end{aligned} \quad (1.70)$$

At this point we observe that choosing

$$\xi_c \equiv \xi_{c_A} = \xi_{c_B} = \xi_{c_1} = \xi_{c_2} \quad (1.71)$$

we have

$$d\sigma_{aux}^{(2)} = 0 \quad (1.72)$$

Since each ξ_{c_i} can be chosen arbitrarily within the range $0 < \xi_{c_i} \leq \xi_{\max}$, this simplification is always possible, allowing us to avoid the tedious calculation of $\mathcal{I}(\xi_{c_i}, \xi_{c_j})$. Arranging the remaining contributions by number of particles, we obtain

$$\sigma^{(2)} = \sigma_n^{(2)}(\xi_c) + \sigma_{n+1}^{(2)}(\xi_c) + \sigma_{n+2}^{(2)}(\xi_c) \quad (1.73a)$$

$$\sigma_n^{(2)}(\xi_c) = \int \left(d\sigma_{vv}^{(2)} + d\sigma_s^{(2)} + d\sigma_{ss}^{(2)} \right) \quad (1.73b)$$

$$= \int d\Phi_n \left(\mathcal{M}_n^{(2)} + \hat{\mathcal{E}}(\xi_c) \mathcal{M}_n^{(1)} + \frac{1}{2!} \mathcal{M}_n^{(0)} \hat{\mathcal{E}}(\xi_c)^2 \right)$$

$$\sigma_{n+1}^{(2)}(\xi_c) = \int d\sigma_f^{(2)} = \int d\Upsilon_1 d\Phi_{n,1} d\xi \left(\frac{1}{\xi^{1+2\epsilon}} \right)_c \xi^2 \mathcal{M}_{n+1}^{(1)f}(\xi_c) \quad (1.73c)$$

$$\sigma_{n+2}^{(2)}(\xi_c) = \int d\sigma_{hh}^{(2)} = \int d\Omega_{n,2} d\xi_1 d\xi_2 \frac{1}{2!} \left(\frac{1}{\xi_1^{1+2\epsilon}} \right)_c \left(\frac{1}{\xi_2^{1+2\epsilon}} \right)_c \left(\xi_1^2 \xi_2^2 \mathcal{M}_{n+2}^{(0)} \right) \quad (1.73d)$$

The latter two contributions $\sigma_{n+1}^{(2)}$ and $\sigma_{n+2}^{(2)}$ are finite by construction, while the three integrands of $\sigma_n^{(2)}$ are separately divergent. However, expanding the YFS split (1.43) up to $\mathcal{O}(\alpha^2)$, as required at NNLO, we obtain

$$\mathcal{M}_n^{(2)f} = \mathcal{M}_n^{(2)} + \hat{\mathcal{E}}(\xi_c) \mathcal{M}_n^{(1)} + \frac{1}{2!} \mathcal{M}_n^{(0)} \hat{\mathcal{E}}(\xi_c)^2 + \mathcal{O}(\alpha^3) \quad (1.74a)$$

$$\sigma_n^{(2)}(\xi_c) = \int d\Phi_n \left(\mathcal{M}_n^{(2)} + \hat{\mathcal{E}}(\xi_c) \mathcal{M}_n^{(1)} + \frac{1}{2!} \mathcal{M}_n^{(0)} \hat{\mathcal{E}}(\xi_c)^2 \right) = \int d\Phi_n \mathcal{M}_n^{(2)f} \quad (1.74b)$$

Each term of (1.73) is now individually finite, even though ξ_c -dependent, unlike their sum $\sigma^{(2)}$. Hence, we can set $d = 4$ everywhere, obtaining

$$\sigma_n^{(2)}(\xi_c) = \int d\Phi_n^{d=4} \mathcal{M}_n^{(2)f} \quad (1.75a)$$

$$\sigma_{n+1}^{(2)}(\xi_c) = \int d\Phi_{n+1}^{d=4} \left(\frac{1}{\xi} \right)_c \left(\xi \mathcal{M}_{n+1}^{(1)f}(\xi_c) \right) \quad (1.75b)$$

$$\sigma_{n+2}^{(2)}(\xi_c) = \int d\Phi_{n+2}^{d=4} \left(\frac{1}{\xi_1} \right)_c \left(\frac{1}{\xi_2} \right)_c \left(\xi_1 \xi_2 \mathcal{M}_{n+2}^{(0)f} \right) \quad (1.75c)$$

In conclusion, we have obtained the generalisation of (1.45) to NNLO.

Matrix elements required at NNLO

At this point, it is necessary to point out the matrix elements required by FKS².

- The renormalised double-virtual matrix $\mathcal{M}_n^{(2)}$ must be known for non-vanishing fermion masses up to $\mathcal{O}(\epsilon_{\text{IR}}^0)$. This is certainly the bottleneck of the calculation, since the solution of the necessary two-loop integrals is known only for a restricted class of processes. The algebraic complexity of these integrals is in fact formidable, unless we neglect the lightest masses involved in the process, violating the hypothesis of FKS². A possible solution is provided by the already mentioned *massification*, which allows to obtain (approximate) massive matrix elements starting from massless ones, according to the master formula

$$\mathcal{M}^{(2)}(m > 0) = \prod_i \sqrt{Z_i} \times S \times \mathcal{M}_n^{(2)}(m = 0) + \mathcal{O}(m/S)$$

where the Z_i are universally known functions and S denotes a process-dependent function to be calculated in eikonal QED [27, 41]. In this way, it is possible to apply the FKS² scheme knowing only the solution of the massless two-loop integrals. However, the massification approach is not yet sufficiently developed to be applied systematically to widely different processes. The computation of the muon decay with a massified electron is discussed in [41, 33]. In this thesis we instead compute $\mu \rightarrow e\nu\bar{\nu}$ up to NNLO accounting for the full electron mass dependency, since the necessary two-loop integrals has been recently solved [27, 83, 84].

- The renormalised real-virtual matrix $\mathcal{M}_{n+1}^{(1)}$ must be known for non-vanishing masses up to $\mathcal{O}(\epsilon_{\text{IR}}^0)$.
- The virtual matrix $\mathcal{M}_n^{(1)}$ must be known for non-zero masses up to $\mathcal{O}(\epsilon_{\text{IR}})$ as required by (1.74b).
- The double-real matrix $\mathcal{M}_{n+2}^{(0)}$ must be known for non-vanishing masses in four dimensions.
- The leading order matrix $\mathcal{M}_n^{(0)}$ must be known for non-zero masses up to $\mathcal{O}(\epsilon_{\text{IR}}^2)$. Although $\mathcal{M}_n^{(0)}$ is non-singular in four dimensions, it is necessary to know it in d dimensions up to $\mathcal{O}(\epsilon_{\text{IR}}^2)$ to properly apply the eikonal subtraction (1.74b). However, this is required only in CDR, since $\mathcal{M}_n^{(0)}$ is strictly four-dimensional in FDH and FDF. The same holds for the real matrix $\mathcal{M}_{n+1}^{(0)}$.

Starting from the knowledge of these matrix elements, the FKS² scheme allows to compute the QED corrections at NNLO precision for any process.

1.4.3 FKS^ℓ: N^ℓLO generalisation

We can now discuss the generalisation of FKS² to an arbitrary perturbative order ℓ , i.e. the FKS^ℓ scheme. Major advances in extending universal schemes beyond NNLO have been made in QCD only recently [85]. However, the simplicity of FKS² allows a straightforward generalisation to N^ℓLO in the context of massive QED. The explicit derivation of FKS³ for N³LO can be found in [27, 33]. Exploiting the formal pattern that clearly emerged in the extension from NLO to NNLO, at N^ℓLO we find

$$d\sigma^{(\ell)} = \sum_{j=0}^{\ell} d\sigma_{n+j}^{(\ell)}(\xi_c) \quad 0 \leq j \leq \ell \quad (1.76a)$$

$$d\sigma_{n+j}^{(\ell)}(\xi_c) = d\Phi_{n+j}^{d=4} \frac{1}{j!} \left(\prod_{i=1}^j \left(\frac{1}{\xi_i} \right)_c \xi_i \right) \mathcal{M}_{n+j}^{(\ell-j)f}(\xi_c) \quad (1.76b)$$

where $\xi_1 \dots \xi_j$ are integration variables included into the four-dimensional phase-space measure and all cut parameters were again chosen equal to ξ_c . As already discussed for NLO and NNLO, $d\sigma^{(3)}$ is ξ_c -independent, i.e. the ξ_c -dependency cancels between the various $d\sigma_{n+j}^{(3)}(\xi_c)$ contributions. The eikonal-subtracted matrix element is given by

$$\mathcal{M}_{n+j}^{(\ell-j)f} = \sum_{k=0}^{\ell} \frac{\hat{\mathcal{E}}^k}{k!} \mathcal{M}_{n+j}^{(\ell-j-k)} \quad \mathcal{M}_{n+\ell}^{(0)f} = \mathcal{M}_{n+\ell}^{(0)} \quad (1.77)$$

For the YFS exponentiation (1.43) each $\mathcal{M}_m^{(\ell)f}$ is explicitly free from soft poles. In conclusion, we have defined a general procedure that allows us to subtract soft singularities from matrix elements and phase spaces at any order in massive QED. The only price to pay is not being able to neglect the mass of any fermion to simplify the algebraic complexity of loop integrals, unless we use the massification approach.

In MCMULE the phase space is integrated numerically in four dimensions through the implementation of the FKS^ℓ scheme. However, it is necessary to observe that such an integration may be problematic due to the potential arising of pseudo-collinear singularities (PCS). In FKS^ℓ collinear singularities are totally absent from phase space, since all fermion masses are non-vanishing. However, if light masses are involved, collinear momenta are related to large (even though finite) contributions, that may significantly worsen the convergence of the numerical integration. An important example is muon decay, as $m_e/m_\mu \approx 1/200$. We will discuss how MCMULE tackles this issue with a careful parametrisation of phase space in Section 1.6.

1.5 Structure of MCMULE

MCMULE is organised in several FORTRAN modules, whose mutual relations are represented in Figure 1.1. In the following, we give a brief description of the individual modules, mentioning the most important variables.

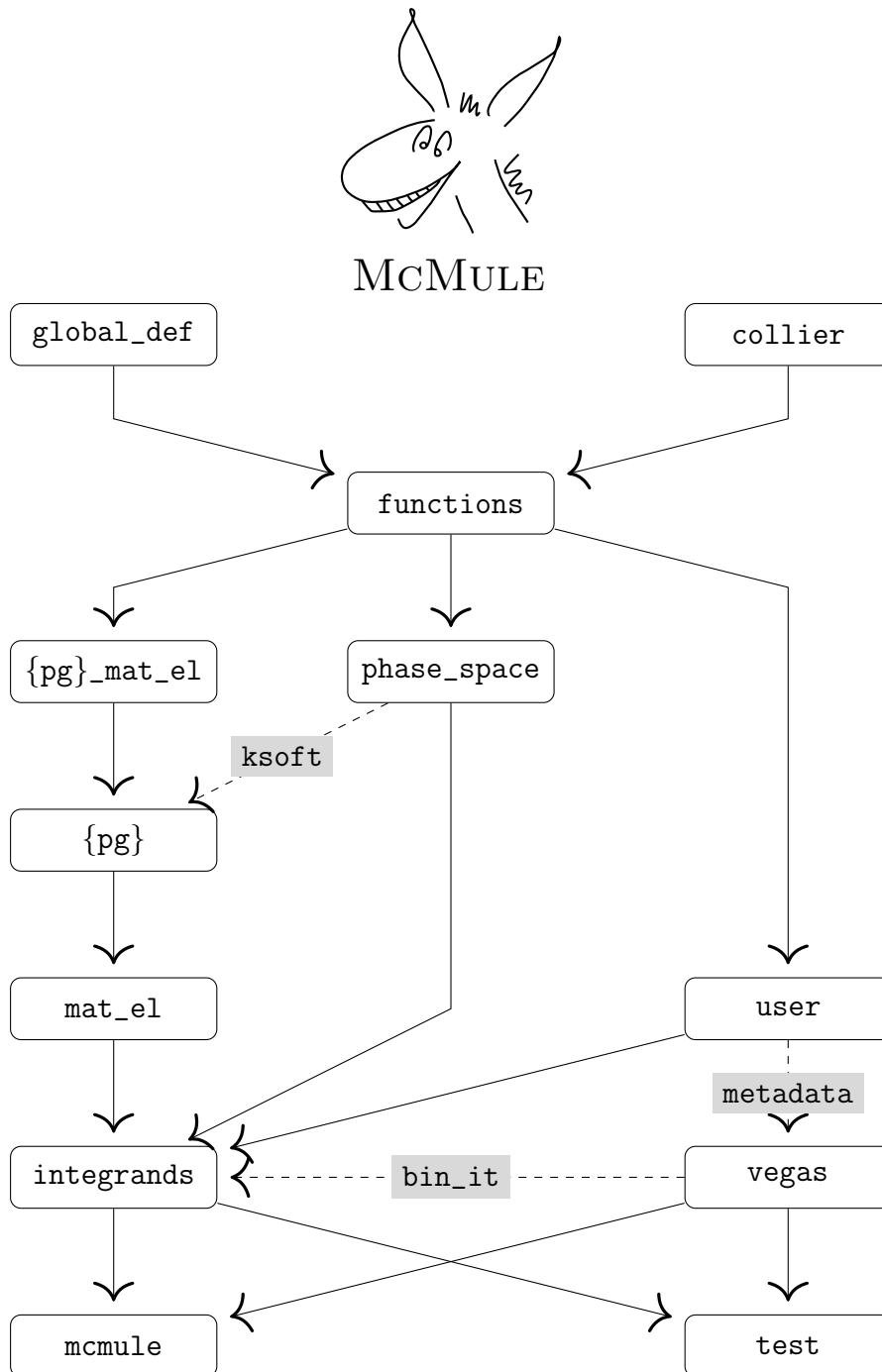


Figure 1.1 The structure of MCMULE.

global_def: A set of global definitions including fermion masses and other physical constants. The module also defines the global parameter **prec**, which allows to fix the floating-point precision of any real parameter. The default option is *double-precision*, corresponding to 64 bit. Furthermore, the module contains the routine **initflavour**, that allows to select several flavour options for the same process, applying the corresponding masses throughout the code. For example, the implementation of $\ell' \rightarrow \ell\nu\bar{\nu}$ includes all possible flavour transitions, selectable through the global parameter **flavour** = {**mu-e**, **tau-e**, **tau-mu**}. The numerical values used in this thesis are reported in Appendix A.

functions: An internal library of special functions that are needed throughout the code. It features dot products, Lorentz boosts, eikonal factors, polylogarithms and one-loop integral functions, among others. Furthermore, it provides functions for the computation of non-trivial kinematic observables, such as pseudo-rapidity or transverse momentum.

collier: An external library for the numerical evaluation of one-loop scalar and tensor integral functions, as implemented in **functions**. In fact, one-loop box and triangle functions are usually too complicated to be implemented and evaluated in FORTRAN without the support of external packages. For this reason, the COLLIER (Complex One-Loop Library in Extended Regularizations) library [86–89] is linked to MCMULE.

phase_space: The module includes all routines for generating the phase-space points. The routines ending with the suffix **FKS** implement the FKS scheme, while the ones ending with **FKS2** implement the FKS² scheme. To allow the implementation of any IR-safe distribution, the ξ_i factors required by (1.76) are omitted and otherwise stored in a set of global variables **xiout**. For any of these variables, the module also provides a variable **ksoft**, corresponding to the momentum of the emitted additional photon without the factor ξ_i . To ensure the numerical stability of the numerical integrator, especially in presence of PCS, it is recommended to tune the phase-space routines to the kinematic scales of the studied process. More details about the generation of the phase-space points are provided in Section 1.6.

pg_mat_el: All implemented matrix elements are separated into *process groups*, according to the class of processes they belong. For example, all implemented muon decay modes are included in the two group **mudec** and **mudecrare**. Each process group contains one or more **mat_el** modules containing all the matrix elements of the group. Thus, these modules constitute the collection of the analytical expression for any implemented $\mathcal{M}_{n+j}^{(\ell)}$ contribution. In addition to the classification according to *process group*, all matrix elements are splitted into *generic process* and *generic piece*, according to the process they belong and their type (R, V, RR and so on). The organisation of the matrix elements regarding the muon decay is shown in Figure 1.2. A matrix element beginning with P

features a polarised initial state, while a matrix element ending with `av` is averaged over the neutrinos states. Furthermore, the module defines the particle identification (PID), i.e. the labels that identify the various particles throughout the code. All PID conventions are reported in MCMULE's user manual [28].

{pg}: In order to allow the implementation of FKS^ℓ, each process group features a `pg` module, providing the soft limit of every matrix element with an unresolved soft photon. According to FKS^ℓ, the limits are obtained by multiplying the matrix elements in `mat_el` with the eikonal factor `eik` provided by `functions` and evaluated through `ksoft` from `phase_space`.

user: This is the only relevant module for the user that wants to run an already implemented process. For any featured process, MCMULE allows to obtain the distribution of any IR-safe observables with arbitrary cuts. Accordingly, in this module the user has to specify the number of quantities to compute (`nr_q`) and for each of them the number of bins (`nr_bins`), the lower bound (`min_val`) and the upper bound (`max_val`). The last three quantities are therefore arrays of length `nr_q`. All of them constitute the *binning metadata* read by the `vegas` module. Furthermore, the measurement function of every quantity has to be defined in terms of the momenta of the external particles in the routine `quant`. Cuts on the phase space, such as geometrical acceptances or trigger preselections, can be applied through the logical variable `pass_cut`. More precisely, `pass_cut` is an array of length `nr_q`, allowing to cut each histogram independently from the others. Finally, the module includes the routine `inituser`, which allows to define further input parameters in addition to those read by the program by default.

vegas: The module features the implementation of the multi-dimensional MC integrator employed in the numerical integration of the phase spaces. As already mentioned, it is based on the adaptive algorithm VEGAS, briefly described in Section 1.6. The module also includes the binning routine `bin_it`, which samples the observables defined in `user` according to the selected binning metadata.

integrands: The module includes the functions to be numerically integrated by `vegas`. According to FKS², the integrands are splitted in three classes: non-subtracted (`sigma_0`), single-subtracted (`sigma_1`) and double-subtracted (`sigma_2`). The matrix elements to be evaluated and the required phase-space routines are respectively obtained from `mat_el` and `phase_space` through the subroutine `initpiece`, which links each matrix element to the correct phase-space routine. The factors ξ_i that were omitted in `phase_space` must be re-introduced here.

mcmule: MCMULE’s main program. It reads the inputs from the user and calls **vegas** to integrate the functions provided by **integrands**. The input parameters required by MCMULE are reported in Table 1.2. During the execution, the code generates a *statefile*, which allows to reconstruct all the intermediate states of the integration, especially should it be interrupted. The output is provided in the form of in-house **.vegas** files, containing all the histograms defined in **user**.

test: In addition to **mcmule**, a separate main program is included to validate the code after each compilation. It performs several tests and comparisons using reference values for matrix elements and one-loop functions, as well as short integrations.

Variable	Type	Short description
nenter_ad	integer	No. of points per interaction in pre-conditioning
itmx_ad	integer	No. of iterations in pre-conditioning
nenter	integer	No. of points per interaction during main run
itmx	integer	No. of iterations during main run
ran_seed	integer	Seed of the pseudo-random number generator
xinormcut	real(prec)	The $0 < \xi_c \leq 1$ parameter required by FKS ^ℓ
delcut	real(prec)	An optional second ξ_c parameter for FKS ²
which_piece	char(10)	The calculation to perform (e.g. m2ennRV)
flavour	char(8)	Flavour of the involved particles (e.g. mu-e)
(optional)	any	Additional input variable defined in userinit

Table 1.2 The input options read by MCMULE from **stdin**. The first four parameters define the statistics of the MC integrator, as explained in Section 1.6.

In addition to the main FORTRAN code, a Python tool named **pymule** is provided to properly analyse MCMULE’s results. The software employs **numpy** [90] for data storage and **matplotlib** [91] for plotting. An alternative ROOT interface is currently planned. Moreover, several MATHEMATICA tools are provided for the analytical calculation of matrix elements. This includes **qgraf.wl**, an in-house implementation of the QGRAF algorithm for the automatic generation of Feynman diagrams [92]. Furthermore, it includes the external libraries **Package-X** [93] and **HPL** [94, 95]. The first implements the Passarino-Veltman (PV) method for reducing one-loop integrals in scalar terms [96, 97]. The latter implements the Remiddi and Vermaseren’s Harmonic Polylogarithms (HPL), ubiquitous in higher-order calculations, as well as their series expansion and numerical evaluation [98]. More technical details about the code and the analysis tools can be found in MCMULE’s user manual [28].

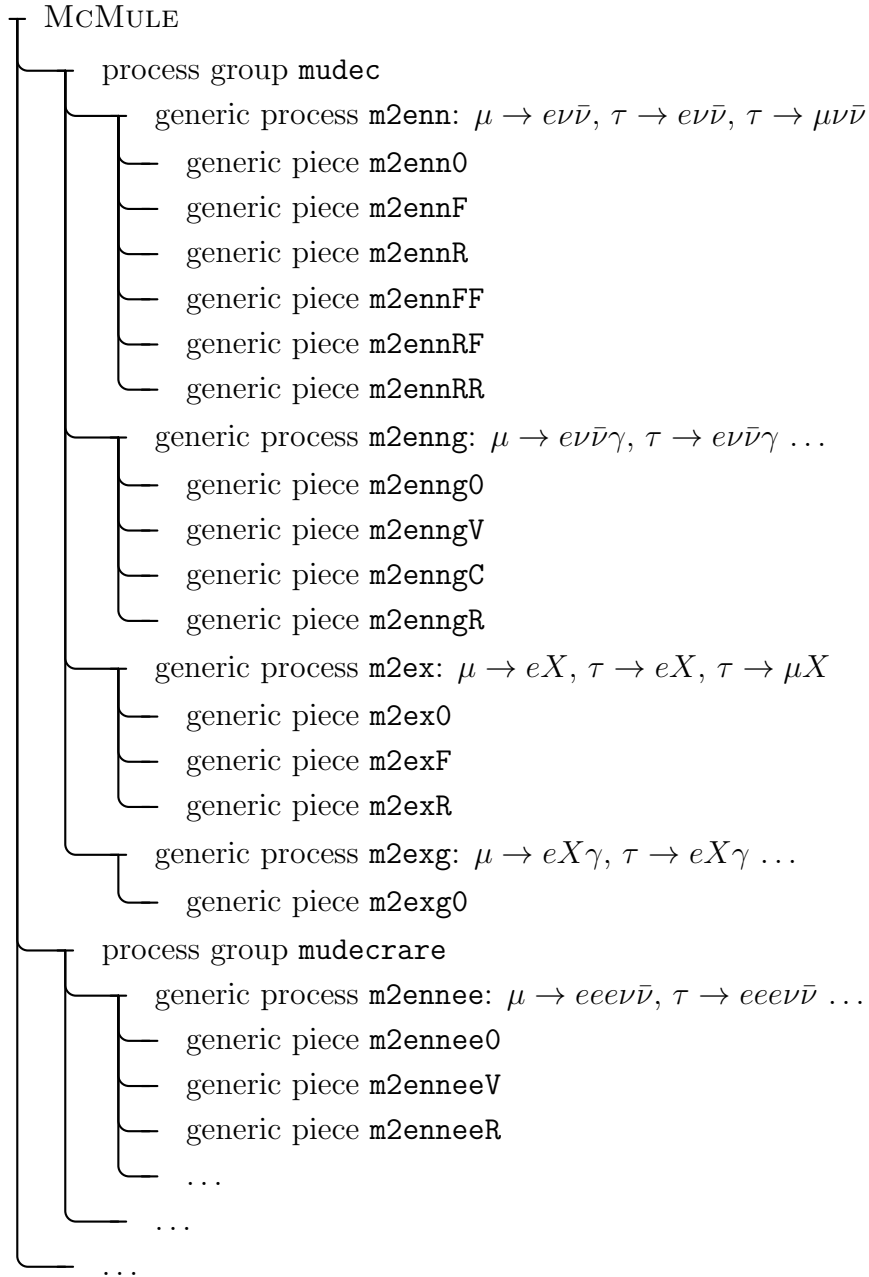


Figure 1.2 The process tree for muon decay, branched in *generic groups*, *generic processes* and *generic pieces*. The suffix 0 indicates a LO contribution, while at NLO the letter F express a virtual correction and R a real one. Similarly, at NNLO the suffix FF indicates a virtual-virtual correction, RF a real-virtual one and RR a real-real one. The groups `mudec` and `mudecrare` also include the corresponding tau modes, since the two process classes differ only by the mass of the involved leptons. As already mentioned, the flavours can be selected through the input parameter `flavour`.

1.6 Monte Carlo integration

1.6.1 VEGAS algorithm

MCMULE employs the MC algorithm VEGAS [36, 37] to numerically integrate the IR-subtracted phase space. The adaptive strategy of VEGAS, based on importance sampling, results in a fast, stable and accurate multidimensional MC integration, even for integrands having large peaks. It is then not surprising that VEGAS has been successfully applied in many computational sciences, including particle physics [99–101], atomic and condensed matter physics [102–104], astrophysics [105, 106] and non-physical sciences [107–109].

Importance sampling in VEGAS

Following [38], we introduce the algorithm in the one dimension, discussing its generalisation afterwards. The basic idea of VEGAS is to evaluate the integral

$$I = \int_a^b dx f(x) \quad (1.78)$$

by redefining the integration variable as $x \rightarrow y(x)$ in order to minimise the MC uncertainty. Thus, we replace (1.78) with the equivalent integral

$$I = \int_0^1 dy J(y) f(x(y)) \quad (1.79)$$

where $J(y)$ denotes the Jacobian of the transformation $y(x)$. Given a set of N random points y_n uniformly distributed between 0 and 1, a naive MC estimation of (1.79) is

$$I \simeq I_{MC} = \frac{1}{N} \sum_{n=1}^N J(y_n) f(x(y_n)) \quad (1.80)$$

We note that the estimate I_{MC} is itself a random number with mean I and variance

$$\sigma_I^2 = \frac{1}{N} \int_0^1 dy \left(J^2(y) f^2(x(y)) - I^2 \right) = \frac{1}{N} \int_a^b dx \left(J(y(x)) f^2(x) - I^2 \right) \quad (1.81)$$

which can be estimated from the MC data by using

$$\sigma_{MC}^2 = \frac{1}{N(N-1)} \sum_{n=1}^N (J^2(y_n) f^2(x(y_n)) - I_{MC}^2) \quad (1.82)$$

The standard deviation σ_I is a straightforward indication of the potential error of the MC integration. In other words, σ_I is the quantity we need to minimise to apply our

strategy. To define a suitable transformation $y(x)$, we start by dividing the x -axis into N_g non-uniform intervals given by

$$x_0 = a, \quad x_1 = x_0 + \Delta x_0, \quad \dots \quad x_{N_g} = x_{N_g-1} + \Delta x_{N_g-1} = b \quad (1.83)$$

where Δx_i denotes the width of each interval. Thus, we define $y(x)$ by requiring that every interval Δx_i map in the y -axis into intervals of the same width $\Delta y = 1/N_g$. Since $y \in [0, 1]$ by construction, we have $y_i = i/N_g$ for $i = 1, \dots, N_g$, where x_i is mapped into y_i . Hence, we can write the inverse transformation $x(y)$ as

$$x(y) = x_{i(y)} + \Delta x_{i(y)} \delta(y) \quad (1.84)$$

where the functions $i(y) \in \mathbb{N}$ and $\delta(y)$ are the integer and the fractional parts of yN_g , i.e.

$$i(y) \equiv \text{floor}(yN_g) \quad (1.85a)$$

$$\delta(y) \equiv yN_g - i(y) \quad (1.85b)$$

In this way, we obtain a discrete map between the original integration region $x \in [a, b]$ and the VEGAS one $y \in [0, 1]$. Specifically, intervals of different widths Δx_i in the x -space map into intervals of the same width Δy in the y -space. The corresponding Jacobian is the step function

$$J(y) = N_g \Delta x_{i(y)} \equiv J_{i(y)} \quad (1.86)$$

whose values are determined by the widths $\Delta x_{i(y)}$. Substituting J_i into (1.81), we obtain

$$\sigma_I^2 = \frac{1}{N} \sum_i J_i \int_{x_i}^{x_i + \Delta x_i} dx (f^2(x) - I^2) \quad (1.87)$$

We can now choose (1.84) such that the standard deviation σ_I is minimal. Treating the J_i as independent variables, constrained by

$$\sum_i \frac{\Delta x_i}{J_i} = \sum_i \Delta y = 1 \quad (1.88)$$

we find that σ_I is minimal for

$$\frac{J_i^2}{\Delta x_i} \int_{x_i}^{x_i + \Delta x_i} dx f^2(x) = \text{constant} \quad (1.89)$$

Thus, the MC integration is optimal when the integration grid is defined so that the average value of $J^2(y(x))f^2(x)$ is the same in every interval Δx_i . We note that this propriety is

particularly advantageous when the integrand $f(x)$ has high peaks, because

$$J = \left| \frac{dx}{dy} \right| \propto \frac{1}{|f(x)|} \quad (1.90)$$

In other words, the Jacobian becomes small near a peak, smoothing the integrand. This means that a uniform sampling of the y -space is mapped in the x -space, so that the random points are concentrated where the integrand has large peaks, increasing the accuracy of the MC integration. On average each interval Δx_i is sampled by the same number of random points ($\approx N/N_g$). Nevertheless, since $J_i \propto \Delta x_i$, the smallest intervals are placed where $|f(x)|$ is largest. This is why such a method is called importance sampling: the samples are concentrated in the most important regions. As we will discuss in the following, MCMULE directly exploit this feature to tackle the pseudo-collinear singularities of the matrix elements.

Iterative adaptation in VEGAS

At this stage we need an efficient method to find the optimal map $x \rightarrow y(x)$ for a given integrand $f(x)$. In VEGAS this is done iteratively by changing the Jacobian (1.86), by varying the widths Δx_i while keeping their sum constant. Specifically, for every interval Δx_i VEGAS compute the average

$$d_i \equiv \frac{1}{n_i} \sum_{x(y) \in \Delta x_i} J^2(y) f^2(x(y)) \quad (1.91)$$

where the sum is extended over the n_i random points generated within the interval Δx_i . According to (1.89), the grid is optimal when all d_i are equal. VEGAS achieves this condition by successive approximations by applying the following iterative procedure:

- (1) Generate N random points y_n uniformly distributed within $[0, 1]$
- (2) Estimate $I \simeq I_{MC}$ for $x = y$
- (3) Compute d_i for every interval Δx_i
- (4) Define a new set of intervals $\{x'_i, \Delta x'_i\}$ so that all d'_i are equal
- (5) Generate N random points y_n uniformly distributed within $[0, 1]$
- (6) Estimate $I_j \simeq I_{MC}$ and $\sigma_j^2 \simeq \sigma_{MC}^2$ with the new map
- (7) Repeat the steps (3) – (6) for K times, i.e. $j = 1, \dots, K$

In short words, VEGAS iteratively adapts the integration grid to the integrand [38]. The one-dimensional algorithm can be easily generalised to any dimensionality, i.e. to the

D -dimensional integral

$$I = \int_a^b d^D x f(x) = \int_0^1 d^D y J(y) f(x(y)) \quad (1.92)$$

where x and y are now D -dimensional vectors, as well as the borders a and b . Thus, the VEGAS integration region is given by the the unit hypercube

$$0 < y^\mu < 1 \quad \mu = 1, \dots, D \quad (1.93)$$

Similarly to the one-dimensional case, each axis of the hypercube is divided in N_g uniform intervals, corresponding in the x -space to intervals of different widths. Thus, the definition (1.91) becomes

$$d_i^\mu \equiv \frac{1}{n_i^\mu} \sum_{x(y) \in \Delta x_i^\mu} J^2(y) f^2(x(y)) \quad (1.94)$$

where the sum is extended over the n_i^μ random points generated within the interval Δx_i^μ . Again, VEGAS iteratively defines the widths of the intervals Δx_i^μ , so that the d_i^μ are all equal, optimising the MC integration.

The final result of the MC integration is given by the weighted average

$$\bar{I} = \left(\sum_{j=1}^K I_j / \sigma_j^2 \right) \left(\sum_{j=1}^K 1 / \sigma_j^2 \right)^{-1} \quad \sigma_{\bar{I}} = \left(\sum_{j=1}^K \frac{1}{\sigma_j^2} \right)^{-\frac{1}{2}} \quad (1.95)$$

The cumulative estimate \bar{I} is usually more reliable than the individual estimates I_j , including the last one (I_K). Furthermore, for sufficiently large values of N , the estimates I_j can be treated as independent Gaussian variables. Hence, an important test on the consistency between the single adaptive steps is given by

$$\chi^2 = \frac{1}{K-1} \sum_{j=1}^K \frac{(I_j - \bar{I})^2}{\sigma_j^2} \quad (1.96)$$

which is expected to be one.

In MCMULE the number of intervals in which each axis of the integration hypercube is divided is fixed to $N_g = 50$. This number is sufficiently large to achieve an efficient importance sampling and at the same time sufficiently large not to excessively load the iterative steps of the algorithm. Typical values of the two statistics-related parameters are $K = 100$ and $N = 10^7$. Furthermore, the VEGAS integration is usually repeated for several random seeds and choices of ξ_c to further increase statistics and reliability. Moreover,

due to the adaptive nature of VEGAS, we perform a low-statistics pre-conditioning run, excluded from the cumulative estimate (1.95), whose typical values are $K_{pc} = 10$ and $N_{pc} = 10^5$. Referring to the input parameters reported in Table 1.2, we have $K_{pc} = \text{itm_ad}$, $N_{pc} = \text{nenter_ad} \times 10^3$, $K = \text{itm}$ and $N = \text{nenter} \times 10^3$.

The described algorithm directly applies to total cross sections σ . However, it can be easily used to sample an arbitrary differential distribution $d\sigma/dS$, exploiting the knowledge of the Jacobian (1.86). Specifically, the module `vegas` computes the weight $d\Phi \times \mathcal{M} \times J$ for any event, placing it into the correct bin of the appropriate histogram. The mean and the standard deviation in each bin is then computed over the iteration steps similarly to (1.95).

1.6.2 Phase-space generation

Since VEGAS only works on hypercubes, we need to generate the phase space by mapping the momenta of the n final particles into the hypercube $[0, 1]^{3n-4}$. In `phase_space` this is achieved by iteratively splitting the phase space into two-particle contributions and finally boosting the generated momenta into the frame under consideration. The first step is done by iteratively considering the two-particle phase space formed by the i -th final particle and the invariant mass of the process without the i -th particle. However, the procedure cannot be applied for unresolved photons in real corrections, in order to properly implement the c -distributions (1.34) required by FKS ^{ℓ} . The issue is easily fixed by explicitly generating the photon momenta as (1.30) for FKS and (1.58) for FKS². At this point, we can implement the c -distributions relevant for FKS ^{ℓ} . For example, at NLO we need

$$\begin{aligned} d\sigma_h^{(1)}(\xi_c) &= d\Upsilon_1 d\Phi_{n,1} \left(\frac{1}{\xi_c} \right)_c d\xi_1 \left(\xi_1^2 \mathcal{M}_{n+1}^{(0)} \right) \\ &= d\xi_1 \frac{1}{\xi_1} \left(d\Upsilon_1 d\Phi_{n,1} \left(\xi_1^2 \mathcal{M}_{n+1}^{(0)} \right) - d\Upsilon_1 d\Phi_{n,1} \left(\mathcal{E} \mathcal{M}_n^{(0)} \right) \theta(\xi_c - \xi) \right) \end{aligned} \quad (1.97)$$

where θ is the Heaviside step function and $0 < \xi_c \leq \xi_{\max}$ as usual. We refer to the first term as *event* and the second as *counter-event*.

Pseudo-collinear singularities

As already mentioned, collinear momenta between photons and light particles are related to pseudo-singularities, that may significantly worsen the performances of the numerical integrator. According to (1.90), the VEGAS integration is optimal when the integrand peaks are aligned to one of the integration variables. Thus, the PCS inefficiency can be

reduced by orders of magnitudes by parametrising the PCS contribution with one of the random number of the MC. Specifically, a PCS arises from

$$\mathcal{M}_{n+1}^{(\ell)} \propto \frac{1}{\xi^2} \frac{1}{1 - \beta \cos \theta} \quad (1.98)$$

where ξ is the energy of the extra photon, β the velocity of the charged fermion and θ the angle between the momenta of the two particles. The matrix element $\mathcal{M}_{n+1}^{(\ell)}$ is pseudo-singular for $\cos \theta = 1$ and $\beta \simeq 1$ simultaneously, which is easily achieved for sufficiently light fermions, such as electrons in muon decay. Hence, we can address the problem by implementing $y \equiv \cos \theta$ as one of the integration variables of VEGAS. Unfortunately, as the number of PCS contributions increases, this approach becomes increasingly difficult to follow. A more general solution involves the subtraction of the PCS contributions with an approach very similar to (1.28). The idea is again to isolate and integrate the PCS-related terms analytically (or at least partially), leaving to the numerical integration only the smoother contributions [110]. A further solution, even more promising, involves the partitioning of the phase space in several regions, each one containing a small number of pseudo-singularities, ideally only one. The phase space is then parametrised to have a one-to-one matching between the numerically dangerous partitions and the integration variables. In this way, it is possible to obtain a stable and reliable integration of the phase space, even in presence of many PCS contributions. The feasibility of both solutions is currently under investigation.

1.7 Implementing new processes in MCMULE

1.7.1 A working example: $\mu \rightarrow eX$

We conclude the description of MCMULE explaining how to implement a new decay or scattering process in the code. To be practical we will refer to $\mu \rightarrow eX$, worked out during this thesis and already part of the first public release of MCMULE. The effective model used to describe the $\mu \rightarrow eX$ process will be discussed in Chapter 3, as well as the results obtained with MCMULE. In the following we will focus only on the technical details of its implementation.

To implement a new process in MCMULE the main steps to follow are:

- (1) If the process to implement does not fit any existing process group, a new one has to be created. This implies the creation of a new `pg` folder and its inclusion in the makefile. Luckily, $\mu \rightarrow eX$ fits the already existing `mudec` group, so we do not need to define a new process group.
- (2) Calculate the tree-level matrix elements required up to NLO, i.e. $\mathcal{M}_n^{(0)}$ and $\mathcal{M}_{n+1}^{(0)}$. This step is mostly straightforward, since both contributions are finite in $d = 4$ and therefore do not require any regularisation procedure.
- (3) Create a new `mat_e1` module in the `pg` folder to collect all matrix elements of the process. In case of tediously long expressions, it is recommended to create more files. This is not our case, so we create a single file `m2ej_mat_e1.f95` to collect all matrix elements of $\mu \rightarrow eX$ up to NLO. For practical purposes the scalar boson X is labelled with `j` in the code.
- (4) Implement $\mathcal{M}_n^{(0)}$ and $\mathcal{M}_{n+1}^{(0)}$ in the new `mat_e1.f95` file. If the computation was performed in MATHEMATICA, the final analytical expressions can be converted in FORTRAN through the command `FortranForm`. One-loop integral functions and other special functions that are common in higher-order calculations are provided in `functions.f95` and must be typed accordingly. Furthermore, the mass of on-shell particles should be calculated locally using the dot function `s(pi, pj) = 2 pi · pj`. Each matrix element function must start with a comment reporting the adopted PID convention. Concretely, the implementation of $\mathcal{M}_{n+1}^{(0)}$ for a polarised initial state should have the following form

```

2  FUNCTION PM2EJG(p1, n1, p2, p3, p4)
4      !! mu+(p1) -> e+(p2) J(p3) y(p4)
      !! mu-(p1) -> e-(p2) J(p3) y(p4)

```

```

6      real (kind=prec) :: p1(4), n1(4), p2(4), p3(4), p4(4)
8      real (kind=prec) :: Mmu2, Mel2, Mj2, Mmu, Mel, Mj
      real (kind=prec) :: s14, s24, s2n, s4n
10     real (kind=prec) :: pm2ejg

12     !! Momentum dot products
      s14 = s(p1,p4); s24 = s(p2,p4)
14     s2n = s(n1,p2); s4n = s(n1,p4)

16     !! On-shell masses
      Mmu2 = sq(p1); Mel2 = sq(p2); Mj2 = sq(p3)
18     Mmu = sqrt(Mmu2); Mel = sqrt(Mel2); Mj = sqrt(Mj2)

20     !! Matrix element
      pm2ejg = (8*(-8*CLj*CRj*Mel*Mmu*(Mel2*s14*(s14 - s24) &
22             + Mj2*s14*s24 - (Mmu2 - s14)*(s14 - s24)*s24) &
              !! [...])
24             !! Complete expression omitted

26     END FUNCTION PM2EJ

```

- (5) Add the needed soft limits in `pg.f95`, using the eikonal factor `eik` defined in `function.f95`. As already explained, `eik` has to be evaluated through the global variable `ksoft` returned by `phase_space.f95`. In our case, we have to include in `mudec.f95` the function

```

2     FUNCTION PM2EJG_S(q1,n1,q2,q3)

4     !! mu+(p1) -> e+(p2) J(p3) y(ksoft)
      !! mu-(p1) -> e-(p2) J(p3) y(ksoft)

6     real (kind=prec) :: q1(4), n1(4), q2(4), q3(4)
8     real (kind=prec) :: pm2ejg_s

10    !! Eikonal soft limit
      pm2ejg_s = 2*eik(q1,ksoft,q2)*pm2ej(q1,n1,q2,q3)
12    pm2ejg_s = (4.*pi*alpha)*pm2ejg_s

14    END FUNCTION PM2EJG_S

```

- (6) Calculate the renormalised one-loop matrix element $\mathcal{M}_n^{(1)}$ and implement the analytical expression in the code, as already done for the previous two contributions. It is recommended to include the divergent terms as well, following the convention

$$\mathcal{M}_n^{(1)} = \frac{(4\pi)^\epsilon}{\Gamma(1-\epsilon)} \left(\frac{c_{-1}}{\epsilon} + c_0 + \mathcal{O}(\epsilon) \right)$$

The implementation should return c_0 by default and optionally c_{-1} through an optional variable `sing`. In our case, we have to add in `m2ej_mat_e1.f95` the function

```
2  FUNCTION PM2EJL(p1,n1,p2,p3,sing)
4    !! [...]
5    !! Declarations omitted
6
7    !! Dot products and useful quantities
8    Mmu2 = sq(p1); Mel2 = sq(p2); Mj2 = sq(p3)
9    Mmu = sqrt(sq(p1)); Mel = sqrt(sq(p2));
10   Mj = sqrt(sq(p3)); nq = s(n1,p2)
11   ss0 = Mel2 + Mmu2 - Mj2
12   LogMeMu = log(Mel2/Mmu2)
13
14   !! RGE logs with scale musq
15   LogMe = log(Mel2/musq)
16   LogMu = log(Mmu2/musq)
17
18   !! Renormalised matrix element c(0)
19   pm2ejl = (-8 + 3*LogMe + 3*LogMu)*(4*CLj*CRj*Mel*Mmu &
20           + CRj2*(-(Mmu*nq) + ss0) + CLj2*(Mmu*nq + ss0)) &
21           !! [...]
22           !! Complete expression omitted
23
24   !! Divergent term c(-1)
25   if (present(sing)) then
26     sing = CRj**2*(Mel2 - Mj2 + Mmu*(Mmu - nq)) &
27           !! [...]
28           !! Complete expression omitted
29     sing = (2.*alpha/pi)*sing
30   endif
31
32  END FUNCTION PM2EJL
```

- (7) Add a new subroutine in `test.f95` to compare each matrix element with a bunch of reference values. This is done by using the routine `check`, which compares the implemented matrix elements with their expected values in a certain phase-space point. The comparison is performed within a selectable numerical threshold, advisedly $\mathcal{O}(10^{-8})$. This procedure allows to debug typing errors, especially in the porting of the matrix elements from MATHEMATICA to FORTRAN. Hence, to check our implementation of $\mathcal{M}_n^{(1)}$ we add

```
2  SUBROUTINE TESTMJMATEL
4    !! [...]
6    !! First check
```

```

      pol1 = (/ 0., 0., 0., 0. /)
 8      y1 = (/0.3 ,0.6 ,0.8 ,0.4 ,0.9/)
      call psd3(y1,p1,Mm,p2,Me,p3,Mj,weight) !! PS1
10      call check("m2ejg", pm2ejg(p1,pol1,p2,p3,p4),
      ↪ 48627.8811945461, threshold=1e-8)

12      !! Second check
      pol2 = (/ 0., 0., 0.85, 0. /)
14      y2 = (/0.3 ,0.6 ,0.8 ,0.4 ,0.9/)
      call psd3(y2,p1,Mm,p2,Me,p3,Mj,weight) !! PS2
16      call check("m2ejg", pm2ejg(p1,pol2,p2,p3,p4),
      ↪ 10722.023858830065, threshold=1e-8)

18      END SUBROUTINE

```

- (8) If none of the phase-space routines already implemented fits the new process, a new one has to be defined in `phase_space.f95`. The phase-space points have to be generated as discussed in Section 1.6. Since $\mu \rightarrow eX$ is the first two-body decay to be implemented in MCMULE, for $\mathcal{M}_n^{(0)}$ and $\mathcal{M}_n^{(1)}$ we need to add the routine

```

 2      SUBROUTINE PSD3(ra,q1,m1,q2,m2,q3,m3,weight)

 4          !!                      in c.m.f.                      !!
          !!                      q1 = q2 + q3                      !!
 6          !!  q1^2 = Mm^2;  q2^2 = m2^2;  q3^2 = m3^2  !!

 8      real (kind=prec), intent(in) :: ra(2), m1, m2, m3
      real (kind=prec), intent(out) :: q1(4), q2(4), q3(4)
10      real (kind=prec), intent(out) :: weight
      integer :: enough_energy

12

14      !! Momentum of the decaying particle
      q1 = (/ 0._prec, 0._prec, 0._prec, m1 /)

16      !! Generate azimuthal and polar angle for one particle
      !! Then impose back-to-back condition to the other
18      call pair_dec(ra(1:2),m1,q2,m2,q3,m3,enough_energy)
      if(enough_energy == 0) then
20          weight = 0._prec
      endif
22      weight = sq_lambda(m1**2,m2,m3)/(8*pi*m1**2)

24      END SUBROUTINE PSD3

```

- (9) In `integrands.f95` add the three matrix elements $\mathcal{M}_n^{(0)}$, $\mathcal{M}_{n+1}^{(0)}$ and $\mathcal{M}_n^{(1)}$ in the routine `initpiece`. This operation includes to associate the correct phase-space routine to each matrix element and specify if the integrand is non-subtracted

(`sigma_0`), single-subtracted (`sigma_1`) or double-subtracted (`sigma_2`). In our case we add to `initpiece` the three cases

```
2  SUBROUTINE INITPIECE(ndim, fxn)
4    !! [...]
6    select case(which_piece)
7      case('m2ej0') !! Leading order
8        call set_func(b'000000', pm2ej)
9        ps => psd3 ; fxn => sigma_0
10       nparticle = 3 ; ndim = 2
11       masses(1:3) = (/ Mm, Me, Mj /)
12       convfac = 0.5/Mm
13       polarised = .true.
14     case('m2ejF') !! Virtual correction
15       call set_func(b'000000', pm2ejf)
16       ps => psd3 ; fxn => sigma_0
17       nparticle = 3 ; ndim = 2
18       masses(1:3) = (/ Mm, Me, Mj /)
19       convfac = 0.5/Mm
20       polarised = .true.
21       xieik1 = xinormcut*(1.-((Me+Mj)/Mm)**2)
22     case('m2ejR') !! Real correction
23       call set_func('000000', pm2ejg)
24       call set_func('000001', pm2ejg_s)
25       ps => psd4_fks ; fxn => sigma_1
26       nparticle = 4 ; ndim = 5
27       masses(1:4) = (/ Mm, Me, Mj, 0._prec /)
28       convfac = 0.5/Mm
29       polarised = .true.
30       xicut1 = xinormcut*(1.-((Me+Mj)/Mm)**2)
32     !! [...]
33     case default
34       print*, "The piece ", which_piece, " is not implemented."
35       stop
36   end select
38 END SUBROUTINE
```

- (10) It is recommended to write a second test routine in `test.f95` to compare short integrations against reference values. Since the MC integration allows to fix the random seed, such a comparison can be performed deterministically.
- (11) Define in `user.f95` the histograms that the program will return in output. This is the only step to follow for anyone who wants to run one of the processes already implemented in MCMULE. As already mentioned in Section 1.5, the first requirement is to specify the binning metadata required by `vegas.f95`, i.e. the number of histograms to compute (`nr_q`) and for each of them the number of bins (`nr_bins`), the

lower limit (`min_val`) and the upper limit (`max_val`). Afterwards, the measurement function of any histogram has to be defined in terms of the external momenta in the routine `quant`. To be practical, we suppose that we want to study the process $\mu^+ \rightarrow e^+ X$ for the MEG II experiment, which features a drift chamber for positrons and a gamma calorimeter for photons. The nominal acceptances are given by

$$\begin{aligned} E_e > 45 \text{ MeV} & \quad |\cos \theta_e| < 0.50 & \quad |\phi_\gamma| > 2\pi/3 \\ E_\gamma > 40 \text{ MeV} & \quad |\cos \theta_\gamma| < 0.35 & \quad |\phi_\gamma| > \pi/3 \end{aligned}$$

where E_e is the positron energy, θ_e the angle between the positron momentum and the antimuon polarisation and ϕ_e the further spherical angle. The same definitions hold for the photon. We further suppose that we want to study $\mu \rightarrow eX$ excluding as much as possible the events including a real photon, whose potential emission was added contextually to the NLO corrections. However, it is clear that the experiment will not be able to reject all $\mu \rightarrow eX\gamma$ events, but only those in which the photon is detected by the gamma calorimeter. Exploiting the fully differentiability of the MCMULE predictions, we can adapt the theoretical distribution for the positron observables by rejecting any event accomplishing at least one of these two conditions:

- (a) the positron is not emitted within the acceptance of the drift chamber
- (b) the positron is emitted within the acceptance of the drift chamber, but a real photon is radiated within the acceptance of the gamma calorimeter.

In `user.f95` we can easily achieve it by setting the `quant` function as

```

2  FUNCTION QUANT(q1,q2,q3,q4)
4     real (kind=prec), intent(in) :: q1(4),q2(4),q3(4),q4(4)
5     real (kind=prec) :: ga(4),gah(4),gas(4)
6     real (kind=prec) :: quant(nr_q),ez(4)
8     !! Set muon polarisation (global)
9     pol1 = (/ 0._prec, 0._prec, -0.85_prec, 0._prec /)
10
11    !! Event rejected by default
12    pass_cut = .false.
13    !! Check positron acceptance
14    if(q2(4) > 45. .and. abs(cos_th(q2, pol1)) < 0.35
15        ↪ .and. abs(phi(q2)) > pi/3) then
16        !! No photon in the calorimeter
17        if(q4(4) < 10. .or. abs(cos_th(q4, pol1)) > 0.35
18            ↪ .or. abs(phi(q2)) < 2*pi/3) then
19            !! The event passes the cut
20            pass_cut = .true.
21        endif
22    endif

```

```

22    !! Positron observables
      names(1) = "Ee"
24    quant(1) = q2(4)
      names(2) = "Cthe"
26    quant(2) = cos_th(q2, pol1)

28    END FUNCTION QUANT

```

- (12) According to the FKS scheme, the virtual and real contributions $\sigma_n^{(1)}$ and $\sigma_{n+1}^{(0)}$ are individually dependent from the unphysical parameter ξ_c . However, their sum $\sigma^{(1)} = \sigma_n^{(1)} + \sigma_{n+1}^{(0)}$, i.e. the complete NLO correction, has to be ξ_c -independent. Performing accurate ξ_c -independence studies on $\sigma^{(1)}$ is therefore a crucial step in order to validate the code, especially its implementation of FKS. Since the ξ_c -dependence is induced by terms like $\xi_c^{-2\epsilon}/\epsilon$, at NLO we have

$$\sigma_n^{(1)}(\xi_c) = a_{0,0} + a_{0,1} \log(\xi_c)$$

$$\sigma_{n+1}^{(0)}(\xi_c) = a_{1,0} + a_{1,1} \log(\xi_c)$$

Hence, the ξ_c -independency of $\sigma^{(1)}$ requires

$$a_{0,1} + a_{1,1} = 0$$

The condition can be verified by evaluating $\sigma_n^{(1)}$ and $\sigma_{n+1}^{(0)}$ for several choices of ξ_c and extracting the parameters $a_{0,1}$ and $a_{1,1}$ through a best fit. We will exhibit this study for $\mu \rightarrow eX$ in Chapter 3.

- (13) The new process is now implemented in MCMULE up to NLO and ready for further validations based on the phenomenological results. If NNLO precision is required, the above steps can also be followed for the three NNLO contributions $\mathcal{M}_n^{(2)}$, $\mathcal{M}_{n+1}^{(1)}$ and $\mathcal{M}_{n+2}^{(0)}$ with only minimal adaptations.

1.7.2 One calculation in MATHEMATICA

In the previous discussion we assumed to know the analytical expression of the required matrix elements. For the sake of completeness, we now provide a working example on how to calculate in MATHEMATICA the virtual one-loop contribution $\mathcal{M}_n^{(1)}$ for our benchmark decay $\mu \rightarrow eX$. The aim is to give a concrete idea of the MCMULE tools for analytical calculations, especially those in-house defined. We will apply the FDF scheme introduced in Section 1.3, calculating the one-loop integrals through the PV reduction method, as implemented in Package-X. Again, we postpone all phenomenological discussions about

$\mu \rightarrow eX$ to Chapter 3.

First, we need to import the in-house package `qgraf`, which includes the automatic graph generation routine and `Package-X`, among others.

```
In[ ]:= Import["qgraf.wl"]
```

The next step is generating the tree-level and one-loop amplitudes `A0` and `A1`, according to the effective interaction Lagrangian

$$\mathcal{L}_{\mu e}^{int} = X \bar{\psi}_\mu (C_L P_L + C_R P_R) \psi_e - e \bar{\psi}_\mu \gamma^\nu A_\nu \psi_\mu - e \bar{\psi}_e \gamma^\nu A_\nu \psi_e$$

discussed in Chapter 3. We encode the two complex Yukawa couplings C_L and C_R in $\mathbb{C}[L]$ and $\mathbb{C}[R]$. Since at the moment `qgraf` includes only SM processes, we initially generate the d -dimensional amplitudes for $\mu \rightarrow e\nu\bar{\nu}$ through the `RunQGraf` function. At this point, the result can be adapted to $\mu \rightarrow eX$ by using the replacements encoded in the list `Yukawas`. We take care to write explicitly the γ^5 matrix in view of its finite renormalisation, required by the FDF scheme.

```
In[ ]:= (* PID:  $\mu$  (M, p)  $\rightarrow$  e (m, q) X (mj, p-q) *)
Yukawas = {_neutrinentensor  $\rightarrow$  1,
DiracMatrix[A___, PL,  $\gamma_{v4}$ , B___]  $\Rightarrow$ 
DiracMatrix[A, C[L]  $\frac{1}{2}$  (1 -  $\gamma_5$ ) + C[R]  $\frac{1}{2}$  (1 +  $\gamma_5$ ), B]};
A0 = "diag1" /. Contract[RunQGraf[{"mum"}, {"elm", "nu"}, 0] /. Yukawas /. e  $\rightarrow$   $\sqrt{4\pi\alpha}$ ;
A1 = "diag1" /. Contract[RunQGraf[{"mum"}, {"elm", "nu"}, 1] /. Yukawas /. e  $\rightarrow$   $\sqrt{4\pi\alpha}$ ;
```

At this point we easily calculate the leading-order matrix element `M0` by squaring `A0` and summing over the final spins for a polarised initial state. This can be done through the in-house function `FermionSpinSumPolarised`, which computes tracks according to the rule $\bar{u}(p, m)u(p, m) \rightarrow (\not{p} - m)(1 - m\gamma^5\not{n})$, where n is the polarisation vector of the initial state. We also define a list `OnShell` to impose energy conservation and on-shell conditions to external particles.

```
In[ ]:= (* Muon polarisation vector: n *)
npol[p] = n; npol[q] = 0;
OnShellV = {p.p  $\rightarrow$   $M^2$ , q.q  $\rightarrow$   $m^2$ , p.q  $\rightarrow$   $(M^2 + m^2 - mj^2)/2$ , n.p  $\rightarrow$  0, n.q  $\rightarrow$   $nq/2$ };
M0 = Simplify[Contract@FermionSpinSumPolarised[A0, A0] /. OnShellV /. d  $\rightarrow$  4]
```

To easily compute one-loop matrix element `M1`, given by the interference term between `A0` and `A1`, we apply the four rules of FDF. First, we use [Rule I](#) to perform the entire

γ -matrices algebra in four dimensions through `FermionSpinSumPolarised`. To keep track of the dimensionality of the loop momentum `k1`, we denote `4[k1]`. [Rule I](#) is then easily achieved by setting

```
In[ ]:= M1 = Block[{d = 4},
  Collect[2 Contract@FermionSpinSumPolarised[A1 /. {
     $\gamma.k1 \rightarrow \gamma.4[k1] + \gamma5 \cdot \mu$ 
  }, A0] /. OnShellV,  $\mu$ , Simplify]
];
```

We continue by applying [Rule II](#), in order to simplify the resulting μ -terms. This simply means setting every odd power of μ to 0.

```
In[ ]:= M1even = Collect[M1,  $\mu$ , Factor] /. {
   $\mu^{n-} /;$  EvenQ[n]  $\rightarrow \mu2^{n/2}$ ,  $\mu \rightarrow 0$ 
}
```

Next, we make the loop momentum d -dimensional again, in order to simplify terms as $k_{[4]}^2/(k_{[d]}^2 - m^2)$ through [Rule III](#). To manage this, we only need the command

```
In[ ]:= M1k1d = Collect[M1even /. {
   $4[k1].4[k1] \rightarrow k1.k1 + \mu2$ ,  $4[k1] \rightarrow k1$ 
},  $\mu2$ , Factor]
```

At this point we can solve the μ -independent integrals with the standard one-loop calculus. As mentioned earlier, we achieve it by exploiting the `Package-X` implementation of the PV reduction method. Concretely, this is possible by using in sequence the two functions `Pro2LoopIntegrate` and `LoopRefine`. The first reduces the loop integrand in terms of PV scalar functions, while the second evaluates the resulting integral. Furthermore, we compute the μ -dependent integration through the in-house functions `μ Integrate` and `μ Refine`, that implement [Rule IV](#) in the context of `Pro2LoopIntegrate` and `LoopRefine`. Finally, we collect the two different contributions in `M1bareFDF` and `M1bareFDF μ` , respectively.

```
In[ ]:= M1bareFDF = LoopRefine[Simplify[ReleaseHold[
  Pro2LoopIntegrate[Coefficient[M1k1d,  $\mu2$ , 0]]]];
M1bareFDF $\mu$  =  $\mu$ Refine[ $\mu$ Integrate[Coefficient[M1k1d,  $\mu2$ , 1], 1]];
```

We have obtained the bare matrix element. To eliminate the UV singularities, we calculate the required counter-term using the renormalisation constants for FDF. They were extensively calculated in [[111](#), [112](#)]. According to MCMULE's conventions, we use

the OS scheme to renormalise α and lepton fields, while we apply the $\overline{\text{MS}}$ scheme for the two Yukawa couplings. Mass renormalisation is not required at one-loop level and we can avoid to renormalise the scalar field X because it is not interacting in QED. Formally, we have $Z_X = 1$ to all α orders. Hence, we add the counter-term M0r , given by

$$\ln[*]:= \text{M0r} = 2 \text{M0} \left(\delta\text{Z}[\text{M}] + \delta\text{Z}[\text{m}] - \frac{\alpha}{4\pi} \left(\frac{\mu^2}{\text{M}^2} \right)^\epsilon \left(1 + \frac{3}{\epsilon} \right) \right) /. \delta\text{Z}[\text{M}_-] \Rightarrow \frac{\alpha}{4\pi} \left(\frac{\mu^2}{\text{M}^2} \right)^\epsilon \left(-\frac{1}{2\epsilon} - \frac{5}{2} \right);$$

Finally, we have to correct the FDF choice of γ^5 introducing the finite renormalisation (1.28). Hence, we add the further counter-term M5 , given by

$$\ln[*]:= \text{M5} = -\frac{\alpha}{\pi} \text{Coefficient} [\text{FermionSpinSumPolarised}[\text{A0} /. \gamma^5 \rightarrow (1 + \delta^5) \gamma^5, \text{A0} /. \gamma^5 \rightarrow (1 + \delta^5) \gamma^5] /. \text{OnShell}, \delta^5]$$

We are now ready to collect together all pieces and convert the final expression in FORTRAN syntax through the function `FortranForm`.

$$\ln[*]:= \text{M1FDF} = \text{Simplify} \left[\text{M1bareFDF} + \frac{1}{4\pi} \text{M1bareFDF} \mu + \text{M0r} + \text{M5} \right];$$

$$\text{FortranForm}[\text{M1FDF}]$$

Chapter 2

Muon decay $\mu \rightarrow e\nu\bar{\nu}$ at NNLO+LL

2.1 Theoretical model

The antimuon decay $\mu^+ \rightarrow e^+\nu_e\bar{\nu}_\mu$ is the dominant SM background when searching for $\mu^+ \rightarrow e^+X$. For low masses of X , as expected for an ALP, the signal is a monochromatic positron close to the high-energy endpoint of the spectrum. As we will discuss throughout the chapter, the QED corrections to $\mu^+ \rightarrow e^+\nu_e\bar{\nu}_\mu$ become very large near the energy endpoint, due to the emission of soft photons. Hence, a reliable experimental search for $\mu^+ \rightarrow e^+X$ requires very precise theoretical predictions for $\mu^+ \rightarrow e^+\nu_e\bar{\nu}_\mu$, far beyond the well-established NLO [113–115]. This means including the full NNLO corrections and possibly the resummation to all orders of the dominant logarithmic terms. In addition, all calculations cannot neglect the positron mass and must include the effect due to an arbitrary antimuon polarisation, as required by the modern low-energy experiments with leptons. Furthermore, the predictions should be fully differential, rather than limited to the positron energy spectrum. In the context of a MC framework, this means that the process needs to be implemented in order to allow the theoretical prediction for any differential distribution $d^n\Gamma/dx_1\dots dx_n$, where x_1, \dots, x_n is an arbitrary set of inclusive variables. This also includes being able to apply arbitrary cuts on the process observables, in order to finely tune the theoretical predictions to the specific experimental context. For instance, the knowledge of the correlation between the positron energy and its emission direction is fundamental to reject the left-handed SM background from potential right-handed $\mu \rightarrow eX$ events [116].

In Chapter 1 we presented the MCMULE framework for fully differential QED corrections for low-energy processes with leptons. Testing, debugging and further developing MCMULE was the first relevant goal of this thesis. The next important goal is to extensively use it to compute reliable predictions for the muon decay, including all QED corrections up to NNLO+LL and accomplishing all aforementioned requests. This original result constitutes the most precise fully differential predictions ever made for $\mu \rightarrow e\nu\bar{\nu}$, as well as the most accurate evaluation of the QED corrections to the positron energy spectrum for such a decay. Until now, fully differential predictions for $\mu \rightarrow e\nu\bar{\nu}$ have been limited

to NLO, while the energy spectrum was calculated up to NNLO by using a numerical loop integration [117]. Only recently the two-loop integrals required for a fully differential NNLO calculation have been solved [41].

Since the MEG II experiment uses an antimuon beam to avoid nuclear captures, we explicitly discuss the antimuon decay $\mu^+ \rightarrow e^+ \nu_e \bar{\nu}_\mu$. However, all the exhibited computations can be easily adapted to the complementary process $\mu^- \rightarrow e^- \bar{\nu}_e \nu_\mu$ by reversing the initial-state polarisation. In the following, we refer to μ^+ as muon rather than antimuon for the sake of simplicity.

2.1.1 Fermi theory

The muon decay $\mu^+ \rightarrow e^+ \nu_e \bar{\nu}_\mu$ is a weak process, mediated in the SM by the gauge boson W^+ . The leading-order transition amplitude, corresponding to the tree-level diagram depicted in Figure 2.1, is given by

$$\mathcal{A}_3^{(0)} = \frac{ig}{\sqrt{2}} \left[\bar{v}_\mu(p_0) \gamma_\alpha P_L v_{\nu_\mu}(q_2) \right] \frac{-i}{k^2 - m_W^2} \left(g^{\alpha\beta} - \frac{k^\alpha k^\beta}{k^2} \right) \frac{ig}{\sqrt{2}} \left[\bar{u}_{\nu_e}(q_3) \gamma_\beta P_L v_e(q_1) \right] \quad (2.1)$$

where $P_L = (1 - \gamma_5)/2$ is the usual left-handed projector and $g = e/\cos\theta_W$ is the SM coupling between the W -boson and the charged leptons. As usual, the subscript denotes the number of particles in the final state and the superscript the number of loops.

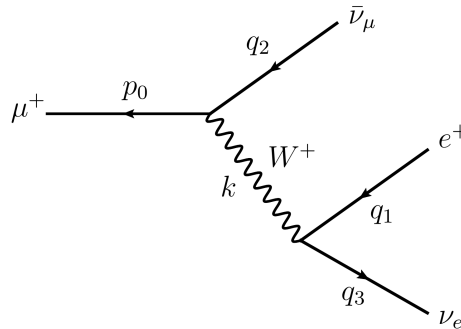


Figure 2.1 Tree-level SM diagram for the muon decay $\mu^+ \rightarrow e^+ \nu_e \bar{\nu}_\mu$.

Since the squared W momentum $k^2 = (p_0 - q_2)^2 \sim \mathcal{O}(m_\mu^2)$ is much smaller than its squared mass m_W^2 , we can expand the W -propagator in power of k^2/m_W^2 , obtaining

$$\frac{-i}{k^2 - m_W^2} \left(g^{\alpha\beta} - \frac{k^\alpha k^\beta}{k^2} \right) = \frac{i}{m_W^2} g^{\mu\nu} + \mathcal{O} \left(\frac{k^2}{m_W^2} \right) \quad (2.2)$$

which leads to

$$\mathcal{A}_3^{(0)} = -i \frac{g^2}{2m_W^2} \left[\bar{\nu}_\mu(p_0) \gamma_\alpha P_L v_{\nu_\mu}(q_2) \right] \left[\bar{u}_{\nu_e}(q_3) \gamma_\alpha P_L v_e(q_1) \right] + \mathcal{O}\left(\frac{k^2}{m_W^2}\right) \quad (2.3)$$

The first order of $\mathcal{A}_3^{(0)}$ is reproduced by the well-known Fermi lagrangian [118]

$$\mathcal{L}_F = -\frac{4G_F}{\sqrt{2}} (\bar{\psi}_\mu \gamma^\alpha P_L \psi_{\nu_\mu}) (\bar{\psi}_{\nu_e} \gamma_\alpha P_L \psi_e) \quad (2.4)$$

where we have introduced the Fermi coupling constant

$$G_F = \frac{\sqrt{2}}{8} \frac{g^2}{m_W^2} \quad (2.5)$$

In (2.4) the weak interaction is approximated to a point-like interaction between the four leptons, encoding the effect due to the W -boson exchange into the effective coupling constant $G_F \propto m_W^{-2}$. According to (2.2), the Fermi theory properly describes the weak interaction as long as the W -boson momentum is far below m_W . Since $m_W \gg m_\mu$, this condition is certainly valid in muon decay. Specifically, since the higher-order contributions due to the W -propagator are suppressed by powers of

$$\frac{k^2}{m_W^2} \sim \frac{m_\mu^2}{m_W^2} \sim 10^{-6} \quad (2.6)$$

we can safely employ the interaction lagrangian

$$\mathcal{L}_{F+QED}^{\text{INT}} = -e \bar{\psi}_\mu \gamma^\alpha A_\alpha \psi_\mu - e \bar{\psi}_e \gamma^\alpha A_\alpha \psi_e - \frac{4G_F}{\sqrt{2}} (\bar{\psi}_\mu \gamma^\alpha P_L \psi_{\nu_\mu}) (\bar{\psi}_{\nu_e} \gamma_\alpha P_L \psi_e) \quad (2.7)$$

to compute the dominant QED corrections to $\mu^+ \rightarrow e^+ \nu_e \bar{\nu}_\mu$. Only beyond $\mathcal{O}(\alpha^2)$ the electroweak (EW) higher-order corrections have a non-negligible impact on the positron observables [119]. The same holds for the hadronic polarisation effects [120].

Since $G_F \propto m_W^{-2}$, the Fermi interaction is non-renormalisable. Nevertheless, the QED higher-order diagrams arising from (2.7) are finite, as shown in [121]. From a conceptual point of view, we are doing perturbation theory in QED, expanding the transition amplitudes in powers of the electromagnetic coupling α while keeping the weak interaction fixed to LO. Since QED is renormalisable, the amplitudes obtained in this way are UV finite. From a formal point of view, we renormalise the coupling G_F order by order, by introducing a further renormalisation constant $G_F \rightarrow Z_F G_F$ to be preferably calculated in the $\overline{\text{MS}}$ scheme. However, by exploiting the chiral symmetry $\psi \rightarrow \gamma^5 \psi \wedge m \rightarrow -m$, it is possible to show that $Z_F = 1$ to all QED orders. This property further simplifies the higher-order computation of $\mu \rightarrow e\nu\bar{\nu}$ in Fermi theory.

2.1.2 Neutrino average

We are not interested in the neutrino pair in $\mu^+ \rightarrow e^+ \nu_e \bar{\nu}_\mu$, because their observables cannot be measured experimentally. The idea is therefore to factorise the corresponding contribution, in order to simplify the calculation of the positron observables as much as possible. We can use the Fierz identities to rearrange the spinor bilinears in (2.7) as

$$\mathcal{L}_{\text{FF+QED}}^{\text{INT}} = -e\bar{\psi}_\mu\gamma^\alpha A_\alpha\psi_\mu - e\bar{\psi}_e\gamma^\alpha A_\alpha\psi_e - \frac{4G_F}{\sqrt{2}} (\bar{\psi}_\mu\gamma^\alpha P_L\psi_e) (\bar{\psi}_{\nu_e}\gamma_\alpha P_L\psi_{\nu_\mu}) \quad (2.8)$$

We note that any transition amplitude arising from (2.8) contains the *neutrino current*

$$\mathcal{N}^\alpha \equiv \bar{u}(q_3)\gamma^\alpha P_L v(q_2) \quad (2.9)$$

which results in a *neutrino tensor* $\mathcal{N}^{\alpha\beta} \equiv \mathcal{N}^\alpha \mathcal{N}^{*\beta}$ in the squared amplitude. Hence, we can factor out $\mathcal{N}^{\alpha\beta}$ and average it over all possible neutrino momenta. To this end, we first note that

$$\mathcal{N}^\alpha \mathcal{N}^{*\beta} = 4q_2^\alpha q_3^\beta + 4q_2^\beta q_3^\alpha + 4q_2 \cdot q_3 g^{\alpha\beta} \quad (2.10)$$

where the sum over the spin states is implicit. We now define the phase-space average of an arbitrary function $f(q_2, q_3)$ as

$$\langle f(q_2, q_3) \rangle = \frac{\int d\Phi_2 f(q_2, q_3)}{\int d\Phi_2} = 8\pi \int d\Phi_2 f(q_2, q_3) \quad (2.11)$$

where $d\Phi_2$ is the measure of the 2-body phase space corresponding to the neutrino pair. Since an average over q_2 and q_3 can only depend on their sum $Q \equiv q_2 + q_3$, the most general ansatz for $\langle q_2^\alpha q_3^\beta \rangle$ is

$$\langle q_2^\alpha q_3^\beta \rangle = A \frac{Q^\alpha Q^\beta}{Q^2} + B g^{\alpha\beta} \quad (2.12)$$

Applying the projectors $g_{\alpha\beta}$ and $Q_\alpha Q_\beta$ and using the on-shell condition $q_3^2 = q_4^2 = 0$, we find the relation $A = 2B = Q^2/6$, which leads to

$$\mathcal{N}^{\alpha\beta} = \langle \mathcal{N}^\alpha \mathcal{N}^{*\beta} \rangle = \frac{4}{3} Q^2 \left(\frac{Q_\alpha Q_\beta}{Q^2} - g^{\alpha\beta} \right) \quad (2.13)$$

The Fierz rearranged Fermi lagrangian (2.8) in conjunction with the neutrino tensor average (2.13) greatly simplifies the calculation of the positron observables for $\mu \rightarrow e\nu\bar{\nu}$, especially beyond tree-level. In the following we always imply the application of this approach.

2.2 Numerical setup

We are interested to study the decay $\mu^+ \rightarrow e^+\nu_e\bar{\nu}_\mu$ for a polarised initial state. Since muons decay at rest in MEG II, we perform all computations in the center-of-mass frame, where the muon 4-momentum becomes

$$p_0 = m_\mu (1, 0, 0, 0) \quad (2.14)$$

Furthermore, we define the z -axis along the muon polarisation, but not necessarily in the same direction. Thus, we can write the initial-state polarisation vector as

$$n_0 = n_\mu (0, 0, 0, 1) \quad -1 \leq n_\mu \leq 1 \quad (2.15)$$

where $|n_\mu|$ is the fraction of polarised muons in the beam, i.e. the probability of the initial-state spin to be oriented along the z -axis. Positive values of n_μ corresponds to a forward polarisation with the z -axis, while negative values corresponds to a backward polarisation. For $n_\mu = 0$ we obtain a beam of totally unpolarised muons. From a formal point of view, it is always possible to define the z -axis in the same direction of the polarisation vector, limiting n_μ only to non-negative values. However, we maintain this additional degree of freedom to easily include the MEG II conventional frame of reference, in which the z -axis results opposite to the muon polarisation ($n_\mu < 0$). At the same time, we do not directly employ this convention, not to exclude the intuitive construction in which the z -axis is oriented along the initial-state polarisation vector ($n_\mu > 0$).

It is worth spending a few words on the MEG II muon beam and its polarisation. At PSI, muons are produced from the decay $\pi^+ \rightarrow \mu^+\nu_\mu$. Neglecting the mass of the muon neutrino, the angular momentum conservation requires the muons to be emitted with spin opposite to their momenta. The produced muons are then collected in a low-energy beam and stopped in a thin target, where they decay at rest. Defining the z -axis along the beam direction we obtain an expected value $n_\mu^{th} = -1$. However, depolarising effects occur during the muon production, propagation and stopping. Consequently, the measured value at the target is [122]

$$n_\mu^{exp} = -0.86 \pm 0.02 \text{ (stat)} \pm 0.05 \text{ (syst)}$$

Accordingly, when referring directly to the MEG II case, we assume $n_\mu = -0.85$ as typical value of polarisation. We note that for such a polarisation, high-energy positrons are preferably emitted backward with the z -axis.

The only decay product we are interested in is the positron⁵. We parametrise its 4-momentum in spherical coordinates as

$$q_1 = (E_e, q_e \sin \theta_e \cos \phi_e, q_e \sin \theta_e \sin \phi_e, q_e \cos \theta_e) \quad E_e^2 = m_e^2 + q_e^2 \quad (2.16)$$

where $0 \leq \theta_e \leq \pi$ and $-\pi \leq \phi_e \leq \pi$. The distribution of ϕ_e is uniform in the allowed range $[-\pi, +\pi]$ for any initial polarisation. Thus, all information on the positron are contained in the double-differential decay width

$$\mathcal{G}_e \equiv \frac{1}{\Gamma_0} \frac{d^2\Gamma}{dE_e d\cos\theta_e} \quad \Gamma_0 \equiv \frac{G_F^2 m_\mu^5}{192\pi^3} \quad (2.17)$$

where Γ_0 is the well-known LO decay width in Fermi theory for $m_e \rightarrow 0$. In addition to factor out a very common factor in muon decay calculations, the division for Γ_0 removes the Fermi constant G_F from all the following computations. The knowledge of \mathcal{G}_e fully characterises the positron emitted in polarised muon decay. Hence, the two-dimensional distribution \mathcal{G}_e is all we need to implement a positron generator in the MEG II simulation and analysis software, as will be required in Chapter 5. The kinematic bounds on E_e and $\cos\theta_e$ are given by

$$m_e \leq E_e \leq \frac{m_\mu}{2} \left(1 + \frac{m_e^2}{m_\mu^2}\right) \simeq \frac{m_\mu}{2} \quad -1 \leq \cos\theta_e \leq 1 \quad (2.18)$$

We will refer to the upper bound on E_e as *energy endpoint* E_p . From \mathcal{G}_e we can easily obtain the positron energy spectrum

$$\mathcal{E}_e \equiv \int_{-1}^{+1} d\cos\theta_e \mathcal{G}_e = \frac{1}{\Gamma_0} \frac{d\Gamma}{dE_e} \quad (2.19)$$

and the angular distribution

$$\mathcal{T}_e \equiv \int_{m_e}^{E_{ep}} dE_e \mathcal{G}_e = \frac{1}{\Gamma_0} \frac{d\Gamma}{d\cos\theta_e} \quad (2.20)$$

The double-differential width \mathcal{G}_e can be formally written as

$$\mathcal{G}_e(E_e, \cos\theta_e) = f(E_e) + n_\mu \cos\theta_e g(E_e) \quad (2.21)$$

We usually refer to $f(E_e)$ as the *isotropic decay function* and to $g(E_e)$ as the *anisotropic*

⁵The positron (electron) produced in $\mu \rightarrow e\nu\bar{\nu}$ is often called *Michel positron (electron)* and its energy spectrum *Michel spectrum*. Similarly, the process $\mu \rightarrow e\nu\bar{\nu}$ is often called *Michel decay*.

decay function. From (2.19) and (2.20) follow that

$$\mathcal{E}_e(E_e) = 2f(E_e) \quad (2.22a)$$

$$\begin{aligned} \mathcal{T}_e(\cos\theta) &= \int_{m_e}^{E_p} dE_e f(E_e) + n_\mu \cos\theta_e \int_{m_e}^{E_p} dE_e g(E_e) \\ &= F + n_\mu \cos\theta_e G \end{aligned} \quad (2.22b)$$

where F and G are two numerical constants. Hence, the isotropic function $f(E_e)$ represent the positron energy spectrum times a trivial factor two. To interpret the anisotropic function $g(E_e)$, we note that \mathcal{T}_e is a linear distribution with gradient the integral of $g(E_e)$ times the polarisation n_μ . Thus, $g(E_e)$ represents the gradient of the angular distribution \mathcal{T}_e for a fixed positron energy E_e and $n_\mu = 1$. By writing

$$\mathcal{G}_e = \sum_{k=0}^{\infty} \left(\frac{\alpha}{\pi}\right)^k \mathcal{G}_k = \sum_{k=0}^{\infty} \left(\frac{\alpha}{\pi}\right)^k \left(f_k(E_e) + n_\mu \cos\theta_e g_k(E_e)\right) \quad (2.23)$$

we can extend the decomposition in f and g order by order, obtaining

$$f(E_e) = f_0(E_e) + \left(\frac{\alpha}{\pi}\right) f_1(E_e) + \left(\frac{\alpha}{\pi}\right)^2 f_2(E_e) + \dots \quad (2.24a)$$

$$g(E_e) = g_0(E_e) + \left(\frac{\alpha}{\pi}\right) g_1(E_e) + \left(\frac{\alpha}{\pi}\right)^2 g_2(E_e) + \dots \quad (2.24b)$$

At LO it is analytically known that

$$f_0(x_e) = \beta_e x_e^2 \left(3 - 2x_e + \frac{1}{4}x_e(3x_e - 4)(1 - \beta_e^2)\right) \quad (2.25a)$$

$$g_0(x_e) = \beta_e x_e^2 \left((1 - 2x_e)\beta_e + \frac{3}{4}x_e^2(1 - \beta_e^2)\beta\right) \quad (2.25b)$$

where

$$x_e \equiv \frac{2E_e}{m_\mu} \quad \beta_e \equiv \sqrt{1 - \left(\frac{m_e}{E_e}\right)^2} \quad (2.26)$$

By neglecting the positron mass ($\beta_e \rightarrow 1$), we obtain

$$f_0(x_e) \simeq (3 - 2x_e)x_e^2 \quad g_0(x_e) \simeq (1 - 2x_e)x_e^2 \quad (2.27)$$

Both f and g can be expressed in terms of energy distributions only. In this regard we

introduce the *forward positron spectrum* \mathcal{E}_e^+ and the *backward positron spectrum* \mathcal{E}_e^- as

$$\mathcal{E}_e^+ \equiv \mathcal{E}_e(\cos \theta_e > 0) = \int_0^{+1} d\cos \theta_e \mathcal{G}_e \quad (2.28)$$

$$\mathcal{E}_e^- \equiv \mathcal{E}_e(\cos \theta_e < 0) = \int_{-1}^0 d\cos \theta_e \mathcal{G}_e \quad (2.29)$$

By using (2.21), we find

$$\mathcal{E}_e^+ = f + n_\mu g \quad \mathcal{E}_e^- = f - n_\mu g \quad (2.30)$$

which leads to

$$f = \frac{\mathcal{E}_e^+ + \mathcal{E}_e^-}{2} \quad g = \frac{\mathcal{E}_e^+ - \mathcal{E}_e^-}{2n_\mu} \quad (2.31)$$

The decomposition can be easily extended order by order. By writing

$$\mathcal{E}_e^+ = \sum_{k=0}^{\infty} \left(\frac{\alpha}{\pi}\right)^k \mathcal{E}_n^+ \quad \mathcal{E}_e^- = \sum_{k=0}^{\infty} \left(\frac{\alpha}{\pi}\right)^k \mathcal{E}_n^- \quad (2.32)$$

we find that

$$f_n = \frac{\mathcal{E}_n^+ + \mathcal{E}_n^-}{2} \quad g_n = \frac{\mathcal{E}_n^+ - \mathcal{E}_n^-}{2n_\mu} \quad (2.33)$$

Introducing the two spectra \mathcal{E}_e^+ and \mathcal{E}_e^- , we have found an efficient way to compute the double-differential distribution \mathcal{G}_e numerically. A naive approach would have been to sample \mathcal{G}_e over a $N \times N$ grid on the $E_e \times \cos \theta_e$ plane. Conversely, by using (2.21) and (2.31) we need only to sample the two spectra \mathcal{E}_e^+ and \mathcal{E}_e^- over N energy bins, reducing the numerical complexity of the problem from N^2 to $2N$. Furthermore, since we need to discretise the positron energy E_e only, we can keep $\cos \theta_e$ as a continuous variable. Finally, since the n_μ -dependence is factorised in (2.21), the knowledge of f and g allows us to easily compute \mathcal{G}_e for any initial-state polarisation. Hence, we will sample \mathcal{E}_e^+ and \mathcal{E}_e^- for a single toy value of n_μ , then we will completely remove its contribution by applying (2.31) to calculate f and g . By directly sampling \mathcal{G}_e , we would have to repeat the procedure for each needed value of n_μ .

Although we will base our discussion on \mathcal{G}_e , we remark that MCMULE allows to compute even more general predictions. Furthermore, it is possible to include arbitrary cuts to tune the theoretical predictions to the experimental acceptances and preselections. For example, it is possible to introduce cuts on the photons radiated beyond LO, in order to distinguish between soft and hard radiations, i.e between detectable and undetectable photons with a certain experimental apparatus.

2.3 LO contribution

The LO contribution to $\mu \rightarrow e\nu\bar{\nu}$ is given by

$$d\Gamma^{(0)} = d\Phi_3 \mathcal{M}_3^{(0)} = d\Phi_3 |\mathcal{A}_3^{(0)}|^2 \quad (2.34)$$

where $d\Phi_3$ is the measure of the 3-body phase space and $\mathcal{M}_3^{(0)}$ is the LO matrix element. Although the two decay functions f and g are analytically known at LO, it is important to compute them numerically to perform a very precise comparison between the MCMULE results and the analytical expressions. This constitutes a straightforward way to validate the code, which we will repeat at NLO, before going into the original results of MCMULE and this thesis.

The first step is the computation of \mathcal{E}_e^+ and \mathcal{E}_e^- at LO. According to (2.32), we have

$$\mathcal{E}_e^+ \simeq \mathcal{E}_{\text{LO}}^+ = \mathcal{E}_0^+ \quad \mathcal{E}_e^- \simeq \mathcal{E}_{\text{LO}}^- = \mathcal{E}_0^- \quad (2.35)$$

To sample the two spectra, we split the positron energy into 4000 bins, organised as reported in Table 2.1. The bin density increases as energy increases. This choice has two motivations. First, the MEG II positron spectrometer has an acceptance $E_e \gtrsim 45$ MeV, which matches the signal region for $\mu \rightarrow e\gamma$ and $\mu \rightarrow eX$ for a light X . Second, the radiative corrections to $\mu \rightarrow e\nu\bar{\nu}$ become very large close to the energy endpoint $E_e^M \approx 52.8$ MeV, due to the emission of soft photons. Hence, a finer sampling of the high-energy region of the positron spectrum is advisable, both experimentally and theoretically. At the same time, we decrease the bin density not to slow down the algorithm with an excessive sampling of the less important low-energy region. The same bin pattern is used throughout the thesis.

Positron energy	No. of bins	Bin width
0–26 MeV	1000	26 keV
26–42 MeV	1000	16 keV
42–50 MeV	1000	8 keV
50–54 MeV	1000	4 keV

Table 2.1 Energy bins used throughout the thesis.

The statistical uncertainty associated to each bin is calculated according to (1.95). The MC sample is set to achieve an error of $\mathcal{O}(1)$ ppm in every bin. As we will discuss at the end of the chapter, this request will allow us to neglect the statistical uncertainty respect to the theoretical one, arising from the uncalculated perturbative orders. At LO such a

precision is achieved by setting the VEGAS statistics parameters to $K \times N = 200 \times 10^8$ after a preconditioning run with $K_{pc} \times N_{pc} = 20 \times 10^6$. The MCMULE results for \mathcal{E}_0^+ and \mathcal{E}_0^- are shown in Figure 2.2. The initial-state polarisation is set to $n_\mu = -0.85$, as in MEG II. Thus, the positron is preferably emitted backward for $E_e \gg m_e$, so that $\mathcal{E}_e^- > \mathcal{E}_e^+$ at sufficiently large energies.

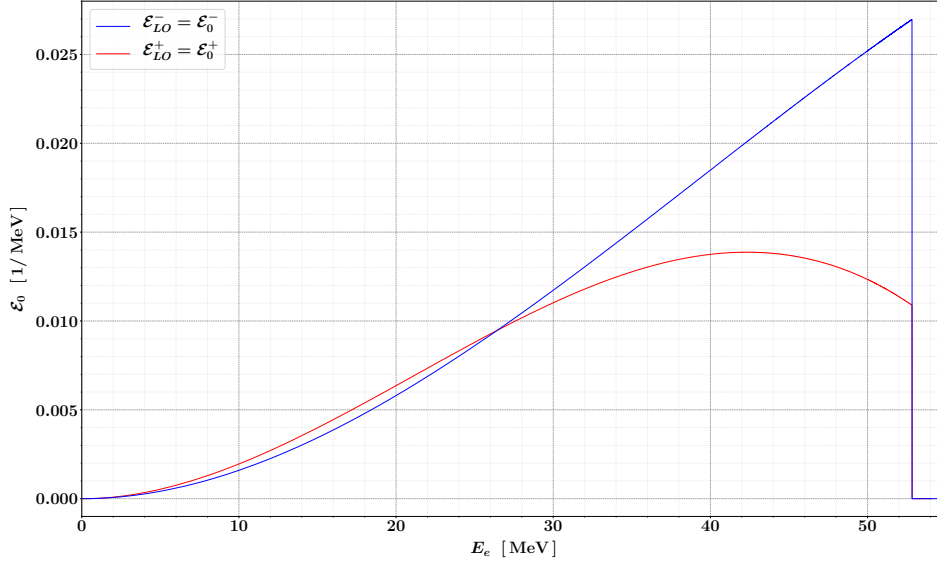


Figure 2.2 Forward energy spectrum \mathcal{E}_e^+ and backward energy spectrum \mathcal{E}_e^- with a MEG-like polarisation $n_\mu = -0.85$.

By using the relations

$$f_{\text{LO}} = f_0 = \frac{\mathcal{E}_0^+ + \mathcal{E}_0^-}{2} \quad g_{\text{LO}} = g_0 = \frac{\mathcal{E}_0^+ - \mathcal{E}_0^-}{2n_\mu} \quad (2.36)$$

we obtain the decay functions reported in Figure 2.3, which corresponds to the double-differential distribution

$$\mathcal{G}_{\text{LO}} = \mathcal{G}_0 = f_0 + n_\mu \cos \theta_e g_0 \quad (2.37)$$

The result for $n_\mu = -0.85$ is shown in Figure 2.4. The MCMULE results for f_0 and g_0 are perfectly compatible with (2.25). To quantify this affirmation, we report in Figure 2.5 the normalised residuals between the numerical and the analytical values of f_0 and g_0 . Since the bins are sufficiently small, the two analytical expressions (2.25) are evaluated at the center of each bins without introducing a relevant error. In both cases, the residuals do not feature any systematic pattern, appearing totally random, in accordance with the statistical nature of MCMULE.

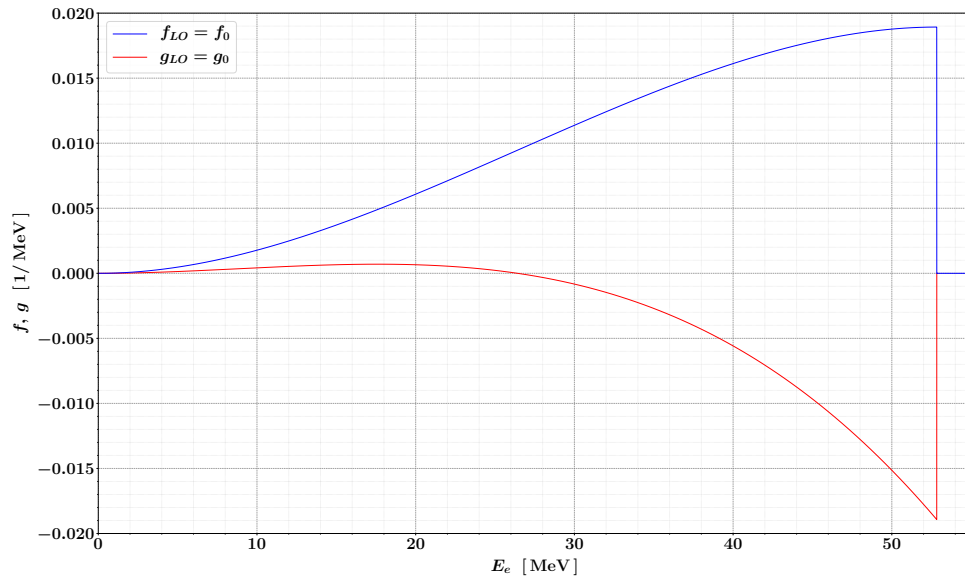


Figure 2.3 Isotropic function $f(E_e)$ and anisotropic function $g(E_e)$ at LO.

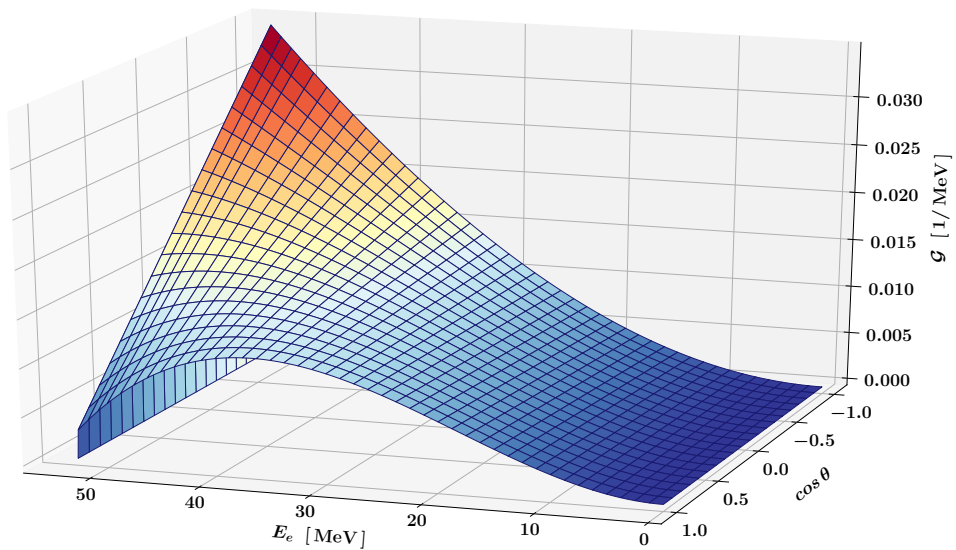


Figure 2.4 Double-differential decay width at LO for $n_\mu = -0.85$.

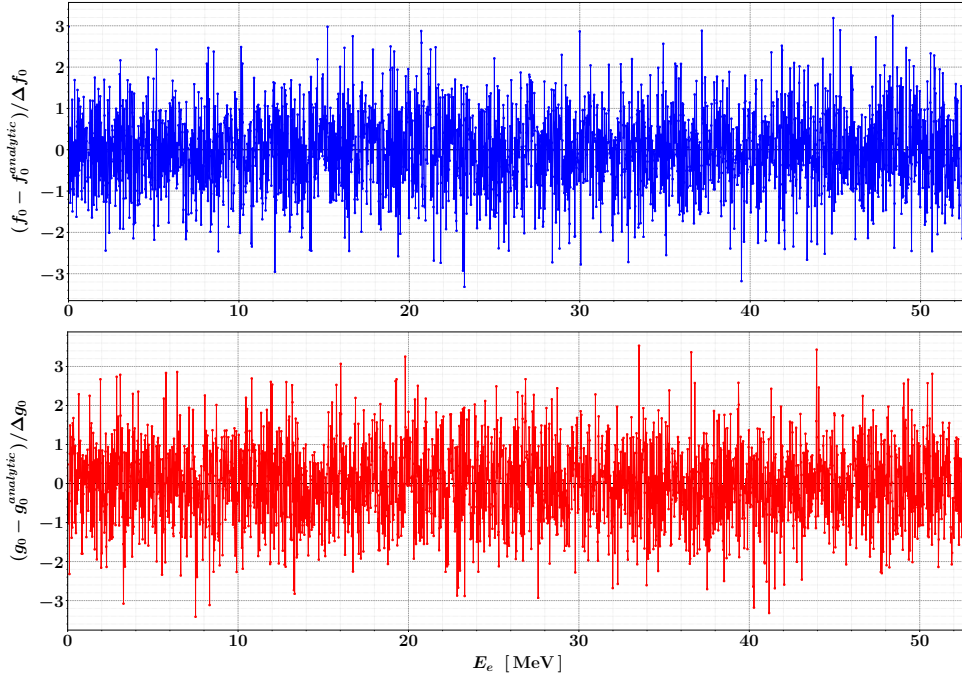


Figure 2.5 Normalised residuals between the numerical and the analytical values of f_0 (upper panel) and g_0 (lower panel).

As discussed in Section 1.6, for a sufficiently large number of random events, a VEGAS integration with expected value I is distributed according to a Gaussian with mean I and variance (1.81). Hence, the result for each bin is expected to be Gaussian distributed around the analytical value (2.25). Since the bins are independent from each other, the reduced χ^2 obtained by summing over all bins is expected to be one. For each of the two decay functions we find

$$\chi_f^2 \simeq 0.99 \qquad \chi_g^2 \simeq 0.98$$

in perfect agreement with the previous discussion.

2.4 NLO corrections

The NLO corrections to $\mu \rightarrow e\nu\bar{\nu}$ are given by

$$\begin{aligned} d\Gamma^{(1)} &= d\Gamma_v^{(1)} + d\Gamma_r^{(1)} \\ &= d\Phi_3 \mathcal{M}_3^{(1)} + d\Phi_{3+1} \mathcal{M}_{3+1}^{(0)} \\ &= d\Phi_3 2 \operatorname{Re} [\mathcal{A}_3^{(0)} \times \mathcal{A}_3^{(1)}] + d\Phi_{3+1} |\mathcal{A}_{3+1}^{(0)}|^2 \end{aligned} \quad (2.38)$$

which includes all contributions proportional to α . According to the notations introduced in Chapter 1, the two individual terms are characterised as follows.

- The virtual matrix element $\mathcal{M}_3^{(1)} = 2 \operatorname{Re} [\mathcal{A}_3^{(0)} \times \mathcal{A}_3^{(1)}]$ is given by the interference term between the tree-level amplitude \mathcal{A}_3^0 and the one-loop amplitude $\mathcal{A}_3^{(1)}$.
- The real matrix element $\mathcal{M}_{3+1}^{(0)} = |\mathcal{A}_{3+1}^{(0)}|^2$ is given by the square of the tree-level amplitude $\mathcal{A}_{3+1}^{(0)}$ with an extra photon in the final state.

The diagrams contributing to $\mathcal{A}_3^{(1)}$ and $\mathcal{A}_{3+1}^{(0)}$ are depicted in Figure 2.6.

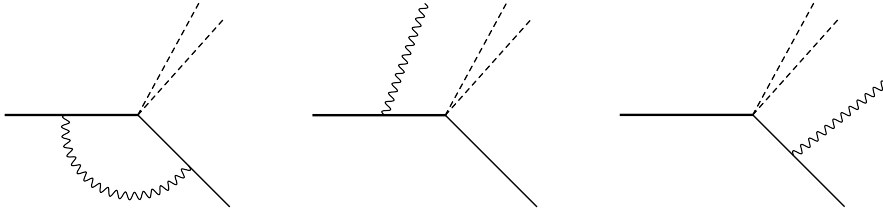


Figure 2.6 Higher-order diagrams contributing to $\mu^+ \rightarrow e^+ \nu_e \bar{\nu}_\mu$ at NLO. The first (from left) represents the one-loop amplitude $\mathcal{A}_3^{(1)}$, while the sum of the latter two represents the tree-level amplitude $\mathcal{A}_{3+1}^{(0)}$. Thick lines correspond to muons, thin lines to positrons, dashed lines to neutrinos, wavy lines to photons.

After OS-renormalisation and FKS-subtraction, $d\Gamma_v^{(1)}$ and $d\Gamma_r^{(1)}$ are separately finite in four dimensions⁶. Thus, both can be integrated numerically over the corresponding phase space. On the other hand, both are dependent on the choice of the cut parameter ξ_c , introduced by FKS to regularise all soft singularities. Hence, the virtual and real corrections are individually unphysical, unlike their sum $d\Gamma^{(1)} = d\Gamma_v^{(1)}(\xi_c) + d\Gamma_r^{(1)}(\xi_c)$, which has to be

⁶We do not explicitly report higher-order matrix elements, due to their prominent length. Nevertheless, the FORTRAN implementation of every matrix element is published at the address <https://gitlab.com/mule-tools/mcmule>, as well as all the code implemented for this thesis.

ξ_c -independent. Accordingly, we need to verify that

$$\frac{d\Gamma^{(1)}}{d\xi_c} = \frac{d}{d\xi_c} \left(\Gamma_v^{(1)}(\xi_c) + \Gamma_r^{(1)}(\xi_c) \right) = 0 \quad (2.39)$$

The numerical achievement of this condition constitutes an important validation of the code, especially the FKS implementation. To this end, we evaluate the full widths $\Gamma_v^{(1)}(\xi_c)$ and $\Gamma_r^{(1)}(\xi_c)$ for several choices of ξ_c . The result is reported in Figure 2.7.

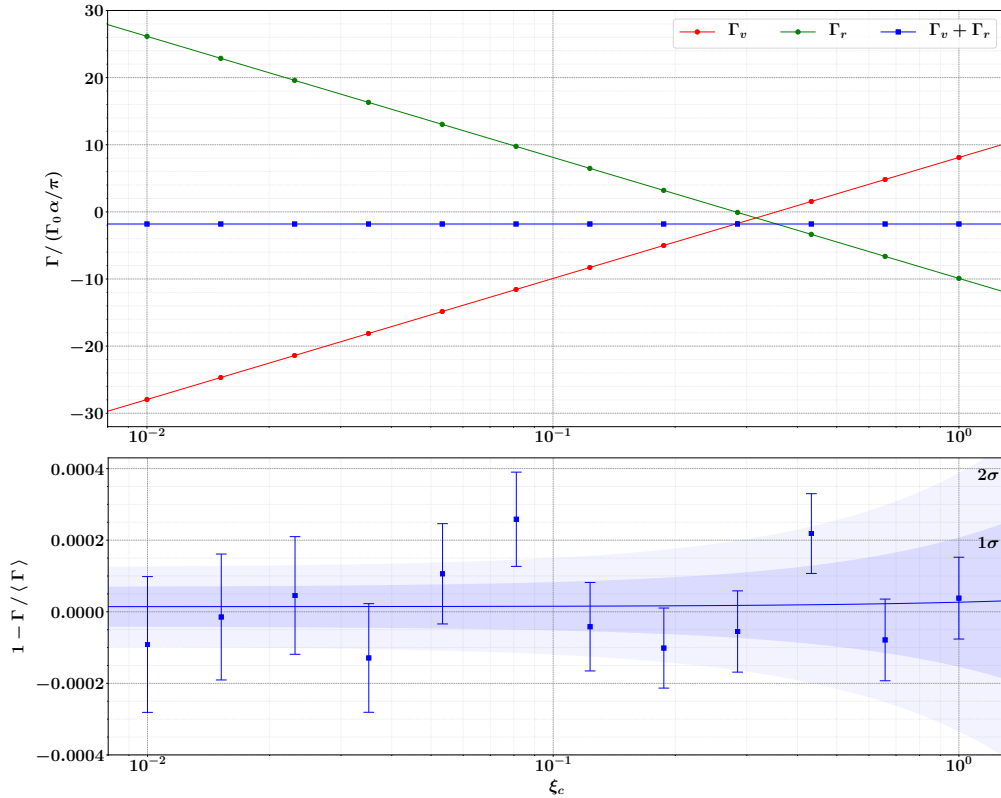


Figure 2.7 ξ_c -independence study for $\mu^+ \rightarrow e^+\nu_e\bar{\nu}_\mu$ at NLO. The upper panel shows the virtual and real corrections ($\Gamma_v^{(1)}$ and $\Gamma_r^{(1)}$) for several choices of ξ_c . The solid lines correspond to the fits discussed in the text. The lower panel shows the sum $\Gamma_v^{(1)}(\xi_c) + \Gamma_r^{(1)}(\xi_c)$, normalised to its average value.

Since the ξ_c -dependence is induced by terms like $\xi_c^{-2\epsilon}/\epsilon$, at NLO we have

$$\frac{1}{\Gamma_0} \Gamma_v^{(1)}(\xi_c) = \left(\frac{\alpha}{\pi}\right) (a_{0,0} + a_{0,1} \log \xi_c) \quad (2.40a)$$

$$\frac{1}{\Gamma_0} \Gamma_r^{(1)}(\xi_c) = \left(\frac{\alpha}{\pi}\right) (a_{1,0} + a_{1,1} \log \xi_c) \quad (2.40b)$$

Hence, the condition (2.39) requires

$$a_{0,1} + a_{1,1} = 0 \quad (2.41)$$

By fitting the data in Figure 2.7, we obtain

$$\begin{array}{lll} \Gamma_v^{(1)} : & a_{0,0} = +8.1032(1) & a_{0,1} = +7.83021(5) & \chi^2 \approx 1.36 \\ \Gamma_r^{(1)} : & a_{1,0} = -9.9105(2) & a_{1,1} = -7.83019(7) & \chi^2 \approx 1.13 \end{array}$$

Thus, we find

$$a_{0,1} + a_{1,1} = 2(9) \cdot 10^{-5}$$

which is consistent with zero, as required by the ξ_c -independence condition (2.41).

The NLO corrections to \mathcal{E}_e^+ and \mathcal{E}_e^- are given by

$$\Delta\mathcal{E}_{\text{NLO}}^+ \equiv \left(\frac{\alpha}{\pi}\right) \mathcal{E}_1^+ = \left(\frac{\alpha}{\pi}\right) \left(\mathcal{E}_v^+(\xi_c) + \mathcal{E}_r^+(\xi_c)\right) \quad (2.42a)$$

$$\Delta\mathcal{E}_{\text{NLO}}^- \equiv \left(\frac{\alpha}{\pi}\right) \mathcal{E}_1^- = \left(\frac{\alpha}{\pi}\right) \left(\mathcal{E}_v^-(\xi_c) + \mathcal{E}_r^-(\xi_c)\right) \quad (2.42b)$$

where

$$\mathcal{E}_v(\xi_c) = \frac{1}{\Gamma_0} \frac{d\Gamma_v}{dE_e}(\xi_c) \quad \mathcal{E}_r(\xi_c) = \frac{1}{\Gamma_0} \frac{d\Gamma_r}{dE_e}(\xi_c) \quad (2.43)$$

The MCMULE results for $\mathcal{E}_v^\pm(\xi_c)$ and $\mathcal{E}_r^\pm(\xi_c)$ are reported in Figure 2.8 and 2.9, respectively. The energy bins are the same used for the LO computation, as well as the initial-state polarisation $n_\mu = -0.85$. Also the number of random events is the same, with the only difference that the MC integration is repeated for different values of ξ_c . Unlike \mathcal{E}_0^\pm , all these spectra are unphysical, due to their explicit dependence on the choice of ξ_c . Only their sum is ξ_c -independent and consequently interpretable in terms of physical processes.

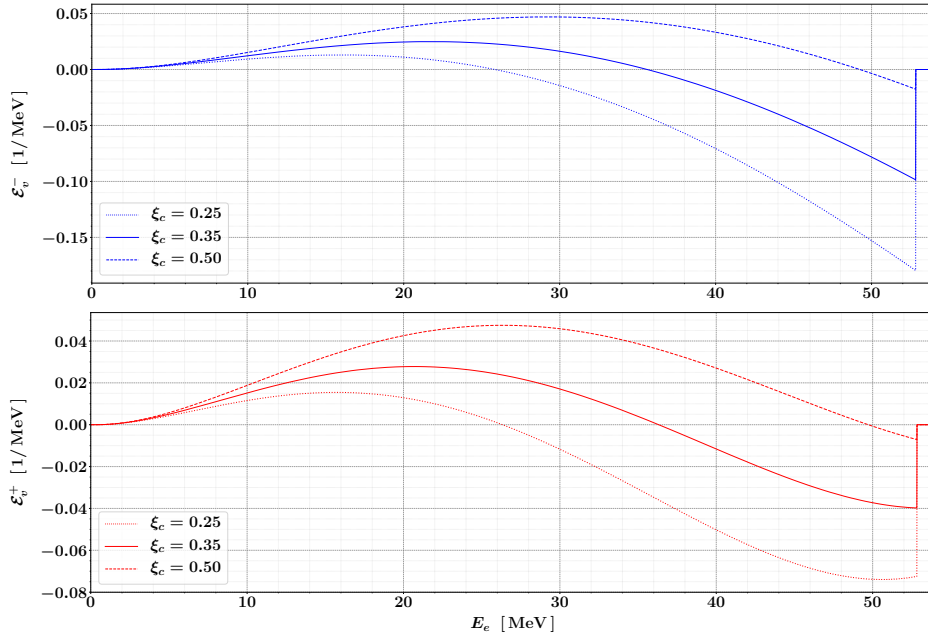


Figure 2.8 Virtual corrections to the forward spectrum \mathcal{E}_e^+ and the backward spectrum \mathcal{E}_e^- for three different choices of ξ_c . The muon polarisation is set to $n_\mu = -0.85$.

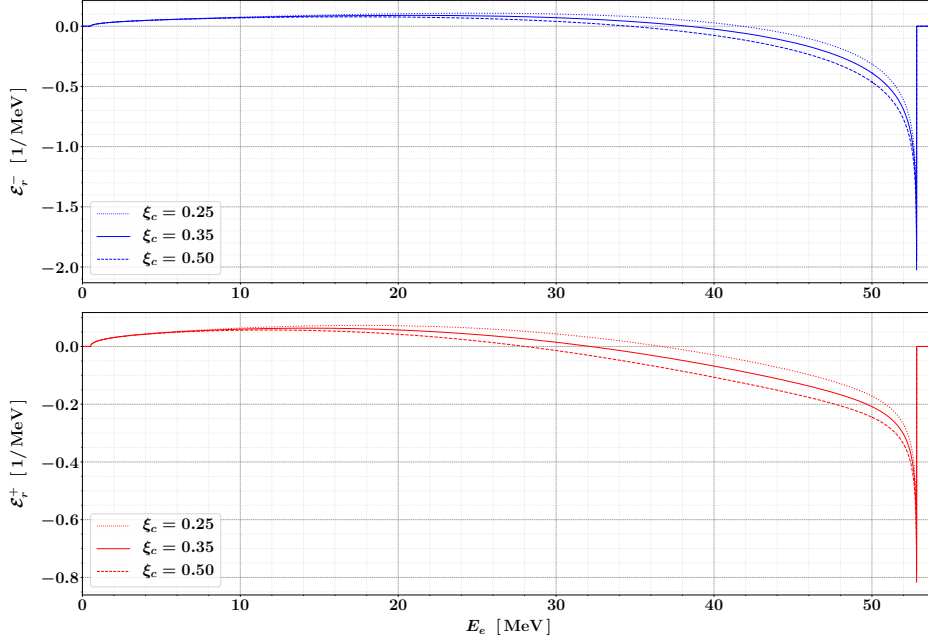


Figure 2.9 Real corrections to the forward spectrum \mathcal{E}_e^+ and the backward spectrum \mathcal{E}_e^- for three different choices of ξ_c . The muon polarisation is set to $n_\mu = -0.85$.

Accordingly, the NLO corrections to f and g are given by

$$\begin{aligned}\Delta f_{\text{NLO}} &\equiv \left(\frac{\alpha}{\pi}\right) f_1 = \left(\frac{\alpha}{\pi}\right) \left(f_v(\xi_c) + f_r(\xi_c)\right) \\ &= \left(\frac{\alpha}{\pi}\right) \frac{1}{2} \left(\mathcal{E}_v^+(\xi_c) + \mathcal{E}_r^+(\xi_c) + \mathcal{E}_v^-(\xi_c) + \mathcal{E}_r^-(\xi_c)\right) \\ &= \frac{1}{2} \left(\Delta\mathcal{E}_{\text{NLO}}^+ + \Delta\mathcal{E}_{\text{NLO}}^-\right)\end{aligned}\quad (2.44a)$$

$$\begin{aligned}\Delta g_{\text{NLO}} &\equiv \left(\frac{\alpha}{\pi}\right) g_1 = \left(\frac{\alpha}{\pi}\right) \left(g_v(\xi_c) + g_r(\xi_c)\right) \\ &= \left(\frac{\alpha}{\pi}\right) \frac{1}{2n_\mu} \left(\mathcal{E}_v^+(\xi_c) + \mathcal{E}_r^+(\xi_c) - \mathcal{E}_v^-(\xi_c) - \mathcal{E}_r^-(\xi_c)\right) \\ &= \frac{1}{2n_\mu} \left(\Delta\mathcal{E}_{\text{NLO}}^+ - \Delta\mathcal{E}_{\text{NLO}}^-\right)\end{aligned}\quad (2.44b)$$

The combination between real and virtual contributions eliminates the unphysical dependence on ξ_c , so that $\Delta f_{\text{NLO}} \propto f_1$ and $\Delta g_{\text{NLO}} \propto g_1$ are the physical NLO corrections to the two decay functions f and g . The resulting values for f_1 and g_1 are plotted in Figure 2.10.

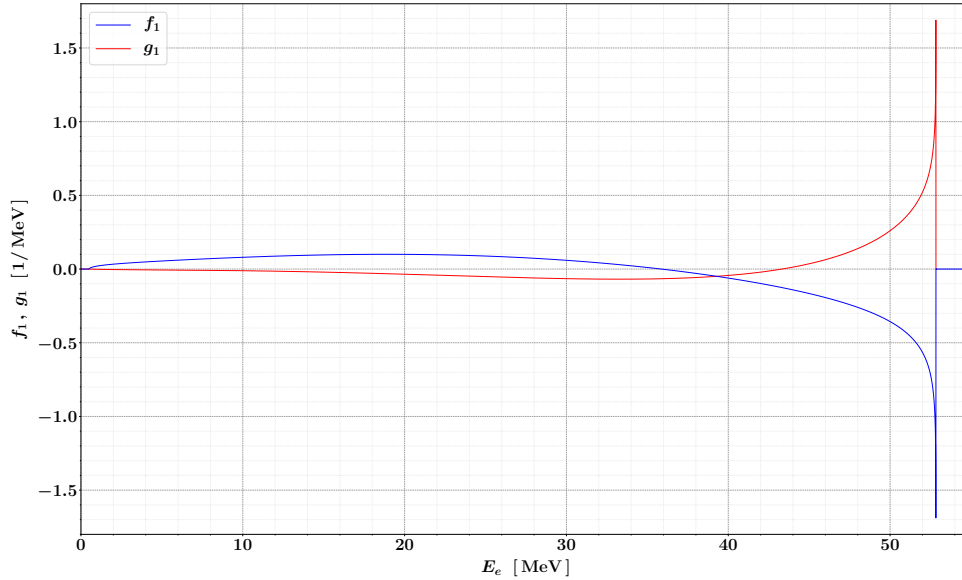


Figure 2.10 NLO corrections to the isotropic function f and the anisotropic function g .

Since the analytical expressions for f_1 and g_1 are known [115], we can repeat the comparison procedure followed at LO. Accordingly, in Figure 2.11 we report the normalised residuals between the numerical and the analytical values of f and g . Again, we evaluate the analytical expressions at the center of each energy bin, introducing a negligible error.

Similarly to LO, the residuals do not feature any systematic pattern, appearing totally random, in accordance with the statistical nature of MCMULE. For each of the two decay functions we find

$$\chi_f^2 \simeq 1.00 \qquad \chi_g^2 \simeq 1.01$$

which further confirms the MCMULE results. In conclusion, at NLO we have

$$f_{\text{NLO}} = f_0 + \left(\frac{\alpha}{\pi}\right) f_1 \qquad g_{\text{NLO}} = g_0 + \left(\frac{\alpha}{\pi}\right) g_1 \qquad (2.45)$$

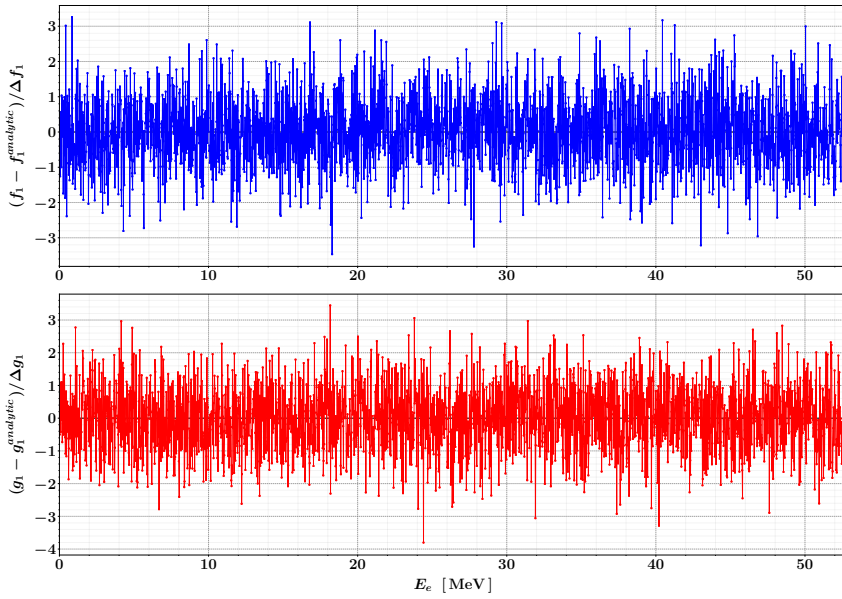


Figure 2.11 Normalised residuals between the numerical and the analytical values of f_1 (upper panel) and g_1 (lower panel).

In Figure 2.12 we compare f_{NLO} and g_{NLO} with f_{LO} and g_{LO} to highlight the impact of the $\mathcal{O}(\alpha)$ corrections. In addition, Figure 2.13 shows the corresponding relative variations. In both cases, the radiative corrections are very large close to the kinematic limits of the spectrum, due to the emission of one soft photon, which tends to advantage the emission of low-energy positrons and disadvantage the emission of high-energy positrons. Similarly, the NLO effect is relatively large close to the lower bound $E_e \simeq m_e$ of the spectrum. Furthermore, the relative corrections to g are divergent across the mid-energy point $E_e \simeq m_\mu/4$, because the emission of a real photon slightly shifts the zero crossing of g . The strength of the radiative corrections in the signal region $E_e \sim \mathcal{O}(m_\mu/2)$ is an unequivocal confirmation of their importance in searching for $\mu \rightarrow eX$, but at the same it is a clear indication that we need to refine f and g beyond NLO. Otherwise, we may not be

able to properly distinguish the signature of $\mu \rightarrow eX$ from an unknown higher-order effect of QED. From a formal point of view, the theoretical uncertainty due to the perturbative approximation can hide or even mimic the signal, introducing a further limiting factor in addition to the experimental ones.

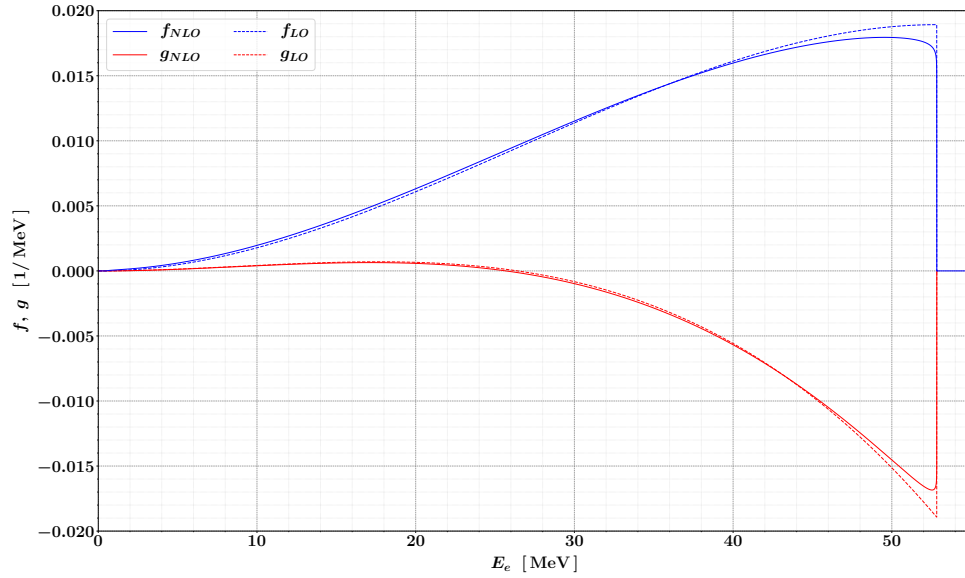


Figure 2.12 Isotropic function f and anisotropic function g at LO and NLO.

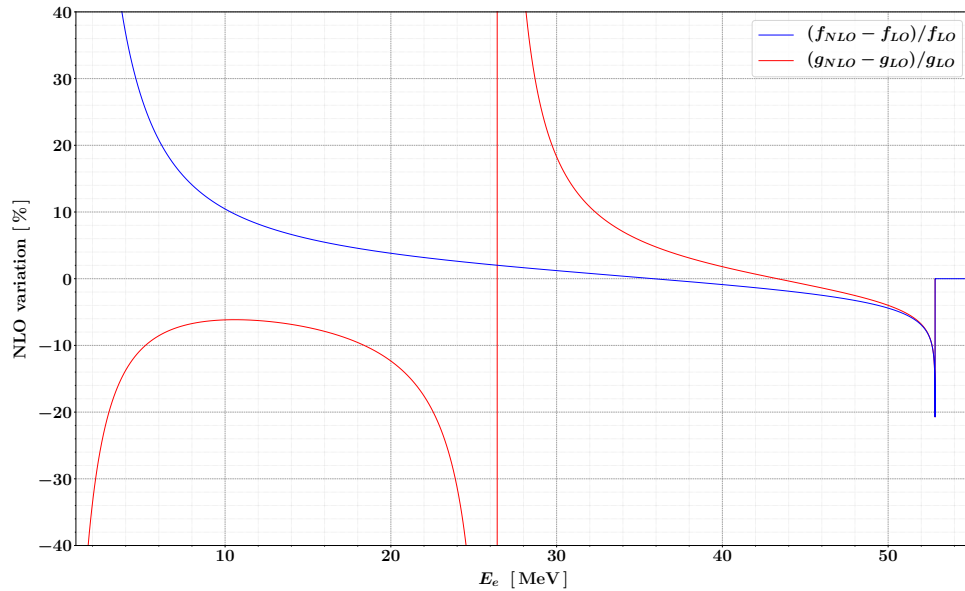


Figure 2.13 Relative variation of f and g due to NLO corrections.

2.5 NNLO corrections

To reduce theoretical uncertainty on the two decay functions f and g , we continue with the QED perturbative expansion. The NNLO corrections to $\mu \rightarrow e\nu\bar{\nu}$ are given by

$$\begin{aligned}
 d\Gamma^{(2)} &= d\Gamma_{vv}^{(2)} + d\Gamma_{rv}^{(2)} + d\Gamma_{rr}^{(2)} + d\Gamma_{pp}^{(2)} \\
 &= d\Phi_3 \mathcal{M}_3^{(2)} + d\Phi_{3+1} \mathcal{M}_{3+1}^{(1)} + d\Phi_{3+2} \mathcal{M}_{3+2}^{(0)} + d\Phi_5 \mathcal{M}_5^{(0)} \\
 &= d\Phi_3 \left[2 \operatorname{Re} [\mathcal{A}_3^{(0)} \times \mathcal{A}_3^{(2)}] + |\mathcal{A}_3^{(1)}|^2 \right] + d\Phi_{3+1} 2 \operatorname{Re} [\mathcal{A}_{3+1}^{(0)} \times \mathcal{A}_{3+1}^{(1)}] \\
 &\quad + d\Phi_{3+2} |\mathcal{A}_{3+2}^{(0)}|^2 + d\Phi_5 |\mathcal{A}_5^{(0)}|^2
 \end{aligned} \tag{2.46}$$

which includes all contributions proportional to α^2 . According to the notations introduced in Chapter 1, the four individual terms are characterised as follows.

- The double-virtual matrix element $\mathcal{M}_3^{(1)} = 2 \operatorname{Re} [\mathcal{A}_3^{(0)} \times \mathcal{A}_3^{(2)}] + |\mathcal{A}_3^{(1)}|^2$ is given by the interference term between the tree-level amplitude \mathcal{A}_3^0 and the two-loop amplitude $\mathcal{A}_3^{(1)}$ (cf. Figure 2.14), plus the squared one-loop amplitude $\mathcal{A}_3^{(1)}$ (cf. Figure 2.6).

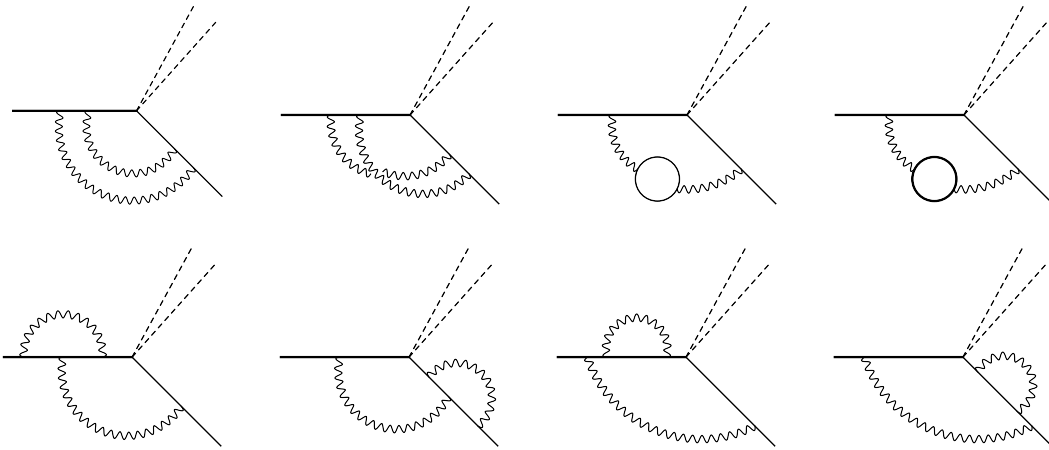


Figure 2.14 Two-loop diagrams contributing to the amplitude $\mathcal{A}_3^{(2)}$.

- The real-virtual matrix element $\mathcal{M}_{3+1}^{(1)} = 2 \operatorname{Re} [\mathcal{A}_{3+1}^{(0)} \times \mathcal{A}_{3+1}^{(1)}]$ is given by the interference term between the tree-level amplitude \mathcal{A}_3^0 (cf. Figure 2.6) and the one-loop amplitude $\mathcal{A}_{3+1}^{(1)}$ (cf. Figure 2.15), both with an extra photon in the final state.

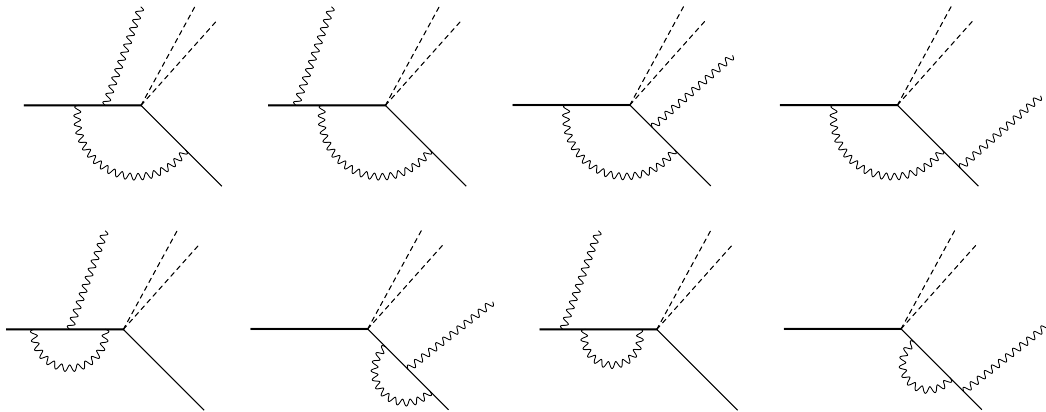


Figure 2.15 One-loop diagrams contributing to the amplitude $\mathcal{A}_{3+1}^{(1)}$.

- The double-real matrix element $\mathcal{M}_{3+1}^{(1)} = |\mathcal{A}_{3+2}^{(0)}|^2$ is given by the squared tree-level amplitude $\mathcal{A}_{3+2}^{(0)}$ (cf. Figure 2.16) with two extra photons in the final state.

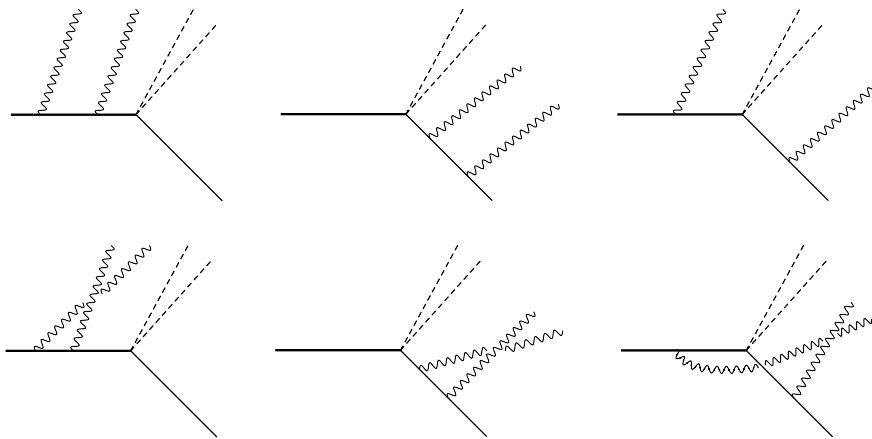


Figure 2.16 Tree-level diagrams contributing to the amplitude $\mathcal{A}_{3+2}^{(0)}$.

- The pair-production matrix element $\mathcal{M}_5^{(0)} = |\mathcal{A}_5^{(0)}|^2$ is given by the squared tree-level amplitude $\mathcal{A}_5^{(0)}$ (cf. Figure 2.17) with an electron-positron pair in the final state. This contribution is often called open-lepton production.

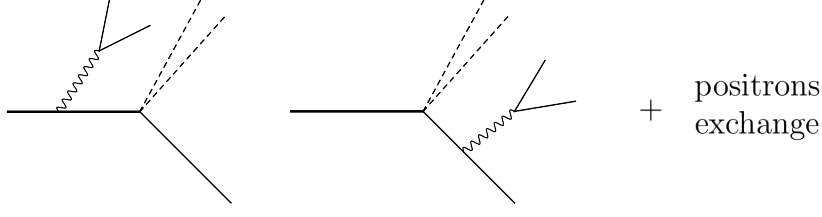


Figure 2.17 Tree-level diagrams contributing to the amplitude $\mathcal{A}_5^{(0)}$.

After OS-renormalisation and FKS²-subtraction, $d\Gamma_{vv}^{(2)}$, $d\Gamma_{rv}^{(2)}$ and $d\Gamma_{rr}^{(2)}$ are separately finite in four dimensions. On the other hand, $d\Gamma_{pp}^{(2)}$ is manifestly finite for $m_e \neq 0$. Thus, it does not require any regularisation treatment and it is not individually dependent on the choice of ξ_c , unlike the first three terms. Accordingly, we need to verify that

$$\frac{d\Gamma^{(2)}}{d\xi_c} = \frac{d}{d\xi_c} \left(\Gamma_{vv}^{(2)}(\xi_c) + \Gamma_{rv}^{(2)}(\xi_c) + \Gamma_{rr}^{(2)}(\xi_c) \right) = 0 \quad (2.47)$$

Repeating the procedure already followed at NLO, we evaluate the full widths $\Gamma_{vv}^{(2)}$, $\Gamma_{rv}^{(2)}$ and $\Gamma_{rr}^{(2)}$ for several choices of ξ_c . The result is reported in Figure 2.18. Since the ξ_c -dependence is induced by terms like $\xi_c^{-2\epsilon}/\epsilon$, at NNLO we have

$$\frac{1}{\Gamma_0} \Gamma_{vv}^{(1)}(\xi_c) = \left(\frac{\alpha}{\pi} \right)^2 (a_{0,0} + a_{0,1} \log \xi_c + a_{0,2} \log^2 \xi_c) \quad (2.48a)$$

$$\frac{1}{\Gamma_0} \Gamma_{rv}^{(1)}(\xi_c) = \left(\frac{\alpha}{\pi} \right)^2 (a_{1,0} + a_{1,1} \log \xi_c + a_{1,2} \log^2 \xi_c) \quad (2.48b)$$

$$\frac{1}{\Gamma_0} \Gamma_{rr}^{(1)}(\xi_c) = \left(\frac{\alpha}{\pi} \right)^2 (a_{2,0} + a_{2,1} \log \xi_c + a_{2,2} \log^2 \xi_c) \quad (2.48c)$$

Hence, the condition (2.47) requires

$$\begin{cases} a_{0,1} + a_{1,1} + a_{2,1} = 0 \\ a_{0,2} + a_{1,2} + a_{2,2} = 0 \end{cases} \quad (2.49)$$

By fitting the data in Figure 2.18, we obtain

$$\begin{array}{llll} \Gamma_{vv}^{(2)} : & a_{0,0} = +29.062(4) & a_{0,1} = +61.993(6) & a_{0,2} = +30.9524(8) & \chi^2 \approx 1.28 \\ \Gamma_{rv}^{(2)} : & a_{1,0} = -85.181(1) & a_{1,1} = -150.721(2) & a_{1,2} = -61.9016(6) & \chi^2 \approx 0.85 \\ \Gamma_{rr}^{(2)} : & a_{2,0} = +49.716(8) & a_{2,1} = +88.733(7) & a_{2,2} = +30.950(1) & \chi^2 \approx 1.66 \end{array}$$

Thus, we find

$$\begin{cases} a_{0,1} + a_{1,1} + a_{2,1} = 0.005(9) \\ a_{0,2} + a_{1,2} + a_{2,2} = 0.0008(14) \end{cases}$$

which are both consistent with zero, as required by the ξ_c -independence condition (2.49).

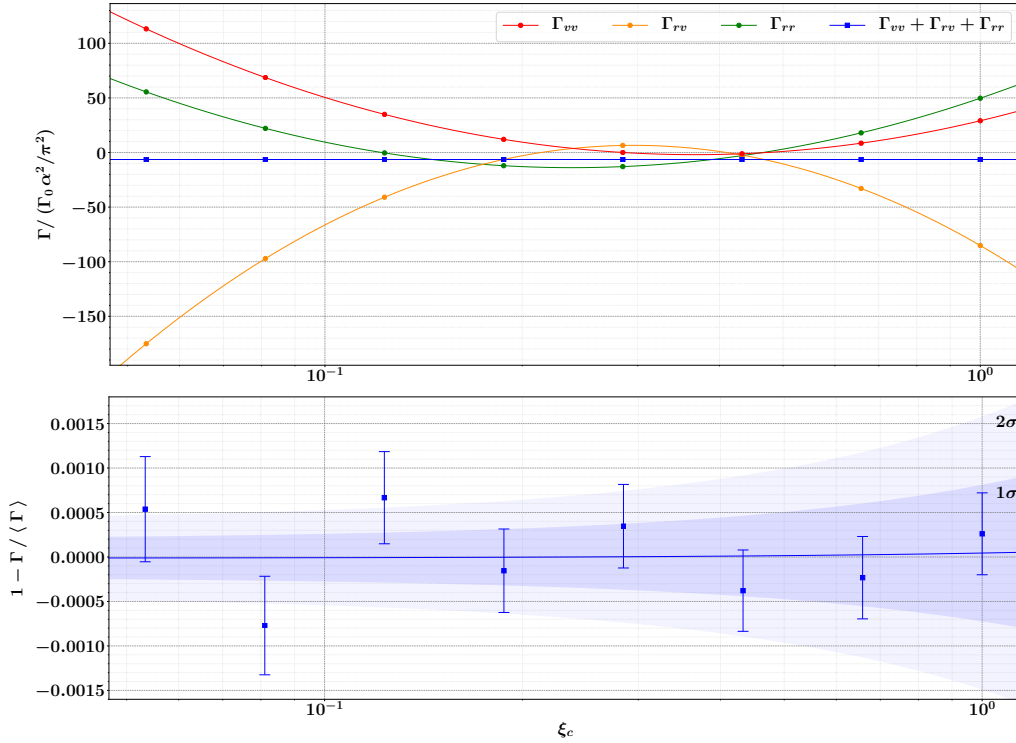


Figure 2.18 ξ_c -independence study for $\mu^+ \rightarrow e^+\nu_e\bar{\nu}_\mu$ at NNLO. The upper panel shows the double-virtual, real-virtual and double-real corrections ($\Gamma_{vv}^{(2)}$, $\Gamma_{rv}^{(2)}$ and $\Gamma_{rr}^{(2)}$) for several choices of ξ_c . The solid lines correspond to the fits discussed in the text. The lower panel shows the sum $\Gamma_{vv}^{(2)} + \Gamma_{rv}^{(2)} + \Gamma_{rr}^{(2)}$, normalised to its average value.

The NNLO corrections to \mathcal{E}_e^+ and \mathcal{E}_e^- are given by

$$\Delta\mathcal{E}_{\text{NNLO}}^+ \equiv \left(\frac{\alpha}{\pi}\right)^2 \mathcal{E}_2^+ = \left(\frac{\alpha}{\pi}\right)^2 \left(\mathcal{E}_{vv}^+(\xi_c) + \mathcal{E}_{rv}^+(\xi_c) + \mathcal{E}_{rr}^+(\xi_c) + \mathcal{E}_{pp}^+ \right) \quad (2.50a)$$

$$\Delta\mathcal{E}_{\text{NNLO}}^- \equiv \left(\frac{\alpha}{\pi}\right)^2 \mathcal{E}_2^- = \left(\frac{\alpha}{\pi}\right)^2 \left(\mathcal{E}_{vv}^-(\xi_c) + \mathcal{E}_{rv}^-(\xi_c) + \mathcal{E}_{rr}^-(\xi_c) + \mathcal{E}_{pp}^- \right) \quad (2.50b)$$

where

$$\mathcal{E}_{vv}(\xi_c) = \frac{1}{\Gamma_0} \frac{d\Gamma_{vv}}{dE_e}(\xi_c) \quad \mathcal{E}_{rv}(\xi_c) = \frac{1}{\Gamma_0} \frac{d\Gamma_{rv}}{dE_e}(\xi_c) \quad (2.51a)$$

$$\mathcal{E}_{rr}(\xi_c) = \frac{1}{\Gamma_0} \frac{d\Gamma_{rr}}{dE_e}(\xi_c) \quad \mathcal{E}_{pp} = \frac{1}{\Gamma_0} \frac{d\Gamma_{pp}}{dE_e} \quad (2.51b)$$

Since we are mainly interested in the high-energy region of the spectrum, the distribution \mathcal{E}_{pp} is always referred to the more energetic of the two emitted positrons. In this way we can continue to treat the process considering a single positron. The MCMULE results for $\mathcal{E}_{vv}^\pm(\xi_c)$, $\mathcal{E}_{rv}^\pm(\xi_c)$, $\mathcal{E}_{rr}^\pm(\xi_c)$ and \mathcal{E}_{pp}^\pm are reported in Figures 2.19, 2.20, 2.21 and 2.22, respectively. The energy bins and the number of random events are the same used for the previous computations, as well as the polarisation $n_\mu = -0.85$. Again, all these spectra are unphysical due to their individual ξ_c -dependency, except for the pair-production contribution, which corresponds to the rare decay $\mu^+ \rightarrow e^+e^-e^+\nu_e\bar{\nu}_\mu$ at LO. We note that \mathcal{E}_{pp}^\pm rapidly decreases when approaching the spectrum endpoint, since it is unlikely that a single particle takes all the available energy in a 5-body decay. Furthermore, the endpoint of \mathcal{E}_{pp}^\pm decreases by $2m_e$, due to the additional mass in the final state.

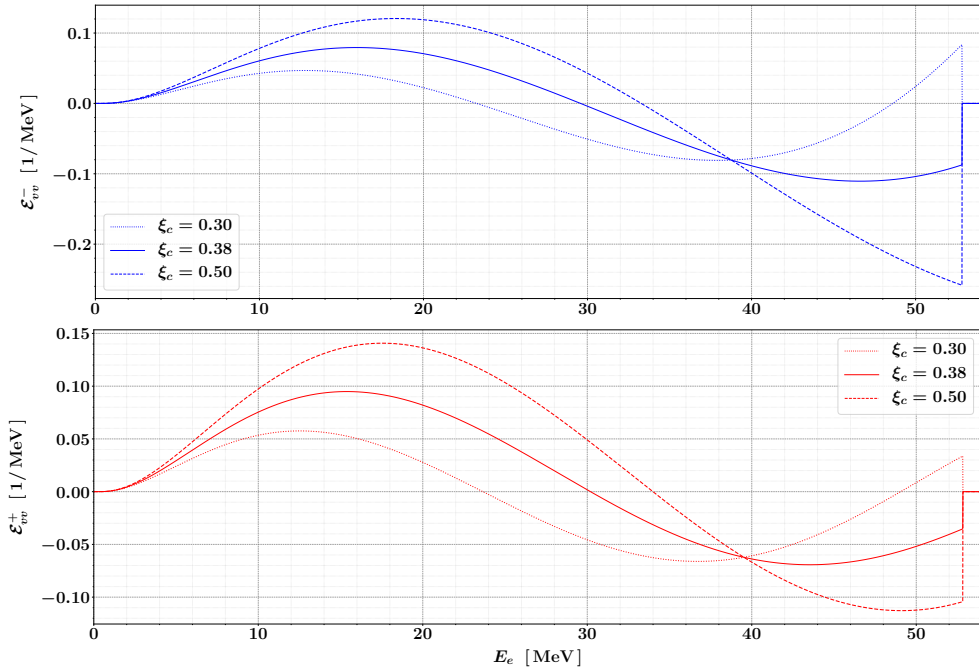


Figure 2.19 Double-virtual corrections to the forward spectrum \mathcal{E}_e^+ and the backward spectrum \mathcal{E}_e^- for three different choices of ξ_c . As usual, the muon polarisation is set to $n_\mu = -0.85$.

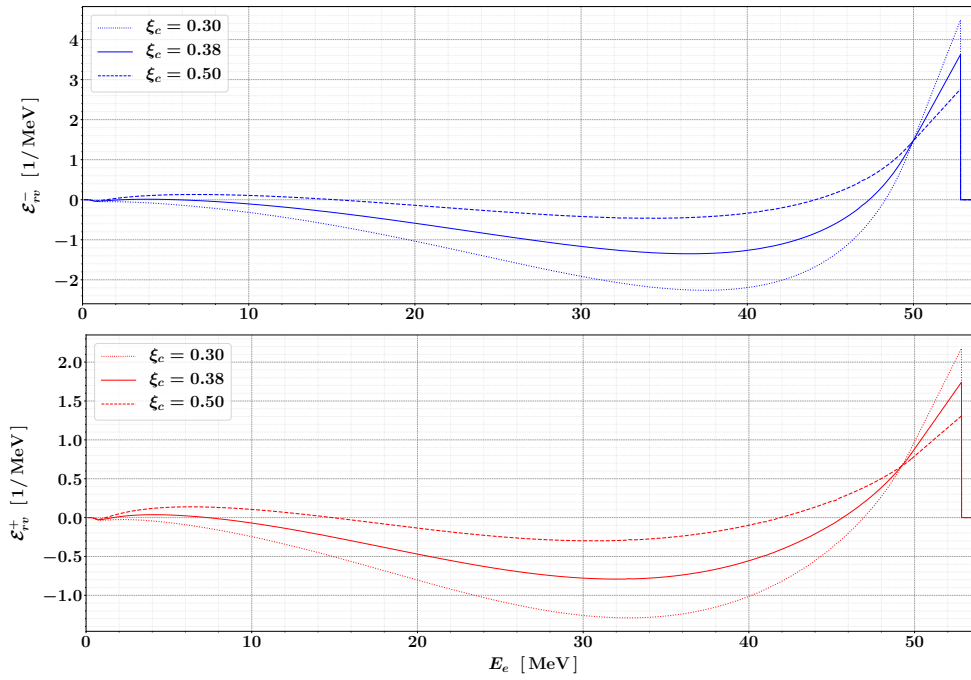


Figure 2.20 Real-virtual corrections to the forward spectrum \mathcal{E}_e^+ and the backward spectrum \mathcal{E}_e^- for three different choices of ξ_c and $n_\mu = -0.85$.

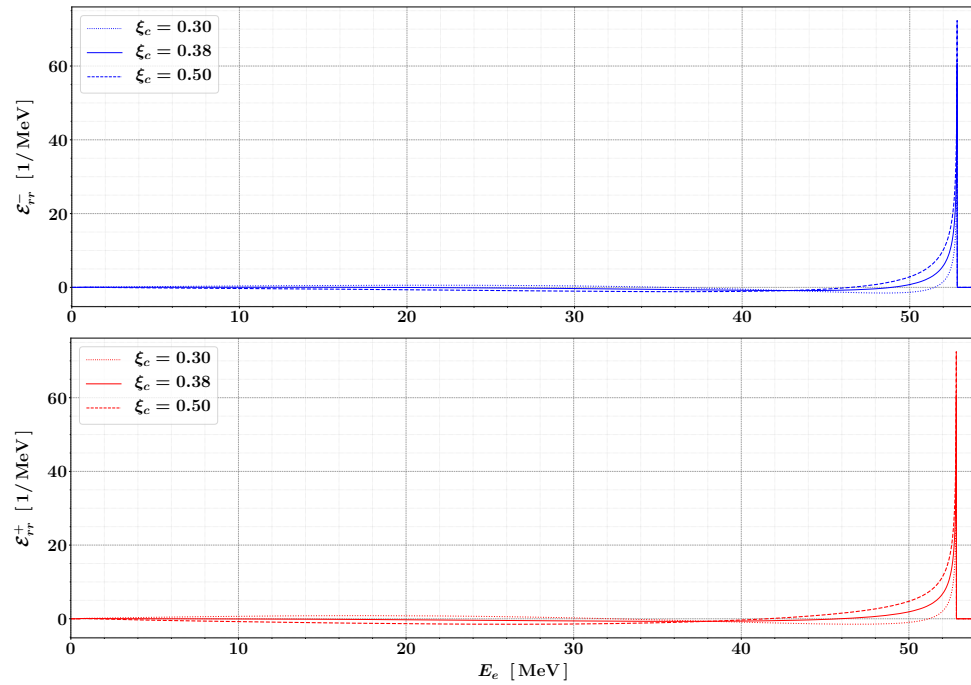


Figure 2.21 Double-real corrections to the forward spectrum \mathcal{E}_e^+ and the backward spectrum \mathcal{E}_e^- for three different choices of ξ_c and $n_\mu = -0.85$.

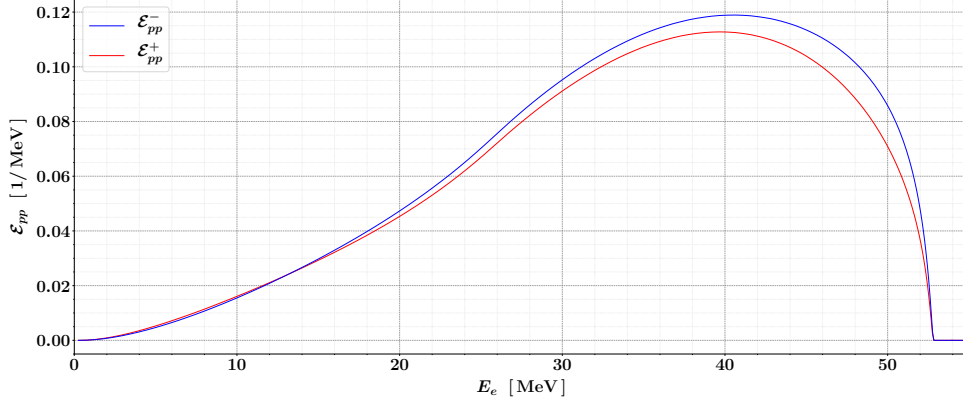


Figure 2.22 Pair-production corrections to the forward spectrum \mathcal{E}_e^+ and the backward spectrum \mathcal{E}_e^- , both independent from the choice of ξ_c . Polarisation set to $n_\mu = -0.85$.

The NNLO corrections to f and g are given by

$$\begin{aligned}
\Delta f_{\text{NNLO}} &\equiv \left(\frac{\alpha}{\pi}\right)^2 f_2 = \left(\frac{\alpha}{\pi}\right)^2 \left(f_{vv}(\xi_c) + f_{rv}(\xi_c) + f_{rr}(\xi_c) + f_{pp} \right) \\
&= \left(\frac{\alpha}{\pi}\right)^2 \frac{1}{2} \left(\mathcal{E}_{vv}^+(\xi_c) + \mathcal{E}_{rv}^+(\xi_c) + \mathcal{E}_{rr}^+(\xi_c) + \mathcal{E}_{pp}^+ \right. \\
&\quad \left. + \mathcal{E}_{vv}^-(\xi_c) + \mathcal{E}_{rv}^-(\xi_c) + \mathcal{E}_{rr}^-(\xi_c) + \mathcal{E}_{pp}^- \right) \\
&= \frac{1}{2} \left(\Delta \mathcal{E}_{\text{NNLO}}^+ + \Delta \mathcal{E}_{\text{NNLO}}^- \right)
\end{aligned} \tag{2.52a}$$

$$\begin{aligned}
\Delta g_{\text{NNLO}} &\equiv \left(\frac{\alpha}{\pi}\right)^2 f_2 = \left(\frac{\alpha}{\pi}\right)^2 \left(g_{vv}(\xi_c) + g_{rv}(\xi_c) + g_{rr}(\xi_c) + g_{pp} \right) \\
&= \left(\frac{\alpha}{\pi}\right)^2 \frac{1}{2n_\mu} \left(\mathcal{E}_{vv}^+(\xi_c) + \mathcal{E}_{rv}^+(\xi_c) + \mathcal{E}_{rr}^+(\xi_c) + \mathcal{E}_{pp}^+ \right. \\
&\quad \left. - \mathcal{E}_{vv}^-(\xi_c) - \mathcal{E}_{rv}^-(\xi_c) - \mathcal{E}_{rr}^-(\xi_c) - \mathcal{E}_{pp}^- \right) \\
&= \frac{1}{2n_\mu} \left(\Delta \mathcal{E}_{\text{NNLO}}^+ - \Delta \mathcal{E}_{\text{NNLO}}^- \right)
\end{aligned} \tag{2.52b}$$

The combination of the three different photonic contributions (double-virtual, real-virtual and double-real) eliminates the unphysical dependence on ξ_c , so that $\Delta f_{\text{NNLO}} \propto f_2$ and $\Delta g_{\text{NNLO}} \propto g_2$ are the physical NNLO corrections to the two decay functions f and g . The

resulting values for f_2 and g_2 are plotted in Figure 2.23. In conclusion, at NNLO we have

$$f_{\text{NNLO}} = f_0 + \left(\frac{\alpha}{\pi}\right) f_1 + \left(\frac{\alpha}{\pi}\right)^2 f_2 \quad g_{\text{NNLO}} = g_0 + \left(\frac{\alpha}{\pi}\right) g_1 + \left(\frac{\alpha}{\pi}\right)^2 g_2 \quad (2.53)$$

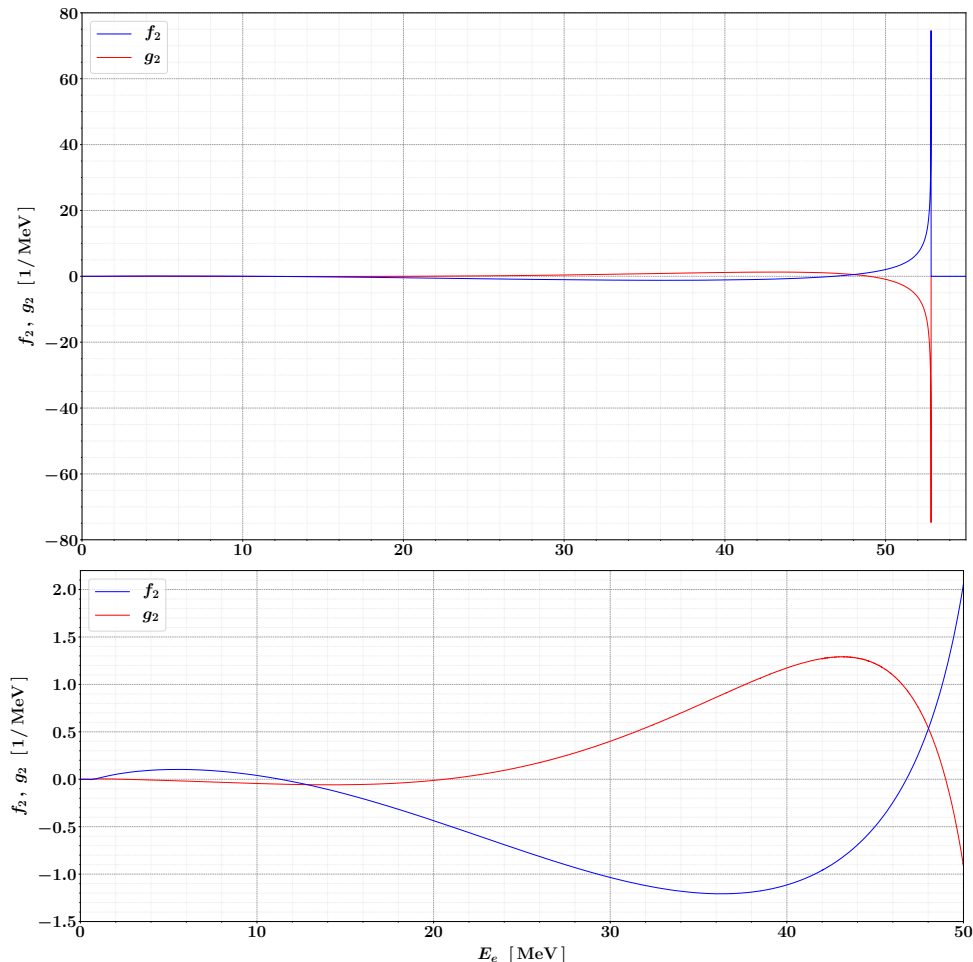


Figure 2.23 NNLO corrections to the isotropic function f and the anisotropic function g . The lower panel shows the region $E_e < 50$ MeV.

In Figure 2.24 we compare f_{NNLO} and g_{NNLO} with the previous orders to highlight the impact of the $\mathcal{O}(\alpha^2)$ corrections. In addition, Figure 2.25 shows the corresponding relative variations. As already noted at NLO, the radiative corrections are more relevant close to the kinematic limit of the spectrum, due to the emission of one or two soft photons. Further, the relative corrections to g are again divergent at $E_e \simeq m_\mu/4$ due to the shift of the zero crossing. Since the NLO and NNLO corrections have the opposite sign, we can interpret the NNLO as a balancing of the NLO, evidently an overestimate of the QED corrections. On the other hand, the NNLO corrections are smaller than the NLO ones by

one order of magnitude only, rather than the 2-3 orders that we might have expected from an additional power of $(\alpha/\pi) \approx 0.2\%$. The NLO corrections themselves are much bigger than $\mathcal{O}(\alpha/\pi)$, at least near the energy spectrum borders.

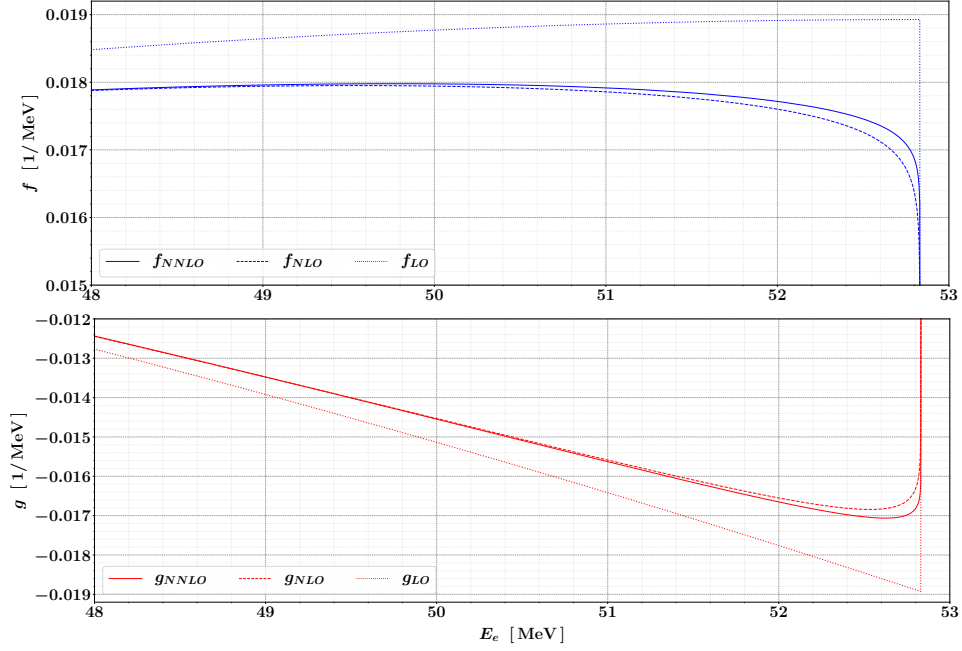


Figure 2.24 Isotropic function f and anisotropic function g at LO, NLO and NNLO.

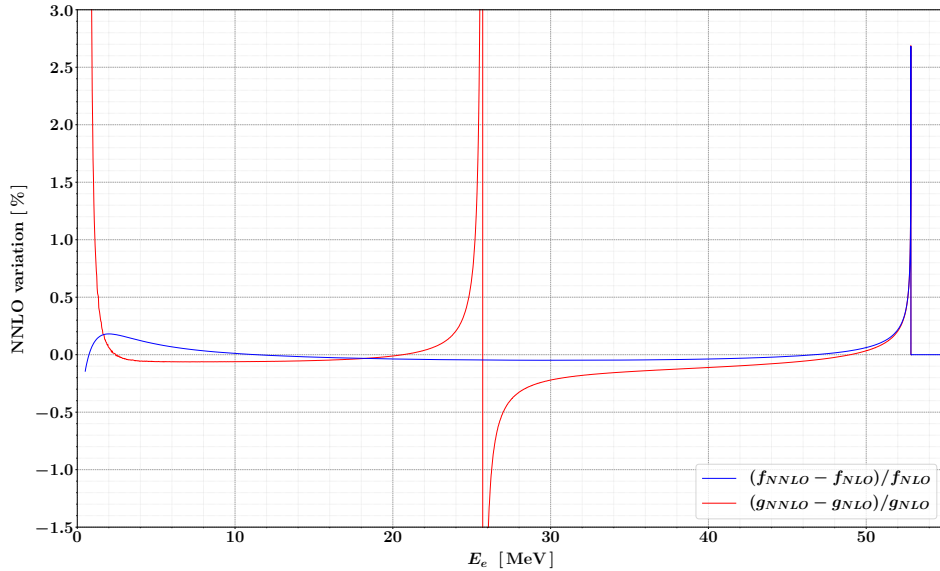


Figure 2.25 Relative variation of f and g due to the NNLO corrections.

2.6 LL corrections

The radiative corrections to both decay functions are enhanced by large logarithms. Specifically, we encounter a *soft logarithm* given by

$$L_x \equiv \log(1 - x_e) \quad x_e \equiv 2E_e/m_\mu \quad (2.54)$$

and a *collinear logarithm* given by

$$L_z \equiv \log(z) \quad z \equiv m_e^2/m_\mu^2 \quad (2.55)$$

The first is divergent in the *soft limit* $x_e \rightarrow 1$, while the second is divergent in the *collinear limit* $m_e \rightarrow 0$. At N^ℓ LO the logarithmic contribution has the form

$$\alpha^\ell \sum_{n_x, n_z} (L_x)^{n_x} (L_z)^{n_z} \quad \text{with} \quad 0 \leq n_x, n_z \leq \ell \quad (2.56)$$

We denote the terms

$$\text{LL: } (\alpha L_x L_z)^\ell \quad (2.57)$$

as the *leading-logarithm* (LL) contribution. Similarly, we denote the terms

$$\text{NLL: } \alpha^\ell L_x^{n_x} L_z^{n_z} \quad \text{with} \quad n_x + n_z = \ell - 1 \quad (2.58)$$

as the *next-to-leading logarithm* (NLL) contribution and so on. Due to their typical magnitude, it is advisable to include these terms beyond NNLO, according to the QED logarithmic expansion (1.9). To this end, we need to introduce a further distinction between them. We refer to the terms

$$\text{sLL: } \alpha^\ell L_x^\ell L_z^{n_z} \quad \text{with} \quad n_z \leq \ell \quad (2.59)$$

as the *soft leading logarithm* (sLL) at N^ℓ LO. Similarly, we denote the terms

$$\text{cLL: } \alpha^\ell L_x^{n_x} L_z^\ell \quad \text{with} \quad n_x \leq \ell \quad (2.60)$$

as the *collinear leading logarithm* (cLL) at N^ℓ LO. We note that the two contributions have in common the term $(\alpha L_x L_z)^\ell$, which must not be counted twice. The cLL terms at N^3 LO, i.e. all terms proportional to $(\alpha L_z)^3$ are already known analytically [123]. Since we are mainly interested in the spectrum endpoint, the sLL terms are the most relevant. In the high-energy region of the spectrum ($x_e \sim 1$), we can analytically resum them to all orders through the so-called *ad-hoc exponentiation*. Since the soft logarithm L_x is singular in the soft limit $x_e \rightarrow 1$, the sLL contribution *exponentiates* according to the YFS

split (1.42). First, we need to consider the soft limit of f_1 and g_1 . From their analytical expression [115], we obtain

$$f_1(x_e \rightarrow 1) \simeq \frac{1 - z + (1 + z)L_z}{\pi(z - 1)} L_x \equiv c_f L_x \quad (2.61a)$$

$$g_1(x_e \rightarrow 1) \simeq -\frac{1 - z + (1 + z)L_z}{\pi(z - 1)} L_x \equiv c_g L_x = -c_f L_x \quad (2.61b)$$

Then, we define the soft-resummed decay functions as

$$f_{resum} \equiv f_0 \exp(\alpha c_f L_x) \quad (2.62a)$$

$$g_{resum} \equiv g_0 \exp(\alpha c_g L_x) \quad (2.62b)$$

The sLL contribution at NLO is reproduced by construction. To validate the ansatz (2.62), we need to verify that the sLL terms at NNLO are correctly reproduced by

$$f_2^{sLL} = \frac{1}{2} f_0 (\alpha c_f L_x)^2 \approx 0.71045 f_0 \left(\frac{\alpha}{\pi}\right)^2 L_x^2 \quad (2.63a)$$

$$g_2^{sLL} = \frac{1}{2} g_0 (\alpha c_f L_x)^2 \approx 0.71045 g_0 \left(\frac{\alpha}{\pi}\right)^2 L_x^2 \quad (2.63b)$$

Specifically, we can compare f_2^{sLL} and g_2^{sLL} to the NNLO corrections computed with MCMULE. In the high-energy limit $x_e \sim 1$, the NNLO corrections can be written as

$$f_2/f_0 = F_0^{(2)} + F_{\text{NLL}}^{(2)} \log(1 - x_e) + F_{\text{LL}}^{(2)} \log(1 - x_e)^2 \quad (2.64a)$$

$$g_2/g_0 = G_0^{(2)} + G_{\text{NLL}}^{(2)} \log(1 - x_e) + G_{\text{LL}}^{(2)} \log(1 - x_e)^2 \quad (2.64b)$$

where the $F^{(2)}$ s and the $G^{(2)}$ s are constants to be determined. We can extract their values by fitting the MCMULE results (cf. Figure 2.23) with (2.64) for sufficiently large values of E_e . Thus, we constrain the fit in the region $E_e \geq E_e^{\text{min}}$. The results obtained for $F_{\text{LL}}^{(2)}$ and $G_{\text{LL}}^{(2)}$ for several choices of E_e^{min} are shown in Figure 2.26. We note that both are independent on the energy cut for $E_e^{\text{min}} \geq 51$ MeV. This is in agreement with (2.63), which predict constant values of $F_{\text{LL}}^{(2)}$ and $G_{\text{LL}}^{(2)}$ for $x_e \sim 1$. By averaging the 10 results such that $E_e^{\text{min}} \geq 51$ MeV, we obtain

$$F_{\text{LL}}^{(2)} = 0.71044(2) \quad G_{\text{LL}}^{(2)} = 0.71044(2)$$

both consistent with (2.63). This is a strong endorsement to the ansatz (2.62). Repeating the same procedure for the two sNLL coefficient, we find

$$F_{\text{NLL}}^{(2)} = 0.70858(2) \quad G_{\text{NLL}}^{(2)} = 0.70858(2)$$

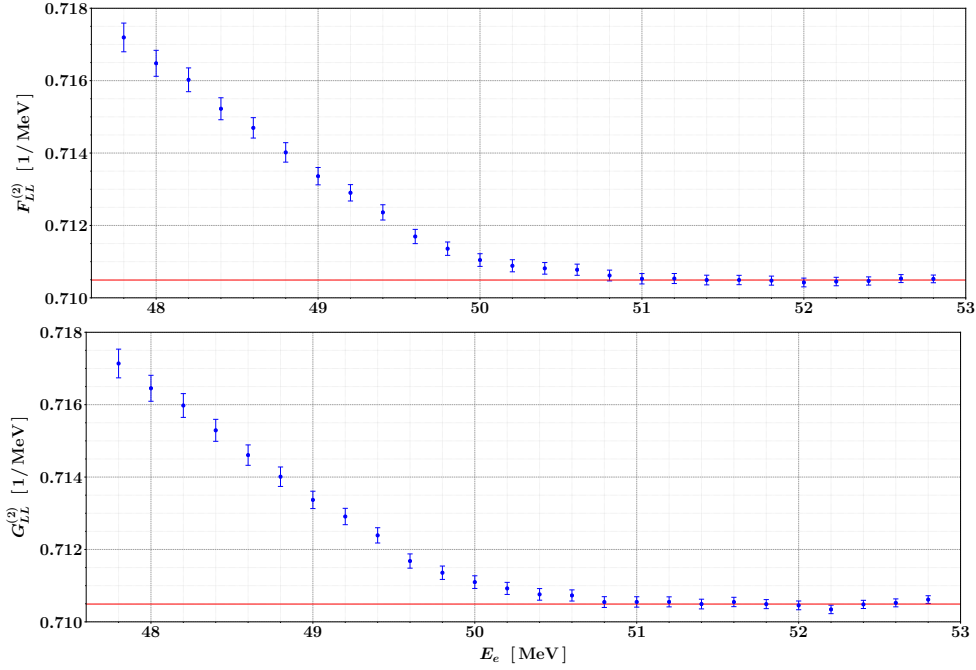


Figure 2.26 Fit results for $F_{LL}^{(2)}$ and $G_{LL}^{(2)}$ for several choices of $E_e \geq E_e^{\min}$.

At this point, we define the LL corrections to f and g as

$$f_{LL} = \left(\frac{\alpha}{\pi}\right)^3 f_3^{cLL} + f_{\text{resum}}^{sLL} \quad (2.65a)$$

$$g_{LL} = \left(\frac{\alpha}{\pi}\right)^3 g_3^{cLL} + g_{\text{resum}}^{sLL} \quad (2.65b)$$

where f_3^{cLL} and g_3^{cLL} are the cLL corrections at N³LO calculated in [115] and

$$f_{\text{resum}}^{sLL} \equiv f_{\text{resum}} - f_0 - f_0 (\alpha c_f L_x) - \frac{1}{2} f_0 (\alpha c_f L_x)^2 - \frac{4}{3} \left(\frac{\alpha}{\pi}\right)^3 L_x^3 L_z^3 \quad (2.66a)$$

$$g_{\text{resum}}^{sLL} \equiv g_{\text{resum}} - g_0 - g_0 (\alpha c_f L_x) - \frac{1}{2} g_0 (\alpha c_f L_x)^2 - \frac{4}{3} \left(\frac{\alpha}{\pi}\right)^3 L_x^3 L_z^3 \quad (2.66b)$$

In (2.66) we have subtracted from f_{resum} and g_{resum} all terms already included up to NNLO, as well as the common term with f_3^{cLL} and g_3^{cLL} . The two LL corrections f_{LL} and g_{LL} are plotted in Figure 2.27, while their impact on the cumulative decay functions is shown in Figure 2.28.

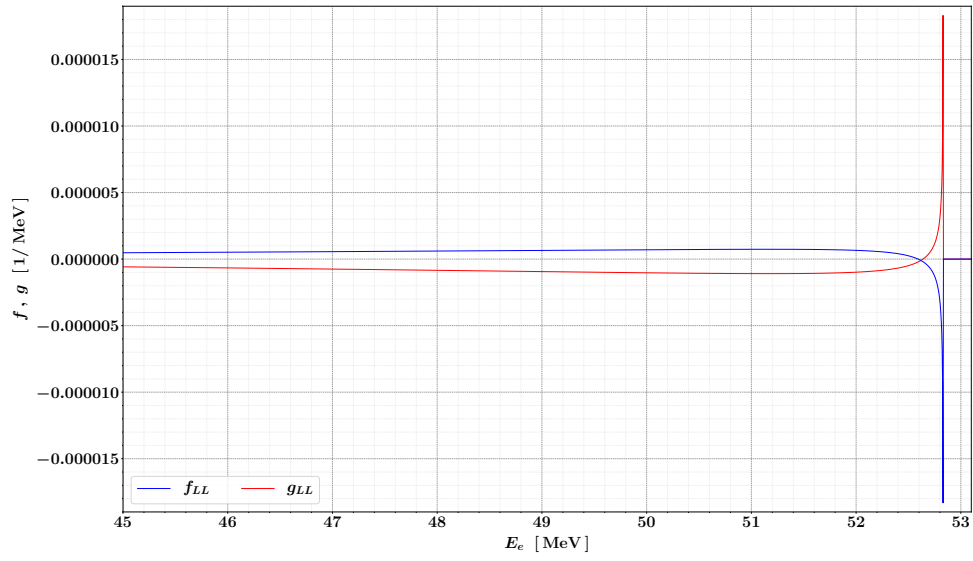


Figure 2.27 LL corrections to the two decay functions f and g .

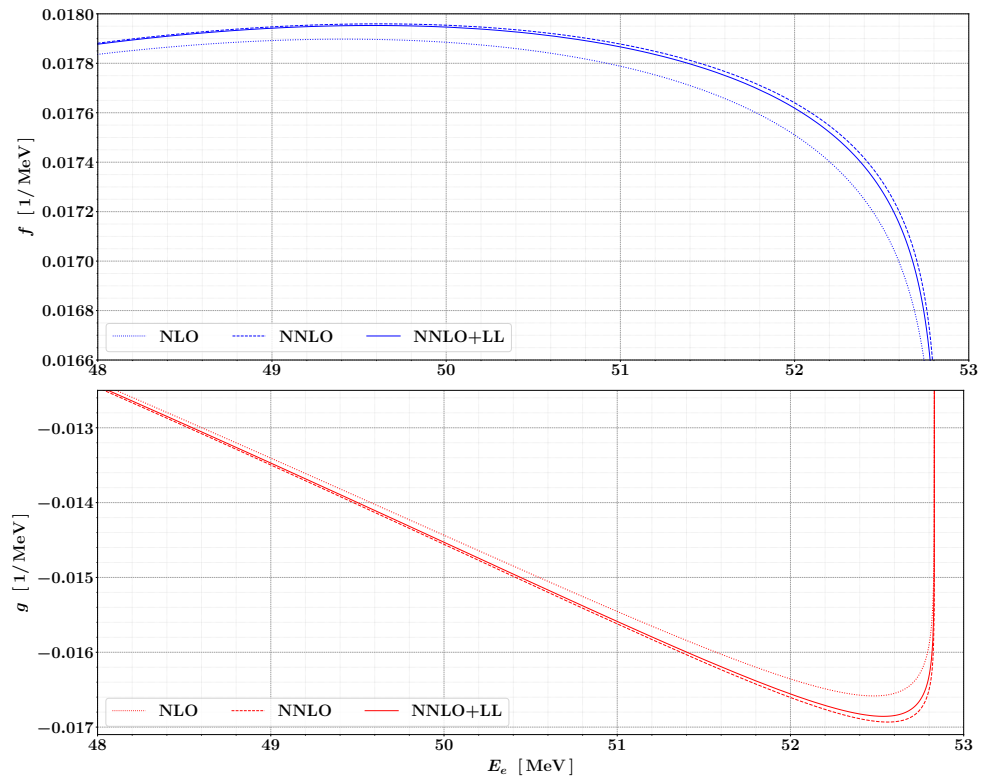


Figure 2.28 Isotropic function f and anisotropic function g at NLO, NNLO and NNLO+LL.

2.7 Final results

We can finally summarise all computations discussed so far. In Figure 2.29 we report the two decay functions $f(E_e)$ and $g(E_e)$ including all contributions up to NNLO+LL, i.e.

$$f \simeq f_{\text{NNLO+LL}} = f_0 + \left(\frac{\alpha}{\pi}\right)^1 f_1 + \left(\frac{\alpha}{\pi}\right)^2 f_2 + \left(\frac{\alpha}{\pi}\right)^3 f_3^{cLL} + f_{\text{resum}}^{sLL} \quad (2.67a)$$

$$g \simeq g_{\text{NNLO+LL}} = g_0 + \left(\frac{\alpha}{\pi}\right)^1 g_1 + \left(\frac{\alpha}{\pi}\right)^2 g_2 + \left(\frac{\alpha}{\pi}\right)^3 g_3^{cLL} + g_{\text{resum}}^{sLL} \quad (2.67b)$$

The final double-differential decay width

$$\mathcal{G}_e \equiv \frac{1}{\Gamma_0} \frac{d^2\Gamma}{dE_e d\cos\theta_e} = f + n_\mu \cos\theta_e g \simeq f_{\text{NNLO+LL}} + n_\mu \cos\theta_e g_{\text{NNLO+LL}} \quad (2.68)$$

is shown in Figure 2.30 for the MEG-like muon polarisation $n_\mu = -0.85$. Hence, the full positron energy spectrum is given by

$$\mathcal{E}_e \equiv \frac{1}{\Gamma_0} \frac{d\Gamma}{dE_e} = \int d\cos\theta_e \mathcal{G}_e = 2f \simeq 2f_{\text{NNLO+LL}} \quad (2.69)$$

and plotted in Figure 2.31. Furthermore, Figure 2.32 shows the spectrum for fixed values of the positron polar angle, obtained by fixing $\cos\theta_e$ in (2.68) for $n_\mu = -0.85$.

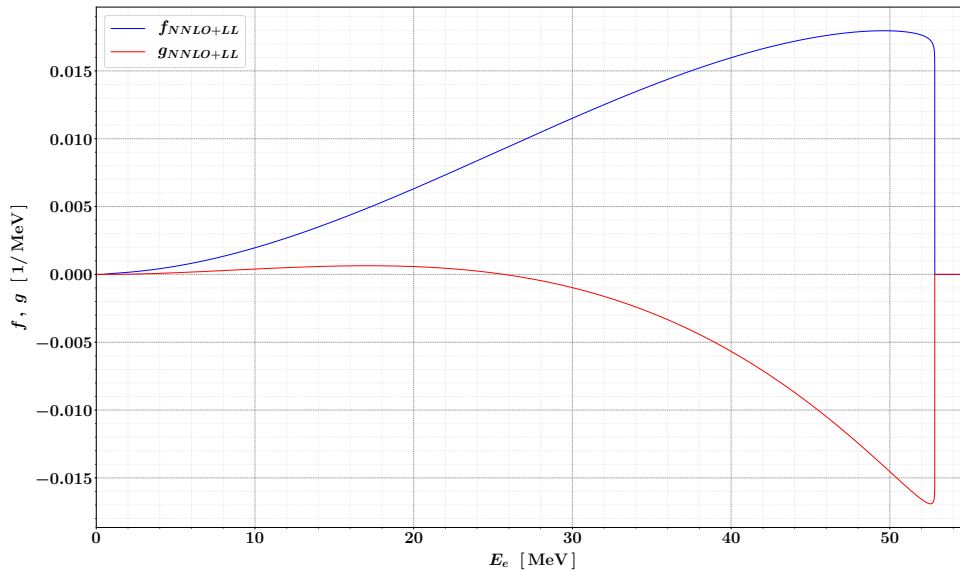


Figure 2.29 Isotropic and anisotropic functions $f(E_e)$ and $g(E_e)$ at NNLO+LL. Both are sampled over 4000 bins, each one with a statistical error around 1 ppm.

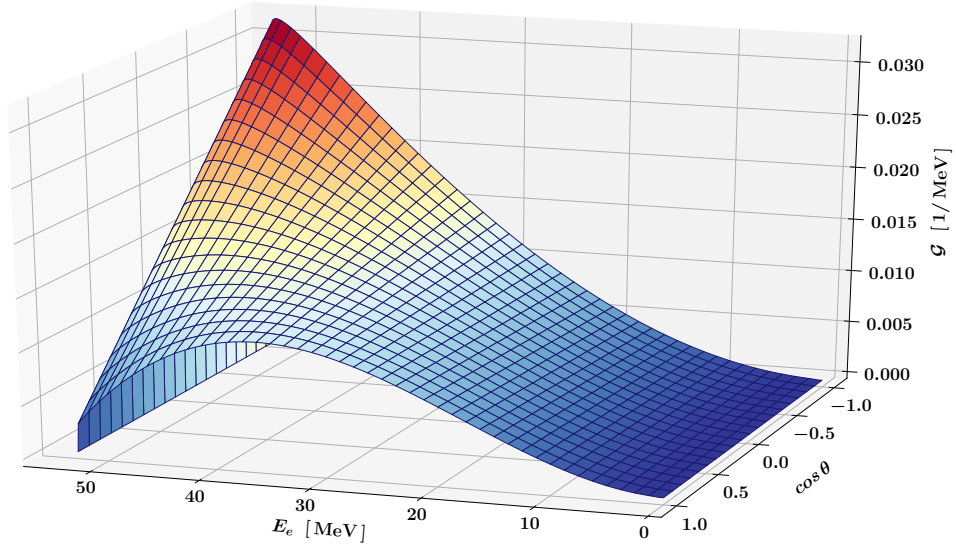


Figure 2.30 Double-differential decay width $\mathcal{G} = (1/\Gamma_0) d^2\Gamma/(dE_e d\cos\theta)$ at NNLO+LL for a muon polarisation $n_\mu = -0.85$.

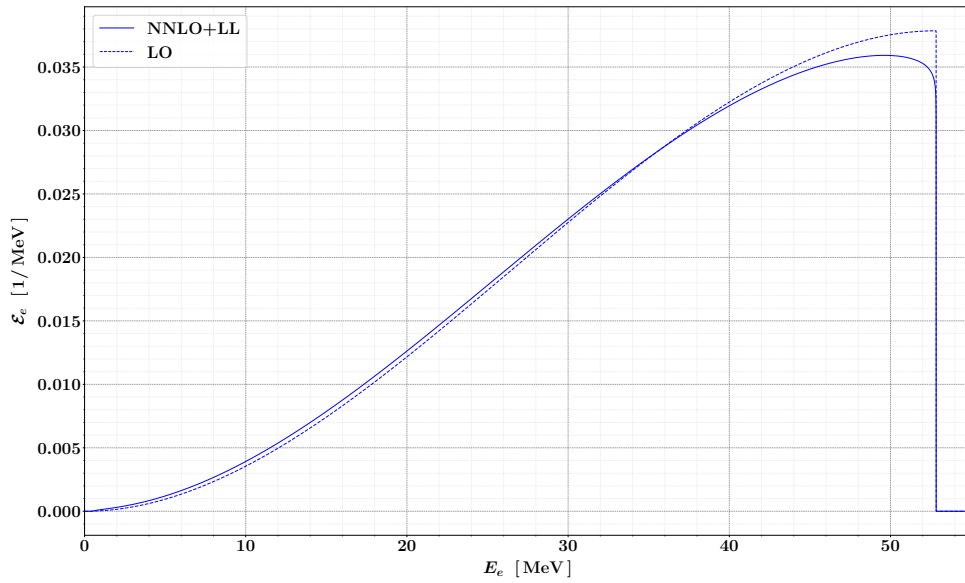


Figure 2.31 Positron energy spectrum $\mathcal{E}_e = (1/\Gamma_0) d\Gamma/dE_e$ at LO and NNLO+LL. The result is independent from the muon polarisation, due to the integration over the entire solid angle.

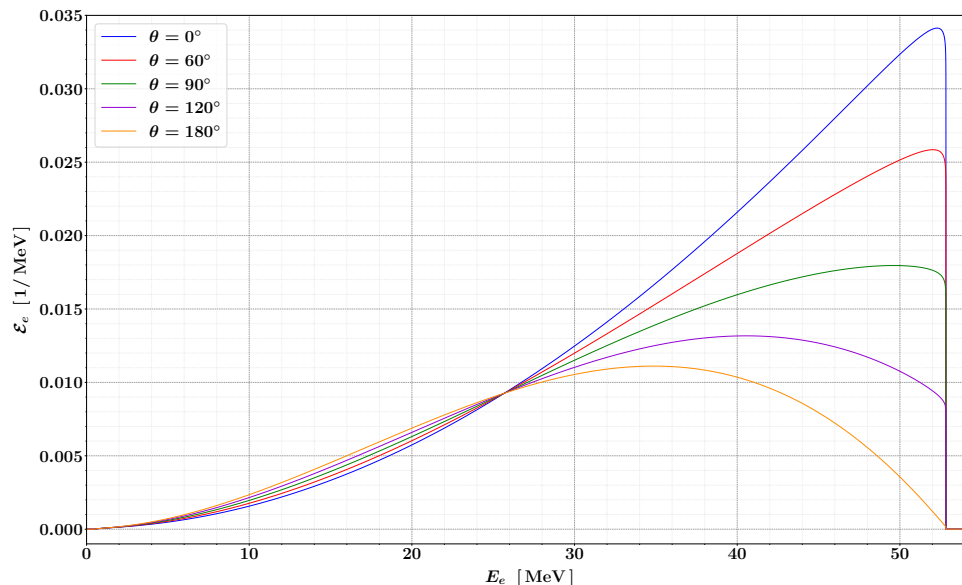


Figure 2.32 Positron energy spectrum $\mathcal{E}_e = (1/\Gamma_0) d\Gamma/dE_e$ at NNLO+LL for fixed values of θ_e . The muon polarisation is set to $n_\mu = -0.85$.

Integrating (2.68) over the entire energy range, we obtain the angular distribution

$$\mathcal{T}_e \equiv \frac{1}{\Gamma_0} \frac{d\Gamma}{d \cos \theta_e} \simeq \int dE_e f_{\text{NNLO+LL}} + n_\mu \cos \theta_e \int dE_e g_{\text{NNLO+LL}} \quad (2.70)$$

The results for several values of muon polarisation n_μ are reported in the left panel of Figure 2.33. Instead, by fixing the positron energy E_e in (2.68), we obtain the angular distributions shown in the right panel of Figure 2.33.

2.7.1 Theoretical error

We conclude the discussion about $\mu \rightarrow e\nu\bar{\nu}$ with the estimation of the theoretical error on $f(E_e)$ and $g(E_e)$ up to NNLO+LL. We can distinguish between three independent sources of uncertainty:

- (1) The *statistical error* due to the MC nature of MCMULE. As already mentioned, its value is around 1 ppm in each energy bin.
- (2) The *experimental error* due to the uncertainty on the measured value of α , m_μ and m_e . Its relative contribution is around 0.2 ppb, especially due to the factor α that multiplies the NLO corrections.

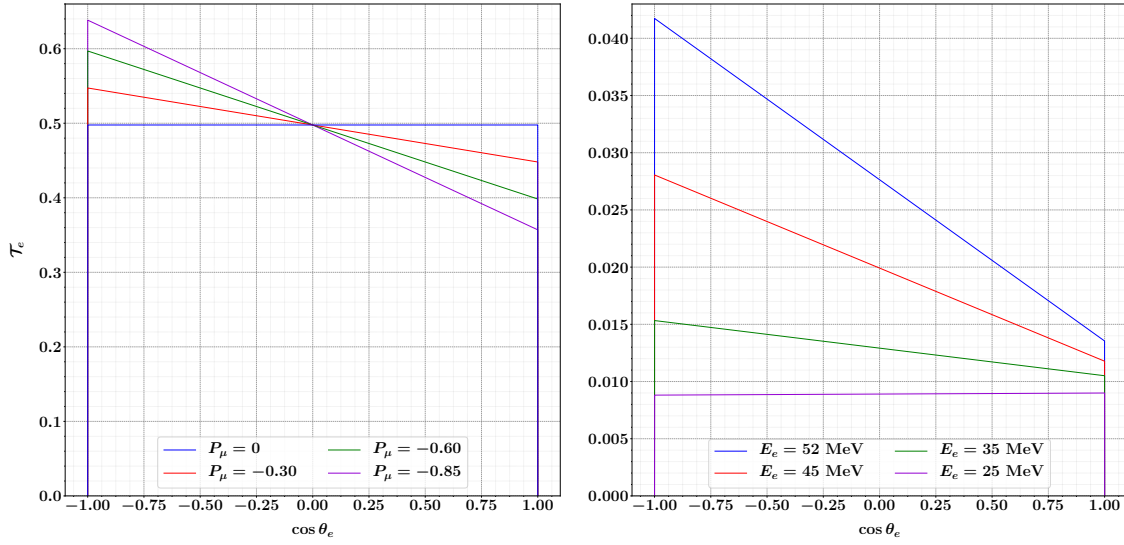


Figure 2.33 Positron angular distribution $\mathcal{T}_e = (1/\Gamma_0) d\Gamma/d \cos \theta_e$ for fixed values of muon polarisation n_μ (left panel) and positron energy E_e (right panel).

- (3) The *perturbative error* due to the higher-order contributions beyond NNLO+LL. This is the dominant uncertainty, therefore it deserves further comment.

The perturbative error is given by the estimation of the most important uncalculated contribution. We have included the full NNLO corrections, the cLL terms at N³LO and the sLL terms to all orders. Thus, close to the energy spectrum endpoint, the most important uncalculated contribution is given by the sNLL terms at N³LO, i.e. all terms proportional to $\alpha^3 L_x^2$. Hence, we can estimate the theoretical uncertainty on f and g as

$$\delta f_{\text{NNLO+LL}} \simeq F_{\text{NLL}}^{(3)} \alpha^3 \log(1 - x_e)^2 \quad (2.71a)$$

$$\delta g_{\text{NNLO+LL}} \simeq G_{\text{NLL}}^{(3)} \alpha^3 \log(1 - x_e)^2 \quad (2.71b)$$

The two coefficients $F_{\text{NLL}}^{(3)}$ and $G_{\text{NLL}}^{(3)}$ are not known. By assuming a weak dependence on the perturbative order, we can approximate

$$\delta f_{\text{NNLO+LL}} \simeq F_{\text{NLL}}^{(2)} \alpha^3 \log(1 - x_e)^2 \quad (2.72a)$$

$$\delta g_{\text{NNLO+LL}} \simeq G_{\text{NLL}}^{(2)} \alpha^3 \log(1 - x_e)^2 \quad (2.72b)$$

where the two coefficients $F_{\text{NLL}}^{(2)}$ and $G_{\text{NLL}}^{(2)}$ are given by the previous fit of the NNLO corrections. The relative errors $\delta f_{\text{NNLO+LL}}/f_{\text{NNLO+LL}}$ and $\delta g_{\text{NNLO+LL}}/g_{\text{NNLO+LL}}$ are shown in Figure 2.34.

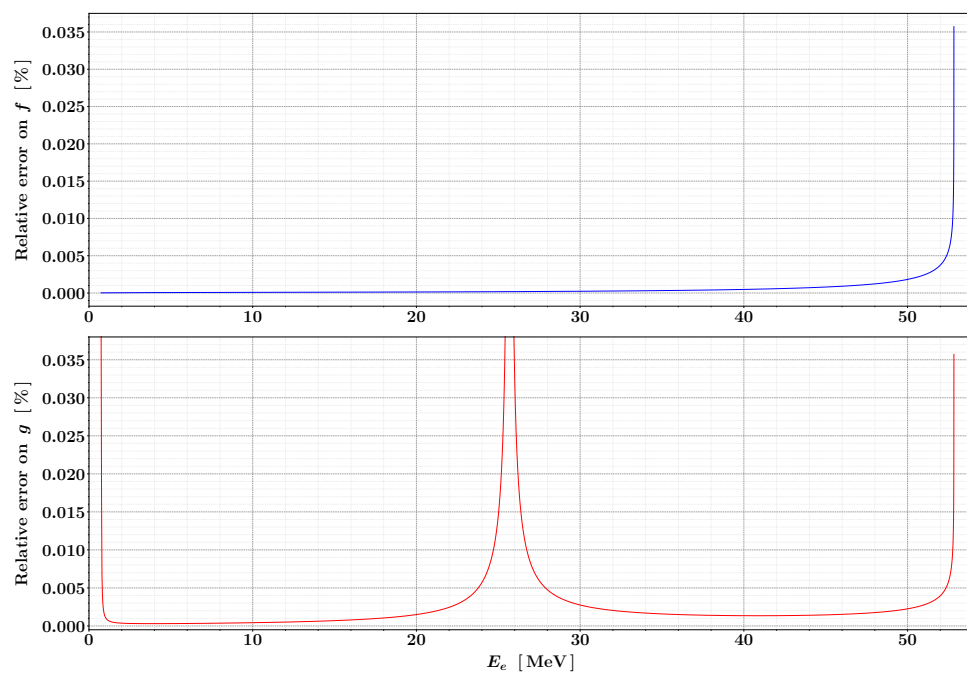


Figure 2.34 Estimate of the relative theoretical uncertainty on $f_{\text{NNLO+LL}}$ (upper panel) and $g_{\text{NNLO+LL}}$ (lower panel) at NNLO+LL.

Chapter 3

Muon decay $\mu \rightarrow eX$ at NLO

3.1 Theoretical model

An axion-like particle (ALP) is a pseudo-Nambu-Goldstone boson (PNGB) arising from the spontaneous symmetry breaking (SSB) of a global $U(1)$ symmetry [8–10]. The broken symmetry depends on the specific theoretical model. It is the total lepton number (or alternatively, the $B - L$ symmetry) in the majoron model [11–13, 124–126], while it is the family lepton number in the familon model [14–16, 127] and the PQ symmetry in the axion model [17–20]. In more recent years, many other models have been proposed starting from those mentioned above. Notable examples are given by the flavon [128, 129], the flaxion [130], the axiflavor [131], the hierarchion [132] and the maxion [133].

In this chapter we follow an effective approach, leaving out the model-dependent dynamics. In all these models the ALP is a light neutral scalar boson X that couples derivatively to the SM fermions. Thus, the interaction between the ALP and the charged leptons is described by the effective lagrangian [8–10, 134, 135]

$$\mathcal{L}_{\text{eff}} = \frac{1}{\Lambda} \partial_\mu X \bar{\ell}_\alpha \gamma^\mu (g_{\alpha\beta}^V + \gamma^5 g_{\alpha\beta}^A) \ell_\beta \quad \alpha, \beta = \{e, \mu, \tau\} \quad (3.1)$$

where Λ represents the SSB mass scale, while the couplings $g_{\alpha\beta}^V$ and $g_{\alpha\beta}^A$ are hermitian matrices in the lepton flavour space. The effective model holds as long as the energy is much less than Λ . In the following, we often refer to the following four paradigmatic configurations of couplings:

- (1) The purely vector (V) couplings

$$g_{\alpha\beta}^V \equiv g_{\alpha\beta} \quad g_{\alpha\beta}^A \equiv 0$$

- (2) The purely axial (A) couplings

$$g_{\alpha\beta}^V \equiv 0 \quad g_{\alpha\beta}^A \equiv g_{\alpha\beta}$$

(3) The left-handed (V-A) couplings

$$g_{\alpha\beta}^V \equiv g_{\alpha\beta}/\sqrt{2} \qquad g_{\alpha\beta}^A \equiv -g_{\alpha\beta}/\sqrt{2}$$

(4) The right-handed (V+A) couplings

$$g_{\alpha\beta}^V \equiv g_{\alpha\beta}/\sqrt{2} \qquad g_{\alpha\beta}^A \equiv g_{\alpha\beta}/\sqrt{2}$$

By integrating by parts, we can rewrite the effective lagrangian as

$$\mathcal{L}_{\text{eff}} = -\frac{i}{\Lambda} X \bar{\ell}_\alpha \gamma^\mu [(m_\alpha - m_\beta) g_{\alpha\beta}^V + \gamma^5 (m_\alpha + m_\beta) g_{\alpha\beta}^A] \ell_\beta \quad (3.2)$$

In this way, the derivative couplings are translated into the yukawa-like couplings

$$y_{\alpha\beta}^V \equiv (m_\alpha - m_\beta) g_{\alpha\beta}^V \qquad y_{\alpha\beta}^A \equiv (m_\alpha + m_\beta) g_{\alpha\beta}^A \quad (3.3)$$

The flavour-violating decay $\mu \rightarrow eX$ arises from the term

$$\mathcal{L}_{\text{eff}} = -\frac{i}{\Lambda} X \bar{\psi}_\mu \gamma^\mu [(m_\mu - m_e) g_V + \gamma^5 (m_\mu + m_e) g_A] \psi_e \quad (3.4)$$

with $g_{\mu e}^A \equiv g_A$ and $g_{\mu e}^V \equiv g_V$. Thus, the LO decay width is given by

$$\begin{aligned} \Gamma(\mu \rightarrow eX) &= \frac{m_\mu^3}{16\pi\Lambda^2} \sqrt{(1-r^2)^2 + z^4 - 2z^2(1+r^2)} \\ &\times [(g_A^2 + g_V^2)(1-z^2)^2 - (g_V^2(1-z)^2 + g_A^2(1+z)^2) r^2] \end{aligned} \quad (3.5)$$

with $r \equiv m_X/m_\mu$ and $z \equiv m_e/m_\mu$. For $r, z \ll 1$ (i.e. $m_e, m_X \ll m_\mu$), we have simply

$$\Gamma(\mu \rightarrow eX) \simeq \frac{m_\mu^3}{16\pi\Lambda_{\mu e}^2} \quad (3.6)$$

with $\Lambda_{\mu e} \equiv \Lambda/\sqrt{g_A^2 + g_V^2}$. In this approximation, the BR is given by

$$\mathcal{B}(\mu \rightarrow eX) \simeq \frac{12\pi^2}{(G_F m_\mu \Lambda_{\mu e})^2} \quad (3.7)$$

The values of $\Lambda_{\mu e}$ excluded by a BR upper limit on $\mu \rightarrow eX$ are shown in Figure 3.1.

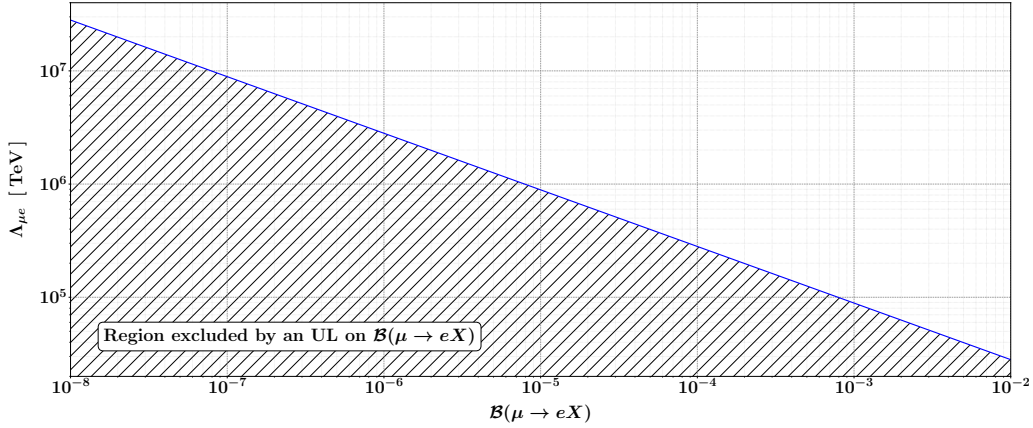


Figure 3.1 Values of $\Lambda_{\mu e}$ excluded by a BR upper limit on $\mu \rightarrow eX$ in the approximation $m_X, m_e \ll m_\mu$.

Including the QED interactions, the effective lagrangian becomes

$$\begin{aligned} \mathcal{L}_{\text{eff}} = & -\frac{i}{\Lambda} X \bar{\psi}_\mu \gamma^\mu [(m_\mu - m_e) g_V + \gamma^5 (m_\mu + m_e) g_A] \psi_e \\ & - e \bar{\psi}_\mu \gamma^\alpha A_\alpha \psi_\mu - e \bar{\psi}_e \gamma^\alpha A_\alpha \psi_e \end{aligned} \quad (3.8)$$

As already discussed for the Fermi theory, we can compute the QED higher-order corrections to $\mu \rightarrow eX$ despite the non renormalisability of the ALP interactions, by keeping the contribution (3.4) fixed to LO.

3.2 QED corrections

At NLO the QED corrections to $\mu \rightarrow eX$ are given by

$$\begin{aligned}
 d\Gamma^{(1)} &= d\Gamma_v^{(1)} + d\Gamma_r^{(1)} \\
 &= d\Phi_2 \mathcal{M}_2^{(1)} + d\Phi_{2+1} \mathcal{M}_{2+1}^{(0)} \\
 &= d\Phi_2 2 \operatorname{Re} [\mathcal{A}_2^{(0)} \times \mathcal{A}_2^{(1)}] + d\Phi_{2+1} |\mathcal{A}_{2+1}^{(0)}|^2
 \end{aligned} \tag{3.9}$$

which includes all the (renormalised) matrix elements proportional to α . As usual, the two individual terms are characterised as follows.

- The virtual matrix element $\mathcal{M}_2^{(1)} = 2 \operatorname{Re} [\mathcal{A}_2^{(0)} \times \mathcal{A}_2^{(1)}]$ is given by the interference term between the tree-level amplitude \mathcal{A}_2^0 and the one-loop amplitude $\mathcal{A}_2^{(1)}$.
- The real matrix element $\mathcal{M}_{2+1}^{(0)} = |\mathcal{A}_{2+1}^{(0)}|^2$ is given by the square of the tree-level amplitude $\mathcal{A}_{2+1}^{(0)}$ with an extra photon in the final state. The real corrections have the relevant effect to make the signal no longer perfectly monochromatic in the center-of-mass reference, being a 3-body rather than a 2-body contribution.

The diagrams contributing to $\mathcal{A}_2^{(1)}$ and $\mathcal{A}_{2+1}^{(0)}$ are depicted in Figure 3.2.

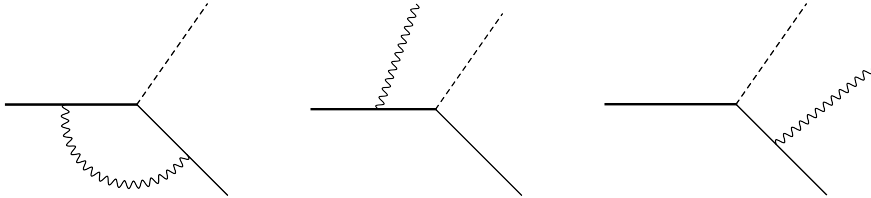


Figure 3.2 Higher-order diagrams contributing to $\mu^+ \rightarrow e^+ X$ at NLO. The first (from left) represents the one-loop amplitude $\mathcal{A}_2^{(1)}$, while the sum of the latter two represents the tree-level amplitude $\mathcal{A}_{2+1}^{(0)}$. Thick lines correspond to antimuons, thin lines to positrons, wavy lines to photons, dashed lines to scalar bosons.

After renormalisation and FKS-subtraction, $d\Gamma_v^{(1)}$ and $d\Gamma_r^{(1)}$ are separately finite in four dimensions. Thus, both can be integrated numerically over the corresponding phase space, as already done for $\mu \rightarrow e\nu\bar{\nu}$. Again, we need to verify that the sum $d\Gamma^{(1)} = d\Gamma_v^{(1)}(\xi_c) + d\Gamma_r^{(1)}(\xi_c)$ is ξ_c -independent. Repeating the procedure outlined for $\mu \rightarrow e\nu\bar{\nu}$, we evaluate the full widths $\Gamma_v^{(1)}$ and $\Gamma_r^{(1)}$ for different values of ξ_c . The result for $m_X = 1$ MeV and V–A couplings is reported in Figure 3.3.

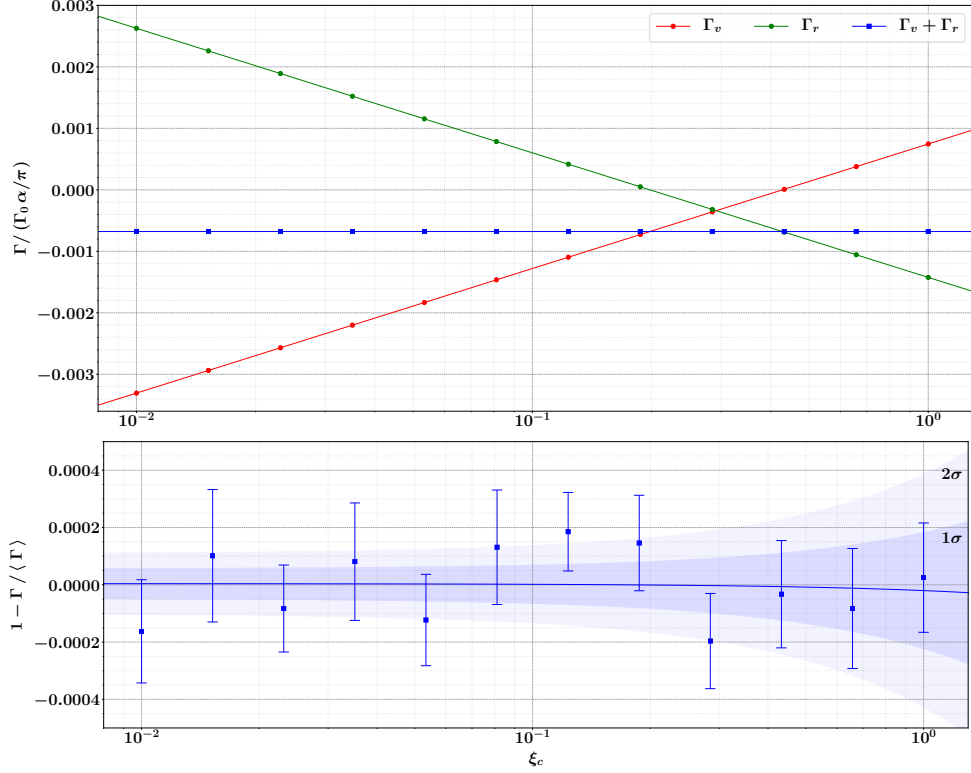


Figure 3.3 ξ_c -independence study for $\mu \rightarrow eX$ at NLO. The upper panel shows the virtual and real corrections ($\Gamma_v^{(1)}$ and $\Gamma_r^{(1)}$) for several choices of ξ_c . The solid lines correspond to the fits discussed in the text. The lower panel shows the sum $\Gamma_v^{(1)}(\xi_c) + \Gamma_r^{(1)}(\xi_c)$, normalised to its average value. The ALP mass is set to $m_X = 1$ MeV, while the decay widths are normalised so that $\mathcal{B}(\mu \rightarrow eX) = 10^{-4}$.

Similarly to $\mu \rightarrow e\nu\bar{\nu}$, at NLO we have

$$\frac{1}{\Gamma_0} \Gamma_v^{(1)}(\xi_c) = \left(\frac{\alpha}{\pi}\right) (b_{0,0} + b_{0,1} \log \xi_c) \quad (3.10a)$$

$$\frac{1}{\Gamma_0} \Gamma_r^{(1)}(\xi_c) = \left(\frac{\alpha}{\pi}\right) (b_{1,0} + b_{1,1} \log \xi_c) \quad (3.10b)$$

Hence, we need to verify that

$$b_{0,1} + b_{1,1} = 0 \quad (3.11)$$

By fitting the data in Figure 3.3, we obtain

$$\begin{aligned} \Gamma_v^{(1)} : \quad & b_{0,0} = +7.4589(4) \cdot 10^{-4} & b_{0,1} = +8.7974(4) \cdot 10^{-4} & \chi^2 \approx 1.04 \\ \Gamma_r^{(1)} : \quad & b_{1,0} = -14.240(1) \cdot 10^{-4} & b_{1,1} = -8.7976(3) \cdot 10^{-4} & \chi^2 \approx 0.96 \end{aligned}$$

Thus, we find

$$b_{0,1} + b_{1,1} = -2(5) \cdot 10^{-8}$$

which is consistent with zero, as required by the ξ_c -independence condition (3.11).

Following the steps outlined for $\mu \rightarrow e\nu\bar{\nu}$, we need to compute the polarised double-differential decay width

$$\mathcal{G}_e \equiv \frac{1}{\Gamma_0} \frac{d^2\Gamma}{dE_e d\cos\theta_e} = f + n_\mu \cos\theta_e g \quad (3.12)$$

which contains all information on the signal positron, whose 4-momentum is again parametrised in the center-of-mass reference according to (2.16). To this end, we introduce the forward positron spectrum \mathcal{E}_e^+ and the backward positron spectrum \mathcal{E}_e^- . At NLO we have

$$\mathcal{E}_{\text{NLO}}^+ = \mathcal{E}_0^+ + \left(\frac{\alpha}{\pi}\right) \mathcal{E}_1^+ = \mathcal{E}_0^+ + \left(\frac{\alpha}{\pi}\right) \left(\mathcal{E}_v^+(\xi_c) + \mathcal{E}_r^+(\xi_c)\right) \quad (3.13a)$$

$$\mathcal{E}_{\text{NLO}}^- = \mathcal{E}_0^- + \left(\frac{\alpha}{\pi}\right) \mathcal{E}_1^- = \mathcal{E}_0^- + \left(\frac{\alpha}{\pi}\right) \left(\mathcal{E}_v^-(\xi_c) + \mathcal{E}_r^-(\xi_c)\right) \quad (3.13b)$$

where $\mathcal{E}_0^\pm \propto \delta(E_e - E_e^X)$ is the LO contribution and

$$\mathcal{E}_v(\xi_c) = \frac{1}{\Gamma_0} \frac{d\Gamma_v}{dE_e}(\xi_c) \quad \mathcal{E}_r(\xi_c) = \frac{1}{\Gamma_0} \frac{d\Gamma_r}{dE_e}(\xi_c) \quad (3.14)$$

Hence, the isotropic function f and the anisotropic function g are given by

$$\begin{aligned} f_{\text{NLO}} &= f_0 + \left(\frac{\alpha}{\pi}\right) f_1 = f_0 + \left(\frac{\alpha}{\pi}\right) \left(f_v(\xi_c) + f_r(\xi_c)\right) \\ &= \frac{1}{2} \left(\mathcal{E}_0^+ + \mathcal{E}_0^-\right) + \left(\frac{\alpha}{\pi}\right) \frac{1}{2} \left(\mathcal{E}_v^+(\xi_c) + \mathcal{E}_r^+(\xi_c) + \mathcal{E}_v^-(\xi_c) + \mathcal{E}_r^-(\xi_c)\right) \\ &= \frac{1}{2} \left(\mathcal{E}_{\text{NLO}}^+ + \mathcal{E}_{\text{NLO}}^-\right) \end{aligned} \quad (3.15a)$$

$$\begin{aligned} g_{\text{NLO}} &= g_0 + \left(\frac{\alpha}{\pi}\right) g_1 = g_0 + \left(\frac{\alpha}{\pi}\right) \left(g_v(\xi_c) + g_r(\xi_c)\right) \\ &= \frac{1}{2n_\mu} \left(\mathcal{E}_0^+ - \mathcal{E}_0^-\right) + \left(\frac{\alpha}{\pi}\right) \frac{1}{2n_\mu} \left(\mathcal{E}_v^+(\xi_c) + \mathcal{E}_r^+(\xi_c) - \mathcal{E}_v^-(\xi_c) - \mathcal{E}_r^-(\xi_c)\right) \\ &= \frac{1}{2n_\mu} \left(\mathcal{E}_{\text{NLO}}^+ - \mathcal{E}_{\text{NLO}}^-\right) \end{aligned} \quad (3.15b)$$

The combination between real and virtual contributions eliminates the unphysical dependence on ξ_c , so that f_1 and g_1 are the physical NLO corrections to f and g . Similarly, f_{NLO}

and g_{NLO} are the ξ_c -independent decay functions up to NLO. One of the numerical results for f_{NLO} and g_{NLO} is shown in Figure 3.4. The reported values correspond to a branching ratio $\mathcal{B}(\mu \rightarrow eX) = 10^{-4}$, an ALP mass $m_X = 1$ MeV and V–A couplings. The energy bins and the number of random events are the same used for the background $\mu \rightarrow e\nu\bar{\nu}$.

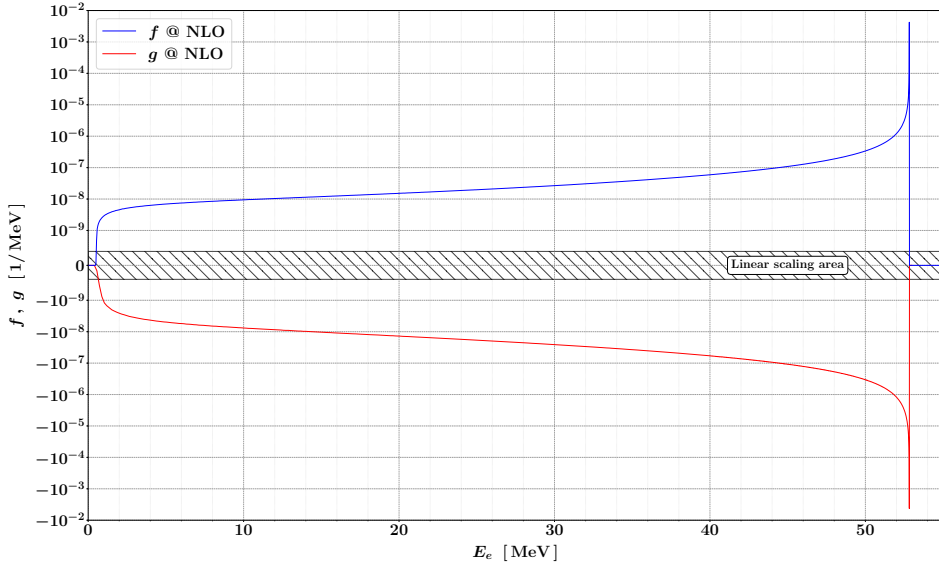


Figure 3.4 Isotropic function $f(E_e)$ and anisotropic function $g(E_e)$ up to NLO for $\mathcal{B} = 10^{-4}$, $m_X = 1$ MeV and V–A couplings. The plot is in logarithmic scale, except in the highlighted region, where the scale is linear in order to allow a finite zero crossing.

At LO the two decay functions f and g are delta functions centred in E_e^X . However, both f_{NLO} and g_{NLO} feature a smooth radiative tail, due to the energy carried away by the real photons emitted at NLO. We find the same pattern in the positron energy spectrum \mathcal{E}_e , which is simply $\mathcal{E}_e = 2f$. In Figure 3.5 we report \mathcal{E}_e for different BRs, while Figure 3.6 shows the results for different values of m_X . We note that the energy spectrum is independent on the couplings for fixed values of BR. At LO this is trivial, because the energy spectrum only depends on the total decay width, which is fixed by the BR. Since the QED interaction is invariant under the transformation $\psi \rightarrow \gamma^5\psi$, the property is extended to NLO. Hence, the coupling mixing only enters in the anisotropic function g , i.e. in the angular anisotropy due to the muon polarisation. In Figure 3.7 we report g_{NLO} for different coupling choices. The same is done in Figure 3.8 for the double-differential distributions \mathcal{G}_e corresponding to a MEG-like polarisation $n_\mu = -0.85$. For V or A couplings the positron emission is independent on the muon polarisation, because the left-handed and right-handed effects cancel each other. The angular dependence is instead specular between the V–A and V+A couplings, according to the fact that the interaction is left-handed in the first case and right-handed in the second one.

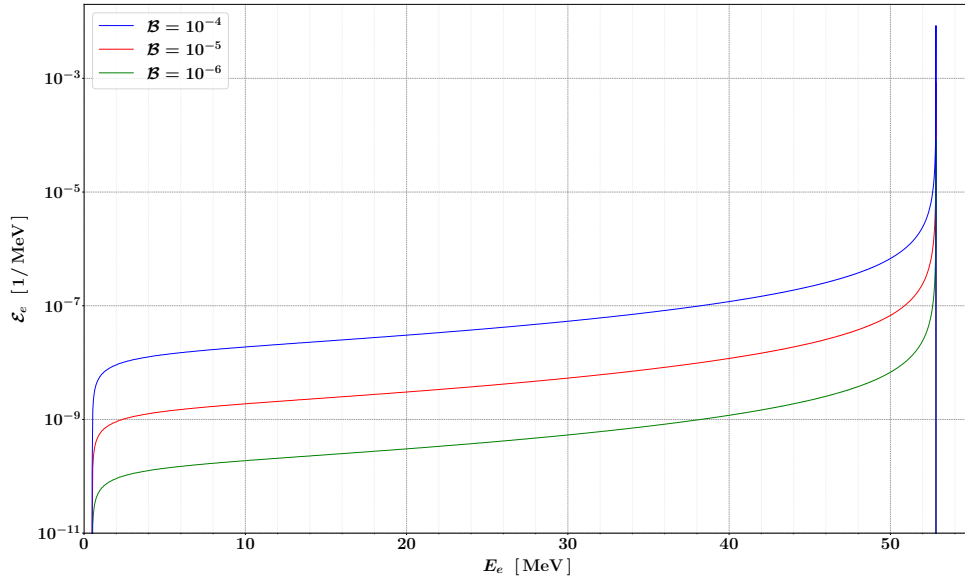


Figure 3.5 Positron energy spectrum $\mathcal{E}_e(E_e)$ up to NLO for $m_X = 1$ MeV and different branching ratios.

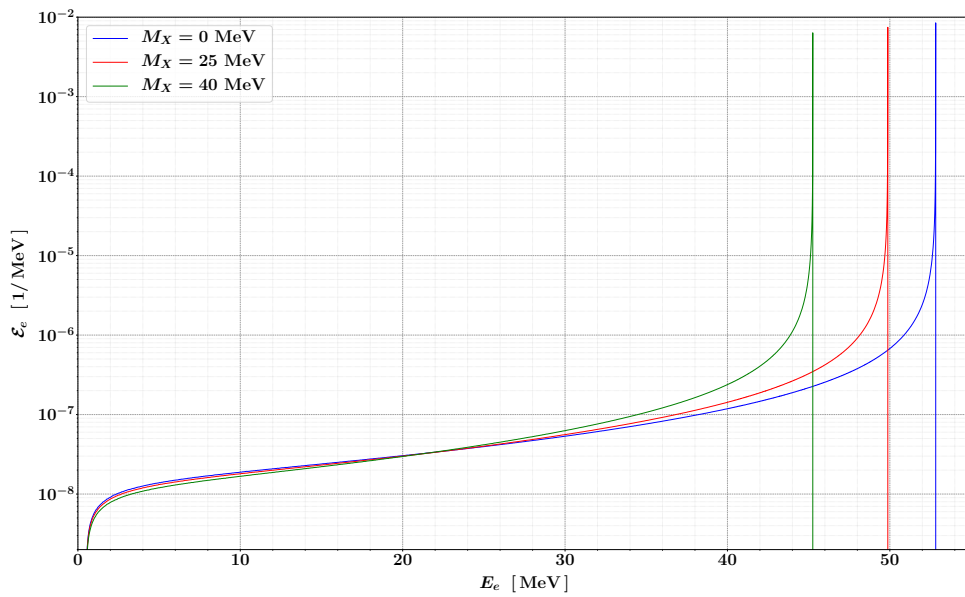


Figure 3.6 Positron energy spectrum $\mathcal{E}_e(E_e)$ up to NLO for $\mathcal{B} = 10^{-4}$ and different masses of the scalar boson.

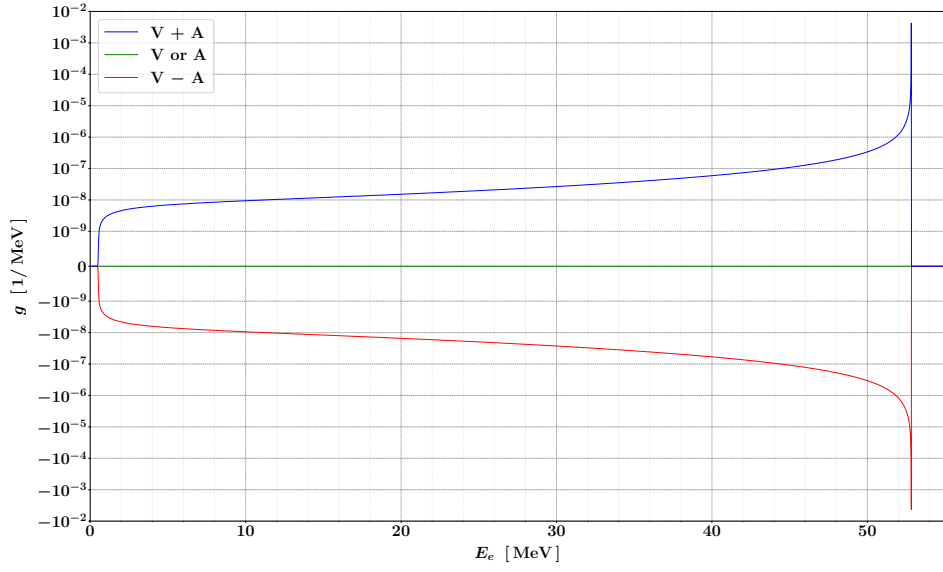


Figure 3.7 Anisotropic function $g(E_e)$ up to NLO for $\mathcal{B} = 10^{-4}$, $m_X = 1$ MeV and different couplings choices.

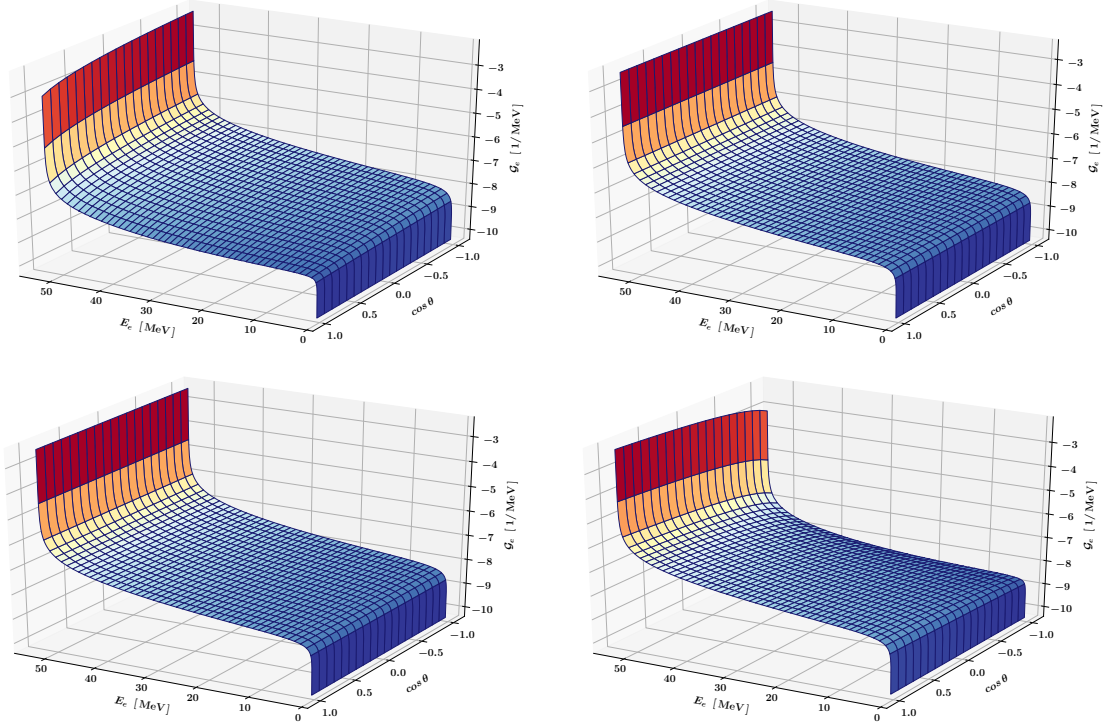


Figure 3.8 Double-differential distributions \mathcal{G}_e up to NLO for $\mathcal{B} = 10^{-4}$, $m_X = 1$ MeV and different coupling choices: V-A (left-upper panel), V (right-upper panel), A (left-lower panel), V+A (right-lower panel). The muon polarisation is set to $n_\mu = -0.85$. The z -axis is in logarithmic scale.

3.3 Background comparison

The comparison between $\mu \rightarrow e\nu\bar{\nu}$ at NNLO+LL and $\mu \rightarrow eX$ at LO is trivial: the background spectrum is a continuous function throughout $m_e \leq E_e \leq E_e^M$, while the signal spectrum is a delta function centred in $E_e^X \in [m_e, E_e^M]$. The situation changes slightly at NLO, because the monochromatic signal is followed by a smooth radiative tail, extended throughout the interval $m_e \leq E_e \leq E_e^X$. A direct comparison between the energy spectra of $\mu \rightarrow e\nu\bar{\nu}$ and $\mu \rightarrow eX$ ($m_X = 1$ MeV), respectively up to NNLO+LL and NLO, is provided in Figure 3.9. The signal $\mu \rightarrow eX$ is normalised in order to correspond to a branching ratio $\mathcal{B} = 10^{-4}$. We clearly distinguish the signal peak close to the energy endpoint. We also note that the signal tends to *fill* the spectrum close to the endpoint. This is straightforward if we consider that the background decreases very quickly for $E_e \rightarrow E_e^M$, while the signal has a peak in $E_e = E_e^X \simeq E_e^M$ if $m_X \ll m_\mu$. As we will exhibit in Chapter 5, the detector response spreads the signal events throughout the endpoint region, so that the signature of $\mu \rightarrow eX$ for small ALP masses is more properly a right-shifted endpoint, rather than a visible peak emerging from the SM background. This makes the experimental search for $\mu \rightarrow eX$ even more difficult, due to the systematic uncertainties on the absolute energy scale.

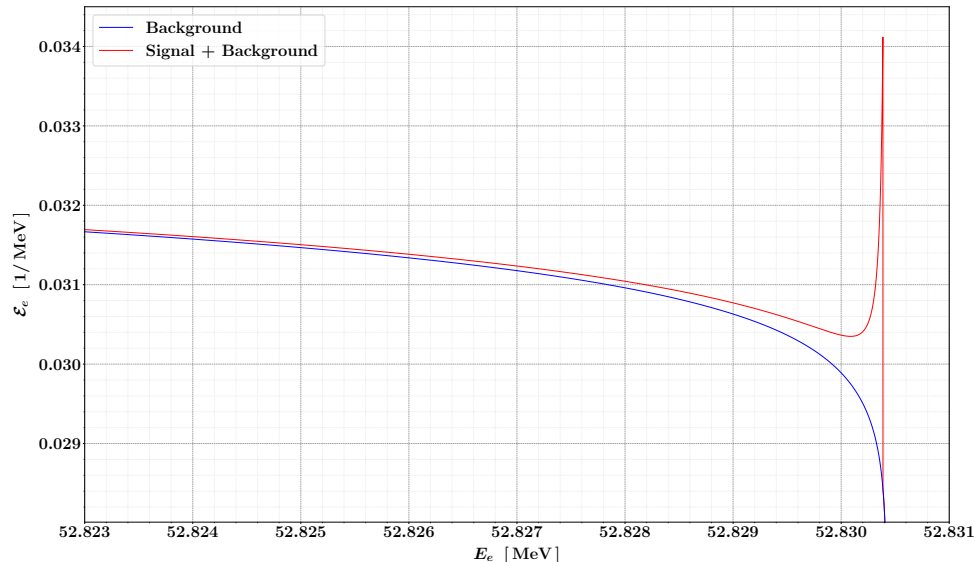


Figure 3.9 Comparison between the energy spectrum of $\mu \rightarrow e\nu\bar{\nu}$ and $\mu \rightarrow eX$, respectively up to NNLO+LL and NLO. The signal is normalised so that $\mathcal{B} = 10^{-4}$, while the mass of the particle X is fixed to $m_X = 1$ MeV.

In addition to the energy spectrum, it is also interesting to consider the positron angular distribution $\mathcal{T}_e = (1/\Gamma_0)d\Gamma/d\cos\theta_e$. Depending on the coupling mixing, the distribution of the signal positrons changes radically for sufficiently polarised muons. In the left panel of Figure 3.10, we report the NLO results for the usual four configurations of couplings (V, A, V–A and V+A) for a MEG-like muon polarisation ($n_\mu = -0.85$). In the right panel, we compare the V+A signal with the SM background, which is well-known to be V–A. A cut $E_e > 50$ MeV is applied to further increase the signal-background ratio in the upstream region $\cos\theta_e > 0$. The V+A case is particularly promising in the experimental context, because the muon polarisation effect can be used to reject the V–A background. We also note that the two isotropic cases (V and A) are totally independent from the initial-state polarisation. This is another difference that can be used to distinguish between signal and background positrons.

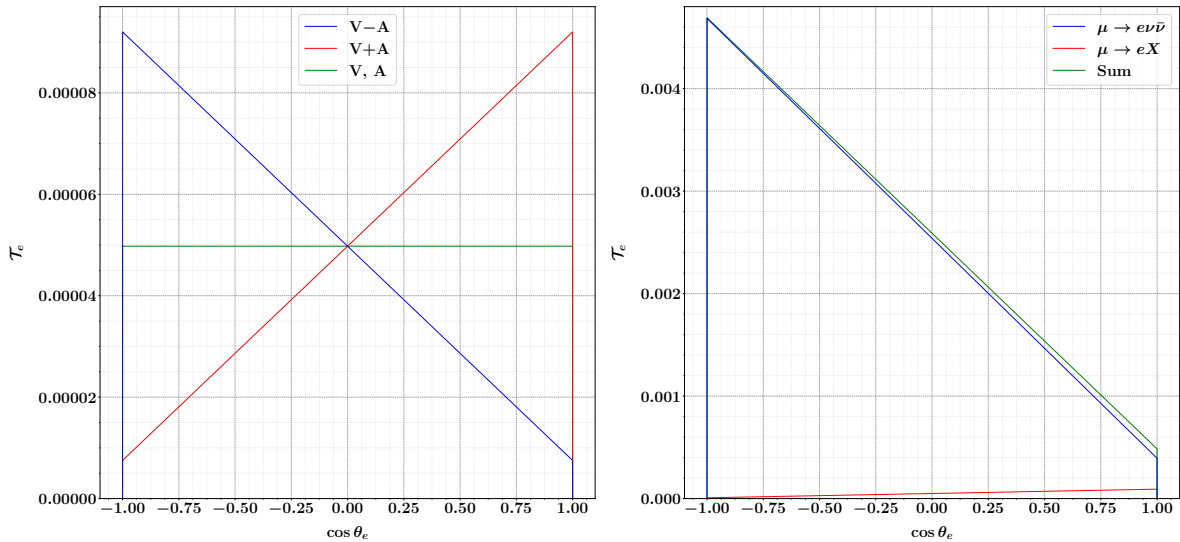


Figure 3.10 Positron angular distribution for the signal $\mu \rightarrow eX$ ($m_X = 1$ MeV) and the background $\mu \rightarrow e\nu\bar{\nu}$. The signal BR is fixed to 10^{-4} , while the muon polarisation is set to $n_\mu = -0.85$.

It is also interesting to compare the signal with the background error (cf. Figure 3.11). In fact, if the signal does not emerge from the theoretical error band of the background, not even an ideal experiment can unambiguously detect it. Before any experimental complication, the signal must be sufficiently strong to allow us to properly distinguish it from an uncalculated higher-order QED effect. This request sets a lower bound \mathcal{B}_{LL}^{th} on the theoretically observable signal BR. Specifically, we define \mathcal{B}_{LL}^{th} as the BR at which the 90% of the signal spectrum is above the background error band. The only way to reduce \mathcal{B}_{LL}^{th} is to compute more precise background predictions. The result obtained by varying the mass m_X is shown in the Figure 3.12.

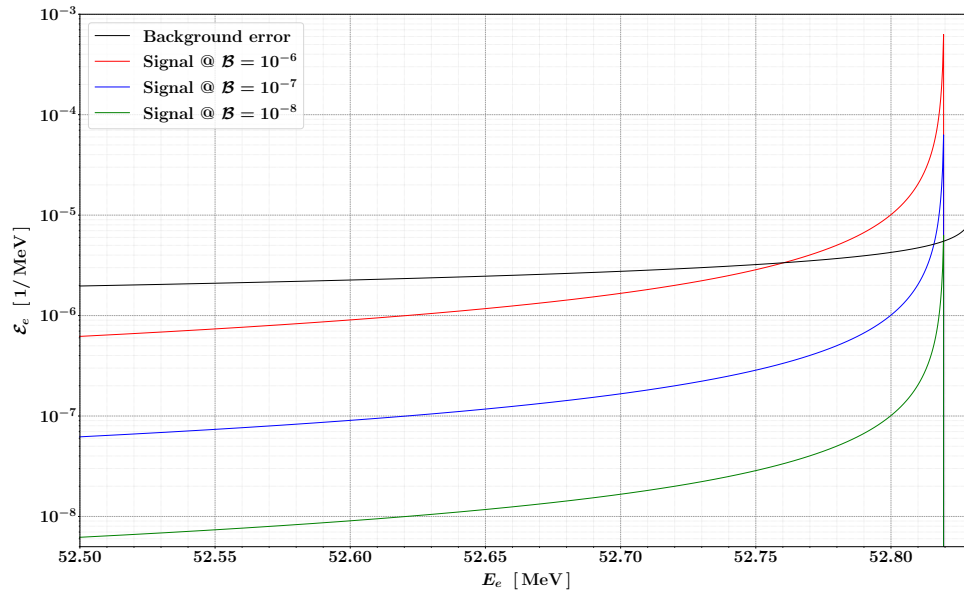


Figure 3.11 Comparison between the $\mu \rightarrow eX$ positron energy spectrum and the corresponding background error for three different BRs. The ALP mass is fixed to 5 MeV.

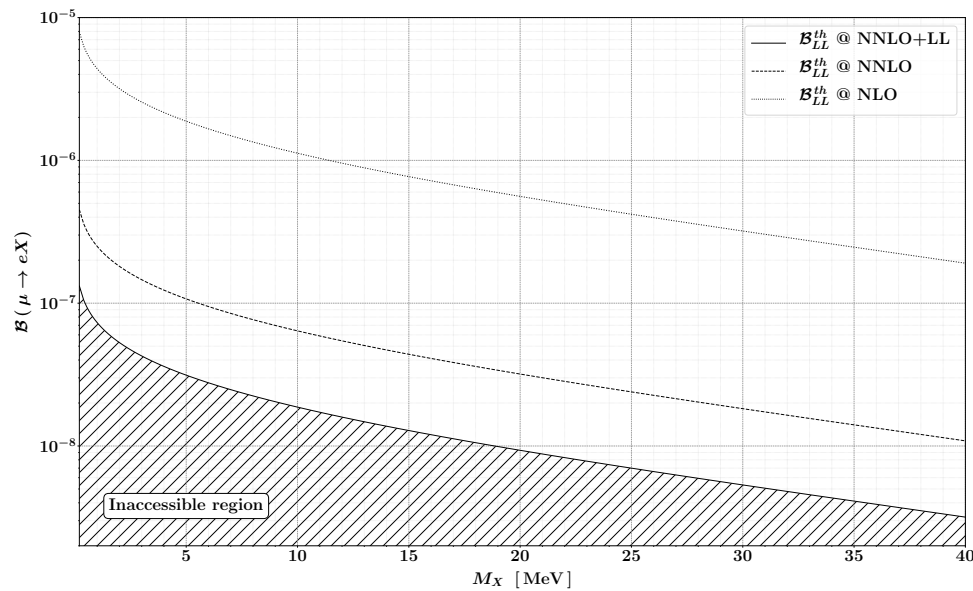


Figure 3.12 Lower limits on the theoretically observable signal for $m_X \leq 40$ MeV. As a reference, the results corresponding to the previous QED orders are also reported. The background error up to NLO and NNLO is estimated a posteriori: the NLO error is given by the NNLO corrections, while the NNLO error is given by the LL corrections.

Chapter 4

The MEG II experiment at PSI

4.1 Muons at PSI

A high rate of muons is an indispensable prerequisite for any experiment that aims to study rare muon decays. The High Intensity Proton Accelerator (HIPA) facility at the Paul Scherrer Institut (PSI) features the most powerful proton accelerator in the world. It delivers a proton current of 2.2 mA at 590 MeV, corresponding to an operative power of 1.3 MW [5]. This unique feature is exploited to create the most intense continuous antimuon beam in the world, which can reach a maximum rate of $5 \cdot 10^8 \mu^+/s$. This makes the PSI an ideal place to search for muon decays beyond the SM, such as $\mu \rightarrow e\gamma$, $\mu \rightarrow eee$ and $\mu \rightarrow eX$. A map of the HIPA facility is provided in Figure 4.1.

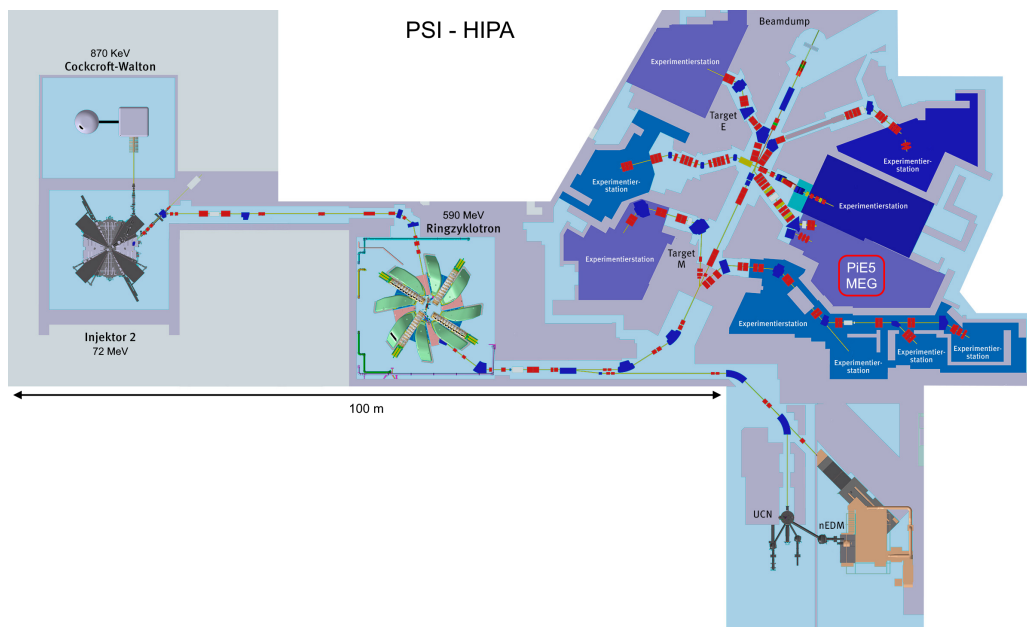


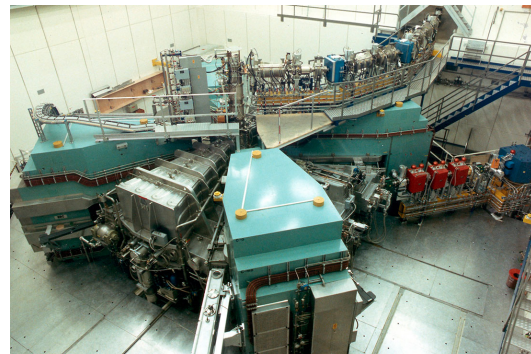
Figure 4.1 Map of the HIPA facility at PSI. The MEG II location is highlighted [136].

The high-intensity proton beamline is originated by a cascade of three accelerators.

- (1) The protons to be accelerated are collected through an Electron Cyclotron Resonance (ECR) ion source, where hydrogen is ionised. Then, they are pre-accelerated to a kinetic energy of 870 keV by a Cockcroft-Walton (CW) accelerator (cf. Figure 4.2a).
- (2) As an intermediate step, the proton beam is delivered to an auxiliary isochronous cyclotron, the so-called Injector II (cf. Figure 4.2b), where it reaches a kinetic energy of 72 MeV.



(a) Cockcroft-Walton (870 KeV)



(b) Injector II (72 MeV)

Figure 4.2 The two PSI proton pre-accelerators [137].

- (3) The pre-accelerated proton beam is finally delivered to the main isochronous cyclotron, known as Ringzyklotron (cf. Figure 4.3a). The accelerator is based on four Radio Frequency (RF) accelerating cavities, operating at 50.6 MHz (cf. Figure 4.3). After exactly 186 revolutions, the protons leave the cyclotron with the final kinetic energy of 590 MeV. The energy is chosen to maximise the pion production, while remaining under the threshold for the kaon production in the scattering with a nuclear target. The accelerator complex delivers a proton current of 2.2 mA, corresponding to a flux of $1.6 \cdot 10^{16} p^+/s$. However, the proton beam is not exactly continuous, but rather structured in bunches of 20 ns, given by the operative frequency of the RF cavities.

The conversion of the proton beam into a high-intensity muon beam is based on the scattering with a meson production target, consisting of a rotating wheel of polycrystalline graphite. The rotation (1 Hz) distributes the huge power delivered by the proton beam over the whole target, avoiding the overheating of the polycrystalline material. The interaction between the protons and the nuclei contained in the target produces a high amount of charged pions according to the four processes



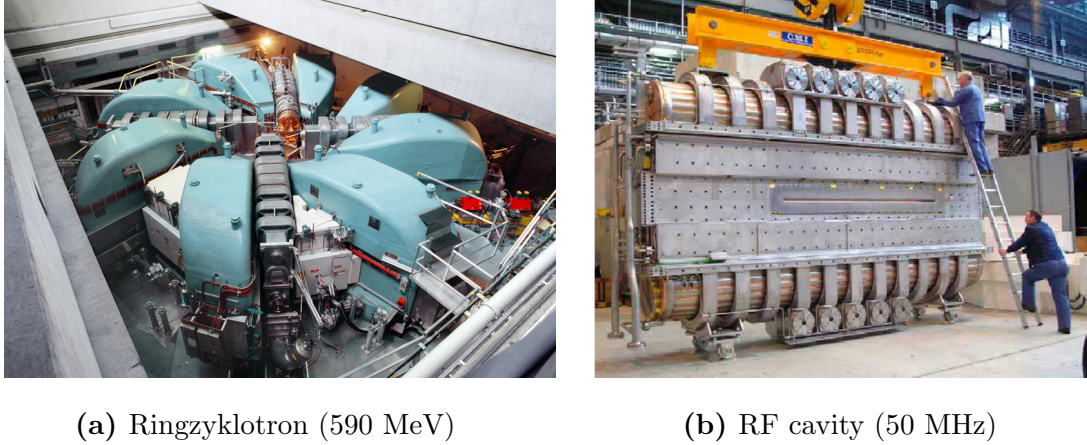


Figure 4.3 The PSI main cyclotron and one of its four RF cavities [137, 138].

The produced pions decay into muons as

$$\pi^+ \rightarrow \mu^+ \nu_\mu \qquad \pi^- \rightarrow \mu^- \bar{\nu}_\mu$$

with a branching ratio of almost 100%. Depending on the initial energy and the production position, the pions can decay outside or inside the target. The muons produced in the first way are called *cloud muons*. Since the decay occurs in-flight, the momentum of such muons is widely distributed. Further, they are typically unpolarised. When the pions decay inside the target, only the muons produced near the surface can escape, due to their low momentum. The muons produced in this way are called *surface muons*. Since the pions tend to decay at rest inside the target, the such muons have a monochromatic momentum around 28 MeV/c. We also note that the surface muons are mostly positive, due to the high cross section for the nuclear capture of the negative pions. Furthermore, if we neglect the muon neutrino mass, the surface antimuons are emitted fully polarised against their momentum. The produced muons are collected in a low-energy beam through a large acceptance dipole magnet, removing the contamination from other particles through an electrostatic separator. Since the π^+ lifetime at rest (≈ 26 ns) is greater than the period of the proton beam bunches (≈ 20 ns), the resulting muon beam is substantially continuous.

The HIPA facility features two low-intensity meson beamlines (IIM1 and IIM3). The first is a high-resolution pion beam, while the second is dedicated to the study of the muon spin resonance (μ SR). The provided high-intensity meson beamlines are five (IIE1 to IIE5). The IIE5 beamline, based on surface antimuons, serves two cLFV experiments: MEG II and Mu3e. In the following we will focus on the first of the two.

4.2 The MEG II experiment

The MEG II experiment [4] searches for the muon cLFV decay $\mu^+ \rightarrow e^+\gamma$, whose discovery would be a clear signal of NP beyond the SM. In three years of data acquisition the experiment is expected to reach a sensitivity of almost one order of magnitude below the BR upper limit set by the previous MEG experiment to [6, 7]

$$\mathcal{B}(\mu^+ \rightarrow e^+\gamma) < 4.2 \cdot 10^{-13} \text{ at 90\% of CL}$$

which is the most stringent constrain on a forbidden process. A schematic representation of the new experimental apparatus is provided in Figure 4.4. In the following we give a brief explanation of each detector.

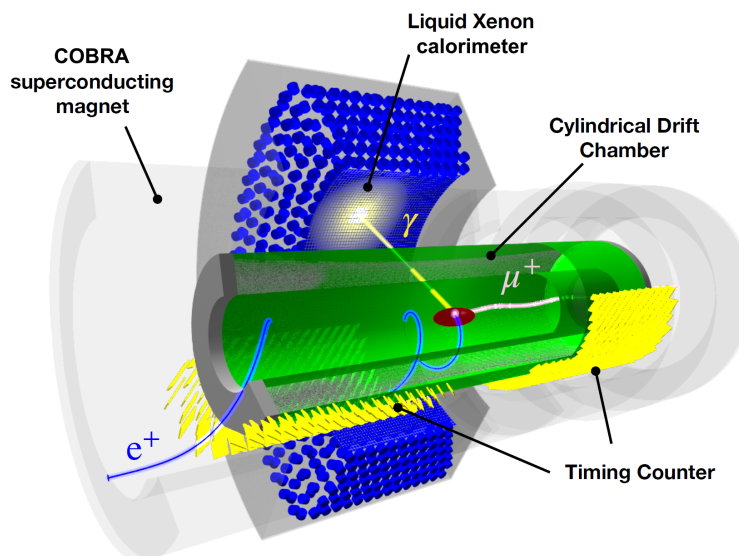


Figure 4.4 Schematic representation of the new MEG II experiment [4].

4.2.1 Signal and background

Since the incoming muons are stopped in a thin target, the signal $\mu^+ \rightarrow e^+\gamma$ is a simple two-body decay. Hence, the positron and the photon are emitted back-to-back ($\theta_{e\gamma} = 180^\circ$) in the center-of-mass frame and at the same time ($t_{e\gamma} = 0$). The energy of both particles is monochromatic, specifically

$$E_e = \frac{m_\mu^2 + m_e^2}{2m_\mu} \simeq \frac{m_\mu}{2} \quad E_\gamma = \frac{m_\mu^2 - m_e^2}{2m_\mu} \simeq \frac{m_\mu}{2} \quad (4.1)$$

The expected number of signal events N_{sig} depends on the rate of decaying muons R_μ , the data acquisition time T and the efficiency in the signal detection ϵ_{sig} . Specifically

$$N_{sig} \propto R_\mu \times T \times \epsilon_{sig} \quad (4.2)$$

In searching for $\mu^+ \rightarrow e^+\gamma$ we need to consider two different types of background events: the muon radiative decay $\mu^+ \rightarrow e^+\nu_e\bar{\nu}_\mu$ (*prompt* background) and the muon standard decay $\mu^+ \rightarrow e^+\nu_e\bar{\nu}_\mu$ with an overlapping photon (*accidental* background). The radiative muon decay (RMD) imitates the signal when the neutrino pair carries away a little amount of energy. However, this decay is generally neither back-to-back nor monochromatic. On the other hand, as for the signal, the positron and the photon are emitted at the same time (hence the adjective *prompt*) and position. In the accidental background the photon is not emitted together with the positron, but comes from an overlap of a separate event. These accidental photons are originated by bremsstrahlung or positron in-flight annihilation (AIF), as well as by the overlap with a RMD event featuring an high-energy photon. The accidental background events can be distinguished from the signal mainly due to the lack of temporal coincidence and of a common vertex between the positron and the photon.

4.2.2 Beamline and target

The 28 MeV/c antimuons provided by the $\Pi E5$ channel are delivered to the stopping target through a beam transport system, depicted in Figure 4.5.

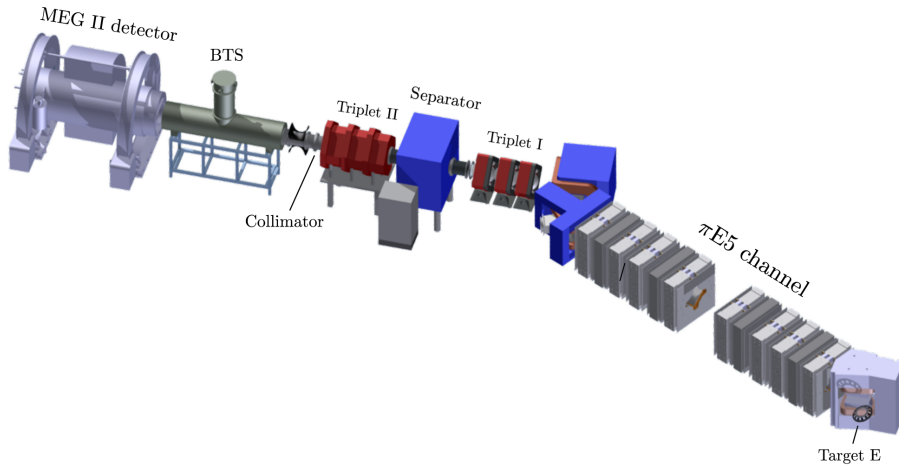


Figure 4.5 Schematic representation of the MEG II beam transport system [139].

The first part is composed of two quadrupole magnet triplets with a cross-field separator in the middle. The two quadrupole triplets focus the beam before and after entering the separator, which applies perpendicular electric and magnetic fields to clean the muon beam

from the positron contamination. After being refocused by the second quadrupole triplet, the muons are brought to the Beam Transport Solenoid (BTS) through a collimator (cf. Figure 4.6a). The BTS transports the muon beam to the stopping target (cf. Figure 4.6b), placed in the center of the COBRA superconductive magnet. Furthermore, the BTS includes a degrader made of a $300\ \mu\text{m}$ thick MYLAR foil, which reduces the muon momentum in order to optimise the stopping efficiency of the target. In addition to the muon beam, a $70.5\ \text{MeV}/c$ negative pion beam and a $52.8\ \text{MeV}/c$ positron beam are available for calibration purposes.

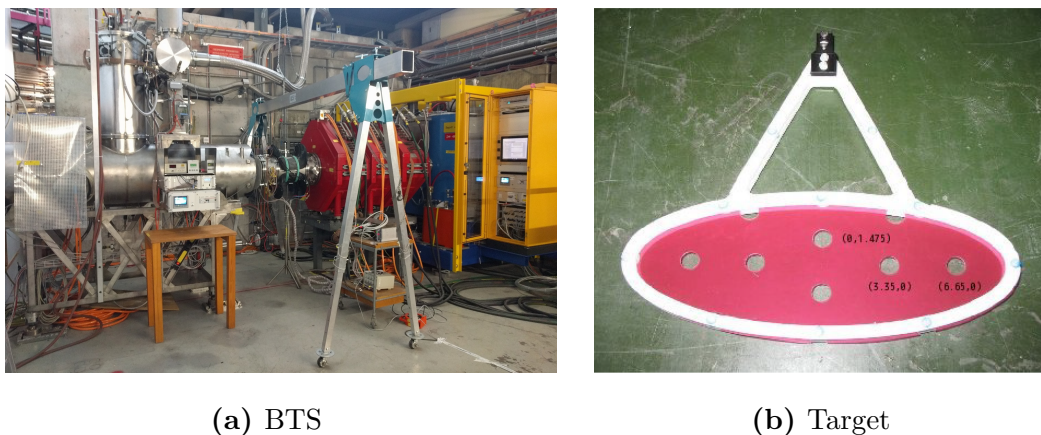


Figure 4.6 The BTS coupled to the second quadrupole triplet and the muon stopping target used by the MEG experiment [6].

The muons are stopped by a $140\ \mu\text{m}$ thick polyethylene foil. The target has two opposite requirements: a very high stopping efficiency for the muons (i.e. a sufficient amount of material) and a small multiple scattering effect on the produced particles (i.e. a short path inside the material). Both requests are satisfied by aligning the target with an angle of 15° w.r.t. the beam direction. This choice maximises the muons path inside the target and at the same minimises the path of the positrons emitted towards the spectrometer. In this way the multiple scattering on the positron trajectory is greatly reduced without sacrificing the muon stopping efficiency. The rate of stopped muons will be $7 \cdot 10^7\ \mu^+/s$.

4.2.3 Photon calorimeter

The photons are detected by a C-shaped calorimeter consisting of $900\ \ell$ of liquid Xenon (LXe) at $165\ \text{K}$, coupled to 668 PMTs and 4092 SiPMs (cf. Figure 4.7). The calorimeter is $38.5\ \text{cm}$ deep, corresponding to approximately 14 radiation lengths ($X_0 = 2.7\ \text{cm}$). The high light yield and the fast decay time of the LXe provide an excellent energy and time resolution for the signal photons. The LXe scintillation light has a peak around $178\ \text{nm}$, i.e. in the vacuum ultra-violet (VUV) region. Special VUV-sensitive PMTs and SiPMs were

developed in collaboration with the Hamamatsu Photonics company. All photosensors are directly immersed in the LXe. The SiPMs are placed throughout the inner face of the calorimeter, while PMTs are placed in throughout the outer face and on the sides. This solution further increases the resolution on the photon observables. The energy resolution for a signal-like photon is around 1%. A typical example of gamma event is provided in Figure 4.8.

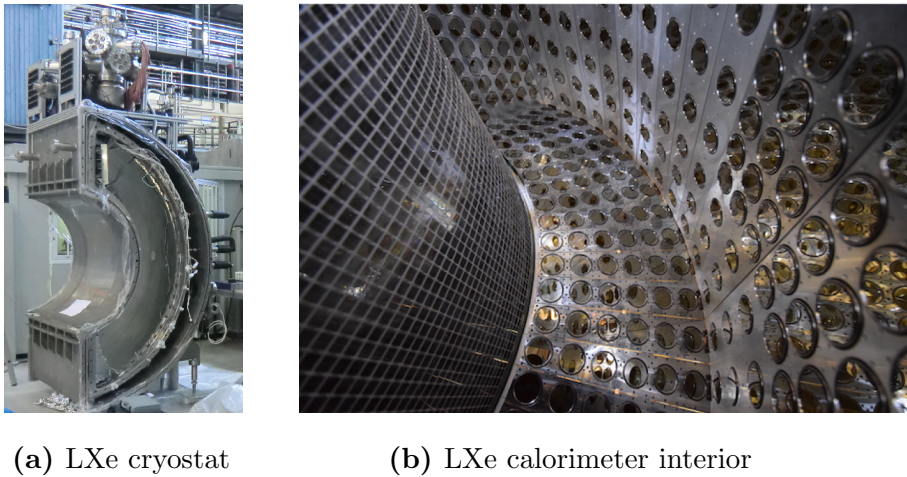


Figure 4.7 The cryostat and the interior of the LXe calorimeter [4].

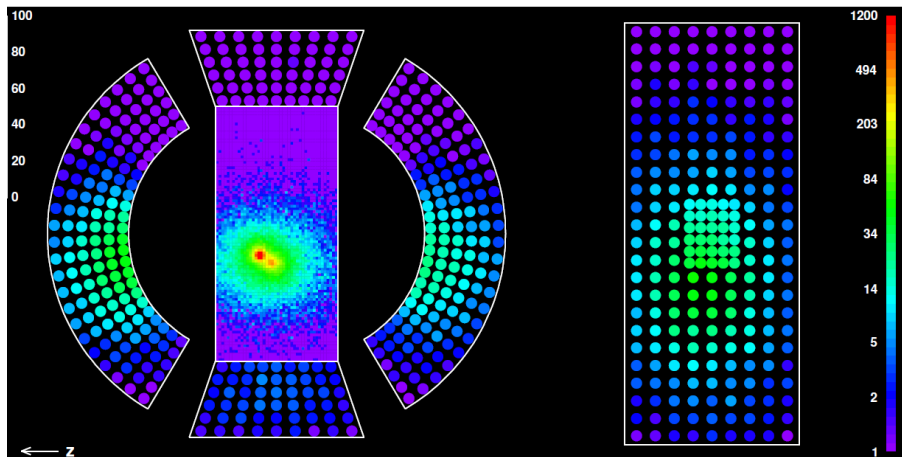


Figure 4.8 Distribution of scintillating light detected by the LXe calorimeter photosensors in a simulated $\mu \rightarrow e\gamma$ event [4].

4.2.4 Positron spectrometer

The MEG II positron spectrometer consists of three different elements:

- (1) The COntant Bending RAdius (COBRA) magnetic field.
- (2) The Cylindrical Drift CHamber (CDCH) for the precise measurement of the muon decay vertex and the positron momentum.
- (3) The pixelated Timing Counter (pTC) for the precise measurement of the positron time of flight (TOF).

Magnetic field

The COBRA magnet is a superconducting solenoid with a gradient along the beam direction, specifically developed for the MEG experiment. In order to produce the longitudinal gradient, the magnet consists of five coils with the three different radii. Additionally, two compensation coils reduce the stray magnetic field to protect the PMTs inside the LXe calorimeter. Otherwise, the gain of each PMT would be reduced of a factor 50 w.r.t. a null magnetic field. The produced magnetic field ranges from 1.27 T at the center to 0.49 T at the sides. A map of the magnetic field is provided in Figure 4.9.

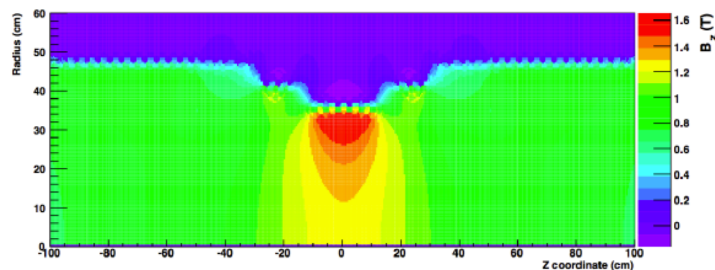


Figure 4.9 Magnetic field produced by the COBRA magnet [6].

The positrons produced in the target are swept away by the magnetic field gradient after a few revolutions inside the spectrometer, regardless of their emission angle (cf. Figure 4.10). Thus, only high momentum positrons can enter the CDCH and the pTC. This unique feature reduces the pile-up effect in the two detectors, as well as enhancing the signal-background ratio in the signal region.

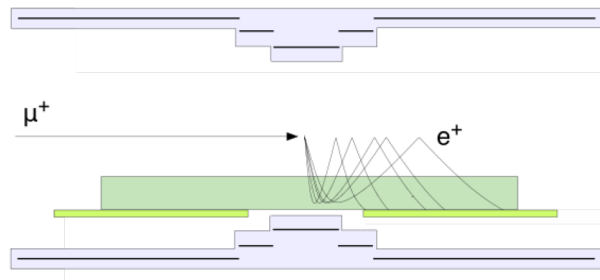


Figure 4.10 Effect of the COBRA magnetic field on a signal-like positron [4].

Drift chamber

The positron momentum and the muon decay position are precisely measured by the CDCH, a single-volume cylindrical drift chamber with a length of 193 cm along the beam direction (cf. Figure 4.11). It consists of multiple-planes of anode and cathode wires in a stereo configuration. The total number of wires is 13056, while the number of drift cells amounts to 1728, arranged in 9 concentric layers. The chamber volume is filled with a very low mass gas mixture (90% Helium, 10% Isobutane) to minimise the multiple scattering of positrons. The high granularity of the drift cells and the very low radiation length per track turn ($1.58 \cdot 10^{-3} X_0$) allow a single hit resolution below $120 \mu\text{m}$, a momentum resolution of $100 - 130 \text{ keV}/c$ and an angular resolution of about 5 mrad .

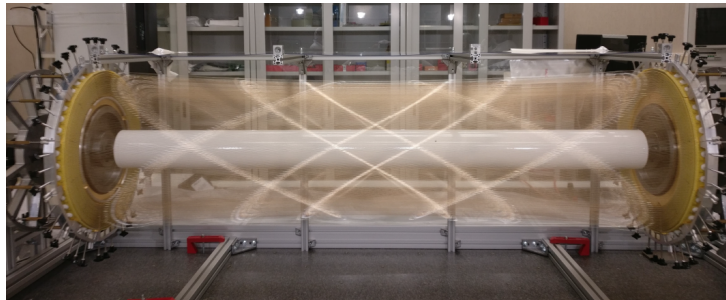
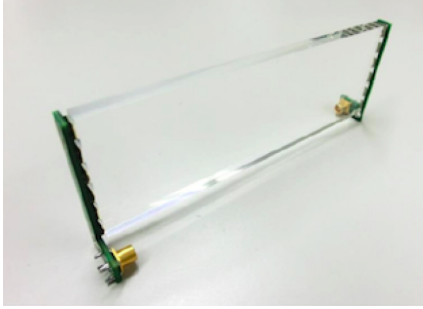


Figure 4.11 The open CDCH with all wires [4].

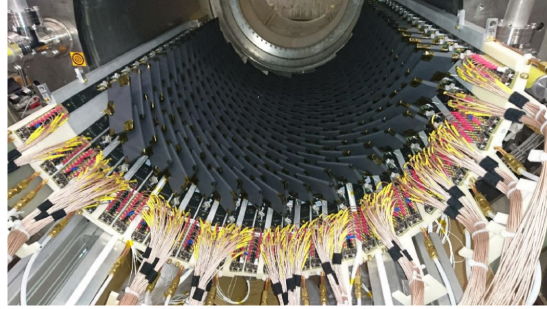
Timing counter

The CDCH cannot provide a precise measure of the positron emission time, indispensable to efficiently reject the accidental background. Thus, the positron time is precisely measured

by the pTC, consisting of 512 plastic scintillator tiles, arranged as shown in Figure 4.12 and positioned outside the CDCH volume. Depending on their longitudinal position, the dimension of a tile is $100 \times 40 \times 5 \text{ mm}^3$ or $100 \times 50 \times 5 \text{ mm}^3$. The scintillation light is collected at both ends by an array of SiPMs. The time resolution of each tile is around 60-70 ps. For 9 hit tiles, the average number for a signal-like positron, the resolution increases to approximately 30 ps.



(a) Individual tile



(b) Assembled tiles

Figure 4.12 A pTC tile coupled to the two SiPMs arrays and the assembled detector [4].

Chapter 5

Search for $\mu \rightarrow eX$ with MEG II

5.1 MEG II beyond $\mu \rightarrow e\gamma$

The MEG II experiment is designed to search for $\mu^+ \rightarrow e^+\gamma$ as precisely as possible. Nevertheless, the experimental apparatus appears to be competitive in searching for more exotic muon decays, in which the lepton flavour violation is mediated by the invisible axion-like particle X . Since the MEG II detectors provide a state-of-art reconstruction of low-energy positrons and photons ($E_e, E_\gamma \sim 50$ MeV), the suitable processes are substantially three: the two-body decay $\mu^+ \rightarrow e^+X$, the radiative decay $\mu^+ \rightarrow e^+X\gamma$ and the double decay $\mu^+ \rightarrow e^+X \rightarrow \gamma\gamma$. The search for these processes is an unique opportunity for MEG II to complement the main search for $\mu^+ \rightarrow e^+\gamma$ with additional competitive physics channels. Hence, the corresponding sensitivities need to be estimated, in order to quantitatively assess the feasibility of each channel.

The decay $\mu^+ \rightarrow e^+X \rightarrow \gamma\gamma$ was recently searched using the full dataset of the previous MEG experiment [140, 141]. Although no significant excess was found, the investigation allowed the MEG collaboration to set the most stringent upper limit on the signal BR. To this end, several assumptions on the mass and lifetime of the particle X were considered. Since MEG II is a direct upgrade of the MEG experiment, this result is a strong indication on the competitiveness of the new apparatus in searches related to the invisible particle X .

In this chapter, we focus on the feasibility of searching for $\mu^+ \rightarrow e^+X$ with the MEG II positron spectrometer. The search for such an elusive signal is certainly subtle. On the other hand, the MEG II spectrometer allows a very accurate measurement of the high-energy region of the positron spectrum, as we will show in the following.

The search for $\mu^+ \rightarrow e^+X$ is significantly disadvantaged, having only one detectable particle. Assuming that muons decay at rest, the only signature of such a decay is a monochromatic positron in the high-energy region of the spectrum. Depending on the

ALP mass m_X , the energy of the signal positron is

$$E_e^X = \frac{m_\mu^2 - m_X^2 + m_e^2}{2m_\mu} \quad (5.1)$$

which becomes simply $E_e^X \simeq m_\mu/2$ for $m_X, m_e \ll m_\mu$. A comparison between the signal energy $E_e^X(m_X)$ and the nominal acceptance of the MEG II positron spectrometer is provided in Figure 5.1. The COBRA magnetic field prevents the low-energy positrons from reaching the active region of the CDCH. This feature greatly enhances the signal-background ratio for $m_X \ll m_\mu$, in addition to decrease the dead-time and pile-up effects. On the other hand, this makes the spectrometer insensitive to $\mu^+ \rightarrow e^+X$ events with $m_X > 40$ MeV.

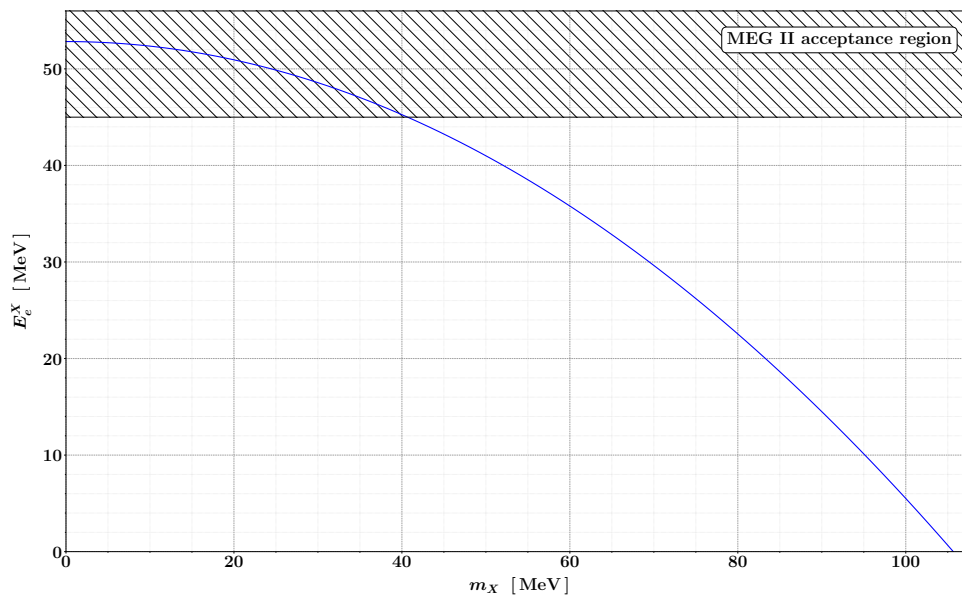


Figure 5.1 Relation between the positron energy and the ALP mass for $\mu \rightarrow eX$.

As already discussed in Chapter 3, the signal is no longer exactly monochromatic at NLO, due to the energy carried away by the undetectable soft photons. Nevertheless, the NLO positron spectrum increases very quickly in the limit $E_e \rightarrow E_e^X$, at which it reaches the maximum value. Hence, we can continue to identify the signal energy with E_e^X , implying the presence of a smooth radiative tail for $E_e < E_e^X$.

5.2 MC event generator

The first step is to implement a new positron MC generator into the MEG II analysis software `meg2`, both for $\mu \rightarrow e\nu\bar{\nu}$ and $\mu \rightarrow eX$. The goal is to update the simulation framework to the theoretical predictions computed in the previous chapters, replacing the former implementation of $\mu \rightarrow e\nu\bar{\nu}$ at NLO and $\mu \rightarrow eX$ at LO. The `meg2` code is mostly written in C++ and it is based on ROME, a multi-purpose ROOT-based framework developed by the MEG collaboration [40]. The software is organised in three main modules: `gem4`, `bartender` and `analyzer`.

gem4: It is dedicated to the event generation and the simulation of the detector response. Thus, the new MC event generator need to be implemented into this module. The passage of particles through matter is simulated using the GEANT4 toolkit [142]. The CDCH drift lines are specifically simulated through the GARFIELD toolkit for gaseous detectors [143]. The output, generated in the ZEBRA format [144], is read by the `bartender` module.

bartender: It is dedicated to the simulation of the TDAQ system. It also manages the mixing of different kinds of events, in order to simulate the pile-up effect due to multiple muon decays within the same TDAQ time window. The output, containing all the simulated variables, is organised in a `sim.root` file and read by the `analyzer` module.

analyzer: It is dedicated to the online and offline data analysis. It contains all the routines for the event reconstruction, selection and display. Notably, the positron tracks are fitted by using the GENFIT [145] implementation of the Kalman filter technique [146–148]. The output, containing all the reconstructed variables with the corresponding uncertainties, is organised in a `rec.root` file.

As already done in the previous chapters, we parametrise the muon polarisation vector as

$$n_0 = n_\mu (0, 0, 0, 1) \quad -1 \leq n_\mu \leq 1$$

and the positron 4-momentum as

$$q_1 = (E_e, q_e \sin \theta_e \cos \phi_e, q_e \sin \theta_e \sin \phi_e, q_e \cos \theta_e) \quad E_e^2 = m_e^2 + q_e^2$$

where $0 \leq \theta_e \leq \pi$ and $-\pi \leq \phi_e \leq \pi$. However, since the muons are supposed to decay at rest inside the stopping target, the center-of-mass frame and the laboratory frame are distinguished by a trivial translation of the origin, given by the decay vertex. The MEG II conventional frame of reference is depicted in Figure 5.2. We imply the use of this frame throughout the chapter.

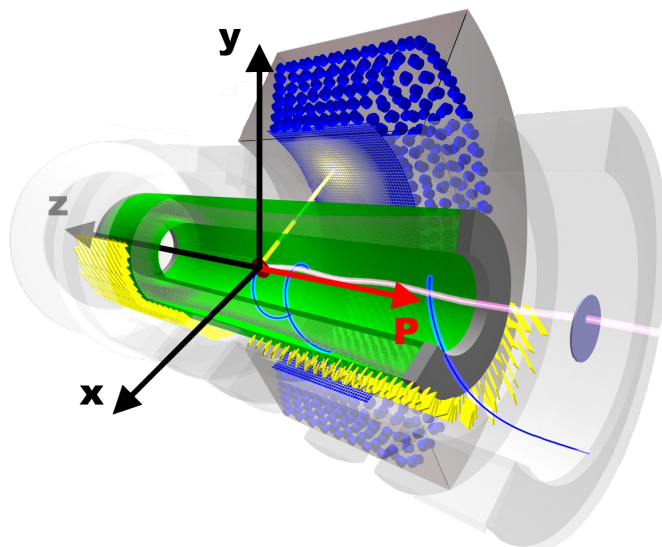


Figure 5.2 Conventional frame of reference of the MEG II experiment. The origin is defined at the center of the muon target. The x -axis points towards the center of the positron spectrometer, while the z -axis is oriented along the muon beam direction. The muon polarisation vector (red arrow) is therefore oriented backward respect to the z -axis.

To generate exhaustive positron events from polarised muons, all we need is the double-differential decay width

$$\mathcal{G}_e(E_e, \cos \theta_e) \equiv \frac{1}{\Gamma_0} \frac{d^2\Gamma}{dE_e d\cos \theta_e} = f(E_e) + n_\mu \cos \theta_e g(E_e) \quad (5.2)$$

computed for the background $\mu \rightarrow e\nu\bar{\nu}$ up to NNLO+LL and for the signal $\mu \rightarrow eX$ up to NLO, respectively in Chapter 2 and 3. We recall that the positron energy E_e was discretised according to the bins reported in Table 2.1, in order to evaluate the two decay functions $f(E_e)$ and $g(E_e)$ numerically. However, in the acceptance region ($E_e > 45$ MeV) the resolution of the MEG II positron spectrometer is expected to be much bigger than the bin width: 90–130 keV against 2–4 keV. Thus, the finite size of the bins has no effect on the distribution of the reconstructed variables, as it can be verified a posteriori by varying the bin width. Accordingly, we treat the energy as a discrete random variable and the two spherical angle θ_e and ϕ_e as continuous random variables.

The implemented algorithm can be summarised as follows.

- (1) The decay vertex is generated by intersecting two conditions:
 - (a) The muons come from a symmetric Gaussian beam, generated by using the Box-Muller method. The beam width is set to 10 mm, according to the beam

profile measurements performed at the COBRA center.

- (b) The muons decay at rest inside the MEG II target. We recall that the angle between the incoming muon beam and the target surface is 15° , in order to maximise the stopping efficiency and minimise the multiple scattering effect on the decay products.

From a geometrical point of view, the two previous conditions define the vertex distribution over the target surface. The depth of the decay is determined in a second moment by simulating the interactions between the incoming muons and the target material through GEANT4.

- (2) The positron energy E_e is generated through the inverse transform sampling method, using the normalised isotropic function $f(E_e)$ as discrete probability distribution. In this regard, we recall that the positron energy spectrum over the entire solid angle is independent on the muon polarisation and equal to $2f(E_e)$. Thus, the two functions coincide after being normalised to one.
- (3) The azimuthal angle ϕ_e of the positron momentum is generated according to an uniform distribution extended within the interval $[-\pi, \pi]$.
- (4) The distribution of the polar angle θ_e is determined by

$$t(\theta_e) \equiv f(E_e) + n_\mu \cos \theta_e g(E_e)$$

where E_e is fixed to the previously generated value. Hence, we generate $\cos \theta_e$ as a continuous variable extended within the interval $[-1, +1]$, by inverting the linear distribution $t(\cos \theta_e)$ after being normalised to one. To solve the ambiguity $\cos(\theta_e) = \cos(-\theta_e)$, the sign of the angle is generated afterwards.

The algorithm can be optimised by generating the positrons only in the nominal acceptance region of the spectrometer, i.e.

$$E_e > 45 \text{ MeV} \quad |\cos \theta_e| < 0.35 \quad |\phi_e| < \pi/3$$

This is easily achieved by shrinking the bounds of the various distributions. In this regard, we note that as long as we constrain the positron generation in a region given by

$$|\cos \theta_e| < a \quad \text{with} \quad a \leq 1$$

the energy spectrum is proportional to $f(E_e)$. To constrain the event generation in a region like

$$b < \cos \theta_e < c \quad \text{with} \quad b \neq -c$$

the positron energy need to be generated according to the function

$$h(E_e) \equiv f(E_e) + n_\mu g(E_e) \int_b^c d\cos\theta_e \cos\theta_e = f(E_e) + \frac{1}{2}(c^2 - b^2) n_\mu g(E_e) \quad (5.3)$$

which is proportional to the energy spectrum in the given region. Since an energy spectrum is always greater than or equal to zero, the function $h(E_e)$ can be used as a probability distribution after a proper normalisation. Concretely, the generator is implemented in C++ into the two files:

- `GEMMichelPositronGenerator.cc` (for $\mu \rightarrow e\nu\bar{\nu}$)
- `GEMMajoronPositronGenerator.cc` (for $\mu \rightarrow eX$)

both linked to the `gem4` module. The required input parameters are:

- The muon polarisation n_μ
- The number of $\mu \rightarrow e\nu\bar{\nu}$ events to generate
- The number of $\mu \rightarrow eX$ events to generate
- The ALP mass m_X and couplings (V, A, V-A, V+A)
- The minimum positron energy to be generated
- The bounds on $\cos\theta_e$ and ϕ_e

In Figure 5.3 we show the distribution of the decay vertex on the surface of the MEG II target, as simulated through the new algorithm. The distribution is not symmetric over the surface plane, due to the 15° inclination between the target and muon beam. We also recognise the shape of the target, especially the holes used to precisely align it.

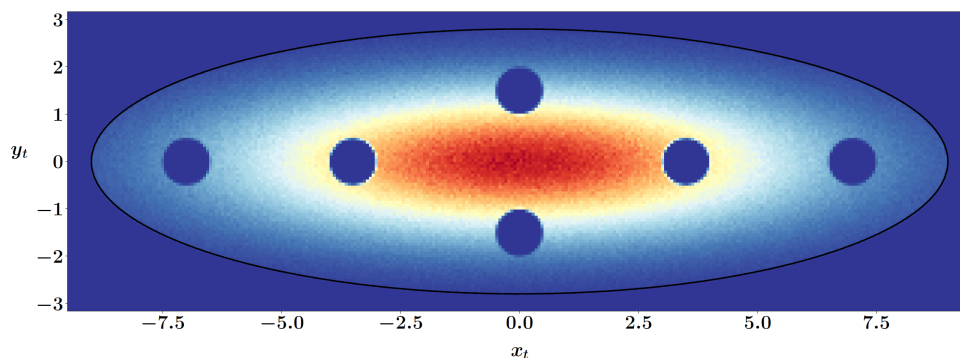


Figure 5.3 Distribution of the decay vertices on the target surface for 10^6 simulated events. The distribution is referred to the generated values, not to the reconstructed ones.

A simple way to validate the algorithm implementation is to compare the generated values with the MCMULE predictions. This is explicitly shown for the positron energy spectrum in Figure 5.4 ($\mu \rightarrow e\nu\bar{\nu}$) and Figure 5.5 ($\mu \rightarrow eX$ with $m_X = 1$ MeV). We remark that both distributions refer to the generated values, not yet to the reconstructed ones.

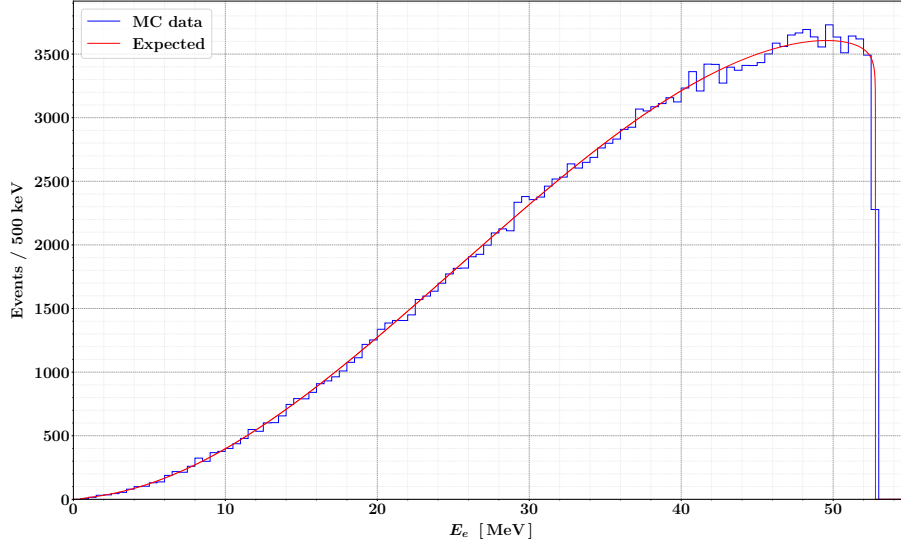


Figure 5.4 Positron energy distribution for 10^5 background events. The reduced χ^2 between the simulated distribution and the MCMULE's expectation is $\chi^2 \approx 0.96$.

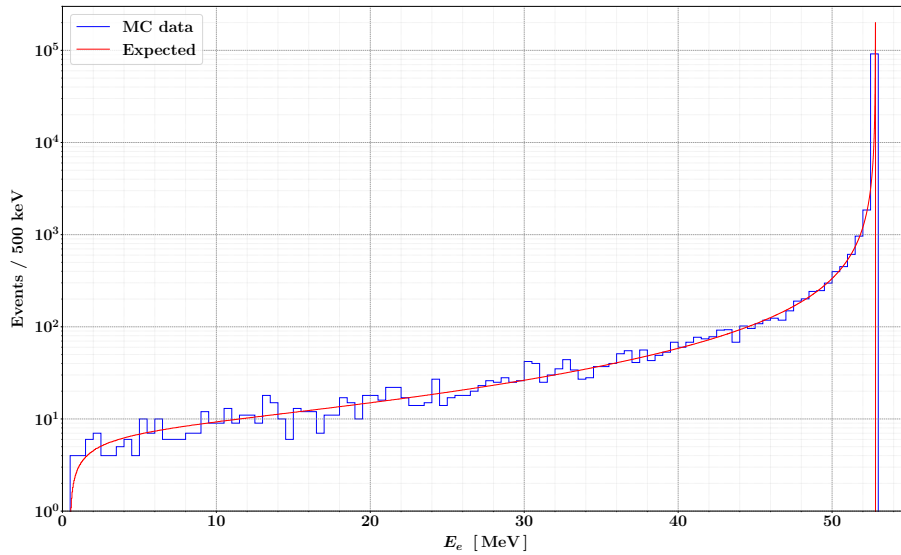


Figure 5.5 Positron energy distribution for 10^5 signal events with $m_X = 1$ MeV. The reduced χ^2 between the simulated distribution and the MCMULE's expectation is $\chi^2 \approx 1.12$.

Figure 5.6 shows the $\mu \rightarrow e\nu\bar{\nu}$ distribution in the $E_e \times \cos\theta_e$ plane for 10^5 simulated positron events. The same is done in Figure 5.7 for the signal $\mu \rightarrow eX$ ($m_X = 1$ MeV, V-A coupling). Again, both distributions refer to the generated values, not yet to the reconstructed ones. The results can be directly compared to the theoretical functions plotted in Figure 2.30 and 3.8.

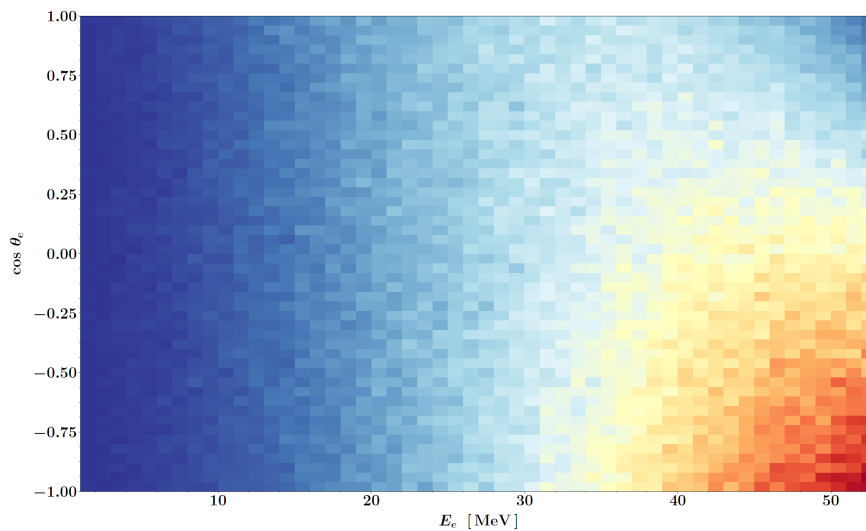


Figure 5.6 Event distribution in the $E_e \times \cos\theta_e$ plane for 10^5 $\mu \rightarrow e\nu\bar{\nu}$ entries. The muon polarisation is set to $n_\mu = -0.85$.

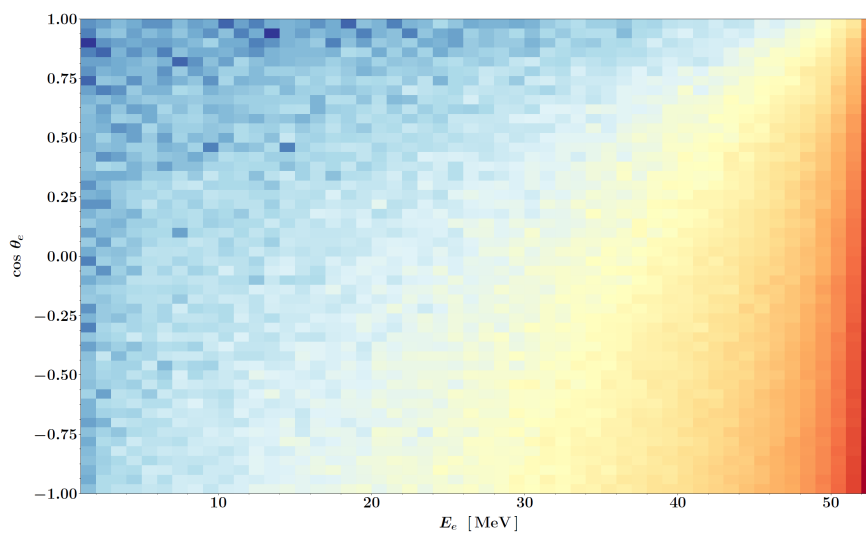


Figure 5.7 Event distribution in the $E_e \times \cos\theta_e$ plane for 10^5 $\mu \rightarrow eX$ entries ($m_X = 1$ MeV, V-A coupling, $n_\mu = -0.85$). The colour scale is logarithmic.

5.3 Positron reconstruction

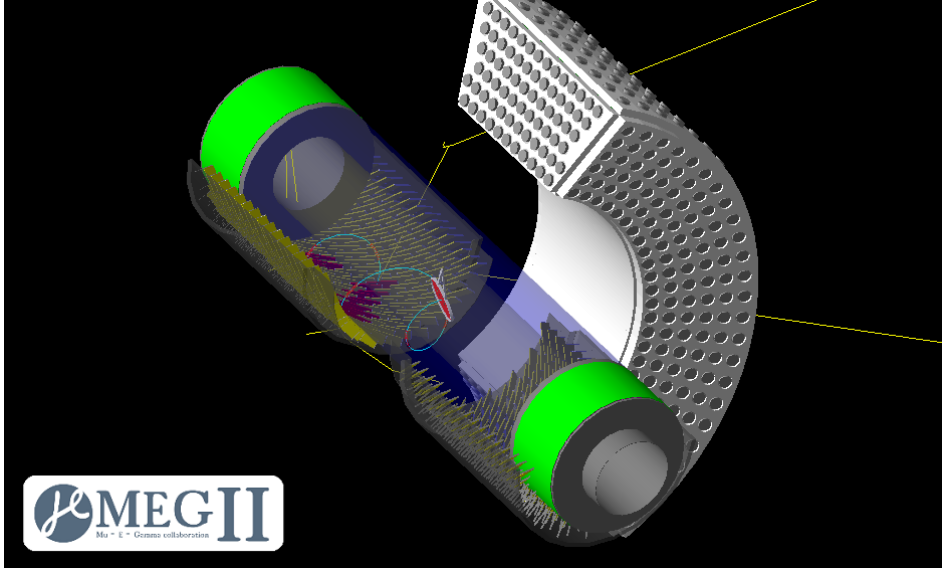


Figure 5.8 Representation of a $\mu \rightarrow eX$ event generated by `gem4`, using the new NLO code. The signal positron is depicted in cyan, while the accidental photons are drawn in yellow. The CDCH hits are highlighted in red, while the pTC hits are drawn in violet. The two accidental photons are originated by the annihilation in-flight (AIF) of the signal positron. Their formation is not relevant in searching for $\mu \rightarrow eX$.

The `meg2` software provides a complete simulation of the MEG II experiment. Hence, after the implementation of the new event generator, we can use the updated code to study the positron reconstruction (cf. Figure 5.8). However, it is certainly interesting to use the former positron generator alongside the new one. In this way, we can evaluate the effect of the new radiative corrections on the MC simulation of the positron reconstruction. The theoretical precision of both generators is summarised in Table 5.1. We imply the use of the new generator, where not otherwise specified.

Event type	MEG default	This thesis
$\mu^+ \rightarrow e^+ (\nu\bar{\nu})$	NLO	NNLO+LL
$\mu^+ \rightarrow e^+ (X)$	LO	NLO

Table 5.1 Theoretical precision achieved by `gem4` in generating $\mu \rightarrow e\nu\bar{\nu}$ and $\mu \rightarrow eX$. The former (default) implementation is compared to the new one. The particles in parentheses are not generated.

The positron reconstruction in MEG II is performed in four main steps: single-hit reconstruction, track finding, track fitting and pTC matching [4, 7]. The reconstruction chain is summarised in Figure 5.9.

Hit reconstruction: The DAQ waveforms are analysed in order to translate each positron hit into raw data, such as the signal charge and time. A first estimate of the hit position in the (x, y) -plane (perpendicular to the beam) is given by the coordinates of the hit wire. The z -coordinate (parallel to the beam) is instead estimated from the asymmetry in the charge collected by the two opposite ends of the anode wire. The time and the position of each pTC hit is reconstructed by comparing the detection time of the SiPMs placed at the opposite ends of each tile.

Track finding: The close hits are grouped into clusters, starting from the outer cells. A first estimate of the track curvature is obtained from the coordinates of the hit wires and used to search for other clusters through an iterative pattern recognition algorithm [149]. A precise estimate of the (x, y) -position of each hit is extracted from the drift time, defined as the difference between the track and hit times. The (x, y) -position of each hit is then recursively updated during the tracking process, as the track information improves.

Track fitting: The positron track is fitted by applying the Kalman filter technique, in order to measure the muon decay position and the positron momentum. The fitting procedure considers the effects on the positron trajectory due to the multiple scattering, the energy loss and the non-uniformity of the magnetic field. The first two corrections are particularly important when the positron track intersects the stopping target after the muon decay. The fitted track is propagated back to the target in order to extract the muon decay position and the positron emission angle from the intersection between the positron trajectory and the target surface.

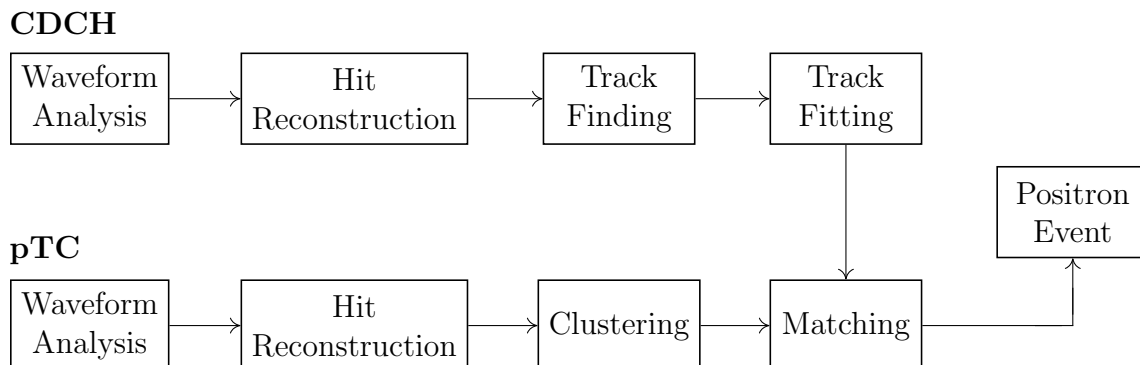


Figure 5.9 The positron reconstruction chain in MEG II.

pTC matching: The track time is refined by matching the CDCH track with the pTC hits. This information is used to recalculate the drift times and consequently further improve the track fit. The decay time is then estimated by subtracting the positron time of flight (TOF) from the pTC hit time.

In the analysis we only consider positron events that respect the following minimum requirements on the track quality. All of them are established a priori by considering the typical performances of the spectrometer.

- (1) The number of single-hits in the CDCH is at least 25.
- (2) The number of turns within the spectrometer volume is not greater than three.
- (3) The CDCH track is matched with at least one pTC hit.
- (4) The reduced χ^2 of the Kalman-fitted track is less than two.
- (5) The reconstructed emission angles θ_e^r and ϕ_e^r are included within the nominal acceptance of the spectrometer, i.e. $|\cos \theta_e^r| < 0.35$ and $|\phi_e^r| < \pi/3$.

In Figure 5.10 we show the MC-simulated positron spectrum for $\mu \rightarrow e\nu\bar{\nu}$, experimentally reconstructed by applying the procedure described above, as implemented in the `analyzer` module. The number of simulated events is $5 \cdot 10^7$, while the number of reconstructed positron is $2.4 \cdot 10^6$. Thus, the total acceptance of the spectrometer for the SM background is around 4.8%. The measured value includes the geometric acceptance of the spectrometer, the CDCH+pTC matching efficiency and the detection efficiency of both detectors. The experimental resolution on the positron energy is investigated in Section 5.4, as well as the energy dependency of the acceptance. Both are indispensable ingredients to fit the positron energy spectrum.

We emphasise that the positrons were generated over the whole solid angle and energy range, in order to evaluate correctly the global acceptance. In the following, we optimise the event generation by limiting it to the nominal acceptance region of the spectrometer (cf. Section 5.2). In this way, the number of the simulated events and the reconstructed positrons is approximately the same. This greatly increases the code performance, although it means losing all information about the total acceptance. The problem is easily solved by scaling the acceptance to the physical value reported above. In Figure 5.11 we show the endpoint region of the background spectrum, obtained by simulating $4 \cdot 10^6$ events towards the spectrometer.

Both results are compared to the MCMULE predictions, computed within the nominal acceptance region only. Since MCMULE is a fully differential framework, which allows the

definition of arbitrary cut on the physical observables, it is straightforward to limit its predictions to a certain phase-space partition.

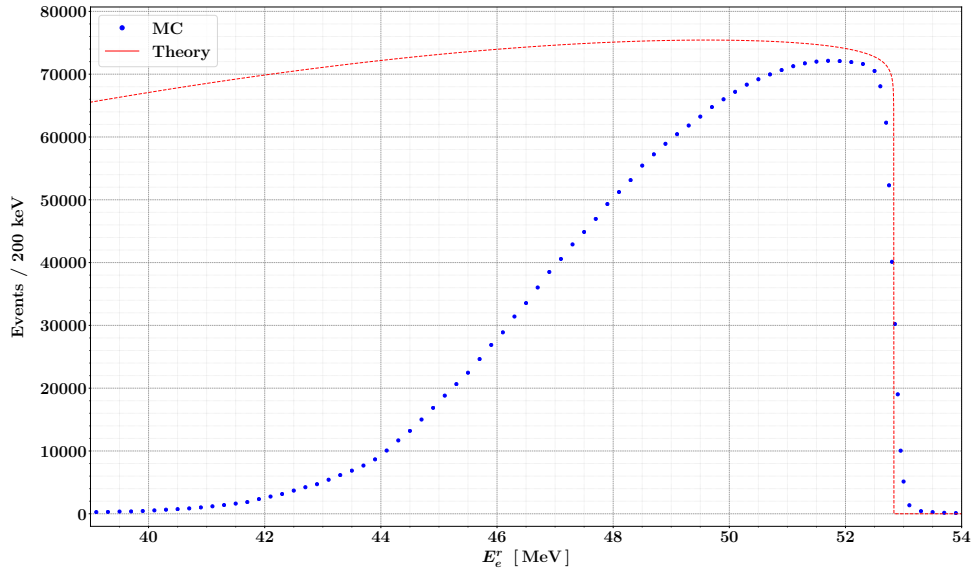


Figure 5.10 Reconstructed positron energy spectrum for $\mu \rightarrow e\nu\bar{\nu}$, obtained by simulating $5 \cdot 10^7$ events over the whole solid angle and energy range.

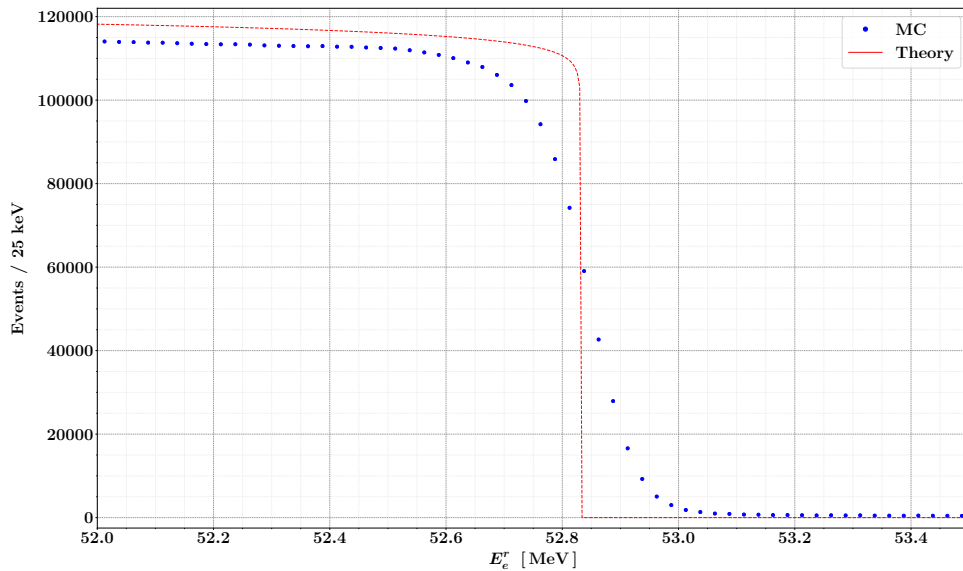


Figure 5.11 Reconstructed positron energy spectrum (endpoint region) for $\mu \rightarrow e\nu\bar{\nu}$, obtained by simulating $4 \cdot 10^6$ events towards the spectrometer.

As already mentioned, it is interesting to evaluate the effect of new radiative corrections on the reconstructed variables. In Figure 5.12 we compare the spectrum endpoint obtained by using both generators of Table 5.1. The difference between the two results is a gaussian-like peak around the theoretical endpoint, in agreement with the theoretical shape of the NNLO+LL corrections convoluted with the spectrometer response. We note that the peak corresponds to a two-body decay signal with a BR around 10^{-5} . Hence, by comparing the experimental data with the NLO simulation, the effect of the NNLO+LL corrections could have been easily confused with a $\mu \rightarrow eX$ signal for $m_X \approx 0$. This statement is consistent with Figure 3.12: the background theoretical error at NLO is too large to search for $\mu \rightarrow eX$ signals having a BR smaller than 10^{-5} , at least for low values of m_X .

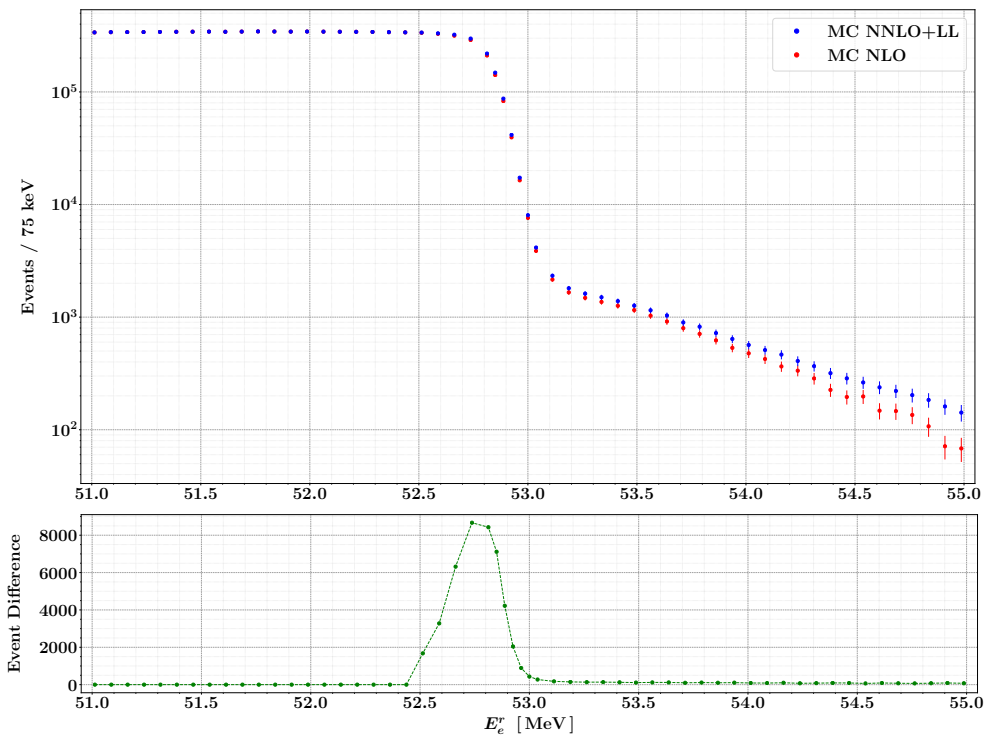


Figure 5.12 Reconstructed positron energy spectrum (endpoint region) for $\mu \rightarrow e\nu\bar{\nu}$, obtained by using both generators of Table 5.1. The number of simulated events is $3 \cdot 10^6$ for both distributions.

The results of the MC simulation for the $\mu \rightarrow eX$ signal ($m_X = 1$ MeV) is shown in Figure 5.13 and 5.14. The corresponding total acceptance is 20.4%, more than four times the value previously obtained for the background. In fact, the COBRA magnetic field prevents the positrons with $E_e \lesssim 45$ MeV from reaching the active region of the CDCH. Since the background spectrum is continuous over the whole energy range, this feature greatly enhances the signal-background ratio for sufficiently low ALP masses.

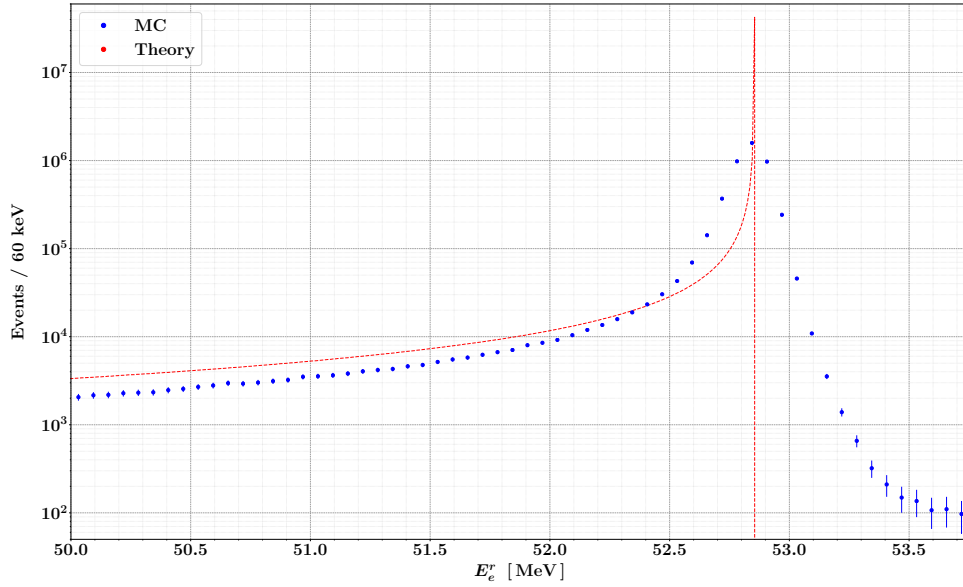


Figure 5.13 Reconstructed positron energy spectrum for $\mu \rightarrow eX$, obtained by simulating $2 \cdot 10^7$ events over the whole solid angle and energy range. The ALP mass is fixed to $m_X = 1$ MeV.

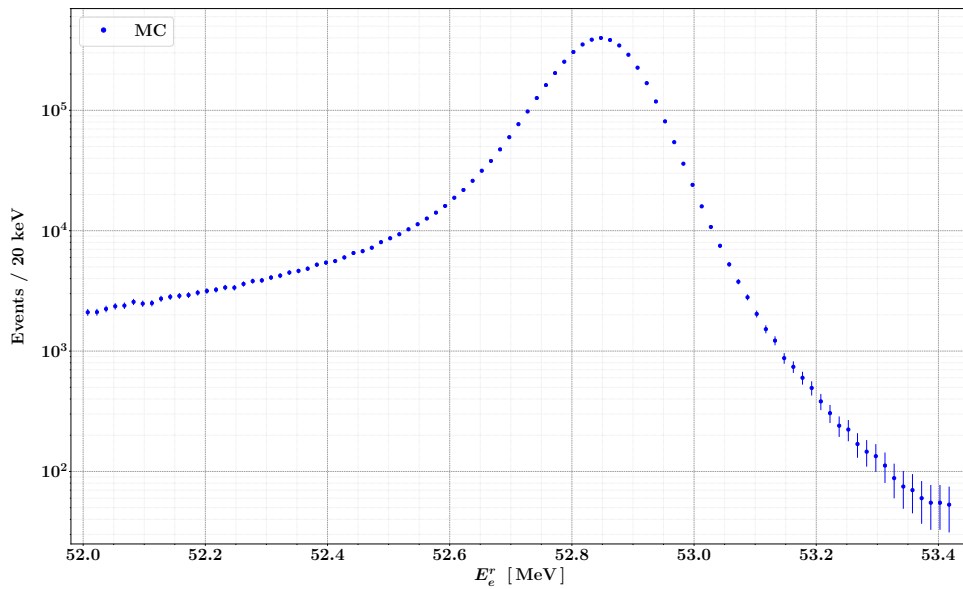


Figure 5.14 Reconstructed positron energy spectrum (endpoint region) for $\mu \rightarrow eX$, obtained by simulating $5 \cdot 10^6$ events towards the spectrometer acceptance. The ALP mass is fixed to $m_X = 1$ MeV.

In Figure 5.15, 5.16 and 5.17 we compare signal and background for different values of $\mathcal{B}(\mu \rightarrow eX)$. Again, the ALP mass is fixed to $m_X = 1$ MeV. For the sake of simplicity, the pile-up effect between signal and background events is not simulated. We note that the spectrometer response tends to spread the signal events throughout the endpoint region. Hence, the signature of $\mu \rightarrow eX$ for small values of m_X is more properly a right-shifted endpoint, rather than a visible peak emerging from the SM background, except for unrealistically high BRs. This makes the experimental search for $\mu \rightarrow eX$ even more difficult, due to the systematic uncertainties on the positron energy. In fact, even a small error in the calibration of the absolute energy scale reproduces a false $\mu \rightarrow eX$ signal close to the spectrum endpoint. We will quantify this statement in Section 5.5.

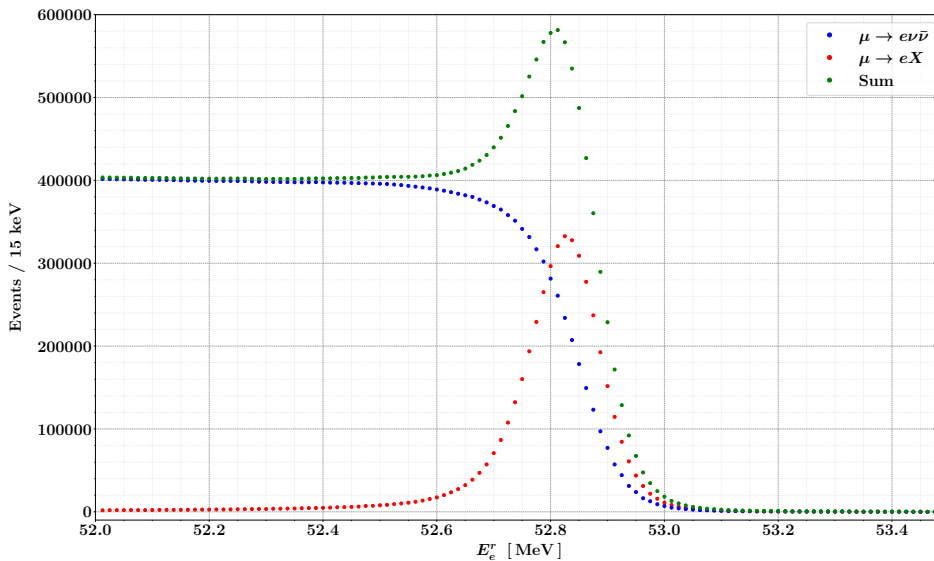


Figure 5.15 Comparison between the energy spectra of $\mu \rightarrow e\nu\bar{\nu}$ and $\mu \rightarrow eX$ for a signal BR of 10^{-3} . The ALP mass is $m_x = 1$ MeV.

In addition to the energy spectrum, it is interesting to study the reconstruction of the positron polar angle θ_e for different assumptions of signal couplings. In this way, it is possible to exploit the anisotropy induced by the muon polarisation to separate the signal from the SM background. The results are reported in Figure 5.18 (V–A) and Figure 5.19 (V+A). We note that the positrons emitted almost orthogonal to the beam ($\cos\theta_e \approx 0$) are more difficult to reconstruct. To explain it, we recall that the COBRA magnetic field features a gradient along the beam direction. Thus, the positrons are usually swept away from the spectrometer after 1-3 revolutions inside the CDCH. This unique feature provides clean positron tracks and reduces the pile-up effect in the CDCH. However, this is not true for orthogonal positrons, as they are insensitive to the longitudinal gradient. Hence, they remain stuck in the spectrometer for many revolutions, leading to very chaotic tracks, most of which are cut by the quality preselections.

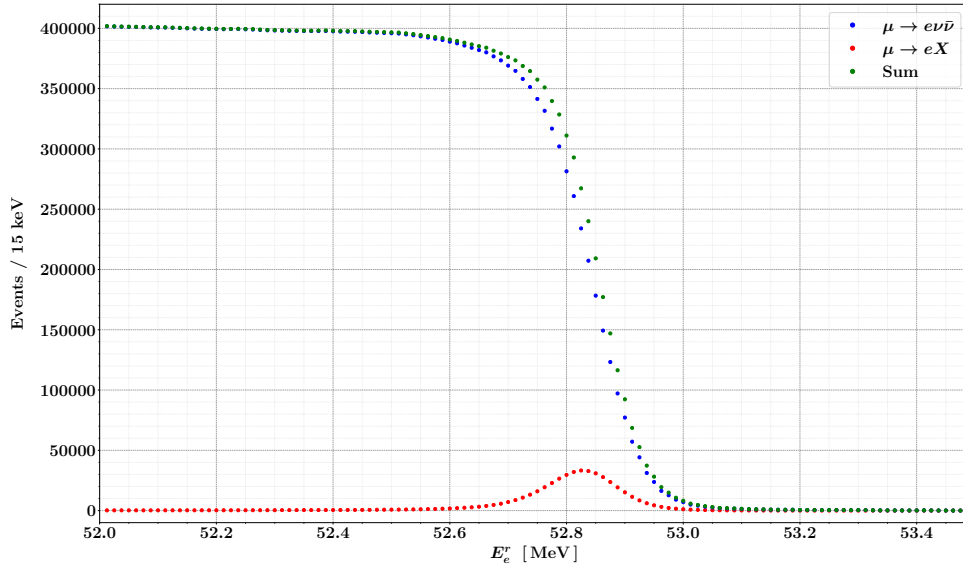


Figure 5.16 Comparison between the energy spectra of $\mu \rightarrow e\nu\bar{\nu}$ and $\mu \rightarrow eX$ for a signal BR of 10^{-4} . The ALP mass is $m_x = 1$ MeV.

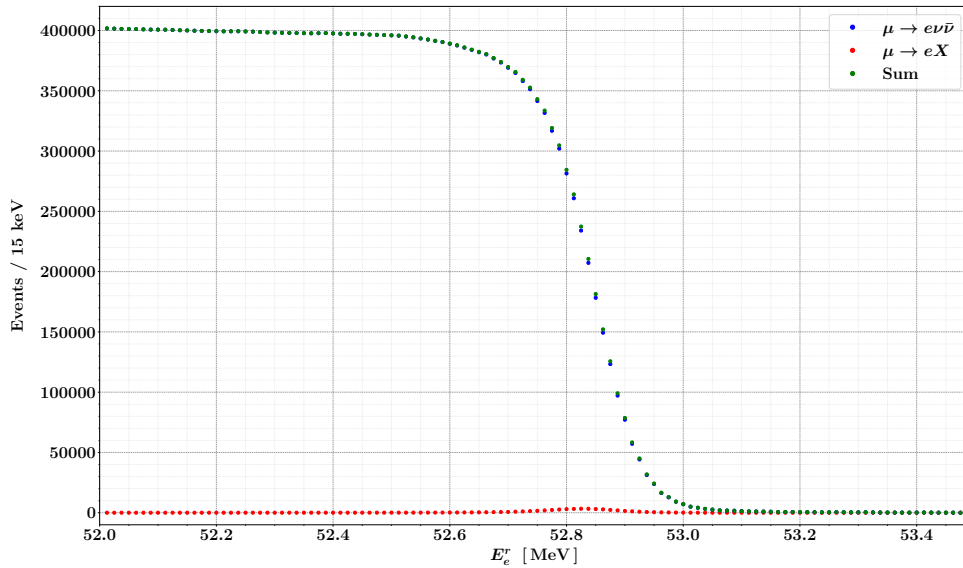


Figure 5.17 Comparison between the energy spectra of $\mu \rightarrow e\nu\bar{\nu}$ and $\mu \rightarrow eX$ for a signal BR of 10^{-5} . The ALP mass is $m_x = 1$ MeV.

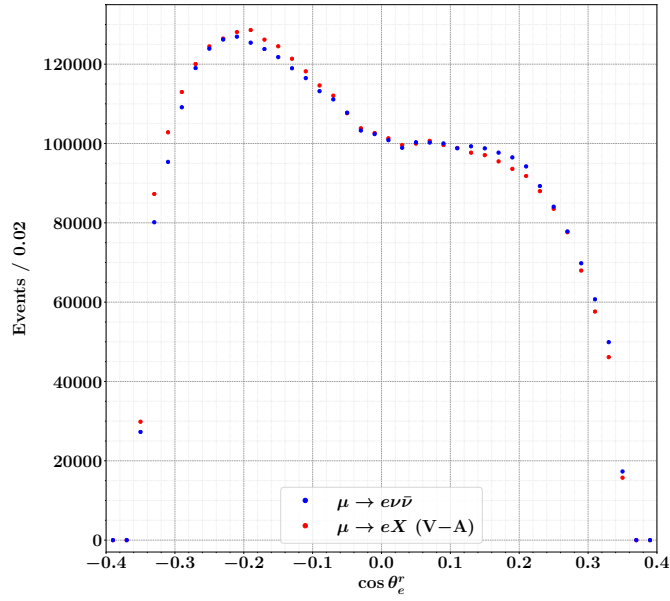


Figure 5.18 Comparison between the polar distributions of $\mu \rightarrow e\nu\bar{\nu}$ and $\mu \rightarrow eX$ ($m_X = 1$ MeV, V-A couplings) for the same number of events ($E_e^r > 50$ MeV). The muon polarisation is set to $n_\mu = -0.85$.

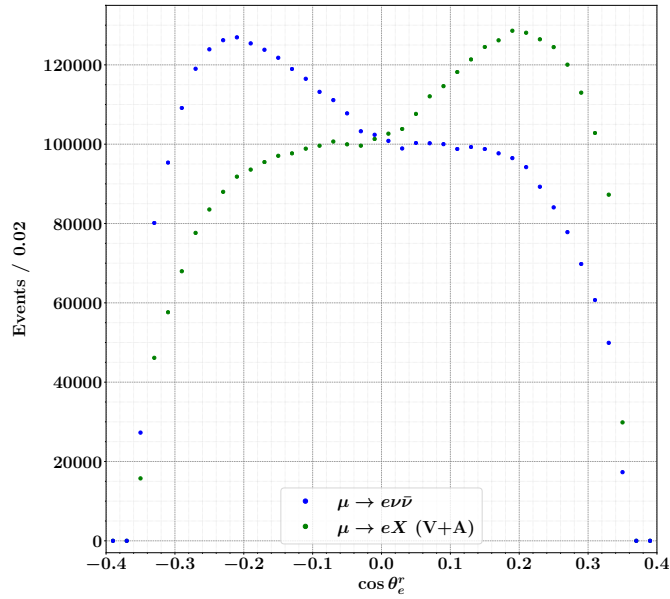


Figure 5.19 Comparison between the polar distributions of $\mu \rightarrow e\nu\bar{\nu}$ and $\mu \rightarrow eX$ ($m_X = 1$ MeV, V+A couplings) for the same number of events ($E_e^r > 50$ MeV). The muon polarisation is set to $n_\mu = -0.85$.

5.4 Positron energy spectrum

The expected energy spectrum, both for $\mu \rightarrow e\nu\bar{\nu}$ and $\mu \rightarrow eX$, can be described as

$$\mathcal{F}_e = (\mathcal{E}_e \times \mathcal{A}_e) \otimes \Sigma_e \quad (5.4)$$

where \mathcal{E}_e denotes the theoretical energy spectrum, \mathcal{A}_e the spectrometer acceptance and Σ_e the spectrometer response, convoluted to $\mathcal{E}_e \times \mathcal{A}_e$. The two functions $\mathcal{A}_e(E_e^r)$ and $\Sigma_e(E_e^r - E_e)$ can be studied explicitly in a MC simulation: $\mathcal{A}_e(E_e^r)$ corresponds to the ratio between the number of reconstructed and simulated events at $E_e = E_e^r$, while $\Sigma_e(E_e^r - E_e)$ corresponds to the distribution of the variable $E_e^r - E_e$. We recall that E_e denotes the simulated positron energy, while E_e^r the measured one. The result obtained for $\mathcal{A}_e(E_e^r)$ from the MC simulation of $\mu \rightarrow e\nu\bar{\nu}$ is shown in Figure 5.20.

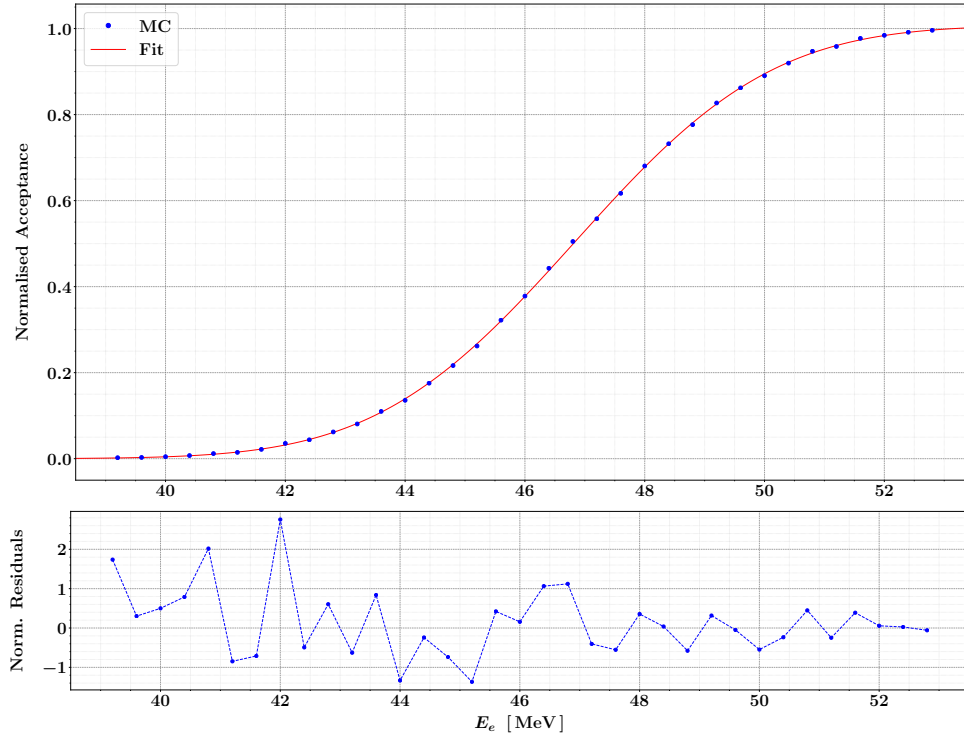


Figure 5.20 Spectrometer acceptance for $\mu \rightarrow e\nu\bar{\nu}$ as a function of the positron energy. The acceptance is normalised to one for $E_e = 52.83$ MeV.

The numerical result is fitted using the error function

$$\mathcal{A}_e(E_e) = A_1 \int_{-\infty}^{E_e} dx e^{-(x-A_2)^2/A_3^2} \quad (5.5)$$

The result is

$$A_1 = 0.3209(5) \quad A_2 = 46.833(9) \text{ MeV} \quad A_3 = 3.68(1) \text{ MeV} \quad \chi^2 \approx 1.12$$

The result obtained for $\Sigma_e(E_e^r - E_e)$ from the MC simulation of $\mu \rightarrow e\nu\bar{\nu}$ is shown in Figure 5.21. The employed fit function is a sum of three independent gaussian

$$\Sigma_e(E_e^r - E_e) = \sum_{i=1}^3 B_i e^{-(E_e^r - E_e - C_i)^2 / D_i^2} \quad (5.6)$$

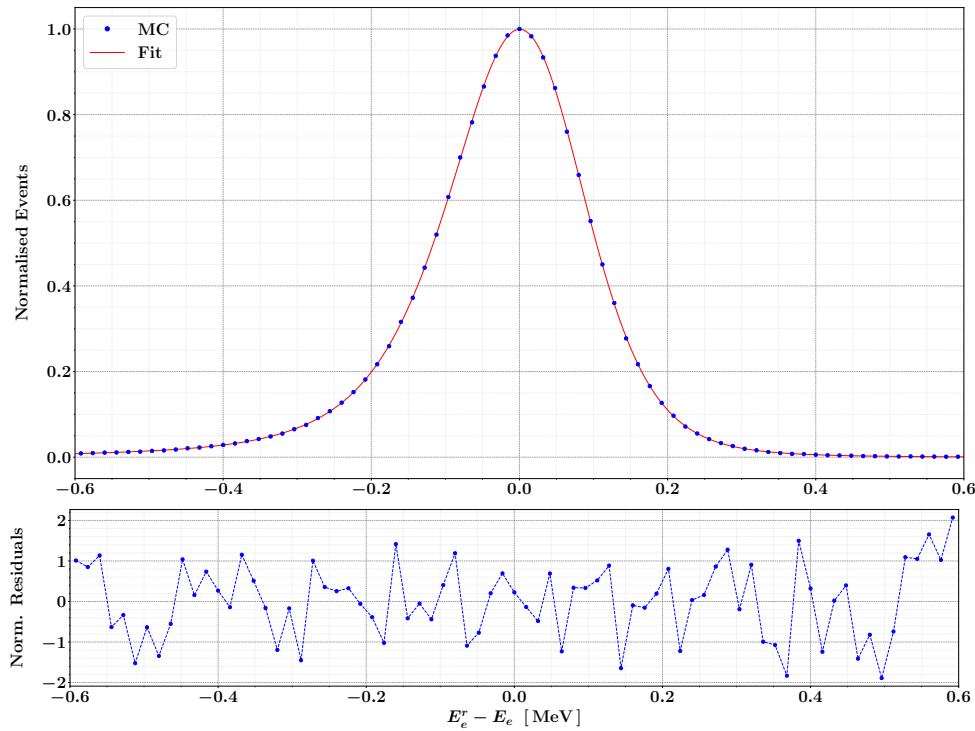


Figure 5.21 Distribution corresponding to the difference between the reconstructed and simulated positron energy for $\mu \rightarrow e\nu\bar{\nu}$. The maximum bin content is normalised to one.

We define the spectrometer resolution $\bar{\sigma}$ as the weighted average of the three standard deviations

$$\bar{\sigma} \equiv \frac{D_1 B_1 + D_2 B_2 + D_3 B_3}{B_1 + B_2 + B_3} \quad (5.7)$$

In particular, the fit returns

$$\bar{\sigma} = 100.76(2) \text{ keV} \quad \chi^2 \approx 1.07 \quad (5.8)$$

We are now ready to fit the positron spectrum using the function $\mathcal{F}_e(E_e^r)$ directly. To this end, we employ the discussed models for $\mathcal{A}_e(E_e^r)$ and $\Sigma_e(E_e^r - E_e)$, using E_e as integration variable in the convolution. In this regard, we note that $\mathcal{A}_e(E_e^r)$ and $\Sigma_e(E_e^r - E_e)$ can separately fitted only for MC data, because the simulated energy E_e is required in the procedure. The previous fits allowed to construct reliable models for the spectrometer acceptance and resolution, but cannot be applied to real data. Instead, by directly fitting $\mathcal{F}_e(E_e^r)$, the simulated energy E_e is integrated out by the convolution. To account for the theoretical spectrum $\mathcal{E}_e(E_e^r)$, the fit routine is directly linked to the corresponding MCMULE's results. The fit result for the background energy spectrum is shown in Figure 5.22, while the result for the signal energy spectrum ($m_X = 1$ MeV) is shown in Figure 5.23.

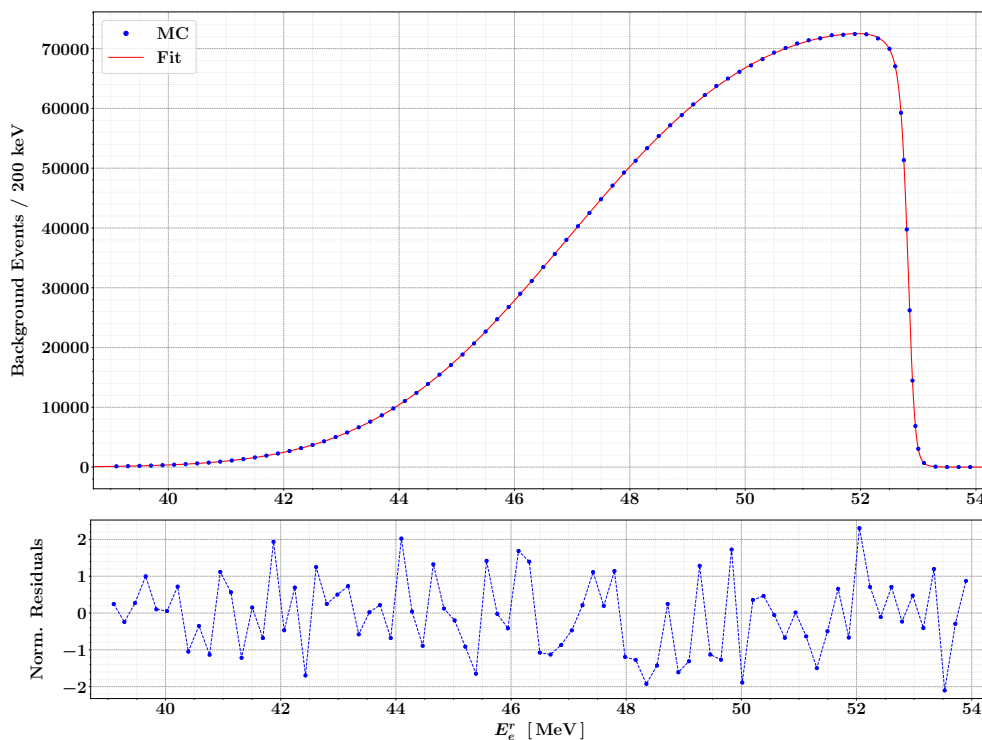


Figure 5.22 Fit of the expected energy spectrum for the background $\mu \rightarrow e\nu\bar{\nu}$ for $4 \cdot 10^6$ events. In particular, we obtain $\bar{\sigma}_b = 100.72(3)$ and $\chi^2 \approx 1.18$.

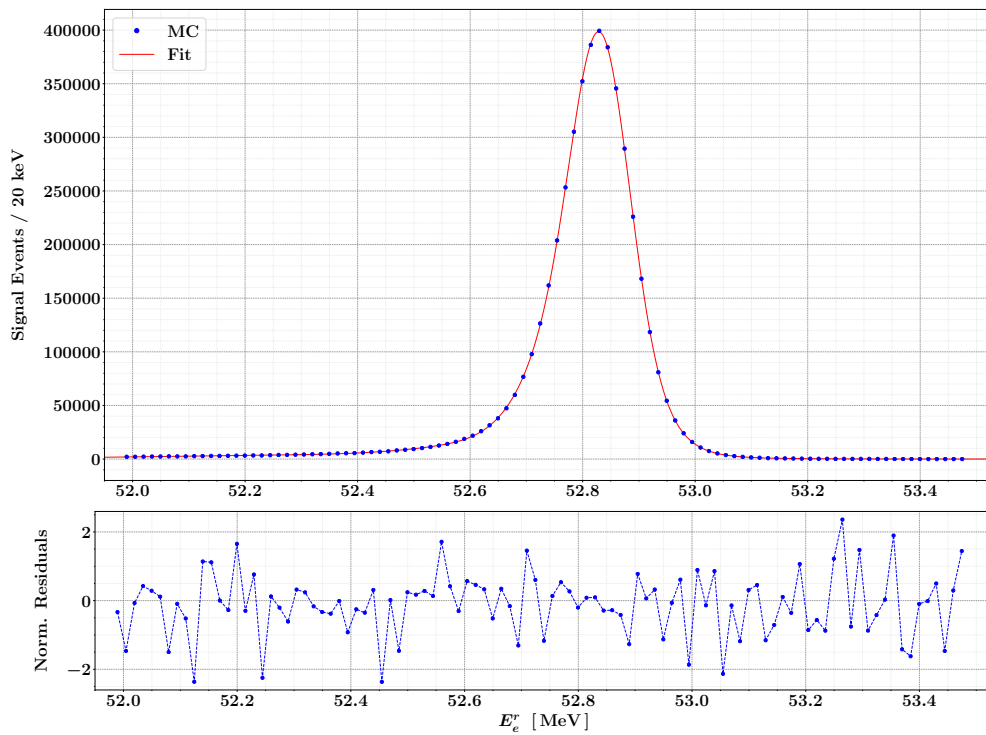


Figure 5.23 Fit of the expected energy spectrum for the signal $\mu \rightarrow eX$ ($m_X = 1$ MeV) for $5 \cdot 10^6$ events. In particular, we obtain $\bar{\sigma}_s = 100.01(2)$ and $\chi^2 \approx 1.03$.

5.5 Expected sensitivity

5.5.1 Statistics

The experimental sensitivity can be estimated from the signal and background probability density functions (PDFs) through a simple *cut-and-count* approach. Considering the positron energy spectrum, we define a *signal bin* centred in $E_e^X(m_X)$ and having a width $\pm 1.64 \bar{\sigma}_s(m_X) \approx 175$ keV, where $\bar{\sigma}_s(m_X)$ denotes the signal energy resolution for a given ALP mass m_X . The signal and background PDFs are estimated by normalising to one the corresponding spectrum fits (cf. Figures 5.22 and 5.23). Approximating the spectrometer response function to a Gaussian distribution with standard deviation $\bar{\sigma}_s(m_X)$, we obtain a bin efficiency of about 90%. The precise bin efficiency is evaluated by integrating the signal PDF over the bin range. The expected number of background events is given by the integral b of the background PDF over the signal bin range, multiplied by the total number N_r of collected events. Since we will consider $N_r = 10^6 \div 10^9$, we can approximate the bin content distribution to a Gaussian. Hence, the upper limit on the signal at 90% of CL is given by $1.64\sqrt{N_r b}/\epsilon$, where ϵ denotes the signal efficiency, which has two separate components: the absolute acceptance of the spectrometer for the signal and the signal bin efficiency, accounting for the finite bin size. The procedure can be repeated for several hypothesis of m_X . The results obtained for different datasets are shown in Figure 5.24.

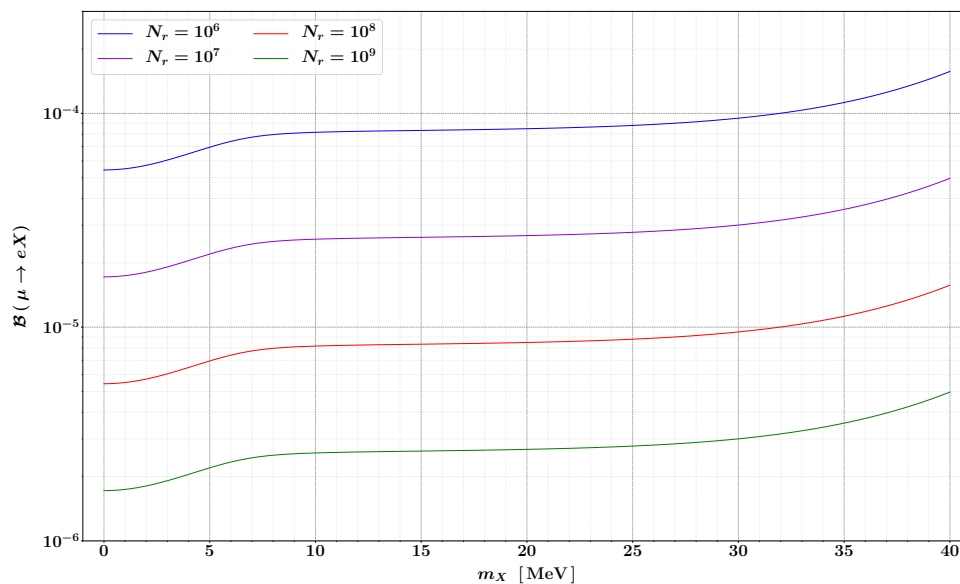


Figure 5.24 MEG II sensitivity on $\mu \rightarrow eX$ at 90% of CL by considering the statistical contribution only.

From a statistical point of view, we obtain the best sensitivities for low ALP masses: the

background is minimal close to the spectrum endpoint, while the signal acceptance is maximal. On the other hand, the sensitivity gets worse as the ALP mass increases, due to the lower acceptance of the spectrometer for low-energy positrons. The sensitivity can be further improved by considering the anisotropy induced by the muon polarisation for different assumptions of $\mu \rightarrow eX$ couplings. A simple way to quantify this effect is to split the event counting between the forward region $\cos\theta_e > 0$ and the backward region $\cos\theta_e < 0$. The results obtained for the usual four cases (V, A, V-A, V+A) are shown in Figure 5.25. Since the spectrometer does not cover the upstream and downstream regions $|\cos\theta_e| > 0.35$, where the polarisation effect is more pronounced, the difference amongst the different coupling assumptions is minimal. In the following we imply the V-A case.

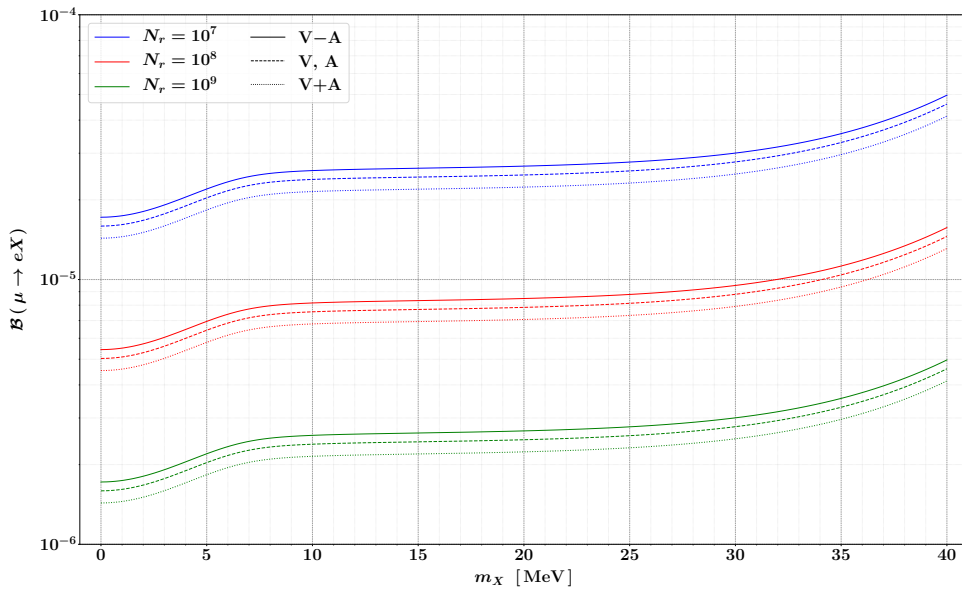


Figure 5.25 MEG II sensitivity on $\mu \rightarrow eX$ at 90% of CL for different assumptions of ALP couplings.

A first important correction to the previous evaluation is given by the inclusion of the theoretical error on the background. In this regard, we vary the background PDF as

$$[\mathcal{E}_e \times \mathcal{A}_e] \otimes \Sigma_e \quad \longrightarrow \quad [(\mathcal{E}_e \pm \delta\mathcal{E}_e) \times \mathcal{A}_e] \otimes \Sigma_e \quad (5.9)$$

where $\delta\mathcal{E}_e$ is given by the theoretical uncertainty (cf. Section 2.7). The maximal variation of signal bin content, w.r.t the null error hypothesis, is then added in quadrature to the contribution coming from the statistical fluctuations. Furthermore, the procedure is repeated at NLO, in order to evaluate the importance of the new radiative corrections. Both results are reported in Figure 5.26. Since the theoretical uncertainty is greater close to the spectrum endpoint, it is relevant for low masses only. The worsening effect is only

visible at NLO, confirming the importance of the NNLO+LL corrections in this context.

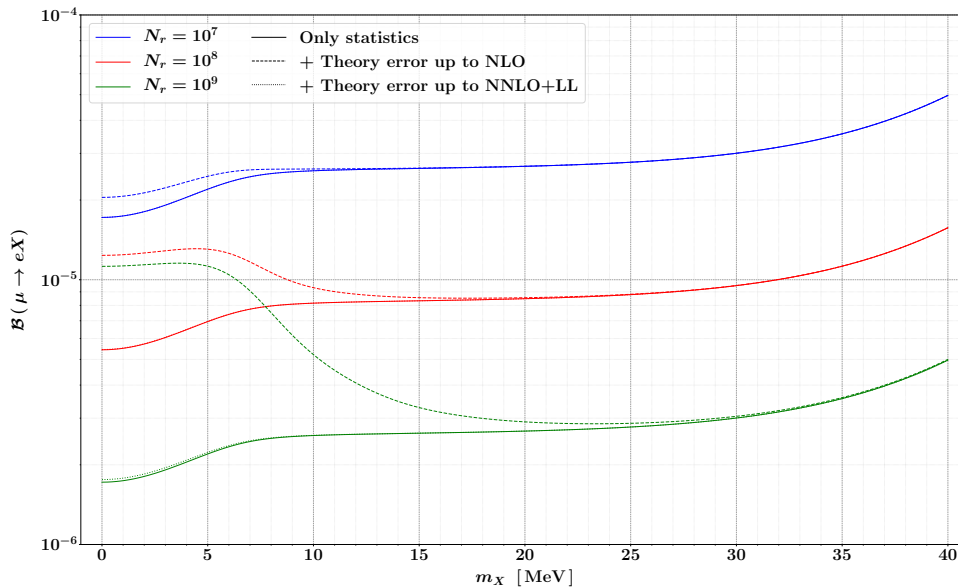


Figure 5.26 MEG II sensitivity on $\mu \rightarrow eX$ at 90% of CL including the theoretical uncertainty.

5.5.2 Systematics

In addition to the statistical and theoretical contributions, we need to consider the presence of potential bias in the positron reconstruction, especially in the determination of the absolute energy scale. The main systematic effects are the following.

Magnetic field knowledge: The track fitting routine requires a very accurate map of the magnetic field in order to extract the positron momentum from the CDCH hits. A difference between the assumed magnetic field and the real one directly results in a bias in the measurement of the positron energy. In this regard, MEG II will use the novel HallCube sensor [150] to perform a punctual survey of the COBRA magnetic field with a precision of $\delta B/B \sim 10^{-4}$. Such an uncertainty results in a systematic error of $0 \div 5$ keV on the positron energy.

Target energy deposit: A precise measurement of the positron energy requires an accurate evaluation of the positron energy loss inside the target. The effect depends on the position of the muon decay, especially its depth. The uncertainty on the vertex reconstruction, much greater than the target thickness, results in a systematic error of $0 \div 5$ keV on the positron energy.

Drift cells deformation: A deep knowledge of the CDCH geometry is required to precisely locate the positron hit position. Although the electrostatic and gravitational effects on the wires is simulated in the `gem4` module, a potential bias of $0 \div 5$ keV must be accounted.

To include the effect of a bias in the absolute energy scale on the sensitivity, we repeat the cut-and-count procedure for different PDFs by introducing a certain offset in the positron energy. The maximal variation of signal bin content, w.r.t the null offset hypothesis, is then added in quadrature to the statistical and theoretical contributions. The results for different offsets and statistics are shown in Figures 5.27, 5.28 and 5.29. We note that the effect is maximal for small ALP masses: since the background decreases very quickly close to the endpoint, a small energy offset reproduces a monochromatic-like signal around $E_e \approx 52.8$ MeV. A very accurate calibration of the spectrometer absolute energy scale, including a punctual control of the systematic effects, is therefore an essential prerequisite to search for $\mu \rightarrow eX$ with $m_X < 10$ MeV. Otherwise, the risk of bias-induced false signals is considerable and must be considered.

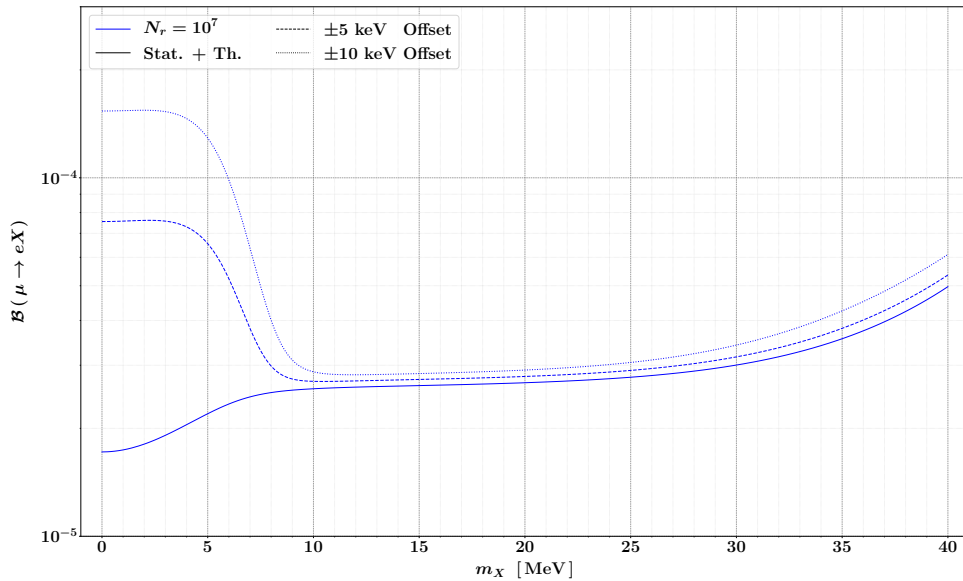


Figure 5.27 MEG II sensitivity on $\mu \rightarrow eX$ at 90% of CL including the effect of an offset in the absolute energy scale ($N_r = 10^7$).

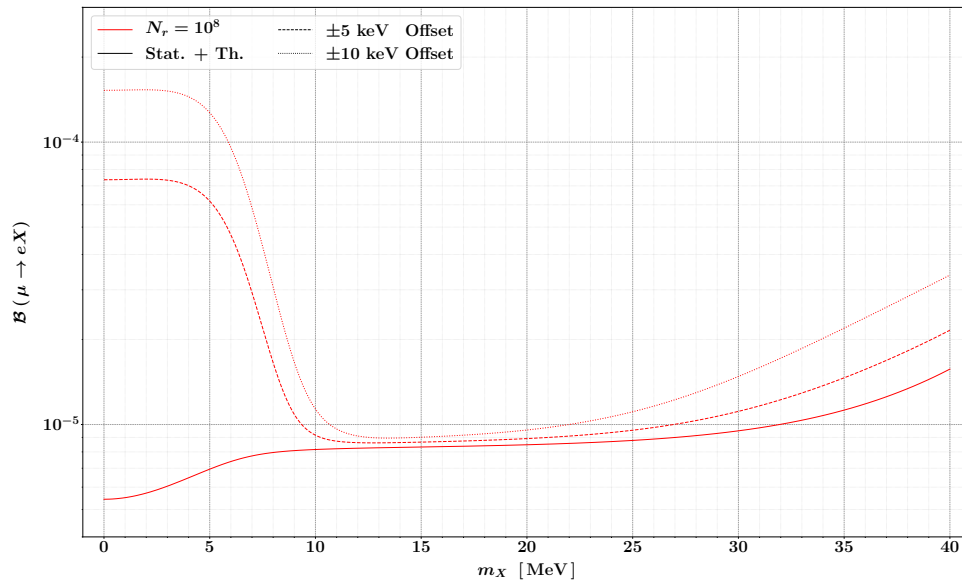


Figure 5.28 MEG II sensitivity on $\mu \rightarrow eX$ at 90% of CL including the effect of an offset in the absolute energy scale ($N_r = 10^8$).

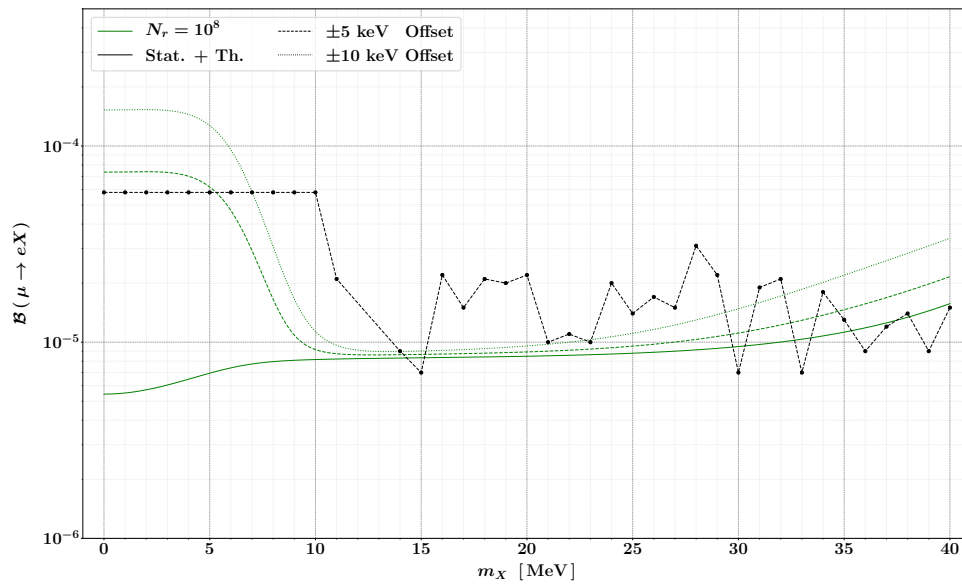


Figure 5.29 MEG II sensitivity on $\mu \rightarrow eX$ at 90% of CL including the effect of an offset in the absolute energy scale ($N_r = 10^9$). The black points correspond to the upper limits set by the TWIST collaboration at 90% of CL for V-A couplings [25].

Chapter 6

Conclusion and outlook

In this thesis we studied the feasibility of searching for $\mu \rightarrow eX$ with the MEG II experiment, working on the theoretical and experimental prerequisites of hunting such an elusive signal. In this regard, a fully-differential higher-order computation of the signal $\mu \rightarrow eX$ and its background $\mu \rightarrow e\nu\bar{\nu}$, as well as an exhaustive MC simulation of the experimental search, have been presented. The fully-differential theoretical predictions on the SM decay $\mu \rightarrow e\nu\bar{\nu}$ have never been computed so precisely as in this thesis.

All theoretical predictions have been computed in the context of the MCMULE framework, which has been optimised and further developed on purpose. MCMULE is the first comprehensive MC framework for the computation of fully-differential NNLO corrections to low-energy processes involving leptons. In the next years, it has all the potential to be a valuable tool for the new generation of experiments at the intensity frontier.

As well-known, once a mule sets out, it is very difficult to stop it. The next important step in the MCMULE's development is the implementation of a QED parton shower (PS) to arbitrarily resum the leading logarithmic terms. In this regard, the initial state collinear logarithms can be resummed by using the parton distribution function (PDF) approach, while the final state collinear logarithms can be resummed through the fragmentation function formalism. Furthermore, since the FKS^ℓ already exploits the YFS structure of soft singularities, MCMULE is particularly inclined to employ it to resum the soft logarithms too.

The physics run of MEG II is expected to start in 2021. After three years of data taking, the experiment is expected to reach an unprecedented sensitivity of

$$\mathcal{B}(\mu \rightarrow e\gamma) = 6 \cdot 10^{-14} \quad \text{at 90\% CL}$$

In addition, the search for processes in which the lepton flavour violation is mediated by a light axion-like particle, turns out to be a reliable opportunity for MEG II to complement the main search for $\mu \rightarrow e\gamma$ with further competitive physics channels. In the specific case of $\mu \rightarrow eX$, the experimental sensitivity is strongly dependent on the control of the systematic effects on the positron energy absolute scale. In this regard, new calibration

methods based on the Mott scattering and the pion decay are currently in development. Furthermore, the feasibility of employing an auxiliary upstream detector, to cover the region left out by the positron spectrometer, is under investigation. An additional upstream detector would allow to exploit the muon polarisation effect on the positron trajectory to reject the SM background, when assuming V+A couplings for the signal. The proposed detector is an electromagnetic calorimeter consisting of a large LYSO (or LaBr₃:Ce) crystal coupled to SiPMs on both sides.

As a result of this thesis, a new working group that brings together experimental and theoretical physicists has been created, in order to continue providing very precise predictions to the MEG II experiment, exploiting as much as possible the synergy between experimental and theoretical physics. The new group is informally called the MEGMULE collaboration [151].

Appendix A

Conventions

System of units

As usual in QFT, we adopted the Heaviside-Lorentz system of units with the choice $\hbar = c = 1$. In this scheme the fine-structure constant becomes

$$\alpha = \frac{e^2}{4\pi} \simeq \frac{1}{137} \quad (\text{A.1})$$

Minkowski space

The Minkowski metric is chosen in the time-like form

$$\eta_{\mu\nu} = \text{diag}(+1, -1, -1, -1) \quad (\text{A.2})$$

Numerical constants

In the numerical evaluations we used the following physical constants, in agreement with the latest review of PDG [152].

Fine-structure constant	$\alpha = 1/137.035999084(21)$
Fermi coupling constant	$G_F = 1.1663787(6) \cdot 10^{-11} \text{ MeV}^{-2}$
Electron mass	$m_e = 0.5109989461(31) \text{ MeV}$
Muon mass	$m_\mu = 105.6583745(25) \text{ MeV}$
Muon mean lifetime	$\tau_\mu = 2.1969811(22) \mu\text{s}$
Conversion constant	$\hbar c = 197.3269804 \text{ MeV fm}$

Acknowledgement

Many deserve my deepest gratitude and must be mentioned by name.

Angela for being the most important teacher of my entire student career. For every advice, correction, explanation, rebuke and encouragement of the last two years. And most importantly, for teaching me what truly means to be a good physicist.

Adrian for introducing me in this wonderful braying project called MCMULE. It was a great honour to be a baby donkey!

Yannick for his constant support throughout this thesis. For answering all my questions with a unique availability, competence and kindness.

Patrick for his indispensable assistance with the MEG II software. And of course for all the chocolate!

All members of the MEG II and MCMULE collaborations for welcoming me in their groups. The gratitude doubles for the members of the MEGMULE collaboration!

Alessio for all his advice on coding and life. And most importantly, for always believing in me, no matter how weird that *me* was.

The Panda's group (Alessandro, Giacomo, Giorgio, Luca⁷ and Matteo) for being my travel companions in the last five years, literally and metaphorically speaking.

My family (mum, dad, sister and bunnies) for their indispensable support in the most difficult moments of this thesis. But especially for teaching me that any goal is achievable with enough dedication and effort.

⁷Giamba

Bibliography

- [1] L. Calibbi and G. Signorelli, *Charged Lepton Flavour Violation: An Experimental and Theoretical Introduction*, *Riv. Nuovo Cim.* **41** (2018) 71 [[1709.00294](#)].
- [2] SUPER-KAMIOKANDE collaboration, Y. Fukuda et al., *Evidence for oscillation of atmospheric neutrinos*, *Phys. Rev. Lett.* **81** (1998) 1562 [[hep-ex/9807003](#)].
- [3] COMET, MEG, MU2E AND MU3E collaboration, A. Baldini et al., *Charged Lepton Flavour Violation using Intense Muon Beams at Future Facilities*, .
- [4] MEG II collaboration, A. Baldini et al., *The design of the MEG II experiment*, *Eur. Phys. J. C* **78** (2018) 380 [[1801.04688](#)].
- [5] M. Seidel et al., *Production of a 1.3 MW Proton Beam at PSI*, *Conf. Proc. C* (2010) TUYRA03.
- [6] MEG collaboration, J. Adam et al., *The MEG detector for $\mu^+ \rightarrow e^+\gamma$ decay search*, *Eur. Phys. J. C* **73** (2013) 2365 [[1303.2348](#)].
- [7] MEG collaboration, A. Baldini et al., *Search for the lepton flavour violating decay $\mu^+ \rightarrow e^+\gamma$ with the full dataset of the MEG experiment*, *Eur. Phys. J. C* **76** (2016) 434 [[1605.05081](#)].
- [8] L. Calibbi, D. Redigolo, R. Ziegler and J. Zupan, *Looking forward to Lepton-flavor-violating ALPs*, *arXiv eprint* (2020) [[2006.04795](#)].
- [9] C. Cornella, P. Paradisi and O. Sumensari, *Hunting for ALPs with Lepton Flavor Violation*, *JHEP* **01** (2020) 158 [[1911.06279](#)].
- [10] J. L. Feng, T. Moroi, H. Murayama and E. Schnapka, *Third generation familons, b factories, and neutrino cosmology*, *Phys. Rev. D* **57** (1998) 5875 [[hep-ph/9709411](#)].
- [11] Y. Chikashige, R. N. Mohapatra and R. Peccei, *Are There Real Goldstone Bosons Associated with Broken Lepton Number?*, *Phys. Lett. B* **98** (1981) 265.
- [12] J. Schechter and J. Valle, *Neutrino Decay and Spontaneous Violation of Lepton Number*, *Phys. Rev. D* **25** (1982) 774.

- [13] G. Gelmini and M. Roncadelli, *Left-Handed Neutrino Mass Scale and Spontaneously Broken Lepton Number*, *Phys. Lett. B* **99** (1981) 411.
- [14] F. Wilczek, *Axions and Family Symmetry Breaking*, *Phys. Rev. Lett.* **49** (1982) 1549.
- [15] D. B. Reiss, *Can the Family Group Be a Global Symmetry?*, *Phys. Lett. B* **115** (1982) 217.
- [16] J. E. Kim, *Light Pseudoscalars, Particle Physics and Cosmology*, *Phys. Rept.* **150** (1987) 1.
- [17] R. Peccei and H. R. Quinn, *CP Conservation in the Presence of Pseudoparticles*, *Phys. Rev. Lett.* **38** (1977) 1440.
- [18] R. Peccei and H. R. Quinn, *Constraints Imposed by CP Conservation in the Presence of Pseudoparticles*, *Phys. Rev. D* **16** (1977) 1791.
- [19] F. Wilczek, *Problem of Strong P and T Invariance in the Presence of Instantons*, *Phys. Rev. Lett.* **40** (1978) 279.
- [20] S. Weinberg, *A New Light Boson?*, *Phys. Rev. Lett.* **40** (1978) 223.
- [21] M. Chiappini et al., *Commissioning of the MEG II tracker system*, *JINST* **15** (2020) C06056 [2005.02242].
- [22] G. Tassielli et al., *The Drift Chamber of the MEG II experiment*, *JINST* **15** (2020) C09051 [2006.02378].
- [23] M. Chiappini, *The construction and commissioning of the ultra low mass MEG II drift chamber for the search of the $\mu^+ \rightarrow e^+\gamma$ decay*. PhD thesis, University of Siena, 2019.
- [24] R. Henderson et al., *Precision planar drift chambers and cradle for the TWIST muon decay spectrometer*, *Nucl. Instrum. Meth. A* **548** (2005) 306 [hep-ex/0409066].
- [25] TWIST collaboration, R. Bayes et al., *Search for two body muon decay signals*, *Phys. Rev. D* **91** (2015) 052020 [1409.0638].
- [26] P. Banerjee, T. Engel, A. Signer and Y. Ulrich, *QED at NNLO with McMule*, *SciPost Phys.* **9** (2020) 027 [2007.01654].
- [27] Y. Ulrich, *McMule - QED Corrections for Low-Energy Experiments*, PhD Thesis, University of Zurich (2020) [2008.09383].

-
- [28] McMULE collaboration, P. Banerjee, T. Engel, L. Gurgone, N. Schalch, A. Signer and Y. Ulrich, *McMule User Manual*. <https://gitlab.com/mule-tools/manual>, 2020.
- [29] Z. Bern and D. A. Kosower, *The Computation of loop amplitudes in gauge theories*, *Nucl. Phys. B* **379** (1992) 451.
- [30] A. Signer and D. Stockinger, *Using Dimensional Reduction for Hadronic Collisions*, *Nucl. Phys. B* **808** (2009) 88 [0807.4424].
- [31] R. A. Fazio, P. Mastrolia, E. Mirabella and W. J. Torres Bobadilla, *On the Four-Dimensional Formulation of Dimensionally Regulated Amplitudes*, *Eur. Phys. J. C* **74** (2014) 3197 [1404.4783].
- [32] C. Gnendiger et al., *To d, or not to d: recent developments and comparisons of regularization schemes*, *Eur. Phys. J. C* **77** (2017) 471 [1705.01827].
- [33] T. Engel, A. Signer and Y. Ulrich, *A subtraction scheme for massive QED*, *JHEP* **01** (2020) 085 [1909.10244].
- [34] S. Frixione, Z. Kunszt and A. Signer, *Three jet cross-sections to next-to-leading order*, *Nucl. Phys. B* **467** (1996) 399 [hep-ph/9512328].
- [35] R. Frederix, S. Frixione, F. Maltoni and T. Stelzer, *Automation of next-to-leading order computations in QCD: The FKS subtraction*, *JHEP* **10** (2009) 003 [0908.4272].
- [36] G. Lepage, *A New Algorithm for Adaptive Multidimensional Integration*, *J. Comput. Phys.* **27** (1978) 192.
- [37] G. Lepage, *VEGAS: An Adaptive Multidimensional Integration Program*. <https://lib-extopc.kek.jp/preprints/PDF/1980/8006/8006210.pdf>.
- [38] G. P. Lepage, *Adaptive Multidimensional Integration: VEGAS Enhanced*, 2009.05112.
- [39] D. Yennie, S. C. Frautschi and H. Suura, *The infrared divergence phenomena and high-energy processes*, *Annals Phys.* **13** (1961) 379.
- [40] P. W. Cattaneo, F. Cei, R. Sawada, M. Schneebeli and S. Yamada, *The Architecture of MEG Simulation and Analysis Software*, *Eur. Phys. J. Plus* **126** (2011) 60 [1102.0106].
- [41] T. Engel, C. Gnendiger, A. Signer and Y. Ulrich, *Small-mass effects in heavy-to-light form factors*, *JHEP* **02** (2019) 118 [1811.06461].

- [42] A. Penin, *Two-loop photonic corrections to massive Bhabha scattering*, *Nucl. Phys. B* **734** (2006) 185 [[hep-ph/0508127](#)].
- [43] A. A. Penin, *Two-loop corrections to Bhabha scattering*, *Phys. Rev. Lett.* **95** (2005) 010408 [[hep-ph/0501120](#)].
- [44] A. Mitov and S. Moch, *The Singular behavior of massive QCD amplitudes*, *JHEP* **05** (2007) 001 [[hep-ph/0612149](#)].
- [45] T. Becher and K. Melnikov, *Two-loop QED corrections to Bhabha scattering*, *JHEP* **06** (2007) 084 [[0704.3582](#)].
- [46] A. Blondel et al., *Research Proposal for an Experiment to Search for the Decay $\mu \rightarrow eee$* , [1301.6113](#).
- [47] MU3E collaboration, K. Arndt et al., *Technical design of the phase I Mu3e experiment*, [2009.11690](#).
- [48] MUSE collaboration, J. Arrington et al., *A Proposal for the Paul Scherrer Institute π M1 beam line: Studying the Proton “Radius” Puzzle with μp Elastic Scattering*, .
- [49] BELLE-II collaboration, T. Abe et al., *Belle II Technical Design Report*, [1011.0352](#).
- [50] BELLE-II collaboration, W. Altmannshofer et al., *The Belle II Physics Book*, *PTEP* **2019** (2019) 123C01 [[1808.10567](#)].
- [51] C. Carloni Calame, M. Passera, L. Trentadue and G. Venanzoni, *A new approach to evaluate the leading hadronic corrections to the muon $g-2$* , *Phys. Lett. B* **746** (2015) 325 [[1504.02228](#)].
- [52] U. Marconi and F. Piccinini, *Measuring the leading hadronic contribution to the muon $g-2$ via the μ - e elastic scattering.*, *EPJ Web Conf.* **179** (2018) 01012.
- [53] MUONE collaboration, *Letter of Intent: The MUonE Project*, *CERN-SPSC-2019-026*, 2019.
- [54] M. Raggi and V. Kozhuharov, *Proposal to Search for a Dark Photon in Positron on Target Collisions at DAΦNE Linac*, *Adv. High Energy Phys.* **2014** (2014) 959802 [[1403.3041](#)].
- [55] D. Becker et al., *The P2 experiment*, [1802.04759](#).
- [56] E. S. Group, *2020 Update of the European Strategy for Particle Physics*. CERN Council, Geneva, 2020, [10.17181/ESU2020](#).
- [57] FCC collaboration, A. Abada et al., *FCC-ee: The Lepton Collider: Future Circular Collider Conceptual Design Report Volume 2*, *Eur. Phys. J. ST* **228** (2019) 261.

-
- [58] M. Aicheler et al., *Conceptual Design Report – eSPS*, 2009.06938.
- [59] CLIC collaboration, T. Charles et al., *The Compact Linear Collider (CLIC) - 2018 Summary Report*, 1812.06018.
- [60] T. Behnke, J. E. Brau, B. Foster, J. Fuster, M. Harrison, J. M. Paterson, M. Peskin, M. Stanitzki, N. Walker and H. Yamamoto, *The International Linear Collider Technical Design Report - Volume 1: Executive Summary*, 1306.6327.
- [61] CEPC collaboration, S. Group, *CEPC Conceptual Design Report: Volume 1 - Accelerator*, 1809.00285.
- [62] C. M. Ankenbrandt et al., *Status of muon collider research and development and future plans*, *Phys. Rev. ST Accel. Beams* **2** (1999) 081001 [physics/9901022].
- [63] MUON G-2 collaboration, J. Grange et al., *Muon (g-2) Technical Design Report*, 1501.06858.
- [64] MU2E collaboration, L. Bartoszek et al., *Mu2e Technical Design Report*, 1501.05241.
- [65] M. Abe et al., *A New Approach for Measuring the Muon Anomalous Magnetic Moment and Electric Dipole Moment*, *PTEP* **2019** (2019) 053C02 [1901.03047].
- [66] COMET collaboration, R. Abramishvili et al., *COMET Phase-I Technical Design Report*, *PTEP* **2020** (2020) 033C01 [1812.09018].
- [67] LHCb collaboration, *Letter of Intent for the LHCb Upgrade*, *CERN-LHCC-2011-001*, 2011.
- [68] T. Kinoshita, *Mass singularities of Feynman amplitudes*, *J. Math. Phys.* **3** (1962) 650.
- [69] T. Lee and M. Nauenberg, *Degenerate Systems and Mass Singularities*, *Phys. Rev.* **133** (1964) B1549.
- [70] C. Bollini and J. Giambiagi, *Dimensional Renormalization: The Number of Dimensions as a Regularizing Parameter*, *Nuovo Cim. B* **12** (1972) 20.
- [71] G. 't Hooft and M. Veltman, *Regularization and Renormalization of Gauge Fields*, *Nucl. Phys. B* **44** (1972) 189.
- [72] K. G. Wilson, *The Renormalization Group and Strong Interactions*, *Phys. Rev. D* **3** (1971) 1818.

- [73] J. C. Collins, *Renormalization: An Introduction to Renormalization, The Renormalization Group, and the Operator Product Expansion*, vol. 26 of *Cambridge Monographs on Mathematical Physics*. Cambridge University Press, Cambridge, 1986, [10.1017/CBO9780511622656](https://doi.org/10.1017/CBO9780511622656).
- [74] Z. Bern and A. Morgan, *Massive loop amplitudes from unitarity*, *Nucl. Phys. B* **467** (1996) 479 [[hep-ph/9511336](https://arxiv.org/abs/hep-ph/9511336)].
- [75] J. Korner, D. Kreimer and K. Schilcher, *A Practicable $\gamma(5)$ scheme in dimensional regularization*, *Z. Phys. C* **54** (1992) 503.
- [76] D. Kreimer, *The Role of $\gamma(5)$ in dimensional regularization*, [hep-ph/9401354](https://arxiv.org/abs/hep-ph/9401354).
- [77] P. Breitenlohner and D. Maison, *Dimensional Renormalization and the Action Principle*, *Commun. Math. Phys.* **52** (1977) 11.
- [78] C. Gnendiger and A. Signer, *γ_5 in the four-dimensional helicity scheme*, *Phys. Rev. D* **97** (2018) 096006 [[1710.09231](https://arxiv.org/abs/1710.09231)].
- [79] S. Larin, *The Renormalization of the axial anomaly in dimensional regularization*, *Phys. Lett. B* **303** (1993) 113 [[hep-ph/9302240](https://arxiv.org/abs/hep-ph/9302240)].
- [80] I. Bierenbaum, M. Czakon and A. Mitov, *The singular behavior of one-loop massive QCD amplitudes with one external soft gluon*, *Nucl. Phys. B* **856** (2012) 228 [[1107.4384](https://arxiv.org/abs/1107.4384)].
- [81] S. Catani and M. Grazzini, *The soft gluon current at one loop order*, *Nucl. Phys. B* **591** (2000) 435 [[hep-ph/0007142](https://arxiv.org/abs/hep-ph/0007142)].
- [82] Y. Ulrich, *Private communication*, 2020.
- [83] T. Engel, *Two-loop corrections to the muon decay*. Master thesis, ETHZ, 2018.
- [84] L.-B. Chen, *Two-Loop master integrals for heavy-to-light form factors of two different massive fermions*, *JHEP* **02** (2018) 066 [[1801.01033](https://arxiv.org/abs/1801.01033)].
- [85] J. Currie, T. Gehrmann, E. Glover, A. Huss, J. Niehues and A. Vogt, *N^3LO corrections to jet production in deep inelastic scattering using the Projection-to-Born method*, *JHEP* **05** (2018) 209 [[1803.09973](https://arxiv.org/abs/1803.09973)].
- [86] A. Denner, S. Dittmaier and L. Hofer, *Collier: a fortran-based Complex One-Loop Library in Extended Regularizations*, *Comput. Phys. Commun.* **212** (2017) 220 [[1604.06792](https://arxiv.org/abs/1604.06792)].
- [87] A. Denner and S. Dittmaier, *Scalar one-loop 4-point integrals*, *Nucl. Phys.* **B844** (2011) 199 [[1005.2076](https://arxiv.org/abs/1005.2076)].

-
- [88] A. Denner and S. Dittmaier, *Reduction schemes for one-loop tensor integrals*, *Nucl. Phys.* **B734** (2006) 62 [[hep-ph/0509141](#)].
- [89] A. Denner and S. Dittmaier, *Reduction of one loop tensor five point integrals*, *Nucl. Phys.* **B658** (2003) 175 [[hep-ph/0212259](#)].
- [90] S. v. d. Walt, S. C. Colbert and G. Varoquaux, *The numpy array: A structure for efficient numerical computation*, *Computing in Science & Engineering* **13** (2011) 22.
- [91] J. D. Hunter, *Matplotlib: A 2d graphics environment*, *Computing in Science & Engineering* **9** (2007) 90.
- [92] P. Nogueira, *Automatic Feynman graph generation*, *J. Comput. Phys.* **105** (1993) 279.
- [93] H. H. Patel, *Package-X: A Mathematica package for the analytic calculation of one-loop integrals*, *Comput. Phys. Commun.* **197** (2015) 276 [[1503.01469](#)].
- [94] D. Maitre, *HPL, a mathematica implementation of the harmonic polylogarithms*, *Comput. Phys. Commun.* **174** (2006) 222 [[hep-ph/0507152](#)].
- [95] D. Maitre, *Extension of HPL to complex arguments*, *Comput. Phys. Commun.* **183** (2012) 846 [[hep-ph/0703052](#)].
- [96] G. Passarino and M. Veltman, *One Loop Corrections for $e^+ e^-$ Annihilation Into $\mu^+ \mu^-$ in the Weinberg Model*, *Nucl. Phys. B* **160** (1979) 151.
- [97] T. Ohl, *Vegas revisited: Adaptive Monte Carlo integration beyond factorization*, *Comput. Phys. Commun.* **120** (1999) 13 [[hep-ph/9806432](#)].
- [98] E. Remiddi and J. Vermaseren, *Harmonic polylogarithms*, *Int. J. Mod. Phys. A* **15** (2000) 725 [[hep-ph/9905237](#)].
- [99] T. Aoyama, M. Hayakawa, T. Kinoshita and M. Nio, *Complete Tenth-Order QED Contribution to the Muon $g-2$* , *Phys. Rev. Lett.* **109** (2012) 111808 [[1205.5370](#)].
- [100] B. P. Kersevan and E. Richter-Was, *The Monte Carlo event generator AcerMC versions 2.0 to 3.8 with interfaces to PYTHIA 6.4, HERWIG 6.5 and ARIADNE 4.1*, *Comput. Phys. Commun.* **184** (2013) 919 [[hep-ph/0405247](#)].
- [101] J. Alwall, R. Frederix, S. Frixione, V. Hirschi, F. Maltoni, O. Mattelaer, H. S. Shao, T. Stelzer, P. Torrielli and M. Zaro, *The automated computation of tree-level and next-to-leading order differential cross sections, and their matching to parton shower simulations*, *JHEP* **07** (2014) 079 [[1405.0301](#)].

- [102] G. Garberoglio and A. H. Harvey, *Path-integral calculation of the third virial coefficient of quantum gases at low temperatures*, *J. Chem. Phys.* **134** (2011) 134106.
- [103] J. S. Dehesa et al., *Quantum entanglement in helium*, *J. Phys. B: At. Mol. Opt. Phys.* **45** (2012) 015504.
- [104] D. Varjas, F. de Juan and Y. M. Lu, *Bulk invariants and topological response in insulators and superconductors with nonsymmorphic symmetries*, *Phys. Rev. B* **92** (2015) 195116.
- [105] J. L. Sanders, *Probabilistic model for constraining the Galactic potential using tidal streams*, *Mon. Not. R. Astron. Soc.* **443** (2014) 423.
- [106] K. Gultekin et al., *The $M - \sigma$ and $M - L$ Relations In Galactic Bulges, and Determination of their Intrinsic Scatter*, *Astrophys. J.* **698** (2009) 198.
- [107] G. Campolieti and R. Makarov, *Pricing Path-Dependent Options on State Dependent Volatility Models with a Bessel Bridge*, *Int. J. Theor. Appl. Finance* **10** (2007) 51.
- [108] J. Ray, Y. M. Marzouk and H. N. Najm, *A Bayesian approach for estimating bioterror attacks from patient data*, *Statist. Med.* **30** (2011) 101.
- [109] F. M. Atay and A. Hutt, *Neural Fields with Distributed Transmission Speeds and Long-Range Feedback Delays*, *SIAM J. Appl. Dyn. Sys.* **5** (2006) 670.
- [110] S. Dittmaier, *A General approach to photon radiation off fermions*, *Nucl. Phys. B* **565** (2000) 69 [[hep-ph/9904440](#)].
- [111] C. Gnendiger, A. Signer and D. Stöckinger, *The infrared structure of QCD amplitudes and $H \rightarrow gg$ in FDH and DRED*, *Phys. Lett. B* **733** (2014) 296 [[1404.2171](#)].
- [112] C. Gnendiger, A. Signer and A. Visconti, *Regularization-scheme dependence of QCD amplitudes in the massive case*, *JHEP* **10** (2016) 034 [[1607.08241](#)].
- [113] R. Behrends, R. Finkelstein and A. Sirlin, *Radiative corrections to decay processes*, *Phys. Rev.* **101** (1956) 866.
- [114] T. Kinoshita and A. Sirlin, *Radiative corrections to Fermi interactions*, *Phys. Rev.* **113** (1959) 1652.
- [115] A. Arbuzov, *First order radiative corrections to polarized muon decay spectrum*, *Phys. Lett. B* **524** (2002) 99 [[hep-ph/0110047](#)].

-
- [116] A. Jodidio et al., *Search for Right-Handed Currents in Muon Decay*, *Phys. Rev. D* **34** (1986) 1967.
- [117] C. Anastasiou, K. Melnikov and F. Petriello, *The Electron energy spectrum in muon decay through $O(\alpha^{**2})$* , *JHEP* **09** (2007) 014 [[hep-ph/0505069](#)].
- [118] R. Feynman and M. Gell-Mann, *Theory of Fermi interaction*, *Phys. Rev.* **109** (1958) 193.
- [119] M. Fael, L. Mercolli and M. Passera, *W-propagator corrections to μ and τ leptonic decays*, *Phys. Rev. D* **88** (2013) 093011 [[1310.1081](#)].
- [120] A. I. Davydychev, K. Schilcher and H. Spiesberger, *Hadronic corrections to the muon decay*, in *16th International Workshop on High Energy Physics and Quantum Field Theory (QFTHEP 2001)*, pp. 214–221, 3, 2002, [hep-ph/0203125](#).
- [121] S. M. Berman and A. Sirlin, *Some considerations on the radiative corrections to muon and neutron decay*, *Annals of Physics* **20** (1963) .
- [122] MEG collaboration, A. Baldini et al., *Muon polarization in the MEG experiment: predictions and measurements*, *Eur. Phys. J. C* **76** (2016) 223 [[1510.04743](#)].
- [123] A. Arbuzov, *Higher order QED corrections to muon decay spectrum*, *JHEP* **03** (2003) 063 [[hep-ph/0206036](#)].
- [124] M. Hirsch, A. Vicente, J. Meyer and W. Porod, *Majoron emission in muon and tau decays revisited*, *Phys. Rev. D* **79** (2009) 055023 [[0902.0525](#)].
- [125] Z. G. Berezhiani and A. Rossi, *Majoron decay in matter*, *Phys. Lett. B* **336** (1994) 439 [[hep-ph/9407265](#)].
- [126] J. Heeck and H. H. Patel, *Majoron at two loops*, *Phys. Rev. D* **100** (2019) 095015 [[1909.02029](#)].
- [127] Z. Berezhiani and M. Khlopov, *Physical and astrophysical consequences of breaking of the symmetry of families. (In Russian)*, *Sov. J. Nucl. Phys.* **51** (1990) 935.
- [128] K. Tsumura and L. Velasco-Sevilla, *Phenomenology of flavon fields at the LHC*, *Phys. Rev. D* **81** (2010) 036012 [[0911.2149](#)].
- [129] M. Bauer, T. Schell and T. Plehn, *Hunting the Flavon*, *Phys. Rev. D* **94** (2016) 056003 [[1603.06950](#)].
- [130] Y. Ema, K. Hamaguchi, T. Moroi and K. Nakayama, *Flaxion: a minimal extension to solve puzzles in the standard model*, *JHEP* **01** (2017) 096 [[1612.05492](#)].

- [131] L. Calibbi, F. Goertz, D. Redigolo, R. Ziegler and J. Zupan, *Minimal axion model from flavor*, *Phys. Rev. D* **95** (2017) 095009 [1612.08040].
- [132] O. Davidi, R. S. Gupta, G. Perez, D. Redigolo and A. Shalit, *The hierarchion, a relaxation addressing the Standard Model's hierarchies*, *JHEP* **08** (2018) 153 [1806.08791].
- [133] E. Ma, T. Ohata and K. Tsumura, *Majoron as the QCD axion in a radiative seesaw model*, *Phys. Rev. D* **96** (2017) 075039 [1708.03076].
- [134] J. Heeck and W. Rodejohann, *Lepton Flavor Violation with Displaced Vertices*, *Phys. Lett. B* **776** (2018) 385 [1710.02062].
- [135] M. Bauer, M. Neubert, S. Renner, M. Schnubel and A. Thamm, *Axionlike Particles, Lepton-Flavor Violation, and a New Explanation of a_μ and a_e* , *Phys. Rev. Lett.* **124** (2020) 211803 [1908.00008].
- [136] *In search of new physics - PSI Media*. <https://www.psi.ch/en/media/our-research/auf-der-suche-nach-einer-neuen-physik-en>.
- [137] *PSI LTP Facilities Home-Page*. <https://www.psi.ch/en/ltp/facilities>.
- [138] H. Fitze, M. Bopp, A. Mezger, J. Raguin, P. Schmelzbach and P. Sigg, *Developments at PSI (including new RF cavity)*, in *17th International Conference on Cyclotrons and Their Applications*, 2004.
- [139] R. Iwai, *Development and commissioning of MEG II Radiative Decay Counter*. Master thesis, The University of Tokyo, 2017.
- [140] MEG collaboration, A. Baldini et al., *Search for lepton flavour violating muon decay mediated by a new light particle in the MEG experiment*, *Eur. Phys. J. C* **80** (2020) 858 [2005.00339].
- [141] M. Nakao, *Search for lepton flavor violating muon decay mediated by a new light particle in the MEG experiment*, Ph.D. thesis, Tokyo U., 2020.
- [142] GEANT4 collaboration, S. Agostinelli et al., *GEANT4—a simulation toolkit*, *Nucl. Instrum. Meth. A* **506** (2003) 250.
- [143] *Garfield - simulation of gaseous detectors*. <http://garfield.web.cern.ch/garfield/>.
- [144] J. Zoll et al., *ZEBRA : Overview of the ZEBRA System*. <https://cds.cern.ch/record/2296399?ln=it>, 2017.

-
- [145] J. Rauch and T. Schlüter, *GENFIT — a Generic Track-Fitting Toolkit*, *J. Phys. Conf. Ser.* **608** (2015) 012042 [[1410.3698](#)].
- [146] R. E. Kalman, *A New Approach to Linear Filtering and Prediction Problems*, *Journal of Basic Engineering* **D82** (1960) .
- [147] P. Billoir, *Track Fitting With Multiple Scattering: A New Method*, *Nucl. Instrum. Meth. A* **225** (1984) 352.
- [148] R. Fruhwirth, *Application of Kalman filtering to track and vertex fitting*, *Nucl. Instrum. Meth. A* **262** (1987) 444.
- [149] M. Chiappini, *The new drift chamber of the MEG-II experiment in search for lepton flavor violations*. Master thesis, University of Pisa, 2016.
- [150] C. Wouters et al., *Design and fabrication of an innovative three-axis Hall sensor*, *Sensors and Actuators. A, Physical* **237** (2016) 6271.
- [151] P. Banerjee, T. Engel, A. Gurgone, A. Papa, A. Signer, P. Schwendimann and Y. Ulrich, *MegMule - Fully differential muon decay predictions at ultimate precision for the MEG II experiment*, 2020.
- [152] PARTICLE DATA GROUP collaboration, M. Tanabashi et al., *Review of Particle Physics*, *Phys. Rev. D* **98** (2018) 030001.